INVESTIGATION OF THE BEHAVIOR OF BEAM-COLUMN JOINTS (BCJS) REINFORCED WITH SHAPE MEMORY ALLOYS (SMAS)

BY

MOHAMMED ABDULKAREM AL-HURI

A Thesis Presented to the
DEANSHIP OF GRADUATE STUDIES

KING FAHD UNIVERSITY OF PETROLEUM & MINERALS
DHAHRAN, SAUDI ARABIA

In Partial Fulfillment of the
Requirements for the Degree of

MASTER OF SCIENCE

In

CIVIL ENGINEERING

MAY, 2016

KING FAHD UNIVERSITY OF PETROLEUM & MINERALS

DHAHRAN- 31261, SAUDI ARABIA

DEANSHIP OF GRADUATE STUDIES

This thesis, written by **MOHAMMED ABDULKAREM AL-HURI** under the direction of his thesis advisor and approved by his thesis committee, has been presented and accepted by the Dean of Graduate Studies, in partial fulfillment of the requirements for the degree of **MASTER OF SCIENCE IN CIVIL ENGINEERING.**

Dr. Ali H. Al-Gadhib
(Advisor)

Dr. Salah U. Al-Dulaijan
Department Chairman

Kalimur Rahman

Dr. Muhammad K. Rahman
(Co-Advisor)

Dr. Salam A. Zummo
Dean of Graduate Studies

Dr. Mohammed H. Baluch
(Member)

19/5/16
Date

Dr. Al Farabi M. Sharif
(Member)

Dr. Mohammed A. Al-Osta
(Member)

DEDICATED TO MY PARENTS,

MY WIFE, AND MY BELOVED SON

ACKNOWLEDGMENTS

In the name of ALLAH, the Most Beneficent, the Most Merciful

All grandeur and honor belong to Allah who provided me with endurance, intensity level, and patient to convey out and complete this work.

Foremost, I would like to express my gratitude and thankfulness to **King Fahd University of Petroleum and Minerals (KFUPM)**, and all the entire faculty members for supplying me with the best character education, which paved my path through my Master studies as well as my thesis work.

I would wish to convey my regards and thanks to my advisor **Dr. Ali H. AlGadhib** for his assistance and support during my research study. As well, I would like to pay my immense regards and admiration to my co-advisor **Dr. Muhammad K. Rahman** for his feedback, motivation, and consistent guidance during the course of this research study. He was always being with me during the experimental work as well as numerical simulation. In addition, he is perpetually there to offer me advice on shaping up my career and future destinations.

I would wish also to show my gratitude and thanks to the committee members **Dr. Mohammed H. Baluch, Dr. Al Farabi M. Sharif** and **Dr. Mohammed Al-Osta** for their assistance, efforts, and supports during the research study.

I owe many thanks to the PRAINSA Industrial Company for serving me in preparing and casting my specimens. As well, I am too much thankful to Mr. Abdulhamid from the RI who helped me in preparing, cutting, and ribbing, the SMA bars.

I owe thanks to Engr. Syed Khaja Najamuddin, Engr. Omer Hussein, & Engr. Syed Imran for their big assistance during testing of my specimens. Thanks also to my friends and colleagues at University for their Friendship during my graduate studies.

I would wish also to show my deep thanks to my beautiful country, Yemen, and Sana'a University for the great service and the financial support during my Master's studies.

Last, but more importantly, I owe many thanks to my beloved family: my parents for their indescribable love, support, and confidence, my wife for her patient, love, being always motivated me, encouraging me, and listening to me. In addition, I am thankful to my brothers and sisters for all their love and supports.

TABLE OF CONTENTS

LIST OF TABLES

LIST OF FIGURES

LIST OF ABBREVIATIONS

BCJ	:	Beam Column Joint
Con	:	Control
DSR	:	Deanship of Research
FEA	:	Finite Element Analysis
NiTi	:	Nickel Titanium
PGA	:	Peak Ground Acceleration
RC	:	Reinforced Concrete
SE	:	Super-Elastic Effect
SMA	:	Shape Memory Alloy
SME	:	Shape Memory Effect
SZN	:	Seismic Zone Number
UBC	:	Uniform Building Code
3 - D	:	Three Dimensional

ABSTRACT

Full Name	:	[MOHAMMED ABDULKAREM HUSSEIN AL-HURI]
Thesis Title	:	INVESTIGATION OF THE BEHAVIOR OF BEAM-COLUMN JOINTS (BCJS) REINFORCED WITH SHAPE MEMORY ALLOYS (SMAS)]
Major Field	:	[CIVIL ENGINEERING]
Date of Degree	:	[MAY, 2016]

Reinforced concrete structures consisting of moment resisting frames have been used generally as resisting systems for lateral loads. These structures are usually sustained devastation resulting from seismic and earthquakes, including collapse and damage where (BCJs) is specified as the weakest zone in the structural systems. If beam-column joints have the ability to retrieve their predetermined strength and shape after a seismic occurred, then many problems, which related to collapse and permanent damage, might be solved. Consequently, the purpose of the study is to predict intelligent BCJs that can experience to greater deformations yet retrieval potentially its predetermined structural integrity after seismic has occurred. Shape Memory Alloys (SMAs) material has the ability to construct of such intelligent reinforced concrete beam-column joints.

SMAs have a relatively smaller hysteretic loop and lower modulus of elasticity comparing to reinforcement, also have high resistance to fire and corrosion. Therefore, using SMAs for strengthening of RC- BCJs may enhance and restore ductility of the joints under different types of loading, making it very practical for the strengthening of RC structures.

This research proposal main objective is for Investigation the behavior of (BCJs) Reinforced with Shape Memory Alloys (SMAs). This investigation will initially show the factors influencing SMAs engineering characteristics, constitutive material models, and the fundamental properties. Furthermore, the investigation will focus on the behavior of BCJs under reverse cyclic and cyclic loading reinforced with super elastic SMAs.

Numerical simulation models of BCJ with and without SMAs will also be conducted by using suitable nonlinear finite element analysis software, which will help to interpret the monitored behavior of BCJs through comparison with the numerical simulation.

This work is done under the Deanship of Scientific Research (DSR) project number (IN121058). The main aim of this work is studying the behavior (BCJ) reinforced with shape memory alloy bars at critical section. All the specimens were prepared and cast at PRAINSA Company then they were conducted and tested in the KFUPM structural lab. Results from experimental tests have been used for the verification of Finite Element simulation of (BCJ).

ملخص الرسالة

الاسم الكامل: محمد عبدالكريم حسين الحوري

عنوان الرسالة: التحقق من كفاءه عناصر التقاء الجسور مع الأعمده عند تسليحها بقضبان تذكر الشكل SMA

التخصص: الهندسة المدنية

تاريخ الدرجة العلمية: مايو 2016

المباني الخرسانيه المسلحه المقاومه للقوى والاحمال الجانبيه كأحمال الرياح والزلازل تتكون من اطارات خاصه مقاومه للعزوم (SMRF) . هذه المباني تتعرض لتشوهات كبيره نتيجة تعرضها للاحمال والقوى الزلزاليه وخصوصا في مناطق الالتقاء بين الجسور والأعمده (BCJ). فإذا امكن تصميم مناطق الالتقاء (BCJ) بحيث يصبح عندها القدره على استرجاع مقاومتها وحالتها الاصليه بعد تعرضها للقوى الزلزاليه ، العديد من المشاكل المتعلقه بانهيارات المباني والمنشئات اثناء وقوع الزلازل سوف يتم تجنبها وبالتالي سيتم الحفاظ على الارواح والممتلكات. لذلك ، فإن الهدف من هذا البحث هو تصميم وانشاء مناطق الالتقاء (BCJ) بحيث تستطيع تحمل تشوهات كبيره ثم يكون لها القدره على الرجوع الى حالتها الاصليه بعد حصول الزلزال. ولكي يتم تصميم وانشاء مثل هذا النوع من مناطق الالتقاء (BCJ) سيتم استخدام ماده تذكر الشكل والتي تُعرف بإسم (SMA) والتي تستطيع من خلال مواصفاتها الخاصه ان تعود الى وضعها الاصلي بعد تعرضها لتشوهات كبيره.

في هذا البحث سيتم دراسة واستكشاف سلوك مناطق الالتقاء (BCJ) والتي يتم تسليحها بقضبان مادة (SMA) في مناطق المفاصل اللدنه والتي تُعرف بإسم (Plastic Hinges) تحت تأثير الاحمال والتشوهات المتناوبه (Cyclic and Reverse Cyclic Loads). هذه الدراسه سوف تشمل دراسة الخصائص الأساسيه والهندسيه لمادة (SMA) وكذلك العوامل والتأثيرات المختلفه لهذه الماده. بالإضافه الى ذلك سوف يتم دراسة سلوك مناطق الالتقاء (BCJ) والتي يتم تسليحها باستخدام حديد التسليح الاعتيادي (Steel Reinforcement) وكذلك المسلحه بقضبان تذكر الشكل (SMA) باستخدام طريقة العناصر المحدده (Finite Element Method) في برنامج التحليل العددي (ANSYS) .

CHAPTER 1

INTRODUCTION

1.1GENERAL

The beam column joints (BCJs) are considered the critical zone in the RC frame since it is the crucial element that subjected to greater loads during acute ground shakes. This behavior has a considerable impact on the behavior of structures, namely with reference to its energy dissipating capability and ductility.

Beam Column Joints (BCJs) could be classified into three parts. First, a strong column / weak beam, which becomes the best case since the collapse in beam is less crucial than the collapse in the column. Second, strong beam / weak column, if the plastic hinge starts to happen in the columns, the axial load will cause a quick degeneration to capable the joint to absorb energy, whereas undergoing cyclic motion. Finally, hinge being formed at the intersection point of the column and beam, which cause a large rotation both, in column and beam, in the conjugation of losing column the capacity of carrying loads and then the failure of the joint. Consequently, BCJs must have a unique attention for appropriate detailing and designing.

The BCJs must be detailed appropriately to guarantee sufficient ductility when a seismic event occurs. Ordinary structures are usually designed and constructed to be safe, where seismic energies are dissipated by yielding of steel bars and its deformations. The most essential design aspects include serviceability of essential facilities and safety of human lives. The earthquake design of structural elements has developed towards using new structural systems and members that have an improved ductility and deformation capacity, minimized and decreased residual crack sizes, higher damage tolerance, concrete confinement, reduced and recovered permanent deformations. If such a reinforced concrete BCJs could be constructed, this will open a new area for structural engineers to enhance the connection's design with improved ductility and reduced damage, therefore, terminating joint repairs after the seismic events. This aim can be accomplished by using SMAs instead of steel in reinforced concrete elements that has not been yet widely detected. If SMAs bars are used in earthquake reinforced concrete structure, it can recover large deformations and at the same time yield under strains resulting from earthquake loads. SMAs rebars could be a great choice for high seismic zone of reinforced concrete structures, particularly in BCJs. For these reasons, as to the assessment of old structures and for strengthening the design of new structures, it is important to further develop the existing knowledge of using smart materials like SMAs.

In recent decade, the dream of constructing intelligent structures is becoming a reality. Civil Engineers with the help of metallurgical science have innovated structural materials that can display predetermined physical properties. SMAs are novel functional materials that can exhibit small residual strain under various types of applying and removing loads even after passing the yielding zone. This material has the capability for remembering its original shape even after a severe deformation.

1.2 KINGDOM OF SAUDI ARABIA SEISMICITY

In the recent years, there is increasing in concern about earthquake activities along the western coasts of Saudi Arabia. Many studies have been conducted to calculate the risk level of earthquake events in the Kingdom of Saudi Arabia. The seismic hazard analysis for Saudi Arabia was carried out. The zonation map, as illustrated in Figure 1 - 1, was created in the Kingdom of Saudi Arabia based on the peak ground acceleration, (PGA), values were determined for a fifty years' lifetime of service with about 10% possibility of being increased.

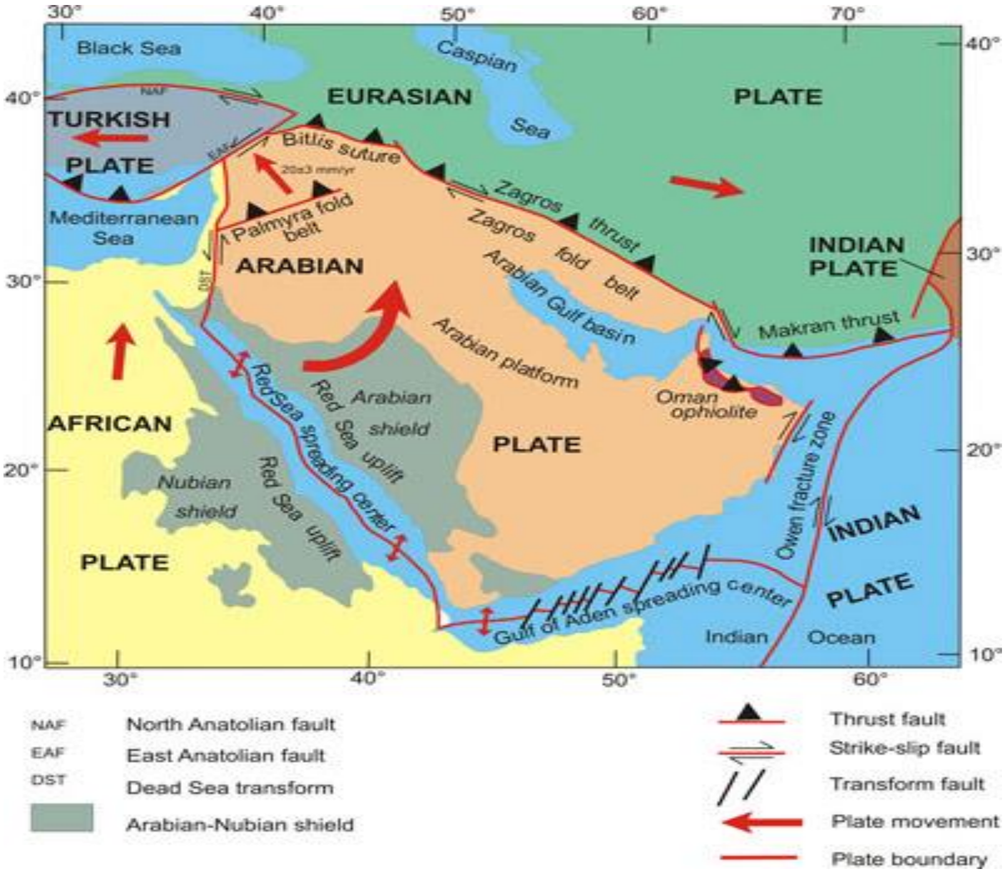

Figure 1 - 1: The seismic zonation map for Saudi Arabia Kingdom

In the following table, the UBC model for Kingdom of Saudi Arabia. Saudi Arabia is divided into 4 zones with seismic zone numbers (SZN) of 0, 1, 2A and 2B as illustrated in the following Table 1 – 1.

Table 1 - 1: The (SZN) and corresponding (PGA) according to the (UBC) code

Seismic Zone Number (SZN)	Peak Ground Acceleration (PGA) in g's
0	Less than 0.05
1	From 0.05 to 0.10
2A	From 0.10 to 0.15
2B	More than 0.15

The framework of ACI code was adopted for designing of RC structures in Saudi Arabia. According to the ACI 318, seismic zones of (SZN) equal to Zero and One are considered as areas with no and very low risk levels, respectively. While seismic zones of (SZN) equal to Two A & B are considered for moderate risk levels. Consequently, according to seismic zonation map of Saudi Arabia most of the Kingdom regions are considered to be of no and low risk levels. However, areas along the western coasts, particularly in the southwest and northwest, fall in the zone of moderate risk level.

Some of the larger towns located in the Eastern Part of the kingdom are very near to the zone of faults. As population growths years by years and many new buildings are developed, seismic risk to infrastructure and the lives of human beings increases.

To minimize the severe damage of new buildings and loss of human lives due to seismic events, there are some approaches for overcoming this issue. One of them is to use a super elastic material, especially for the BCJ, which has the capability to undergo large deformation up to 10% to 20% strain then return to its original shape without any permanent deflections. By using this unique material, which named Shape Memory Alloys (SMAs), buildings can remain safe after earthquakes and cracks in the structural element will close.

1.3 THE IMPORTANCE OF BCJs IN STRUCTURES

BCJs in reinforced concrete moment resisting frames are critical zones for transferring of moments and loads effectively between all connecting elements, such as columns and beams, in structures. It is the crucial element, which subjected to large loads during acute seismic events.

Portion of column which is combined to beam at the intersection is named BCJ. It performs an essential role integrating system of structures. It is the most crucial part in the structures, particularly in the region of high to medium seismicity. Flexural failure, as well as shear failure, of BCJ is classified as one of the major reasons of failure for numerous moment resisting RC frames. These frames are not resistant for seismic events because of low- concrete strength and inappropriate reinforcement details of the BCJ components.

Unsafe design as well as detailing within BCJ regions could jeopardize the whole structures as illustrated in Figure 1 - 2 even if the other elements are conforming to the requirements for design. For the past four decades, many researches have been performed on studying and analyzing of the behavior of BCJ under earthquake conditions by experimental, analytical, and numerical investigations.

Figure 1 - 2: Several examples of BCJ failure

If BCJ has the ability to retrieve its original capacity and geometry form after an earthquake, many problems that related to collapse and permanent damage of structures might be solved. In addition, for the purpose of reducing the structure cost and at the same time ensuring the earthquake safety, using a unique material such as (SMAs) in strengthening of new structures need to be improved. Significant progress was being done in this field. Using smart material as shape memory alloys (SMAs) for strengthening of new RC building;

this method of strengthening structures with SMAs is a focus of intensive research and reinforced the BCJs in the new construction with SMAs bars.

1.4 NEED FOR THIS RESEARCH

Recent consciousness of possible earthquake events in the moderate to low seismicity regions of the Kingdom have led to the concerns of vulnerability and safety of RC structures. Many of these structures were designed and constructed based on gravity loads only. Because of that, their responses during an earthquake event would be non-ductile that might lead to severe economic disruption and losing of human life. Therefore, using new technics in the construction of new buildings would solve the disaster that might occur during seismic ground shaking.

During earthquakes, cracking and permanent deformation occurs at the BCJ interface due to yielding of reinforcing steel. These deformations cannot be repaired to rehabilitate the structures. Therefore, the potential of SMA to recover large deformation on unloading can be exploited at the BCJ interface to avoid such permanent deformation.

Based on literature review, it was found that only limited research has been conducted on the usage of super elastic SMA in the BCJs.

This research aims to investigate the behavior of super elastic SMA bars at the BCJ interface in new constructions so they can close the cracks after Earthquakes, restore the serviceability of structures, and enhance the ductility of BCJ during Earthquakes.

1.5 OBJECTIVES

The primary objective of this research work is to investigate the behavior and suitability of SMA in reinforced concrete structures. This will be determined by studying, modeling, and analyzing the response of BCJs strengthened with SMAs and subjected to reverse cyclic and cyclic loads.

The following investigations will be carried out in order to meet the above-stipulated objective:

1. Investigate the mechanical properties of SMA bars subjected to a tensile force.
2. Investigate experimentally the behavior of BCJs reinforced with embedded SMA and normal steel bars under flexural failure at the interface subjected to cyclic and reverse cyclic loadings.
3. Develop a mechanistic model for calculating the load capacity of BCJ specimens and maximum crack width.
4. Develop (3–D) Finite Element Models of BCJ reinforced with SMA and regular steel bars under cyclic and reverse cyclic loadings.
5. Verify the proposed finite element (3–D) models using the experimental test results of SMA - BCJ specimens.

CHAPTER 2

LITERATURE REVIEW

2.1 INTRODUCTION

Reinforced concrete (RC) structures constitute essential parts of the national wealth in many cities. They often need evaluation, observation, and repairing at regular periods because of decay and aging. Yet, if structures are made intelligent and have the ability to adjust their own damage, adopt changes in their loading conditions, and have the ability to repair their conditions, many problems associated to RC structure management might be terminated. This idea raises the need for intelligent structures and materials, that are prepared to improve life cycle performance, fit the environment, reduce usage of energy, supply the best operating conditions, and significantly minimize costs of maintenance (UIIakko 1996). SMA is a unique material that can undergo greater deformations and return to the original shape either by removing loads or by heating. These unique and distinct properties of shape memory alloys make them smart materials that have the ability to be used in intelligent structures and buildings, which adapt and respond to various environmental conditions (Hardwicke 2003). SMA is used in a large assortment of applications in various industries, for instance, implants, medical equipment, and aviation. In addition, they are used as valves, actuators, clamping devices, and switches. For example, shape memory alloys are used as vibration dampers in space technology (Bauer et al. 1998).

Shape memory alloys (Nitinol) that derived from Titanium and Nickel were first patented in Naval Ordnance Laboratory by Wiley and Buehler in 1965. Depending on material temperature, shape memory alloys can be martensite phase, austenite phase or the mixture of them. In fact, this material is particularly beneficial when great deformation and retrieval of the shape is observed under a less rate of temperature or stress. Recent years, these two essential properties of shape memory alloys have a higher interest of many researchers for application to intelligent structural system. One property of SMAs is the shape memory effect (SME), in which a sample exhibits high residual strains after applying and removing of the loads, which can be fully retrieved its shape upon increasing the temperature of the material. This retrieval stress can be used to introduce forces in the structures. The other unique characteristic of SMAs is super-elastic effect (SE), in which a sample achieves a very great strain by the transformation from austenite to martensite phase by applying loads then it fully retrieved in a hysteresis loop by removing loads and without changing its temperature. Furthermore, both phenomena (SME) and (SE) are because of phase transformation. Because of these two unique characteristics, researchers have started carrying out on smart RC structures using shape memory alloys.

There are many applications of SMA in the civil engineering. Some researchers have discussed those applications and provided in details some of experimental results on mechanical characteristics of SMA.

2.2 PREVIOUS BCJ EXPERIMENTAL WORK AT KFUPM

BCJ experimental tests were first initiated at KFUPM by Mr. Danish Ahmed in 2012. The response of poor detailed BCJs under vertical static and cyclic loads was investigated. Three exterior RC BCJ specimens were cast and tested at KFUPM lab. The BCJ specimens were mainly 12 mm and 18 mm diameter steel reinforcement bars. In addition, the difference between bent in and bent out steel reinforcement bars in the joint region of BCJ specimens has been investigated.

After that, experimental test was performed in the BCJ research area by Mr. Abdulsamee Halahela in 2014. The main objective of the research proposal, which entitled Experimental and Numerical Study for Using of CFRP for Upgrading the BCJs Behavior Under Cyclic Loads, was to investigate the response of BCJ under cyclic loads for two scenarios. First, normal RC - BCJ and second CFRP wrapped externally around existing reinforced concrete beam column joints for retrofitting.

Then, experimental tests were performed for BCJ specimens by Mr. Anas Al-Khatib in 2015. The research objective of his thesis was to investigate of the behavior of BCJ strengthened with a certain percentage of steel fiber mixed with concrete in the joint region. Around twelve exterior RC – BCJ specimens have been cast and tested at KFUPM lab with different scenarios: (1) Normal RC – BCJ specimens, and (2) BCJ specimens strengthened with steel fiber in the joint region for both 12 mm and 18 mm diameter steel bars.

2.3 FABRICATION OF SMAs

Shape memory alloy materials are fabricated by heating the alloys to the melting point in an inert gas environment or in a high vacuum to avoid contamination resulting from a probability reaction between melted alloys and oxygen. Then, the materials are cold or hot worked to a proper shape, such as bars, tubes, wires, sheets, or ribbons. The last process of the fabrication stage is the SMAs treatment that specialize the SMAs from other structural materials, in which materials sustain to some proper thermo-mechanical processing to exhibit super elasticity behavior and SME. The heat treatment temperature is remained usually less than the recrystallization temperature for shape memorization (Khantachawana et al. 1999). It must be noticed that the hot worked materials respond less reliably to the shape setting heat treatment than the cold worked materials. As a result, the alloy materials will be in a complete shape with improved mechanical characteristics (Hodgson 2000).

2.4 TRANSFORMATION TEMPERATURES

SMAs reveal polymorphism like other metals and alloys, i.e. it possesses more than one crystal structure having almost an equivalent chemical composition. At a comparatively high temperature, SMAs remain in the austenite phase. When decreasing the temperature, it starts to transform to the martensite phase. The predominant crystal phase is related to both temperature, stress, and is governed by both thermo-mechanical processing and chemical composition (Dolce and Cardone 2001a). In the stress Free State, SMAs is identified by four different transformation temperatures as illustrated in Figure 2 - 1: martensite start (M_s), martensite finish (M_f), austenite start (A_s), and austenite finish (A_f).

Table 2 - 1 contains some values of the transformation temperatures for various types of alloys in the stress free state.

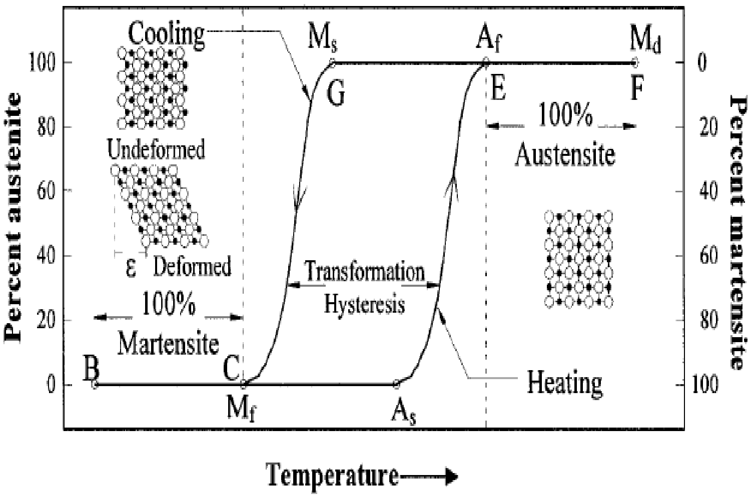

Figure 2 - 1: Changing and transformation in the crystalline structures of shape memory alloys from austenite phase to martensite phase and vice versa as a function of temperature (Dolce and Cardone 2001a)

Shape memory alloy materials remain in a fully austenite phase when their temperature (T) is more than (A_f), and in a fully martensite phase when their temperature (T) is less than (M_f). While changing from austenite to martensite phase and vice versa, both phase's austenite, and martensite occurs.

The transformation phase of SMAs during cooling and heating is approximately as shown in Figure 2 - 2. When increasing temperature of the alloys to the austenite start temperature (A_s), the alloys start to change progressively from martensite to austenite phase. The transformation is almost complete when the temperature reaches the austenite finish temperature (A_f). Cooling the SMAs will cause a change from austenite phase at a temperature more than martensite start temperature (M_s) to martensite phase when the temperature reaches the martensite finish temperature (M_f). If the material temperature increases more than (M_d) (T»A_f), the material will lose the super elasticity behavior.

Table 2 - 1: Transformation temperatures of SMAs for stress free state

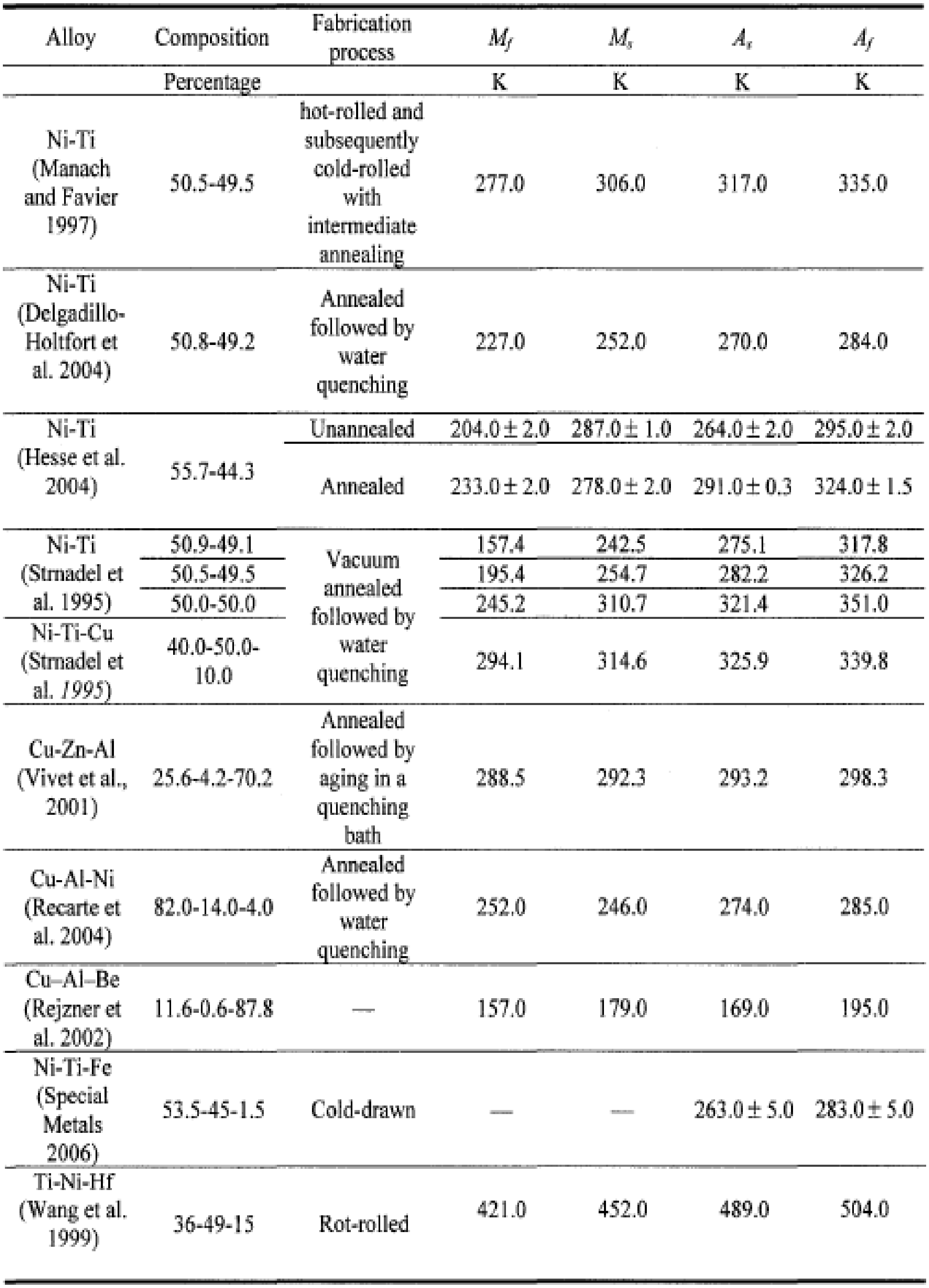

Alloy	Composition	Fabrication process	M_f	M_s	A_s	A_f
	Percentage		K	K	K	K
Ni-Ti (Manach and Favier 1997)	50.5-49.5	hot-rolled and subsequently cold-rolled with intermediate annealing	277.0	306.0	317.0	335.0
Ni-Ti (Delgadillo-Holtfort et al. 2004)	50.8-49.2	Annealed followed by water quenching	227.0	252.0	270.0	284.0
Ni-Ti (Hesse et al. 2004)	55.7-44.3	Unannealed	204.0 ± 2.0	287.0 ± 1.0	264.0 ± 2.0	295.0 ± 2.0
		Annealed	233.0 ± 2.0	278.0 ± 2.0	291.0 ± 0.3	324.0 ± 1.5
Ni-Ti (Strnadel et al. 1995)	50.9-49.1	Vacuum annealed followed by water quenching	157.4	242.5	275.1	317.8
	50.5-49.5		195.4	254.7	282.2	326.2
	50.0-50.0		245.2	310.7	321.4	351.0
Ni-Ti-Cu (Strnadel et al. *1995*)	40.0-50.0-10.0		294.1	314.6	325.9	339.8
Cu-Zn-Al (Vivet et al., 2001)	25.6-4.2-70.2	Annealed followed by aging in a quenching bath	288.5	292.3	293.2	298.3
Cu-Al-Ni (Recarte et al. 2004)	82.0-14.0-4.0	Annealed followed by water quenching	252.0	246.0	274.0	285.0
Cu–Al–Be (Rejzner et al. 2002)	11.6-0.6-87.8	—	157.0	179.0	169.0	195.0
Ni-Ti-Fe (Special Metals 2006)	53.5-45-1.5	Cold-drawn	—	—	263.0 ± 5.0	283.0 ± 5.0
Ti-Ni-Hf (Wang et al. 1999)	36-49-15	Rot-rolled	421.0	452.0	489.0	504.0

2.5 MECHANICAL PROPERTIES OF SMA MATERIALS

SMA material has the ability to undergo large deformation, and reach up to 10% to 20%, and recovering back to the original undeformed shape either by removing of the applied loads, known as super elastic effect or by application of heat, known as shape memory effect (SME) (Qoan et al. 2010).

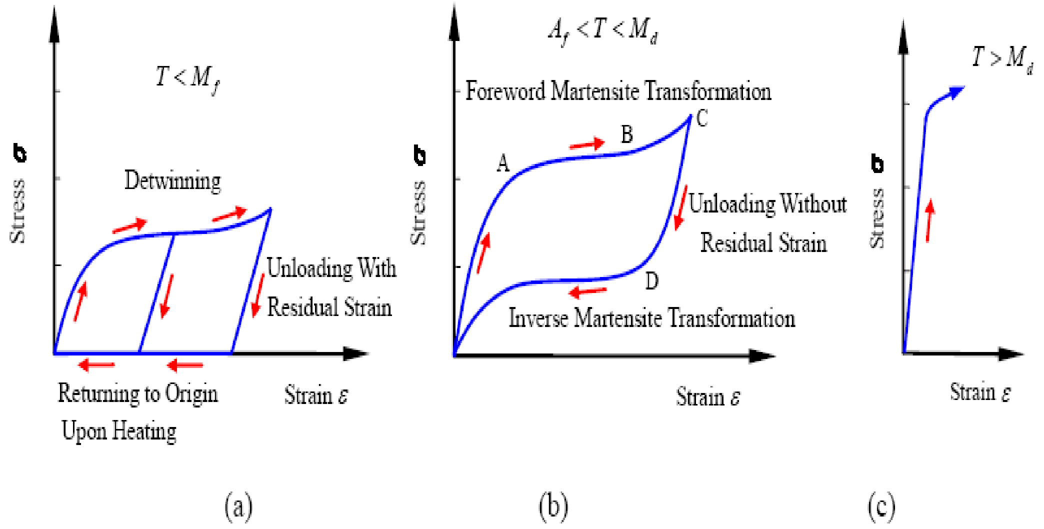

Figure 2 - 2: Stress-Strain diagrams of SMAs Ni-Ti (a) SME behavior; (b) Superelasticity behavior; (c) Ordinary plastic deformation (H.Qoan et al. 2010)

Each shape memory alloy extremely varies in properties. Such change due to the atomic arrangement in the austenite and martensite phases of the shape memory alloys which depends on heat treatment and thermo-mechanical processing. Even a small variation in the relative proportion of the constitutive materials within the same alloy could significantly affect some of the mechanical properties (Strnadel et al. 1995). The diverse parameters defining the most widely used SMAs properties are summarized in Table 2 - 2 (i.e. Ni-Ti). Other shape memory alloys properties are presented in Table 2 - 3.

2.5.1 COMPRESSIVE AND TENSILE BEHAVIOR

A standard stress strain diagram of shape memory alloys (martensite or austenite phase) subjected to compressive and tensile loads is given in Figure 2 - 3. This curve is composed of four linear branches, which are linked to each other by smooth curves. These linear branches are supposed to intersect as displayed by the dotted lines (Liu et al. 1998). The material is examined under both compressive and tensile loads. The values of properties such as axial stresses (f), axial strains (ε), and Young's modulus (E_y) are presented in Tables 2 - 2 & 2 - 3.

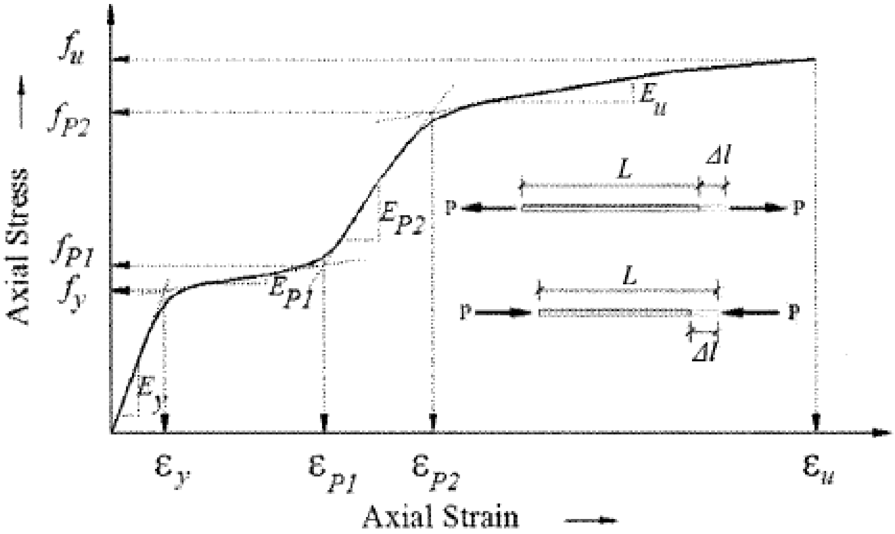

Figure 2 - 3: Typical stress strain diagram of SMA subjected to compression/tension (Liu et al. 1998)

DesRoche et al. (2004) investigated the response of SMA under cyclic loads. The cyclic characteristics of 25.4 mm diameter bars have been compared to 1.8 mm diameter SMA wires to investigate the effect of loading history and bar size on the characteristics of the SMA material. Figures 2 - 4 & 2 - 5 illustrate the ideal properties obtained for the SMA wire and bar. However, the bars results of Shape Memory Alloy showed lower damping and strength properties compared to the wires.

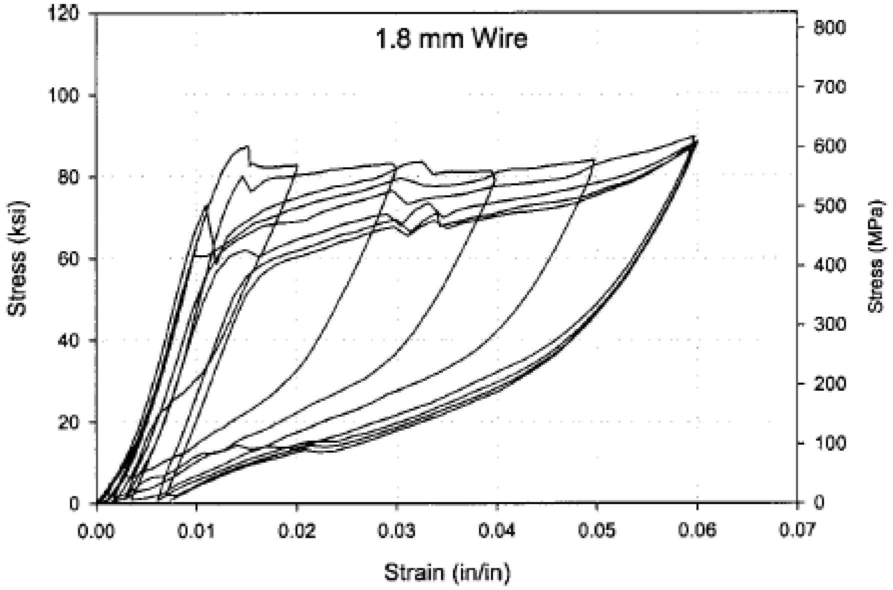

Figure 2 - 4: Stress - Strain curve for 1.8 mm SMA wire under cyclic loads (DesRoche et al. 2004)

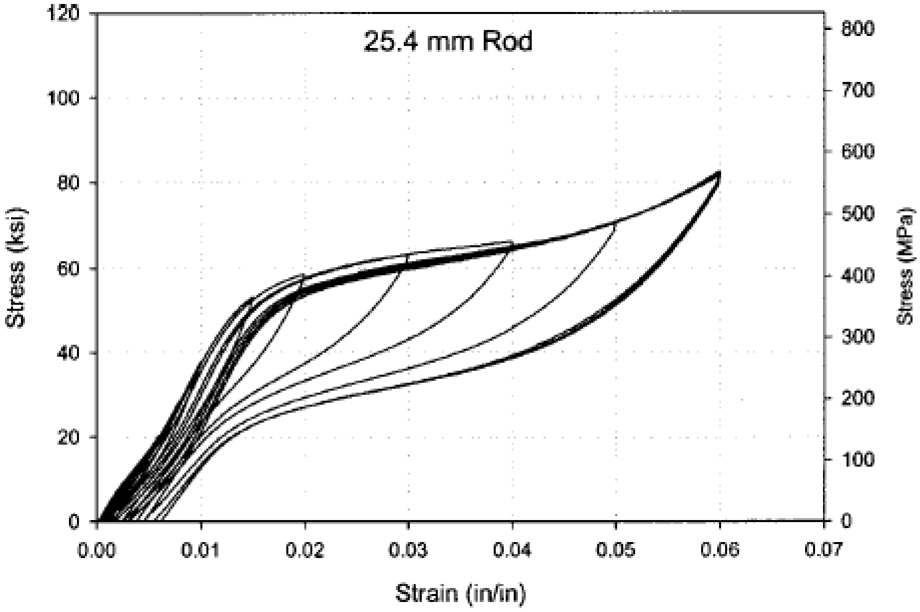

Figure 2 - 5: Stress - Strain curve for 25.4 mm SMA bar under cyclic loads (DesRoche et al. 2004)

Table 2 - 2: The mechanical characteristics of SMA

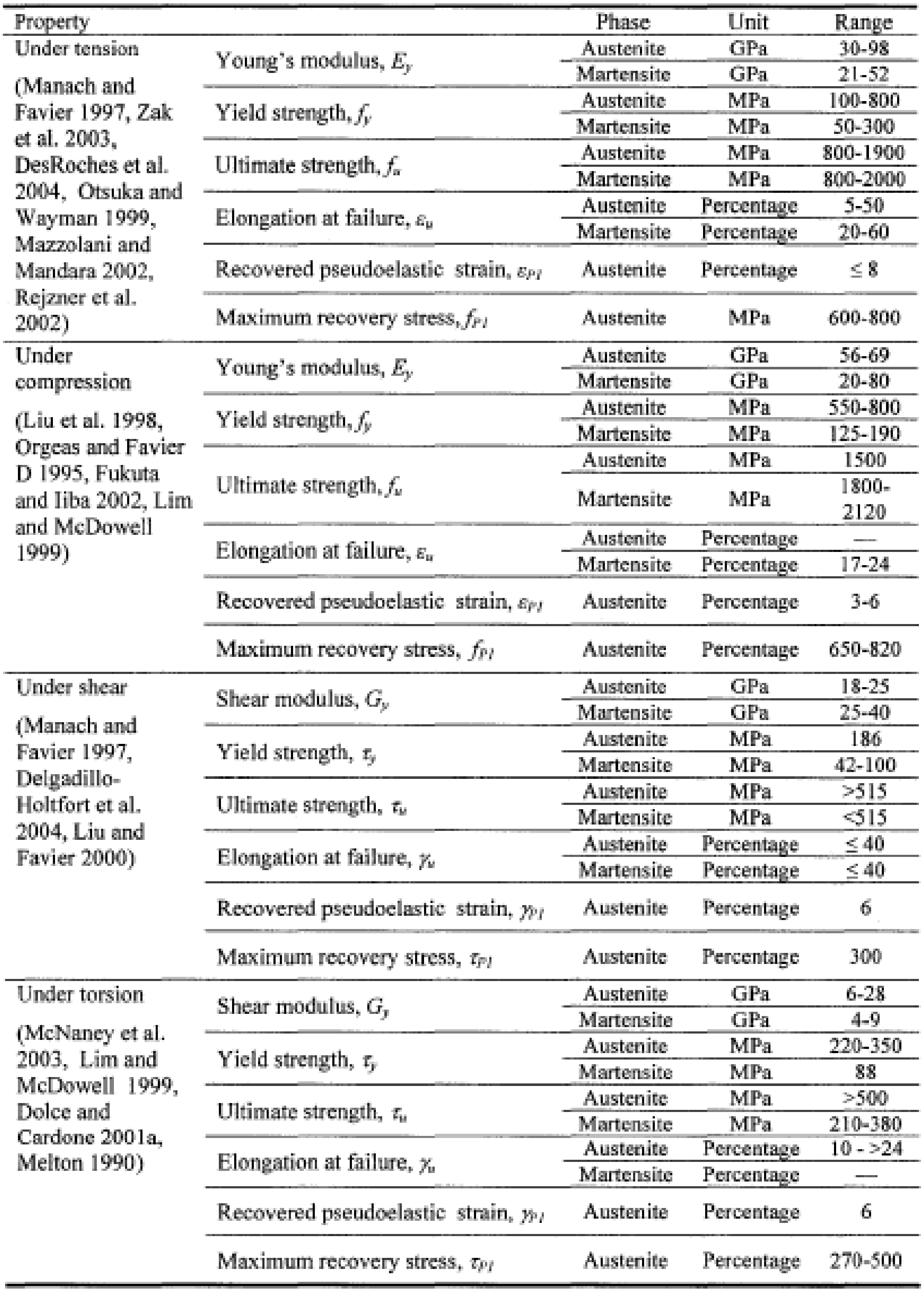

Property		Phase	Unit	Range
Under tension (Manach and Favier 1997, Zak et al. 2003, DesRoches et al. 2004, Otsuka and Wayman 1999, Mazzolani and Mandara 2002, Rejzner et al. 2002)	Young's modulus, E_y	Austenite	GPa	30-98
		Martensite	GPa	21-52
	Yield strength, f_y	Austenite	MPa	100-800
		Martensite	MPa	50-300
	Ultimate strength, f_u	Austenite	MPa	800-1900
		Martensite	MPa	800-2000
	Elongation at failure, ε_u	Austenite	Percentage	5-50
		Martensite	Percentage	20-60
	Recovered pseudoelastic strain, ε_{PI}	Austenite	Percentage	≤ 8
	Maximum recovery stress, f_{PI}	Austenite	MPa	600-800
Under compression (Liu et al. 1998, Orgeas and Favier D 1995, Fukuta and Iiba 2002, Lim and McDowell 1999)	Young's modulus, E_y	Austenite	GPa	56-69
		Martensite	GPa	20-80
	Yield strength, f_y	Austenite	MPa	550-800
		Martensite	MPa	125-190
	Ultimate strength, f_u	Austenite	MPa	1500
		Martensite	MPa	1800-2120
	Elongation at failure, ε_u	Austenite	Percentage	—
		Martensite	Percentage	17-24
	Recovered pseudoelastic strain, ε_{PI}	Austenite	Percentage	3-6
	Maximum recovery stress, f_{PI}	Austenite	Percentage	650-820
Under shear (Manach and Favier 1997, Delgadillo-Holtfort et al. 2004, Liu and Favier 2000)	Shear modulus, G_y	Austenite	GPa	18-25
		Martensite	GPa	25-40
	Yield strength, τ_y	Austenite	MPa	186
		Martensite	MPa	42-100
	Ultimate strength, τ_u	Austenite	MPa	>515
		Martensite	MPa	<515
	Elongation at failure, γ_u	Austenite	Percentage	≤ 40
		Martensite	Percentage	≤ 40
	Recovered pseudoelastic strain, γ_{PI}	Austenite	Percentage	6
	Maximum recovery stress, τ_{PI}	Austenite	Percentage	300
Under torsion (McNaney et al. 2003, Lim and McDowell 1999, Dolce and Cardone 2001a, Melton 1990)	Shear modulus, G_y	Austenite	GPa	6-28
		Martensite	GPa	4-9
	Yield strength, τ_y	Austenite	MPa	220-350
		Martensite	MPa	88
	Ultimate strength, τ_u	Austenite	MPa	>500
		Martensite	MPa	210-380
	Elongation at failure, γ_u	Austenite	Percentage	10 - >24
		Martensite	Percentage	—
	Recovered pseudoelastic strain, γ_{PI}	Austenite	Percentage	6
	Maximum recovery stress, τ_{PI}	Austenite	Percentage	270-500

Table 2 - 3: Mechanical characteristics of different types of SMA

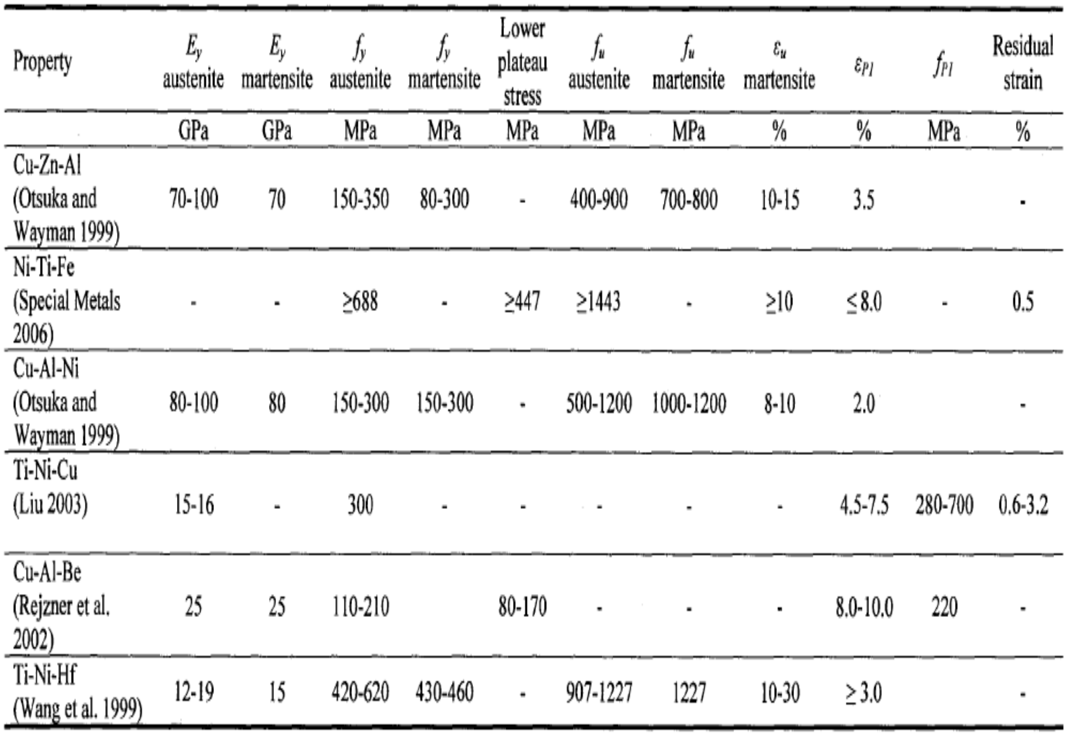

Property	E_y austenite	E_y martensite	f_y austenite	f_y martensite	Lower plateau stress	f_u austenite	f_u martensite	ε_u martensite	ε_{PI}	f_{PI}	Residual strain
	GPa	GPa	MPa	MPa	MPa	MPa	MPa	%	%	MPa	%
Cu-Zn-Al (Otsuka and Wayman 1999)	70-100	70	150-350	80-300	-	400-900	700-800	10-15	3.5		-
Ni-Ti-Fe (Special Metals 2006)	-	-	≥688	-	≥447	≥1443	-	≥10	≤8.0	-	0.5
Cu-Al-Ni (Otsuka and Wayman 1999)	80-100	80	150-300	150-300	-	500-1200	1000-1200	8-10	2.0		-
Ti-Ni-Cu (Liu 2003)	15-16	-	300	-	-	-	-	-	4.5-7.5	280-700	0.6-3.2
Cu-Al-Be (Rejzner et al. 2002)	25	25	110-210		80-170	-	-	-	8.0-10.0	220	-
Ti-Ni-Hf (Wang et al. 1999)	12-19	15	420-620	430-460	-	907-1227	1227	10-30	≥3.0		-

2.5.2 TORSION AND SHEAR BEHAVIOR

Typical stress strain diagram of shape memory alloy subjected to either shear or torsion as shown in Figure 2 - 6 follows the same pattern as the stress strain diagram subjected to tension. Property parameters of shear modulus (G), shear strain (γ), and shear stress (τ), are indicated by: G_y, G_{p1}, G_{p2}, G_u, γ_y, γ_{p1}, γ_{p2}, γ_u, τ_y, τ_{PI}, τ_{P2}, and τ_u.

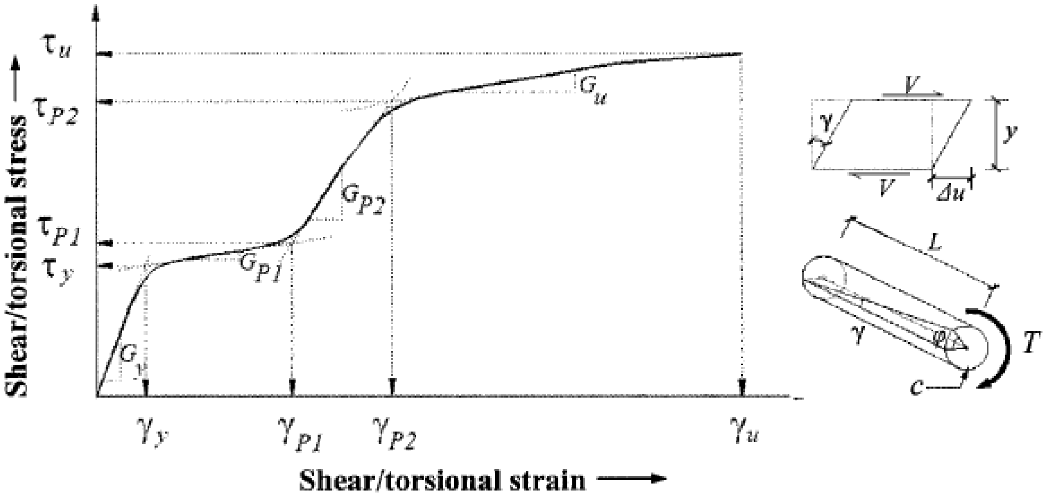

Figure 2 - 6: Typical stress strain diagram of SMAs subjected to torsion / shear (Liu et al. 1998)

2.6 CONSTITUTIVE MATERIALS MODELING OF SMAs

Because of using the SMA material in a various types of applications, for example, civil engineering, mechanical engineering, aerospace, and medical sciences, the development of appropriate constitutive numerical models starts to become an essential prerequisite in designing, analyzing, and modeling of SMAs structures and devices. The peculiar thermo mechanical response of shape memory alloy with SME and pseudo elasticity has made a 3-D constitutive modeling difficult problem because the choosing of appropriate tonsorial parameters to express the response of shape memory alloy under multi axial behavior is very complex. Shape Memory Alloy for civil engineering applications is usually modeled using phenomenological method approach.

2.6.1 PHENOMENOLOGICAL MODELING

Because most applications of SMAs in civil engineering are related to using wires and bars, 1-D phenomenological models are often considered favorable. Many researchers have proposed uniaxial phenomenological models. The superelastic behavior of is becoming incorporated in numbers of finite element packages like ANSYS 12.0 where the material model is implemented from Auricchio et al. (1997). The parameters, which are important to define the SMA material model in finite element software packages, including. 1) Starting stress from austenite to martensite stage, 2) finishing stress from austenite to martensite, 3) starting stress from martensite to austenite, 4) finishing stress from martensite to austenite, 5) maximum residual strain or super elastic plateau strain length, 6) modulus of elasticity at austenite phases, and 7) the ratio of transformation stresses under compression and tension. Figure 2 - 7 illustrates the one dimensional - superelastic model, which used in ANSYS 12.0. Figures 2 – 8 a, b & c show stress strain diagrams with a complete transformation path followed by a) partial loading (PL) and partial unloading (PU), b) partial loading (PL) and complete unloading (CU), and c) complete loading (CL) and partial unloading (PU), respectively

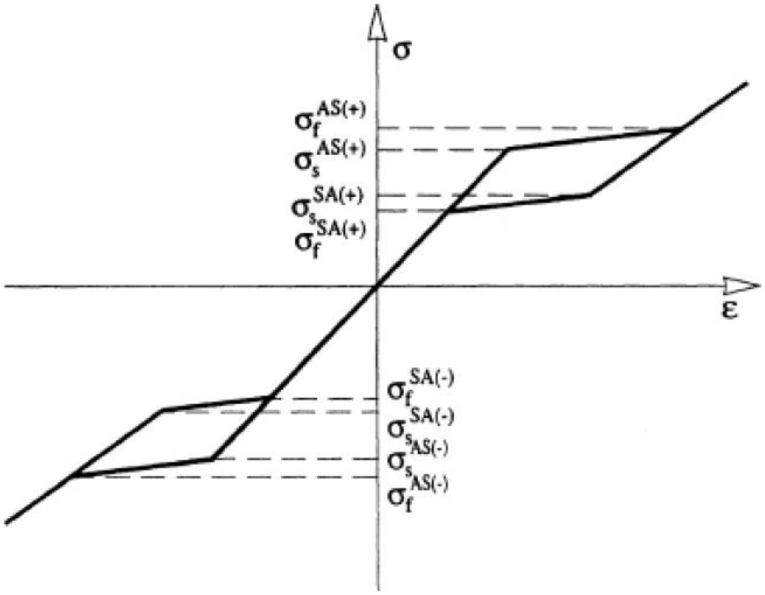

Figure 2 - 7: One Dimensional- models of SMA implemented in FE package (ANSYS VERSION 12.0) (Auricchio et al. 1997)

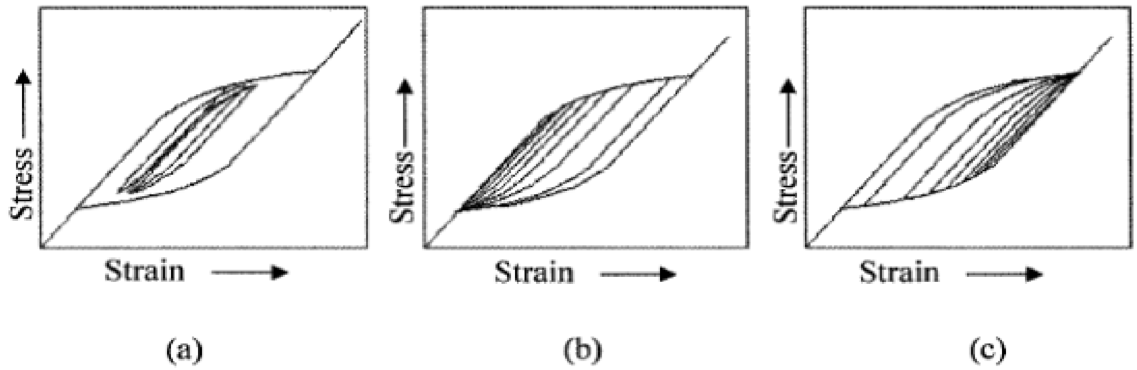

Figure 2 - 8: One Dimensional - models of SMA at constant temperature where the stress strain diagrams are drawn after a complete transformation path followed by a) PL and PU, b) PL and CU, and c) CL and PU

Delmont and DesRoches (2002) performed a numerical study on Shape Memory Alloy bars as a restrainer to be used in bridges. A number of three-bridge spans have been used for numerical modeling. Similar to typical cable restrainers, the Shape Memory Alloy restrainers were connected from the bottom flange of the beam to the pier cap. For assessing the performance of steel and SMA restrainer bars, numerical nonlinear analysis of a typical bridge was performed. The Numerical results illustrated that steel bars were less effective than Shape Memory Alloy bars in limiting relative displacement at abutments and piers.

The response of RC - SMA Bridge piers has been studied numerically by Alam et al. (2008). Number of two $\frac{1}{4}$ - Scale reinforced concrete columns, which represent RC Bridge piers, designed, constructed, and then tested previously using a shaking table by Wang et al. (2004). SMA bars have been placed in the plastic hinge regions and connected to steel reinforcement bars. The behavior of the piers showed an excellent re-centering ability when subjected to seismic loadings. It was illustrated that RC - SMA columns were superior to the conventional reinforced concrete columns in limiting relative top deflection and residual deflections.

2.7 APPLICATIONS OF SMAs IN CONCRETE STRUCTURAL ELEMENTS

Structures must be designed and constructed to resist earthquake loads and act elastically under seismic events. In ordinary earthquake design, reinforcement steel bars are expected to be yielding and dissipate energy whereas enduring permanent deformation. SMA is a unique material that can undergo greater deformations and return back to its shape either by removing loads or by heating. Consequently, if the shape memory alloy is used in structures as reinforcement bars, they will be yield under high earthquake loads, yet the permanent deformation will not be significant (Wang 2004).

The behavior of BCJ specimens reinforced with Shape Memory Alloy material has been investigated by (Alam et al. 2007). A number of two large-scale BCJ specimens were cast and tested under reverse cyclic loads. One of the BCJ specimens was reinforced with ordinary steel reinforcement bars (BCJ1), whereas second BCJ specimen was reinforced with Shape Memory Alloy bars (BCJ2) as illustrated in Figure 2 – 9. The behavior of these BCJ specimens, energy dissipation ability, moment-rotation envelope relationship, and their load-story drift, were analyzed, and compared under reverse cyclic loadings. The results illustrated that the Shape Memory Alloy-reinforced BCJ specimen is able to recover most of its deformation. The beam tip loads - story drifts relationship diagrams for both (BCJ1) and (BCJ2) specimens were shown in Figure 2 – 10 a & b

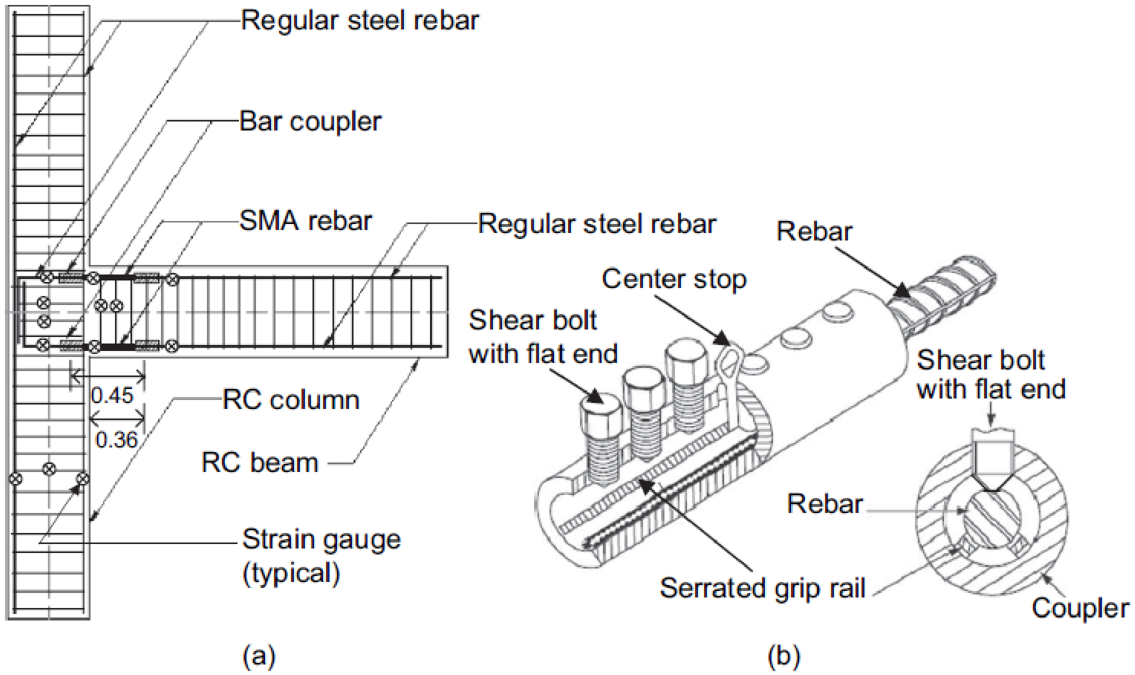

Figure 2 - 9: (a) The details of the specimen JBC-2 and locations of the strain gauges; (b) regular single barrel screw-lock mechanical coupler for connecting regular steel rebar and SMA rebar (Alam et al. 2007)

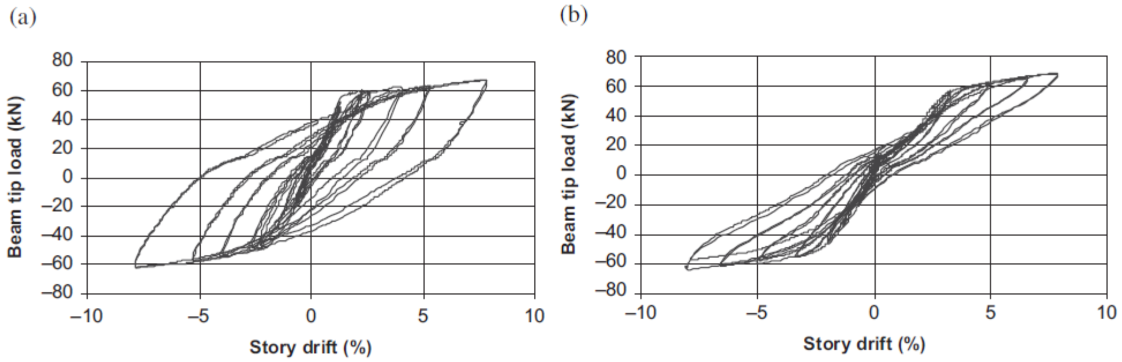

Figure 2 - 10: Beam tip loads - story drifts relationship of specimens: (a) BCJ1 specimen; (b) BCJ2 specimen. (Alam et al. 2007)

Saiidi and Wang (2006) have investigated the contribution of SMAs for reducing the residual displacement in columns reinforced with SMA bars in the plastic hinge region. The earthquake behavior and damage in an SMA-reinforced column repaired using engineered cementitious composites (ECC) were evaluated. A $\frac{1}{4}$ - Scale, spiral reinforced concrete column Figure 2 – 11 with SMA longitudinal reinforcement in the plastic hinge was tested on the shaking table. After the column was damaged by simulating earthquakes, it was repaired using ECC in the plastic hinge region and retested. The tests demonstrated that SMA-reinforced columns were able to recover nearly all of the post-yield deformation Figure 2 – 12 and the use of ECC reduced the concrete damage significantly, thus requiring minimal repair even after a strong earthquake. Then, he proposed a new hysteresis model for SMA-reinforced members, which was able to satisfactorily predicted displacement histories.

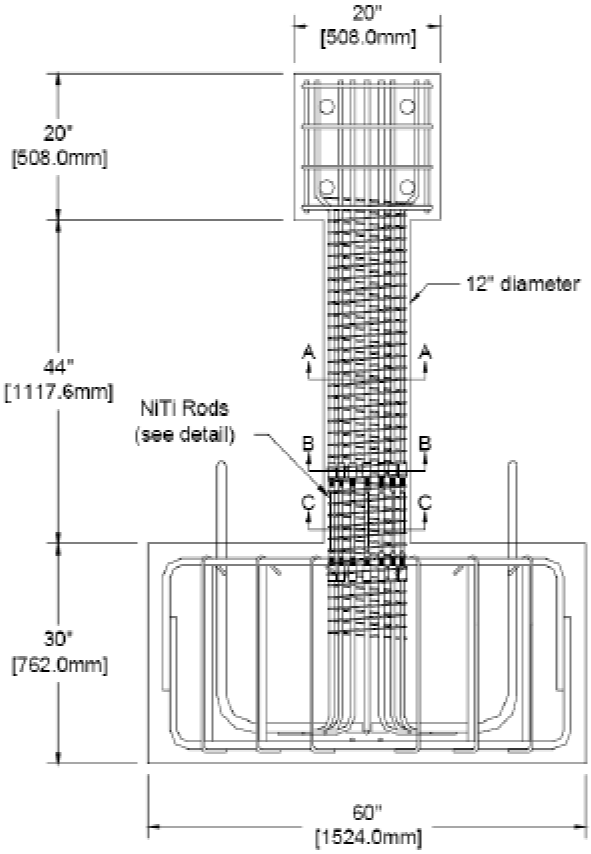

Figure 2 - 11: Details of columns specimen reinforced with super elastic SMAs material (Saiidi and Wang 2006)

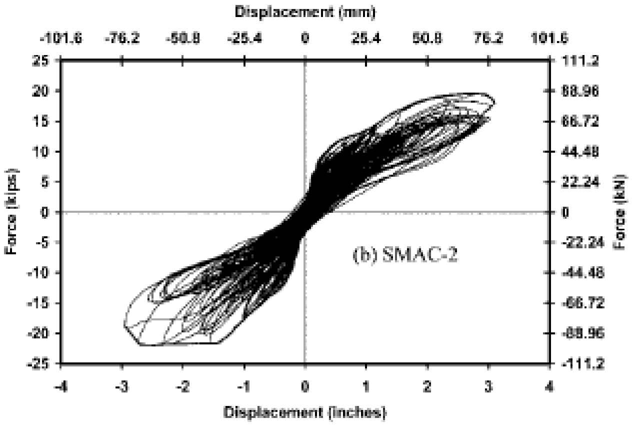

Figure 2 - 12: Measured cumulative hysteresis curves for columns reinforced with SMAs (Saiidi and Wang 2006)

(Ayoub et al. 2003) has studied the behavior of small – scale concrete beams that, reinforced by SMA (NiTi) bars under half-cyclic loading as shown in Figure 2 - 13.

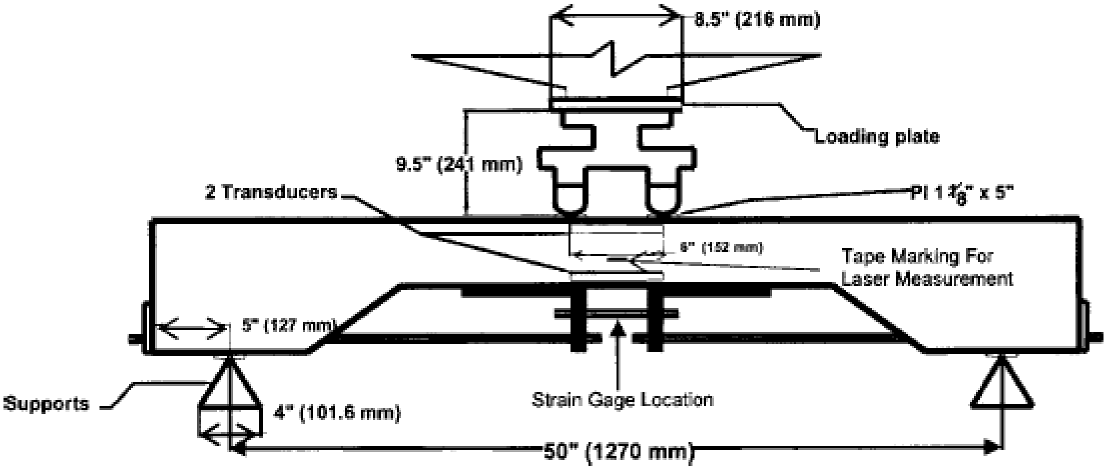

Figure 2 - 13: Experimental setup of the beam Test (Ayoub et al. 2003)

Figure 2 - 14 shows the testing results which indicate that average residual displacement in beams reinforced with SMA bars was less than one-fifth comparing to beams reinforced with steel bars.

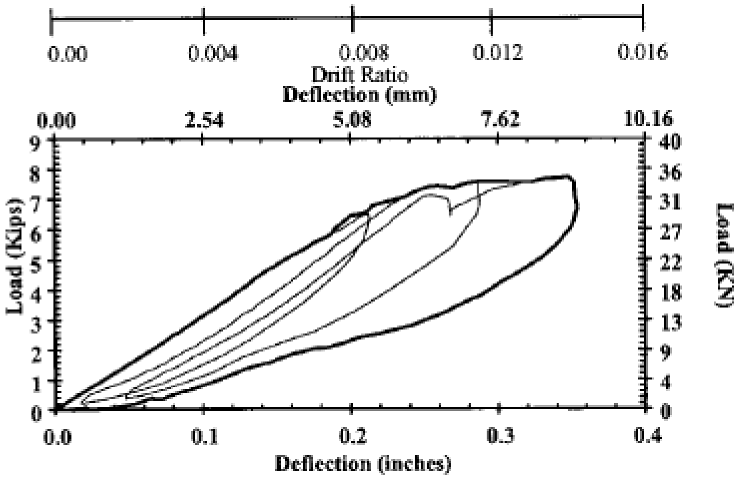

Figure 2 - 14: Load – Displacement response for beams reinforced with SMA bars (Ayoub et al. 2003)

SMA - FRP hybrid system was investigated by Nehdi et al. (2010) to develop corrosion free structural elements with the capability to recover large deformations upon unloading process. A RC - BCJ was cast and tested under reverse cyclic loadings where SMA bars have been used in the plastic hinge area and FRP bars in the other areas. The splicing was replaced by regular single barrel screw-lock mechanical couplers for connecting the SMAs bars with FRP as illustrated in Figure 2 – 15.

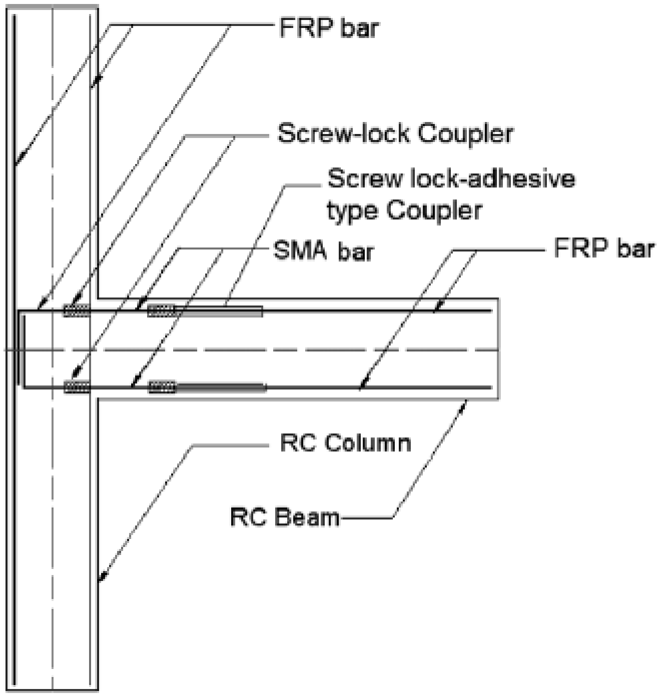

Figure 2 - 15: Splice details of the test specimen (Nehdi et al. 2010)

The results have been compared in terms of load-story drifts Figure 2 -16, moment-rotations and energy dissipation capacity Figure 2 – 17 to those of a similar RC - BCJ specimen reinforced with ordinary steel reinforcement bars. Dissipated energy, maximum drift, and ultimate strength were comparable in both specimens. Nevertheless, the capability of the SMA in re-centering was not shown due to significant slippage of the FRP bars inside the mechanical couplers.

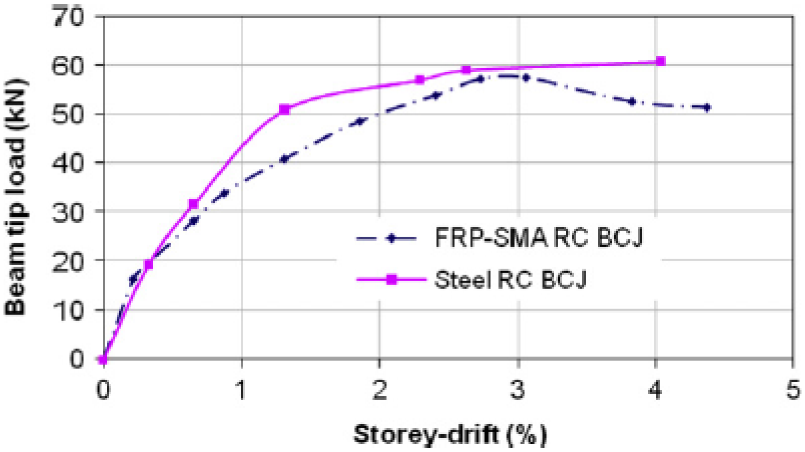

Figure 2 - 16: Beam tip load vs. story drift envelope of BCJ specimens (Nehdi et al. 2010)

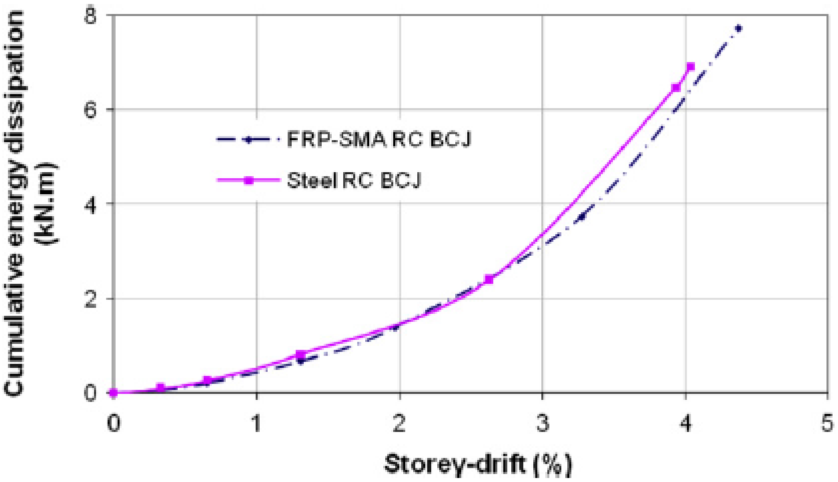

Figure 2 - 17: Cumulative energy dissipation-Story drift behavior of BCJ specimens (Nehdi et al. 2010)

(Abdulridha et al. 2013) focused in his testing program on flexural large – scale concrete beams which reinforced with SMA bars in critical sections as shown in Figure 2 – 18. These beams were subjected to reverse cyclic, cyclic, and monotonic loadings.

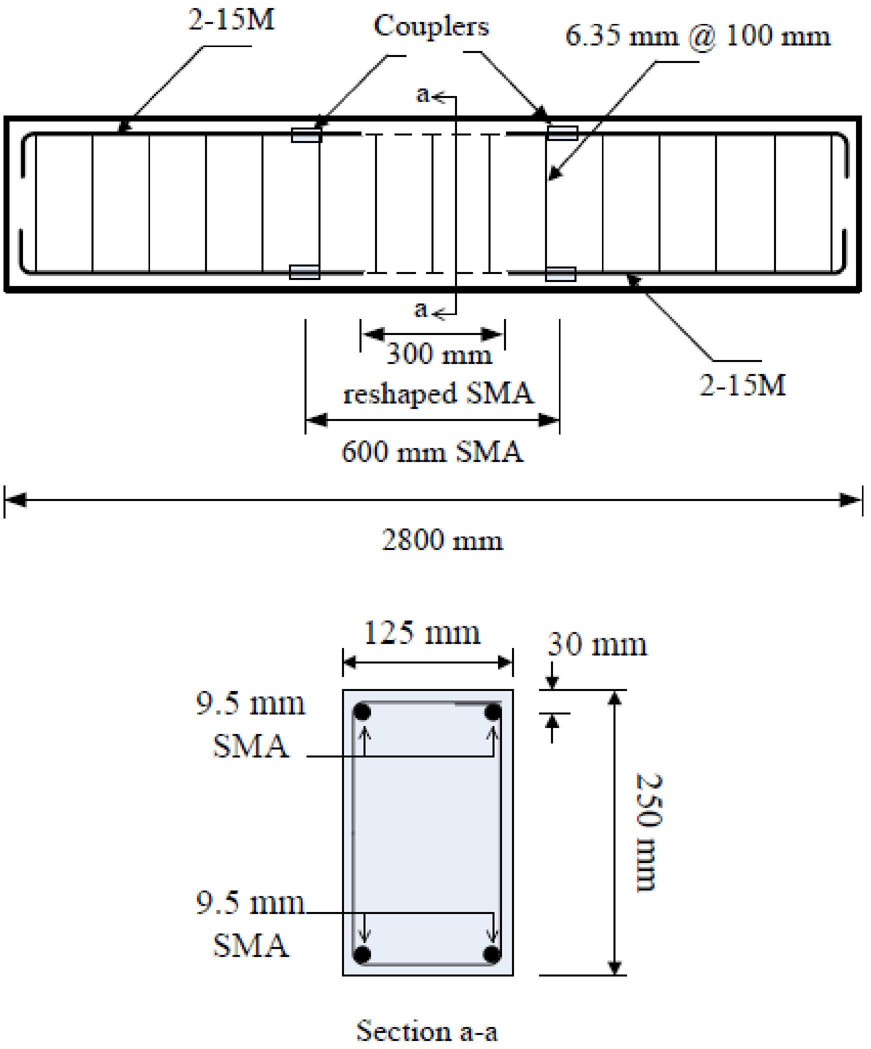

Figure 2 - 18: Details of SMA bars and couplers in the beam (Abdulridha et al. 2013)

Results of experimental tests were compared and verified with hysteretic constitutive modeling of Shape Memory Alloy. It shows that superelastic SMA bars were superior to ordinary steel reinforcement in limiting the crack width and residual displacement in concrete beams. In addition, SMA beams subjected to cyclic loadings dissipated same energy like ordinary steel reinforcement while with reverse cyclic loadings, SMA reinforced beams dissipated about 54 % of the energy that has dissipated by ordinary steel reinforced beams.

The ability of beams reinforced with SMA to recover displacements was further illustrated in Figure 2 – 19, which shows the mid span deflection recovery capacity for beams under both cyclic as well as reverse cyclic loadings.

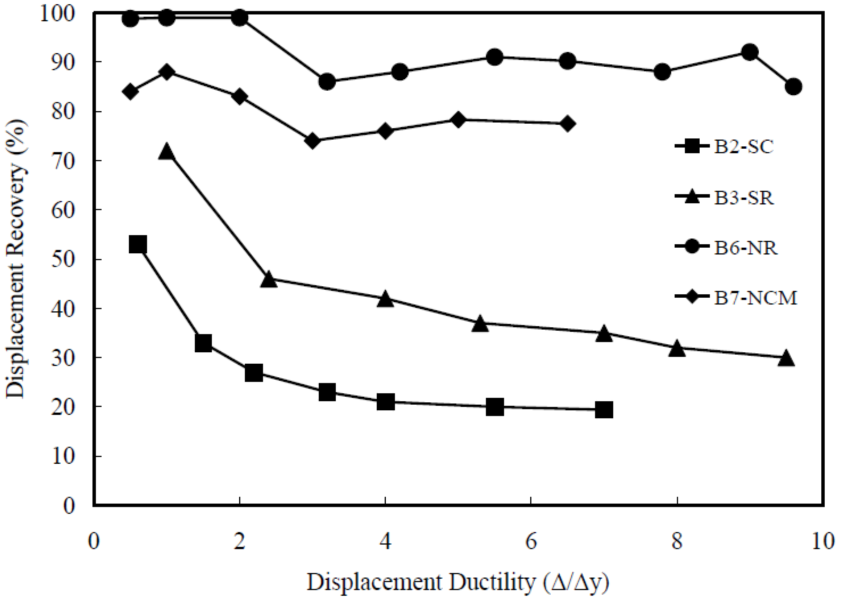

Figure 2 - 19: Recovery capacity-displacement ductility behavior (Abdulridha et al. 2013)

Hong-Nan Li et al. (2006) investigated Self-rehabilitation of Intelligent Beams, which Reinforced with SMAs. In this study, SMAs cable /strands were used in reinforced concrete structures. SMAs strands are made of small diameter wires. For comparison, three samples were cast: a conventional beam reinforced with steel reinforcement bars only and two beams reinforced with SMA and steel bars with various configurations as shown Figure 2 - 20 & 2 - 21 respectively. The results of the tests show that with appropriate reinforcement and shape memory alloys, the sample's cracks can be closed by the SMAs upon unloading as illustrated in Figure 2 - 22.

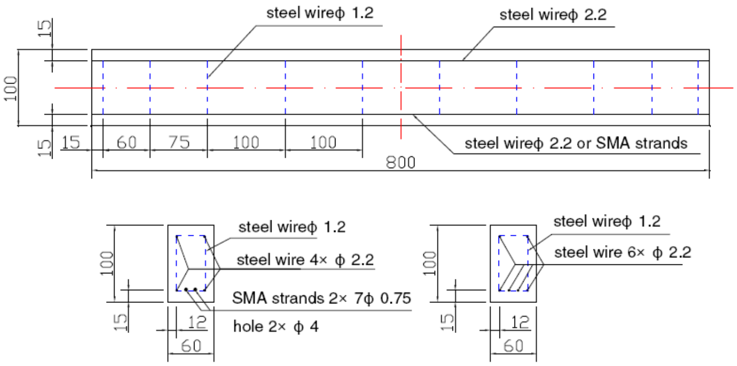

Specimen 2 Specimen 1

Figure 2 - 20: Reinforcement details of the model 1 and 2 (Hong-Nan Li et al. 2006)

Figure 2 - 21: Reinforcement used in sample (the bottom longitudinal reinforcement only uses super elastic shape memory alloys bars) (Hong-Nan Li et al. 2006)

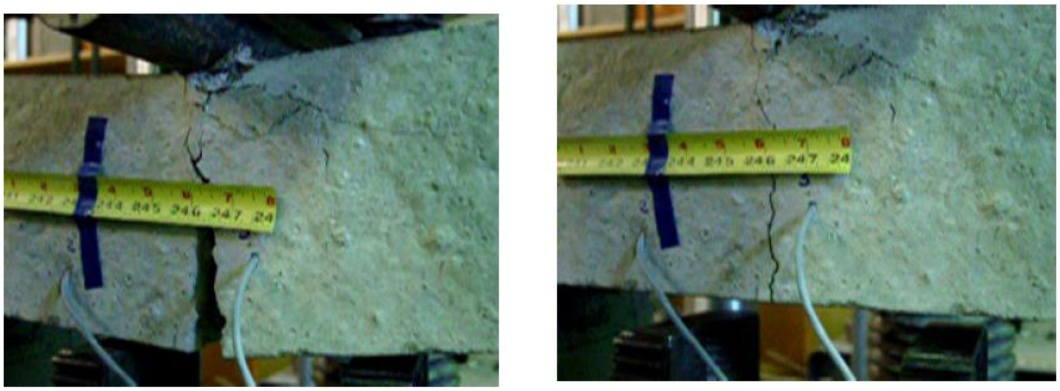

(a) **(b)**

Figure 2 - 22: a) A large crack observed during the loading Test b) The crack closes after unloading the specimen (Hong-Nan Li et al. 2006)

CHAPTER 3

TRAINING, TESTING, AND PREPARATION OF (SMA) BARS

3.1 INTRODUCTION

SMA bars, which have been used in this research, were brought from Xi'an Saite Metal Materials Development Co., Ltd - China. All SMA bars are 12 mm in diameter. An XRF test was performed to get the exact chemical composition of the SMA material. Table 3 - 1 illustrates the chemical compositions of SMA bars.

Table 3 - 1: The chemical compositions of SMA material used in this research

Composition	Percentage %
Nickel	51.92 %
Titanium	45.87 %
Iron	0.96 %
Aluminum	0.33 %
Impurities	0.92 %

3.2 TRAINING OF SMA BARS

SMA bars were heated to 350 C^o in appropriate furnace for one and a half hours, and then they were taken out from the furnace and immediately water quenched. Figure 3 - 1 shows the furnace which has been used for heating the shape memory alloy bars. Figure 3 - 2 shows the shape memory alloy bars after putting in cool water immediately after heating.

Figure 3 - 1: The furnace during heating of the SMA bars

Figure 3 - 2: Putting of SMA bars in cool water immediately after heating

3.3 TESTING OF SMA BAR

For getting the needed parameters to be used in numerical modeling and mechanistic model's calculations, SMA material has been tested in tension. For this purpose, the SMA bar has been formed according to ASTM standards as shown in Figure 3 - 3 and has been used for testing at a speed of (2 mm/min). (100 kN) Instron series 8000 equipment was used for the tensile testing as illustrated in Figure 3 - 4.

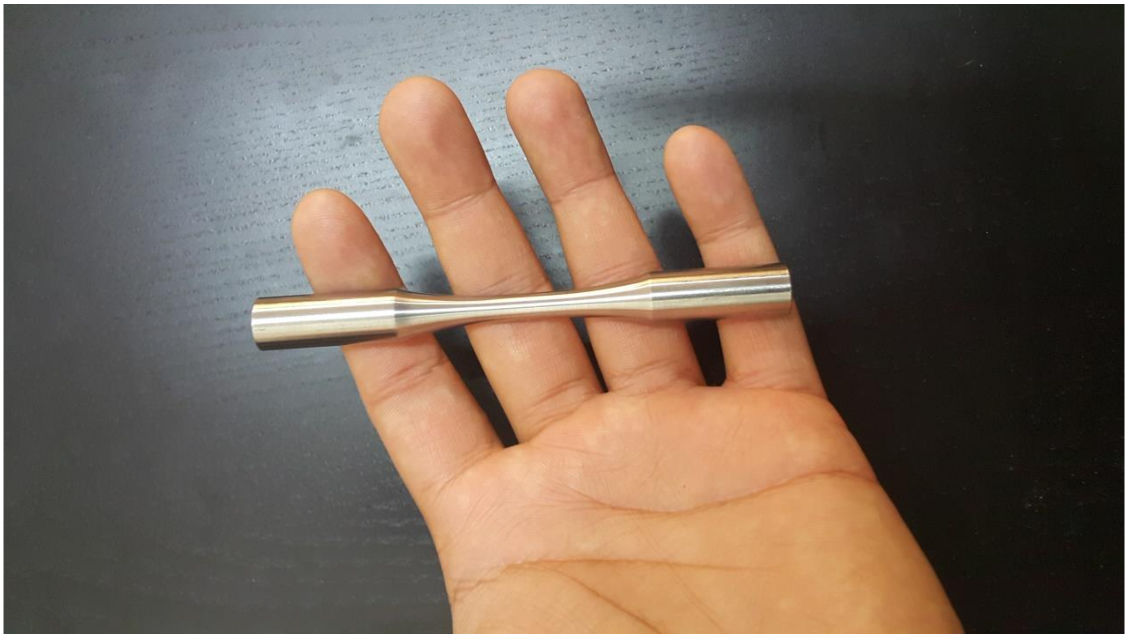

Figure 3 - 3: SMA bar which has been used for tension test

Figure 3 - 4: Testing of SMA bar using (100 kN) Instron machine

First, the bar was tensioned to 5 % strain directly; to avoid any slippage could occur between SMA bar and the grips. Then numbers of cycles have been applied to the bar to get its real behavior.

Figure 3 - 5 shows the SMA 12 mm diameter bar response to the tension test. For modeling purpose, a suitable idealization has been applied to the SMA tension diagram curve. Figure 3-6 shows the idealized curve of the SMA bar for constitutive modeling in ANSYS software.

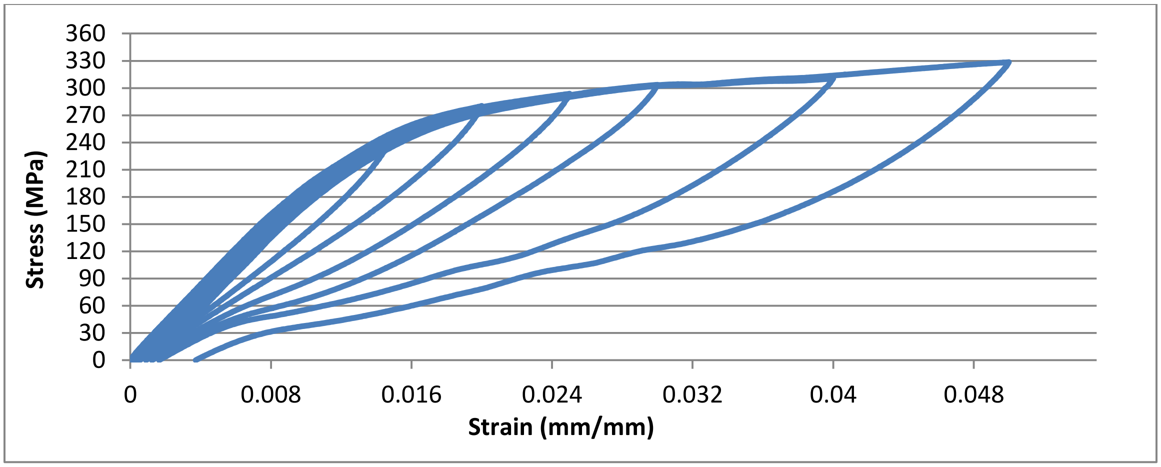

Figure 3 - 5: Stress – strain diagram curve of SMA bar

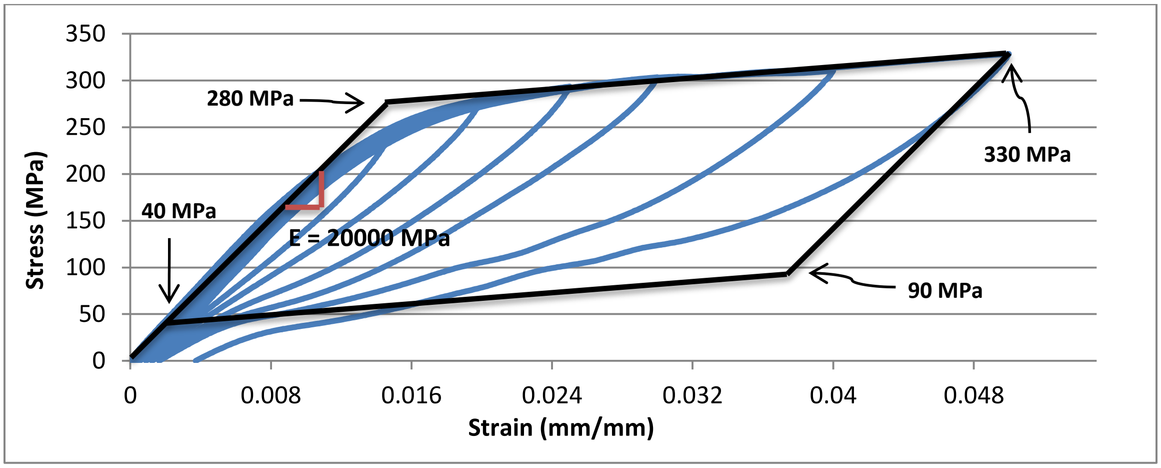

Figure 3 - 6: Idealized stress – strain curve of SMA bar for numerical simulation

3.4PREPARATION OF SMA BARS FOR CASTING

A number of five SMA bars were ribbed using a very special machine at the Research Institute (RI) in KFUPM using ASTM standards. This operation was very difficult since that SMA material is very hard and it cannot be cut or ribbed easily. Figure 3 - 7 illustrates the procedure of ribbing the SMA bars. Figure 3 - 8 shows the SMA bar before and after ribbing.

Figure 3 - 7: Using a special equipment to make ribs for SMA bars

Figure 3 - 8: SMA bar before and after ribbing

Then, single-barrel, regular type screw locks couplers have been employed for connecting the steel reinforcement bars with SMA bars in all BCJ specimens. These types of couplers are complying with ASTM A615 and compatible with reinforcing bars. In these couplers, each bar reinforcement end is inserted in the end of the coupler to the middle position that can be indicated by a small hole in the middle. Then, bolts were tightened with appropriate torque until their heads go inside the bars. After putting the SMA bars in the couplers, a very high strength epoxy – Sikador 330 - was injected to reduce the chance of slippage between SMA bars and couplers. Figure 3 - 9 shows the coupler that has been used in the BCJ specimens and a Sikador 330 epoxy that has been injected between SMA bars and couplers. Figure 3 - 10 shows the procedure of preparing the SMA bars and couplers for epoxy injection.

Figure 3 - 9: The mechanical coupler and Sikador 330 epoxy

Figure 3 - 10: Preparation of SMA bars and couplers for epoxy injection

CHAPTER 4

MECHANISTIC MODEL FOR BCJs AND CRACK CALCULATIONS

4.1 LOADS ACTING IN EXTERIOR (BCJs)

The response of BCJs in the RC structures is not that easy to be understood. Numbers of stresses contiguous members converges at the same point. Axial loads as well as shear stress are transmitted into the BCJ region from the column, whereas bending moments as well as shear stress are transmitted from the beam into the BCJ region. Therefore, to understand the forces and stresses in the joint, loadings on both beams and columns should be known.

4.1.1 FORCES ON THE BEAM

The bending moment reaction, which occurred at the BCJ interface, (M_n) is given by equation [4.1]

$$M_n = P \times l_b \tag{4.1}$$

where:

P= Load acting on the beam tip.

l_b= Distance from the column face to the tip of the beam where the load in applied as illustrated in Figure 4 - 1.

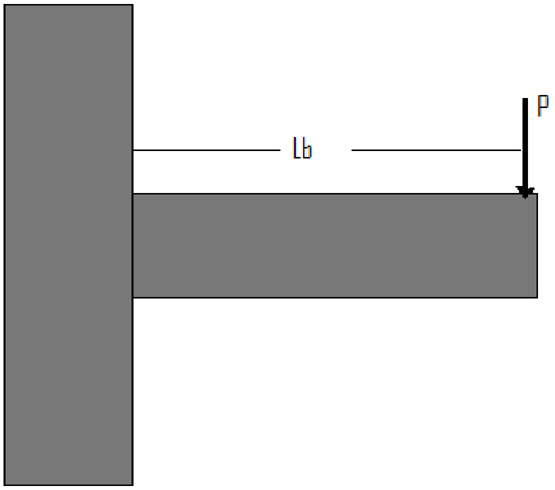

Figure 4 - 1: Forces acting at the beam

4.1.2 FORCES ON THE COLUMN

In that respect, an assumption was made that at the halfway point of the column between slabs there is the inflection point in the column where bending moment is equal to zero. For BCJs, a moment at the end of the beam is equal to the moment in the column, M_n.

Therefore, shear forces in the columns of BCJ can be calculated using equation [4.2]

$$V_C' = {}^{M_n}\!/_{l_{pc}} \tag{4.2}$$

where:

V_C'= Shear force in column

l_{pc}= The distance between the inflection points

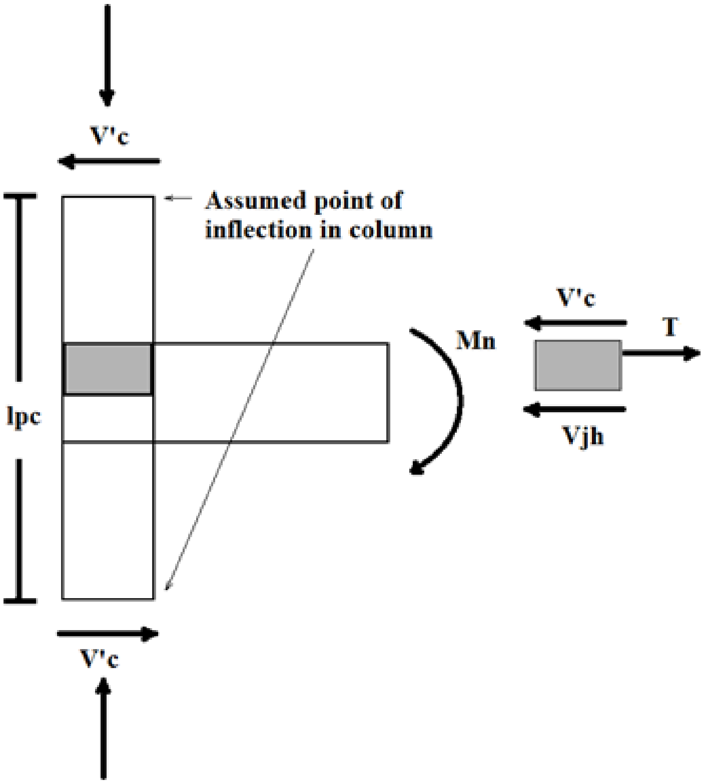

Figure 4 - 2: Forces acting in the BCJ

Figure 4 - 3 illustrates that horizontal shear force is the combination of tensile force in the beam reinforcement bars framing into the joint and the shear which carried down through the column as illustrated in equation [4.3]

$$V_{jh} = T - V_C' \tag{4.3}$$

where:

T= The tensile load in the longitudinal steel reinforcement bars of the beam

V_C'= The total shear occurred above the joint in the column.

4.2 EXTERIOR BCJ SHEAR STRENGTH REQUIREMENTS

The principal tensile shear stress is usually employed for specifying the joint shear strength capacity as illustrated in Figure 4 - 3.

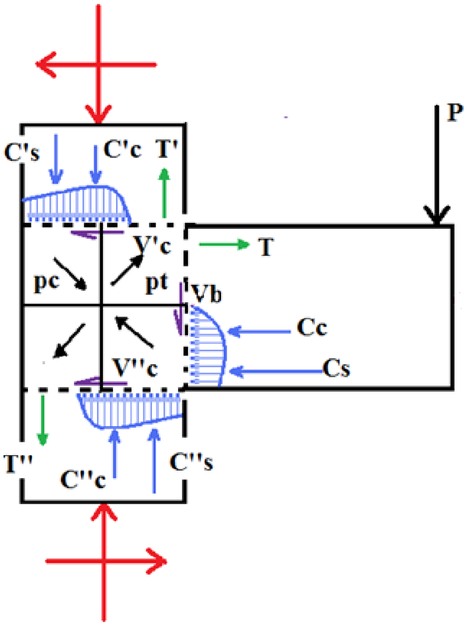

Figure 4 - 3: Principle tensile shear stress in the (BCJ)

From a Mohr's circle, the principle tensile shear stress can be expressed in equation [4.4]

$$\sigma_{1,2} = \frac{\sigma_x+\sigma_y}{2} \pm \sqrt{\left(\frac{\sigma_x-\sigma_y}{2}\right)^2 + \tau_{xy}^2} \qquad (4.4)$$

where:

σ_x = The stress on the plane which is parallel to the longitudinal axis of the member which is equal to the axial (σ_a) on the column

σ_y = The normal stress on the plane perpendicular to the axis of member, which is zero for the joint

τ_{xy}= The shear stress, which is equal to v_{jh} ; therefore, for the exterior BCJ, the equation [4.4] could be written as:

$$P_t = -\frac{\sigma_a}{2} + \sqrt{\left(\frac{\sigma_a}{2}\right)^2 + v_{jh}^2} \tag{4.5}$$

where:

σ_a= Column axial stress $\left(\frac{N}{A_g}\right)$, and v_{jh}= Horizontal shear stress $\left(\frac{V_{jh}}{A_j}\right)$

4.3 FAILURE MODE IN EXTERIOR BCJ

If the shear tensile stress of the joint is more than or equal to the tensile strength of concrete, which is given by equation [4.6]

$$\emptyset V_{nj} = \emptyset\gamma\sqrt{f_c'}A_j \tag{4.6}$$

Therefore, BCJ will fail in shear and diagonal cracks will form in the joint region. Whereas, if the shear tensile stress of joint is less than the tensile strength of concrete, the joint will fail in flexural at the BCJ interface.

4.4 CALCULATION OF LOAD CAPACITY FOR BCJ – FLEXURAL FAILURE

To calculate the load capacity at yielding point of steel reinforcement bars for the flexural failure of BCJ, simple mechanistic equations of cantilever beam can be used as shown in Figure 4 – 4. Since there no shear failure at the joint region and concrete strength of the joint is more than the applied principle stresses, the column is acting like a support for the beam in the BCJ specimens.

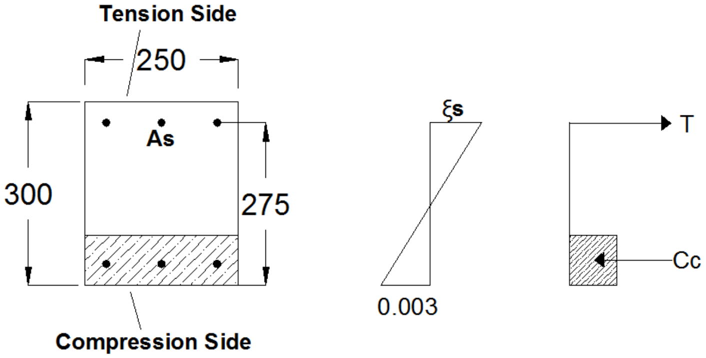

Figure 4 - 4: Stress and strain diagrams for the beam

$$T = C \qquad \Rightarrow \qquad 0.85 \times f_c^{/} \times a \times b = A_s \times f_y \qquad \Rightarrow \qquad a = \frac{A_s \times f_y}{0.85 \times f_c^{/} \times b} \qquad (4.7)$$

$$\because z = d - \frac{a}{2} \qquad \Rightarrow \qquad Capacity\ moment\ (M) = A_s \times f_y \times z \qquad (4.8)$$

$$\because M = P \times L \qquad \Rightarrow \qquad Capacity\ load\ (P) = \frac{M}{L} \qquad (4.9)$$

4.5 CRACK CALCULATIONS

The maximum crack recovery for experimental tests is given by the following equation:

$$\mathit{Maximum\ Crack\ Recovery} = \frac{\mathit{Maximum\ Crack\ Width\ with\ applied\ load} - \mathit{Maximum\ Crack\ Width\ after\ removing\ the\ load}}{\mathit{Maximum\ Crack\ Width\ with\ applied\ load}} \quad (4.10)$$

The crack width and crack spacing are difficult to calculate in practice. However, some empirical equations have generally been used to compute the crack spacing as well as crack width. The following sections show the best-known equations that have been used in most academic research for crack width and crack spacing calculations

4.5.1 OH AND KANG

Oh and Kang have proposed the following equations to predict the maximum crack width (W_{max}) and the average crack spacing(S_m).

$$w_{max} = a_o \times d_b \times (\varepsilon_s - 0.002) \times \frac{h_2}{h_1} \qquad (4.11)$$

$$a_o = 159 \times \left[\frac{C + {d_b}/{2}}{h_2}\right]^{4.5} + 2.83 \times \left[\frac{{A_{ceff}}/{n}}{A_{s1}}\right]^{\frac{1}{3}} \qquad (4.12)$$

$$S_m = d_b \times \left[25.7 \times \left(\frac{C + {d_b}/{2}}{h_2}\right)^{4.5} + 1.66\left(\frac{{A_{ceff}}/{n}}{A_{s1}}\right)^{\frac{1}{3}} + \frac{0.236 \times 10^{-6}}{{\varepsilon_s}^2}\right] \qquad (4.13)$$

where:

C= Clear cover of RC member

d_b= Diameter of the bars

n= Number of steel reinforcement bars

h_1= The distance from the natural axis to the centroid of tension bars

h_2= The distance from the natural axis to the extreme tension edge

A_{s1}= The area of each steel reinforcement bar

A_{ceff}= Effective tension area of concrete surrounding the tension bars and having the same centroid of steel reinforcement bars

ε_s= Steel tensile strain

4.5.2 CEB – FIP CODE

According to the CEB – FIP Code, the mean crack spacing, (S_m), average crack width (W_m), and maximum crack width (W_{max}) can be calculated using the following equations:

$$S_m = 2 \times \left[C + \frac{S}{10}\right] + K_1 \times K_2 \times \frac{d_b}{\rho_{eff}} \qquad (4.14)$$

$$W_m = \varepsilon_1 \times S_m \qquad (4.15)$$

$$W_{max} = 1.7 \times W_m \qquad (4.16)$$

where:

C= Clear cover of RC member

S= Maximum spacing between longitudinal steel reinforcement bars

K_1= 0.4 for deformed bars and 0.8 for plain bars

K_2=$0.125 \times \frac{(\varepsilon_1+\varepsilon_2)}{\varepsilon_1}$

ε_1 & ε_2= The maximum and minimum tensile strains in the effective zone

d_b= Diameter of the bars

$\rho_{eff} = \frac{A_s}{A_{ceff}}$

A_s= Steel reinforcement area in tensile zone

A_{ceff}= Effective tension area of concrete surrounding the tension bars and having the same centroid of steel reinforcement bars

4.5.3 CHOWDHURY AND LOO

Chowdhury and Loo predicted the following equation to calculate the average crack spacing, (S_m), average crack width (W_m), and maximum crack width (W_{max})

$$S_m = 0.6 \times \left(C - S_{avg}\right) + 0.1 \times \frac{d_b}{\rho} \qquad (4.17)$$

$$W_m = S_m \times \frac{f_s}{E_s} \qquad (4.18)$$

$$W_{max} = 1.5 \times W_m \qquad (4.19)$$

where:

S_{avg}= Average spacing between steel reinforcement bars

d_b= Diameter of the bars

ρ= Steel reinforcement ratio

f_s= Stresses in the bars at service load

E_s= Modulus of elasticity

4.5.4THE EURO CODE

Euro Code recommended the following equation to calculate the average crack spacing, (S_m) and the crack width (W)

$$S_m = 50 + 0.25 \times K_1 \times K_2 \times \frac{d_b}{\rho} \qquad (4.20)$$

$$W = S_m \times \varepsilon_s \times \gamma \qquad (4.21)$$

where:

K_1= 0.8 for deformed bars and 1.6 for plain bars

K_2=1.0 for members subjected to tension and 0.5 for members subjected to bending

d_b= Diameter of the bars

ρ= Steel reinforcement ratio

ε_s= Steel tensile strain

γ= 1 for mean crack width and 1.7 for maximum crack width

CHAPTER 5

EXPERIMENTAL PROGRAM OF BCJ SPECIMENS WITH SMAs

5.1 INTRODUCTION

For the investigation of the response of the BCJ reinforced with embedded SMA bars, eight BCJ specimens were cast then tested under static, reverse cyclic and cyclic loadings. Three control specimens contain ordinary steel reinforcement bars only and five specimens contain SMA bars at the critical section of beam with steel reinforcement in different configurations. One of the five SMA specimens was cast using untrained SMA bars and the remaining specimens were cast using trained SMA bars. In addition, several experimental tests have been carried out to perform nonlinear simulation in ANSYS software, including testing of the mechanical properties of concrete and steel reinforcement bars.

5.2 SPECIMEN DETAILS

Eight specimens were fabricated and cast by PRAINSA Company using a 51 MPa compressive strength concrete. All bars included main steel reinforcement and SMA bars were 12 mm in diameter. 8 mm diameter bars were used as transverse reinforcement for all specimens. Table 5 - 1 summarizes all the BCJ specimens' details.

Table 5 - 1: BCJ Specimens Details

NUMBER OF SPECIMENS	SPECIMENS NAME	DETAILS	FIGURE NO.	TYPE OF TEST
3	Con-BCJ-1 Con-BCJ-2 Con-BCJ-3	All reinforcement of beams and columns are 12 mm diameter bars	5 - 3	Monotonic, Cyclic, and Reverse Cyclic
1	NiTi-BCJ-1	3 Ribbed SMA trained bars were used at the Top critical section of the beam	5 - 4	Cyclic
1	NiTi-BCJ-2	2 Ribbed SMA trained bars with 1 Steel bar were used at the Top critical section of the beam	5 - 5	Cyclic
1	NiTi-BCJ-3	2 Plain SMA trained bars ONLY were used at the Top and Bottom critical sections of the beam	5 - 6	Reverse Cyclic
1	NiTi-BCJ-4	1 Plain SMA trained bar with 2 Steel bars were used at the Top and bottom critical section of the beam	5 - 7	Reverse Cyclic
1	NiTi-BCJ-5	3 Plain SMA UN Trained bars were used at the Top critical section of the beam	5 - 8	Cyclic

Con: Control **NiTi: Nickel Titanium** **BCJ: Beam Column Joint**

5.2.1 BEAM COLUMN JOINT SPECIMEN SIZE

All BCJ samples were created with the same dimensions 300 mm depth by 250 mm width, the total height of the column was 1400 mm and the cantilever length of the beam was 900 mm. Figure 5 - 1 shows the Geometric Size and dimensions of BCJ specimens used for the experimental testing program. These BCJ dimensions have been selected as approximately to represent the average sized of real BCJ. Moreover, there were many limitations such as the ultimate load capacity and dimensions of the testing frame that is available in KFUPM lab and the deflection capacity as illustrated in Figure 5 - 2.

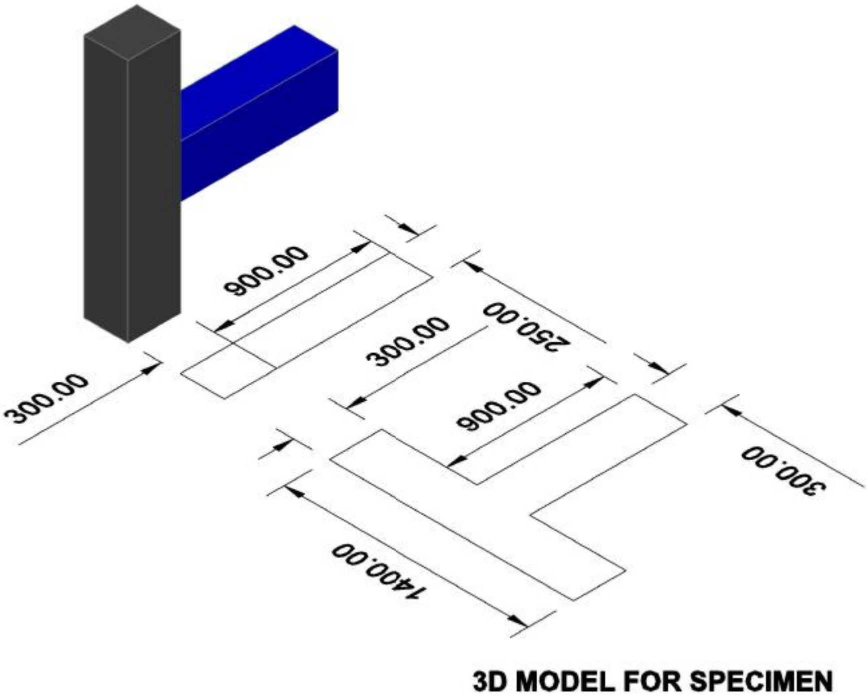

Figure 5 - 1: Geometric size of BCJ specimens

Figure 5 - 2: Existing frame available for BCJ testing in KFUPM lab

5.2.2 BEAM COLUMN JOINT SPECIMEN'S CAGES

For all specimens, a number of six 12 mm diameter bars have been used in columns as main reinforcement whereas 8 mm diameter ties have been used for transverse reinforcement. Similarly, three 12 mm diameter bars have been used at both bottom and top main reinforcement in all beams except for NiTi-BCJ-4 specimen in which two main reinforcement bars have been used at the bottom and top of the beam. In addition, 8 mm diameter closed stirrups have been used as transverse reinforcement for all beams. Moreover, there were two 8 mm diameter ties were put in the joint for all the specimens. Geometry and reinforcement for all specimens are given in Figure 5 - 3 to Figure 5 -8.

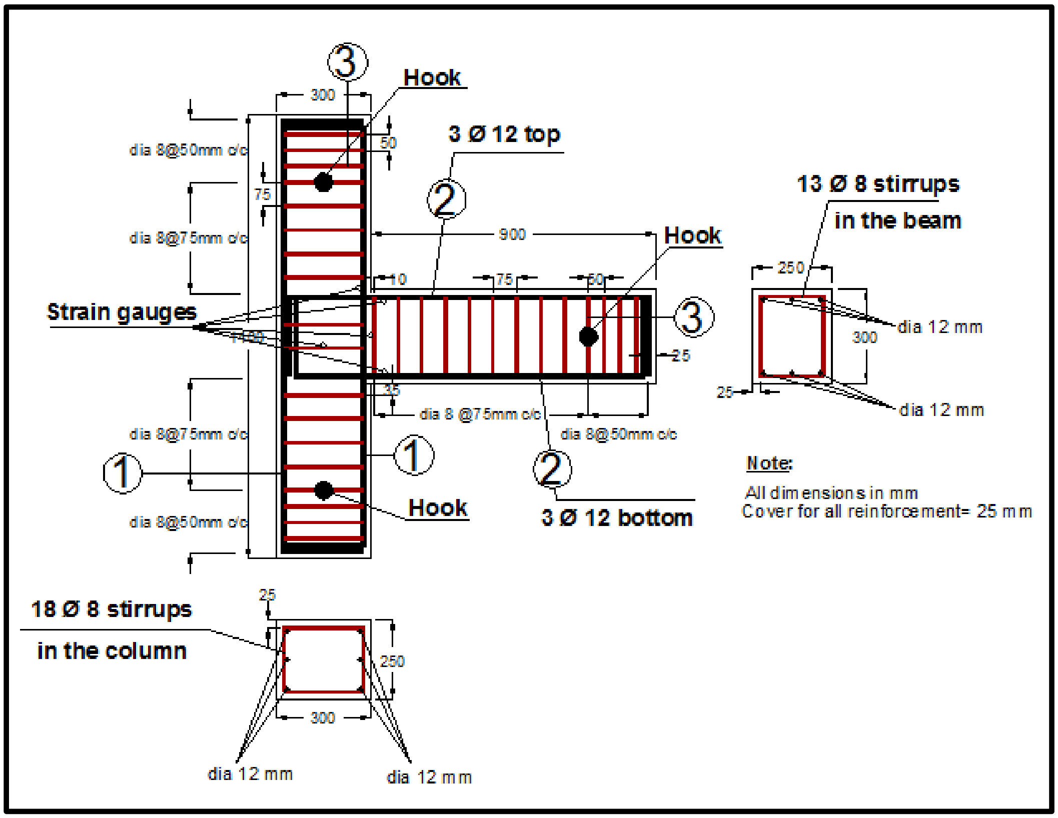

Figure 5 - 3: Geometry and reinforcement details of Con-BCJ-1, 2, and 3 specimens

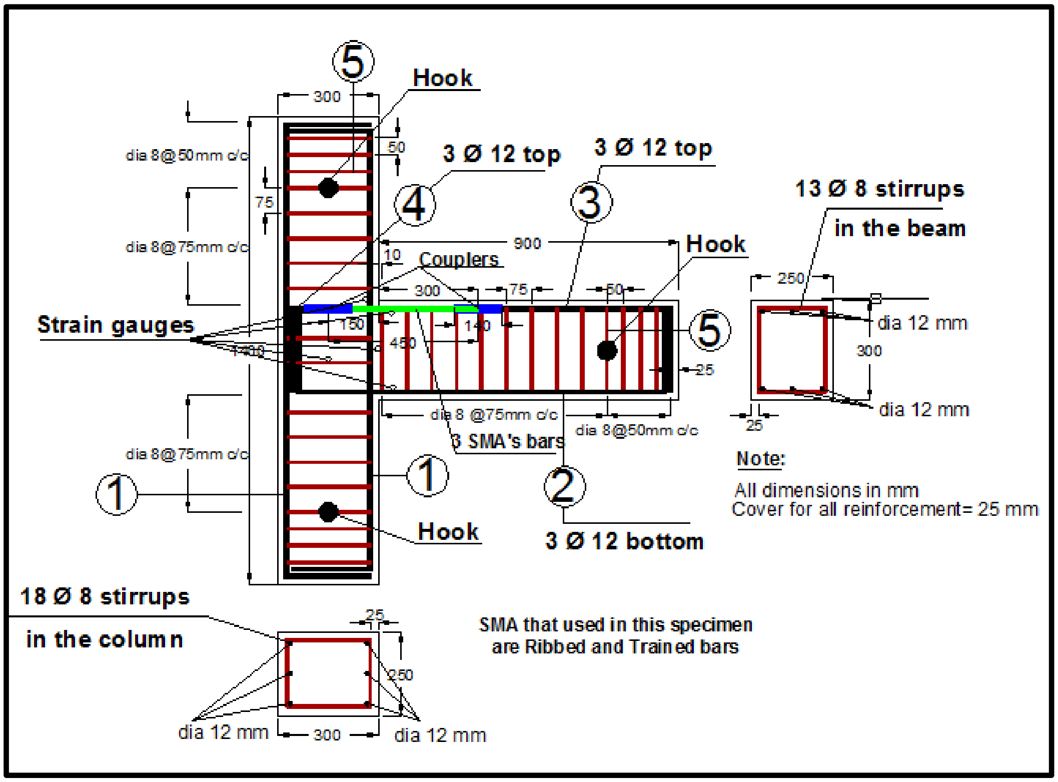

Figure 5 - 4: Geometry and reinforcement details of NiTi-BCJ-1 specimen

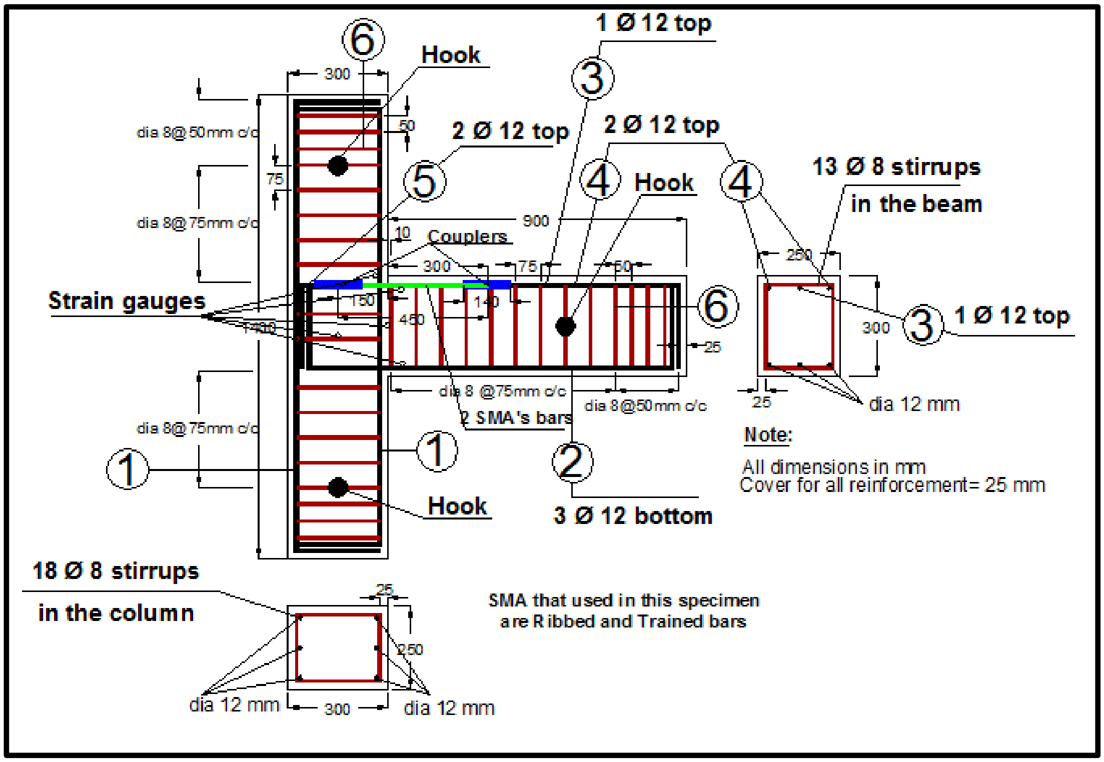

Figure 5 - 5: Geometry and reinforcement details of NiTi-BCJ-2 specimen

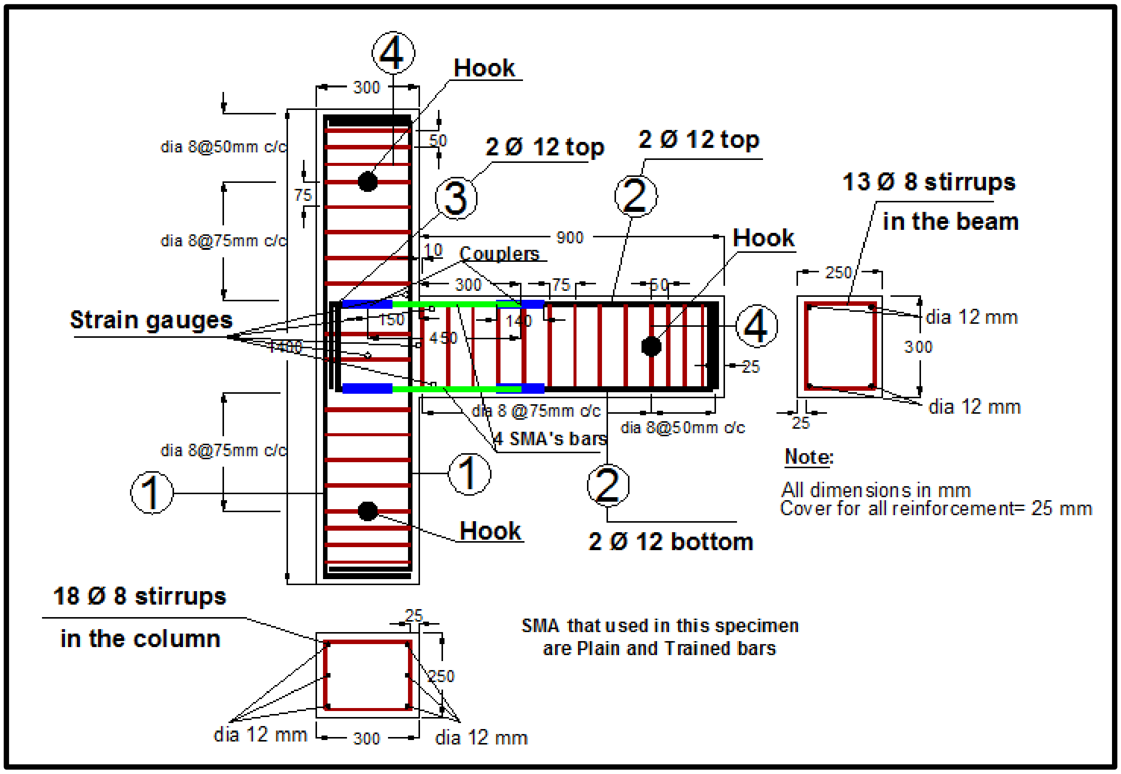

Figure 5 - 6: Geometry and reinforcement details of NiTi-BCJ-3 specimen

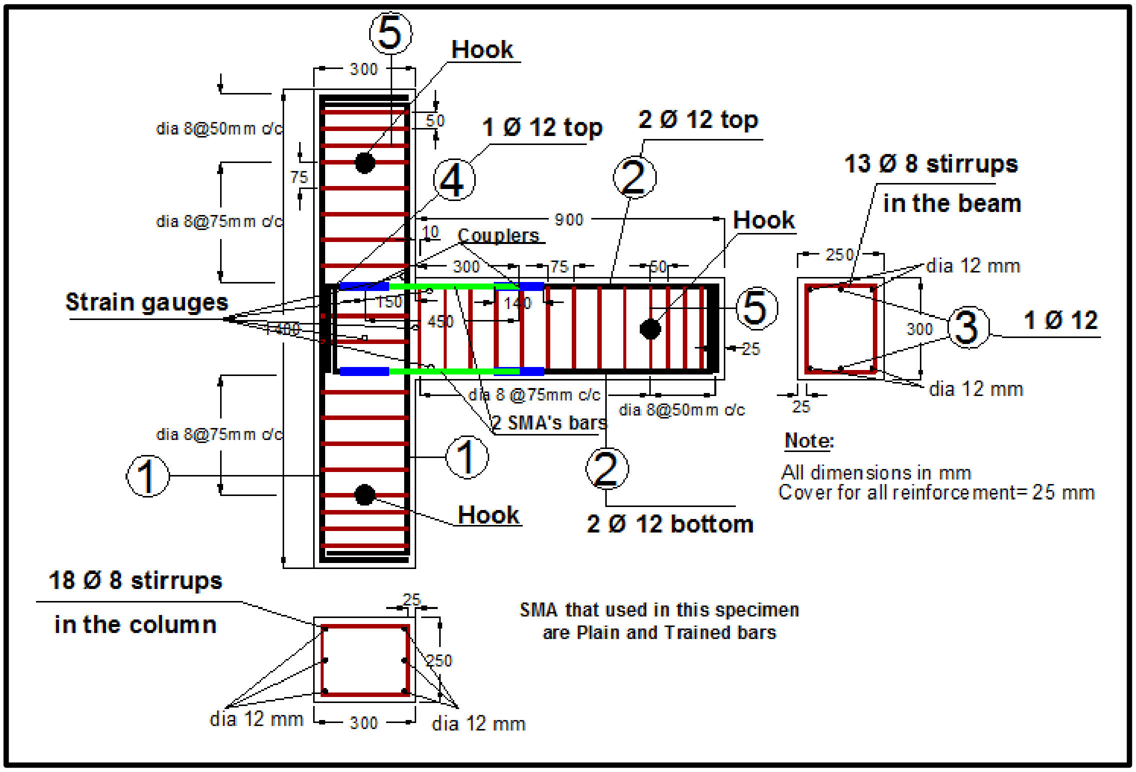

Figure 5 - 7: Geometry and reinforcement details of NiTi-BCJ-4 specimen

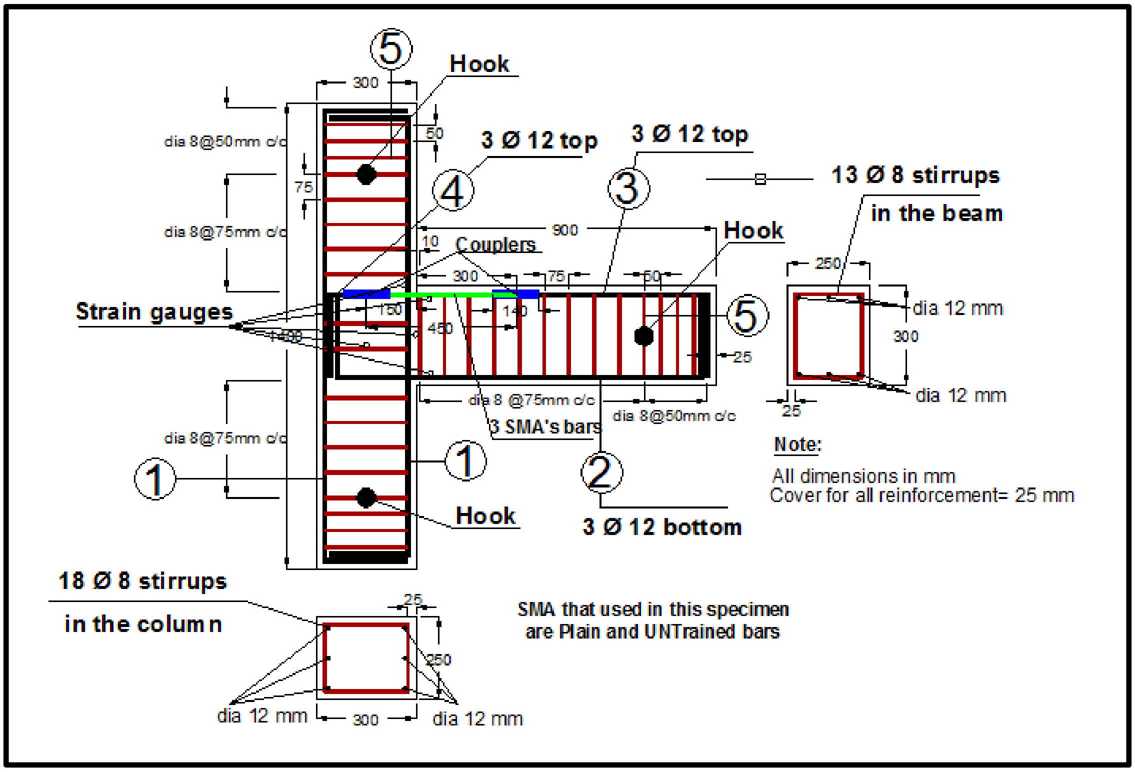

Figure 5 - 8: Geometry and reinforcement details of NiTi-BCJ-5 specimen

5.3 MECHANICAL PROPERTIES OF CONCRETE

All the specimens were fabricated and cast in PRAINSA Company using a concrete strength of 51 MPa. Several standard concrete cylinder specimens with dimensions of (75*150) mm as illustrated in Figure 5 -9 were cast and tested in the lab to get the compressive strength, tensile strength, and the stress - strain diagram curve. Figure 5 -10 shows the concrete cylinder specimens after casting at the factory.

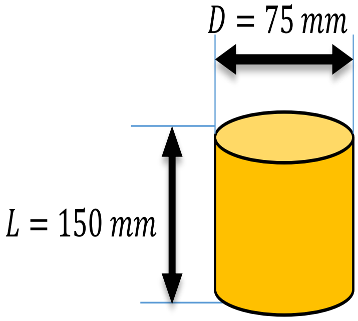

Figure 5 - 9: Dimensions of concrete cylinder specimens

Figure 5 -11 shows the concrete cylinder specimens during and after the compressive strength test. Compressive strength of concrete could be calculated using the following equation:

Figure 5 - 10: The concrete cylinder specimens after casting at the factory

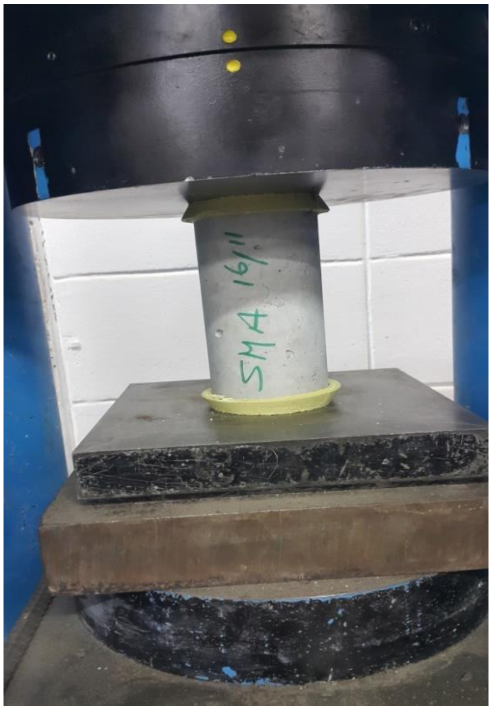

Figure 5 - 11: concrete cylinder specimens during and after compressive strength test

$$f_c^{/} = \frac{P}{A} = \frac{P}{\pi D} \qquad [5-1]$$

where P: Applied compression load

D: Diameter of concrete cylinder specimen (75 mm)

From the results of the test, the strength of concrete is equal to 51 MPa. Table 5 -2 shows the test results of the three cylinder specimens.

Table 5 - 2: Compressive strength of concrete

SAMPLE NO.	COMPRESSIVE STRENGTH in MPa	AVERAGE COMPRESSIVE STRENGTH
1	54.66	51 MPa
2	47.54	
3	50.82	

In addition, a split tensile experiment was performed for the concrete cylinder specimens to get the tensile strength of the concrete. Figure 5 -12 illustrates the depiction of the concrete cylinder specimen which has been used for the tensile split test.

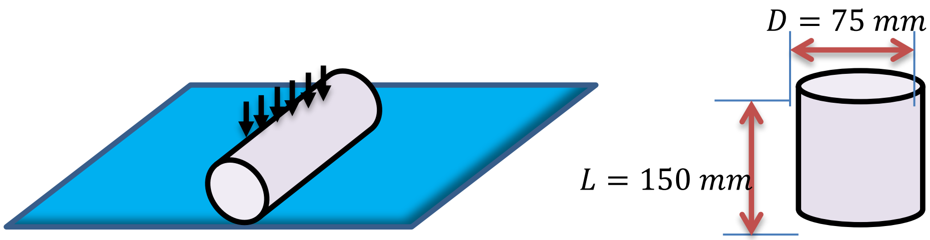

Figure 5 - 12: Depiction a split teste cylinder used in split test.

Splitting tensile strength could be calculated using the following equation:

$$f_t = \frac{2P}{\pi L D} \qquad [5-2]$$

where:

P: The applied tensile load

L: The length of concrete cylinder specimen (150 mm)

D: The diameter of concrete cylinder specimen (75 mm)

From the results of the split test, the tensile stress is equal to 4.5 MPa as shown in Table 5 -3. Figure 5 -13 shows the concrete cylinder specimens during and after the split tensile test.

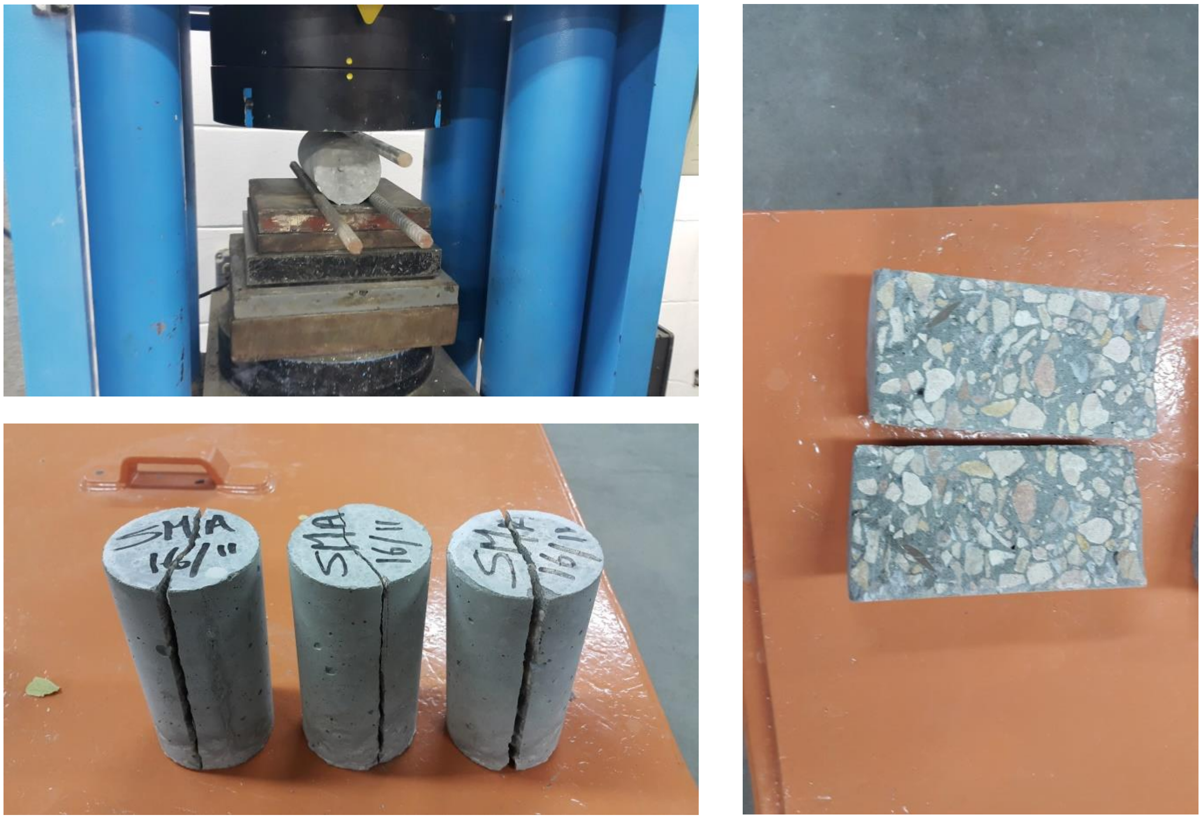

Figure 5 - 13: Concrete cylinder specimens during and after the split tensile test

Table 5 - 3: Splitting tensile strength of concrete

CYLINDER NO.	TENSILE STRENGTH (MPa)	AVERAGE TENSILE STRENGTH
1	4.59	4.5 MPa
2	4.30	
3	4.62	

In addition, two concrete cylinder specimens were tested in compression using strain gauges and LVDTs to draw the stress – strain diagram curve and to find the Poisson ratio. Figures 5 - 14 & 5 -15 show the test set up during and after the test respectively. The stress - strain diagram curve of concrete was drawn and illustrated in Figure 5 -16.

Figure 5 - 14: Concrete cylinder specimen during the stress-strain compression test

Figure 5 - 15: Concrete cylinder specimen after the stress-strain compression test

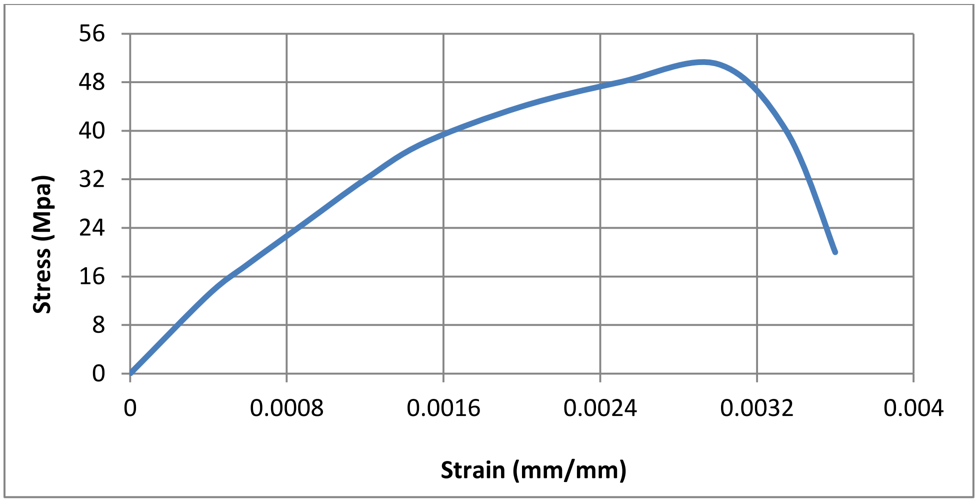

Figure 5 - 16: Stress - Strain diagram curve for concrete cylinder specimen

5.4MECHANICAL PROPERTIES OF STEEL REINFORCEMENT

For all BCJ samples, the diameters of transverse and longitudinal reinforcement bars are 8 mm, and 12 mm respectively. Tensile tests were conducted to calculate the actual yielding tensile strength for reinforcement bars. Table 5 - 4 shows the summarized properties of 12 mm and 8 mm diameter steel reinforcements. Stress strain curves of 12 mm and 8 mm diameter steel reinforcement bars are illustrated in Figures 5 - 17 & 5 – 18 respectively.

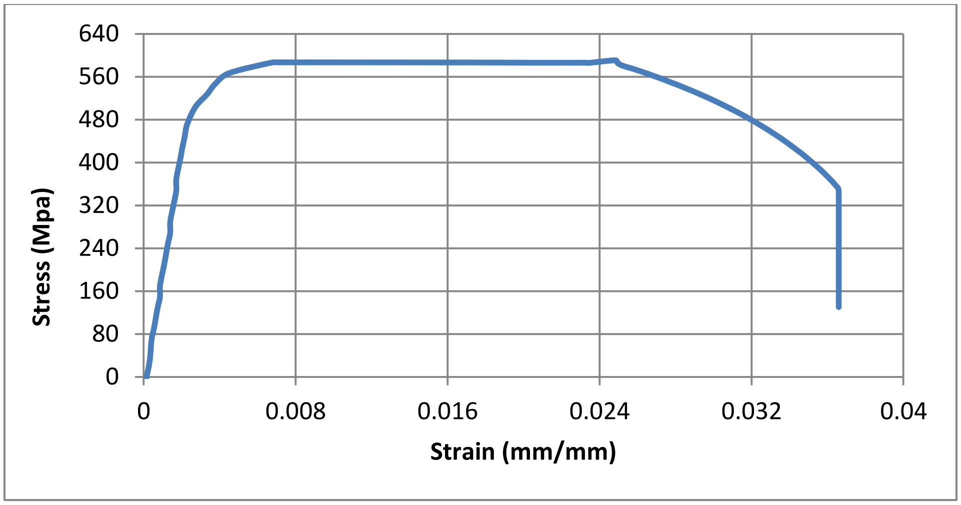

Figure 5 - 17: Stress - Strain diagram curve for 8 mm diameter bar

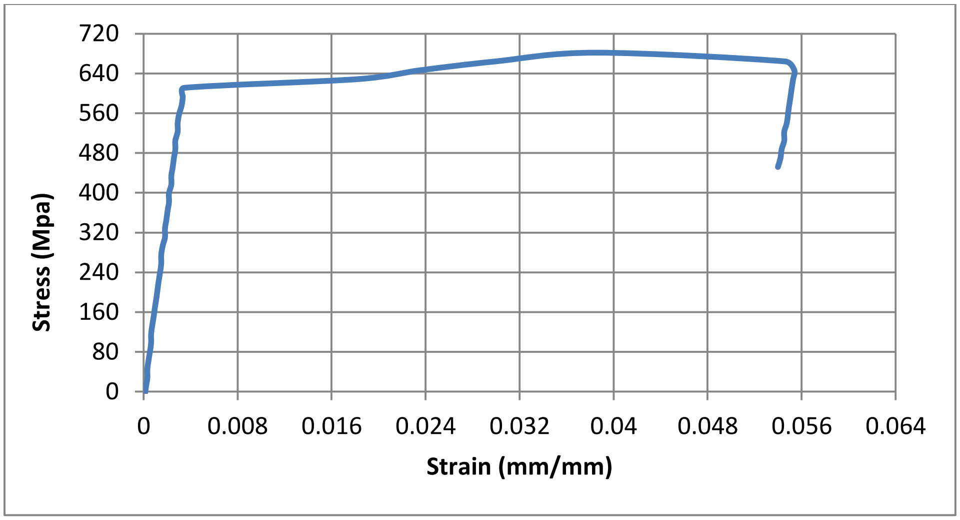

Figure 5 - 18: Stress - Strain diagram curve for 12 mm diameter bar

Table 5 - 4: Mechanical properties for steel bars

Steel bars	Diameter in mm	Fy in MPa
Φ 8	8	576
Φ 12	12	610

5.5 STRAIN GAUGES

Fifteen (15) strain gauges have been installed in each specimen. These gauges were installed at places in the BCJ reinforcement as illustrated in Figure 5 - 19. Two (2) gauges were placed on top reinforcement at the BCJ interface and other two (2) were placed on top reinforcement but at a distance of (25 mm) from the first stirrup. Other two (2) strain gauges were placed near the mechanical coupler of the top reinforcement. Moreover, same numbers of strain gauges have been used at bottom reinforcement bars of the beam. In addition, one (1) strain gauge was placed at the column reinforcement and two (2) on stirrups and joint ties. The unique adhesive glue has been used for pasting the strain gauges on the bar surfaces, then wrapped by a tape and waterproof as shown in Figure 5 - 20.

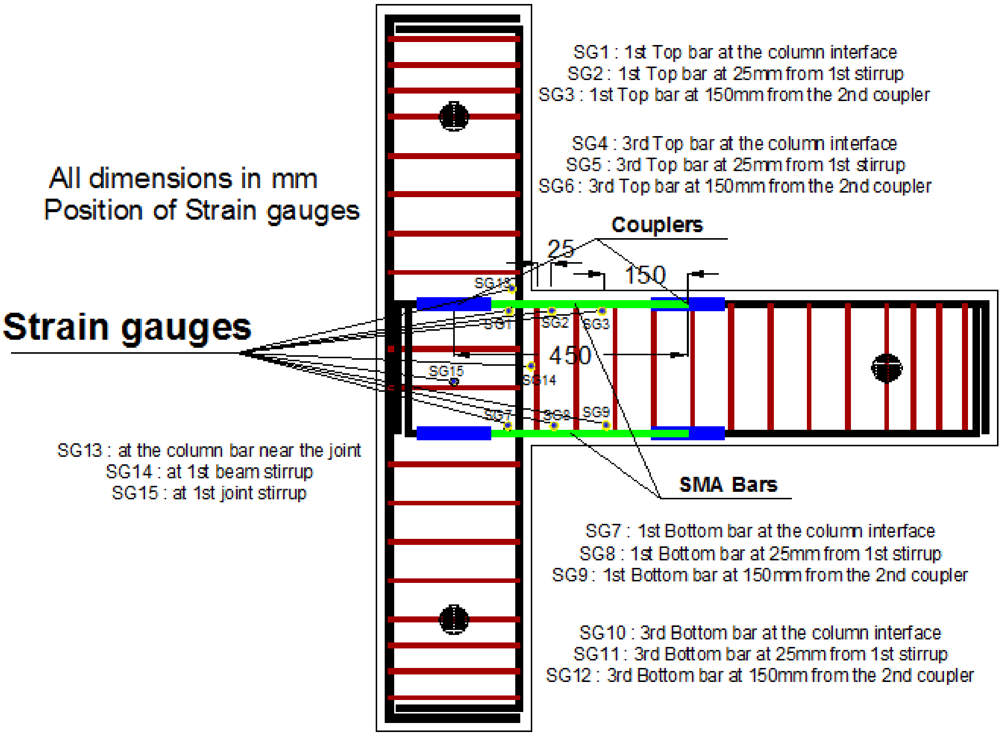

Figure 5 - 19: Locations of strain gauges for reinforcement

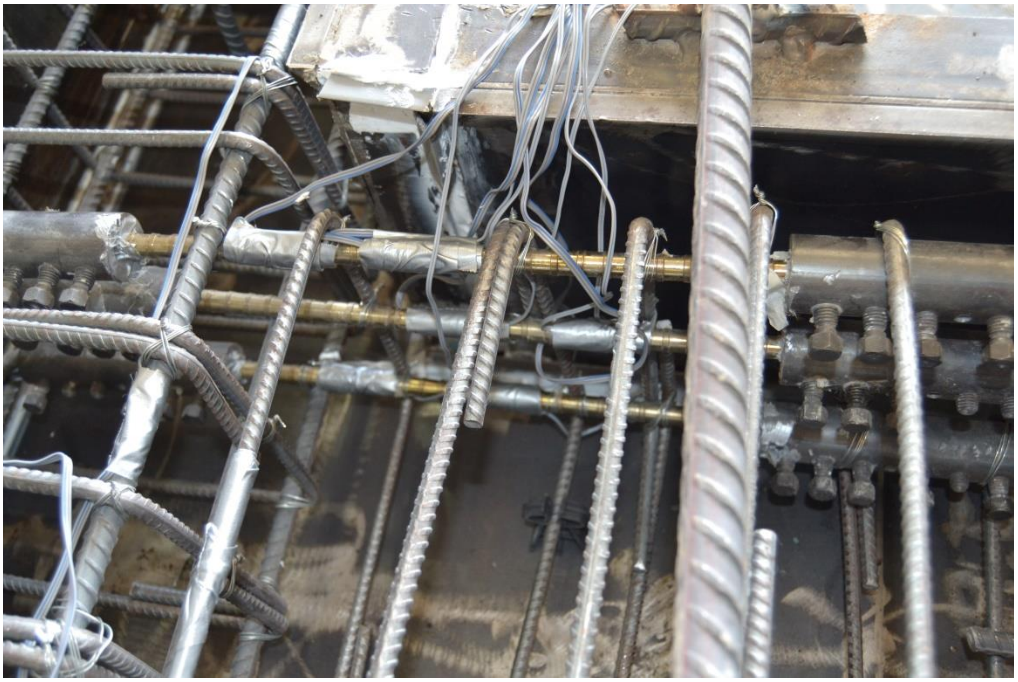

Figure 5 - 20: Strain gauges after wrapping with tape and waterproof

Figure 5 - 21 shows the preparation of steel reinforcement cages of BCJ specimens at PRAINSA factory. All SMA bars and couplers are installed and fixed in their position at the BCJ specimens with appropriate configuration as illustrated previously in Table 5 - 1. Figures 5 - 22 & 5 - 23 show the installation of the strain gauges into the BCJ specimens and the exact location of strain gauges after the installation into the BCJ specimen respectively. ‘Figure 5 - 24 shows the BCJ specimens ready for casting.

Figure 5 - 21: The preparation of steel cages of BCJ specimens at PRAINSA factory

Figure 5 - 22: The installation of the strain gauges into the BCJ specimens

Figure 5 - 23: Locations of strain gauges after the installation into the BCJ specimens

Figure 5 - 24: The BCJ specimens ready for casting

5.6 CASTING OF BEAM COLUMN JOINTS SPECIMENS

All steel cages and steel formwork have been prepared by PRAINSA Company and all specimens were cast in the factory. Eight steel forms have been fabricated for casting using a mechanical vibrator and a delivery mixer as shown in Figure 5 - 25. Three specimens have been prepared using ordinary steel reinforcement and other five specimens, which reinforced partially with SMA bars, have been fabricated. Figure 5 - 26 shows the BCJ specimens after casting and finishing procedure of the surface.

Figure 5 - 25: Casting of BCJ specimens at PRAINSA factory

Figure 5 - 26: Finishing procedure of the concrete surface after casting of specimens.

5.7 TESTING ARRANGEMENTS

All BCJ samples have been tested at self-reaction floor loading at KFUPM lab. The extra clamping system has been made to the testing frame for holding the BCJ samples at both ends of columns and at the beam tip for applying the displacement and the loads from a hydraulic jack, which is illustrated in Figure 5 - 27. Two jacks have been used for applying the loads. One hydraulic jack (A) was placed on the top surface of column to apply 150 kN as an axial load. The other jack (B) was placed at the beam tip to apply displacement and loads on the tip of the beam as illustrated in Figure 5 - 28.

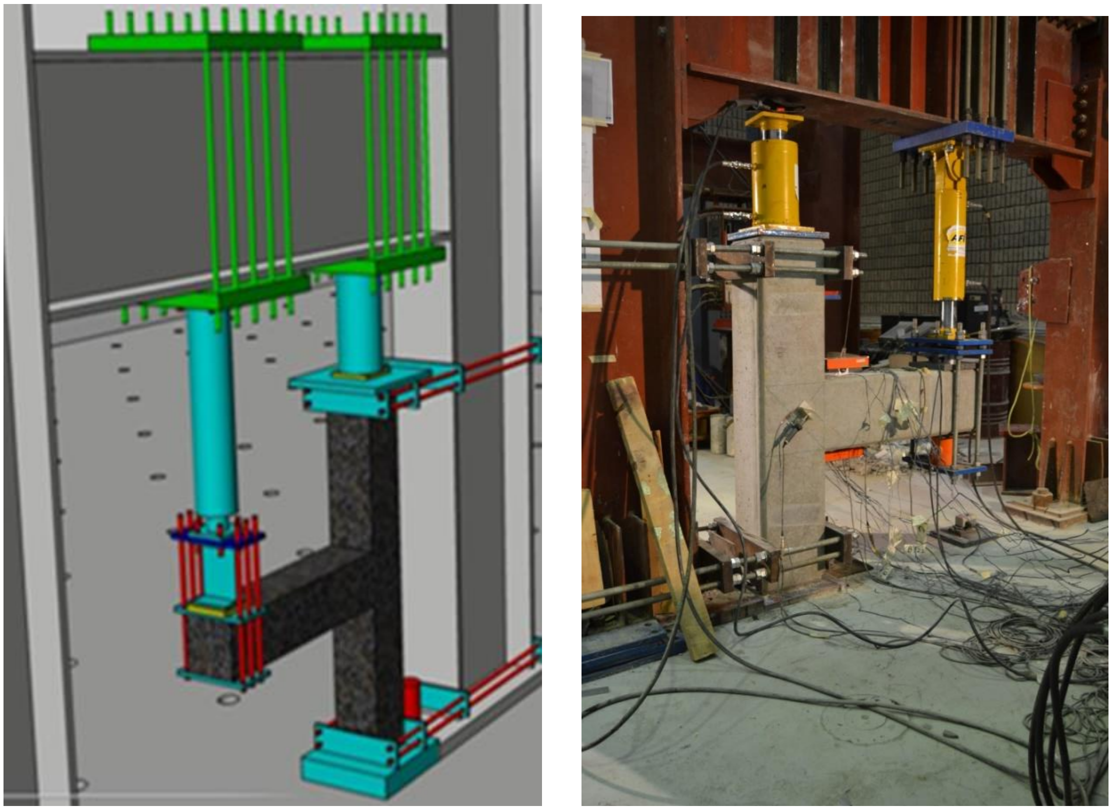

Figure 5 - 27: Extra clamping system for holding the samples during the BCJ testing

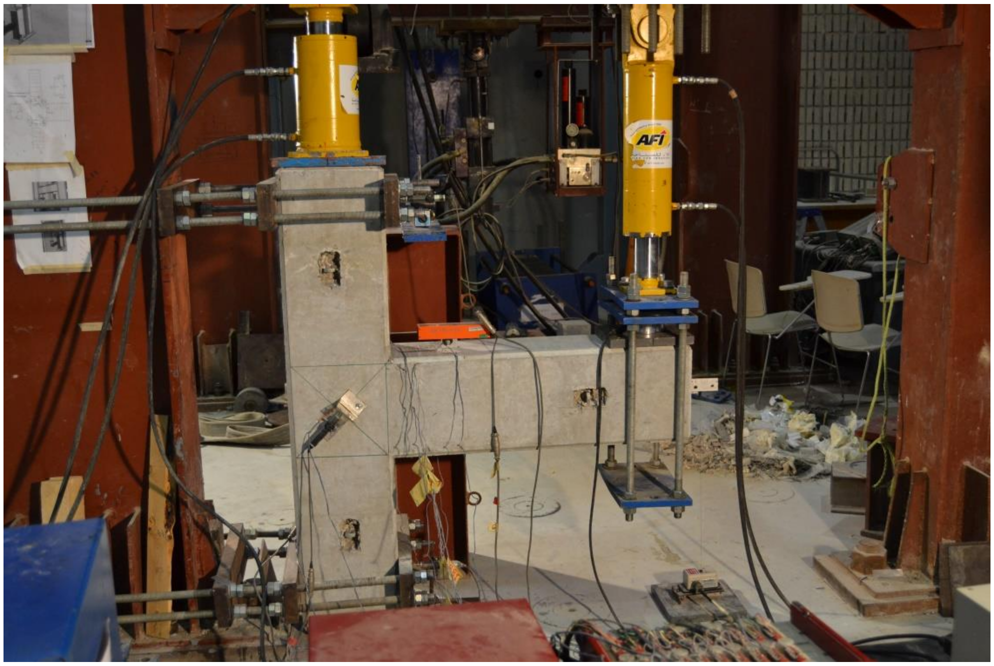

Figure 5 - 28: Hydraulic jacks (A) & (B) used to test BCJ specimens

5.7.1 INSTRUMENTS FOR TESTING

Concrete stain gauges, LVDT's, and Load cells, have been installed for all BCJ samples to record deflections, strains, and loads. Two load cells named (LC1 & LC2) with a capacity of 100 tons were placed at the bottom and top of beam tip. One Load cell named (LC3) with 20 tons capacity was placed on top of column as illustrated in Figures 5 - 29 & 5 - 30

Figures 5 - 31 & 5 - 32 illustrate one patriot LVDT named (B2) - string type - has been placed at the beam tip to record deflections during BCJ specimens testing. 2 LVDT's named (C1 & C2) have been placed at the bottom and top of the column to measure any movements or rotations. Two LVDT's named (J1 and J2) have been placed in the joint region for observing and measuring if any diagonal crack occurred. In addition, two LVDT's named (K1 and K2) have been installed at the critical section bottom and top of the beam for measuring the crack width during the test as shown in Figure 5 - 33. Besides that, a crack-measuring card has been used in each cycle to measure the crack width after and before applying the load as illustrated in Figure 5 - 34. Concrete strain gauges were placed on the tension and compression side of column and beam for measuring strains on concrete surface as illustrated in Figure 5 - 35.

Figure 5 - 29: Load cells that have been used to test BCJ specimens

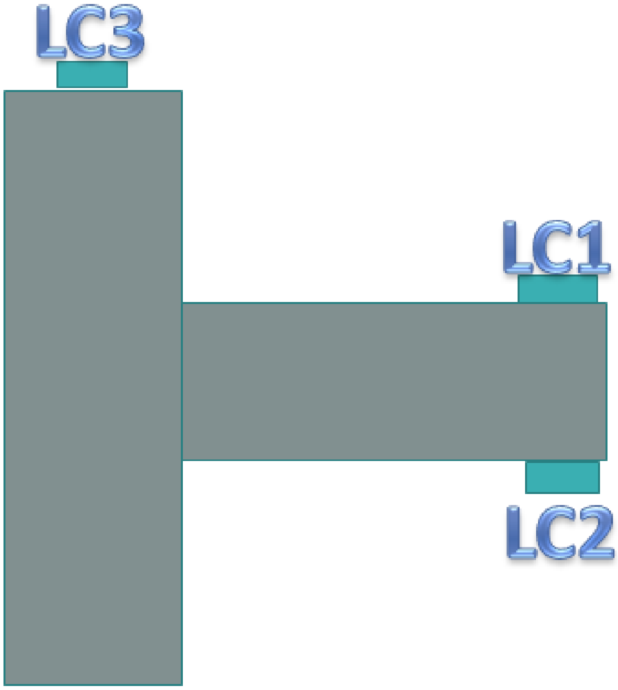

Figure 5 - 30: Locations of load cells during testing of BCJ specimens

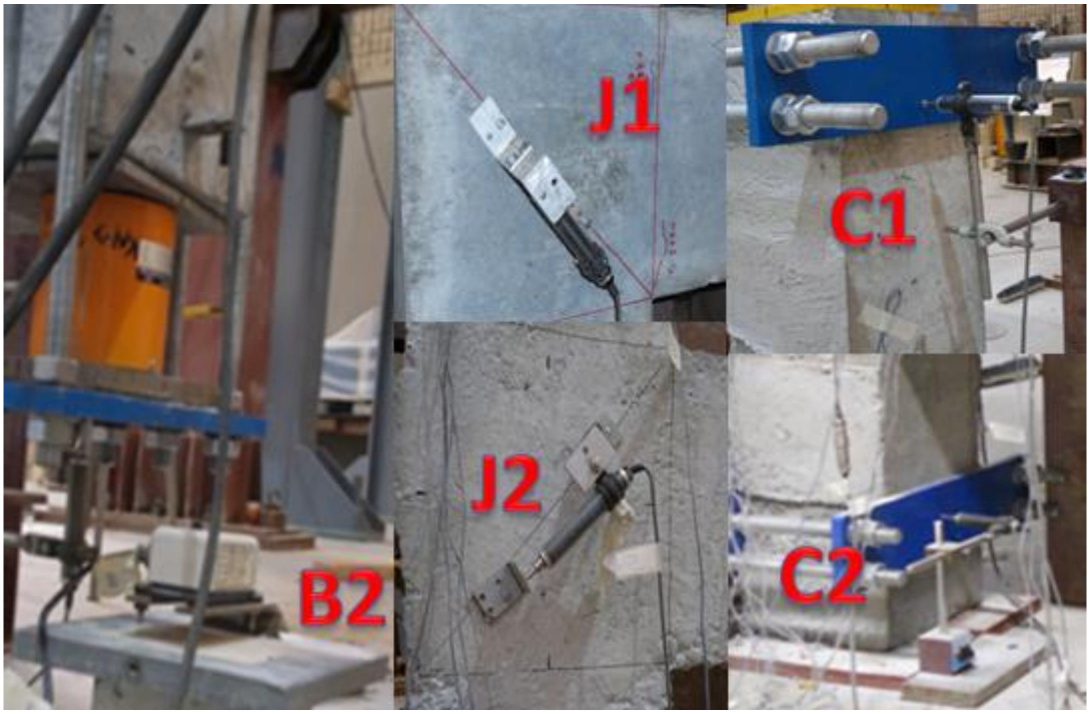

Figure 5 - 31: LVDT's locations that have been used during testing of BCJ specimens

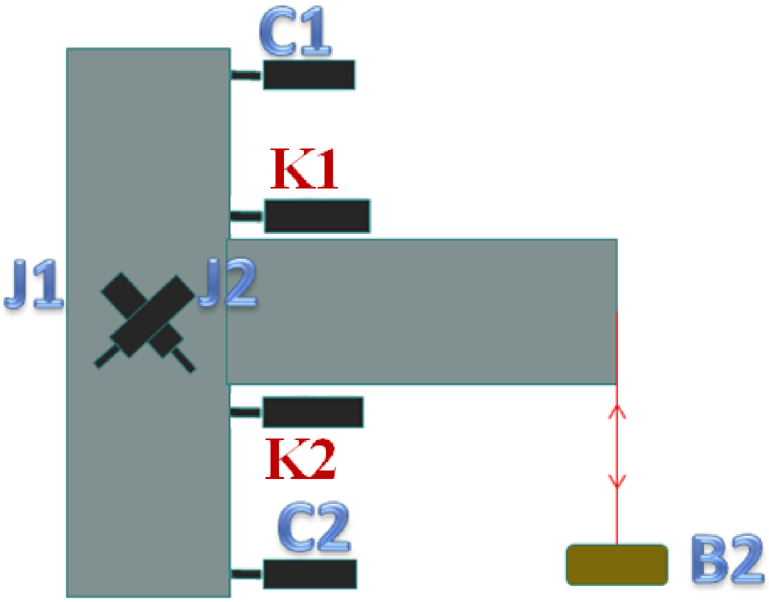

Figure 5 - 32: Locations of (LVDT's) which attached to BCJ specimens during testing

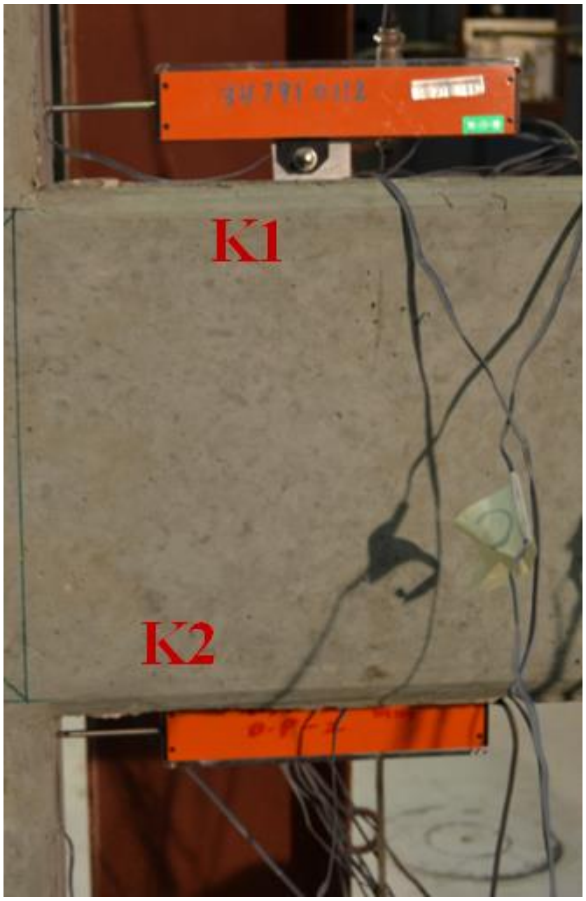

Figure 5 - 33: LVDT's positions used for measuring crack width during the BCJ test

Figure 5 - 34: Using of a crack-measuring card for the measurement of crack width

Figure 5 - 35: Strain gauges for concrete surface applied to the BCJ specimen

5.8 TESTING PROCEDURE

The BCJ specimens were tested under displacement control method. As illustrated in Figure 5 - 36, the specimens were subjected to two types of loads. A constant axial load which applied on top of the column (150 kN) and an increase in beam tip deflection on push side for monotonic and cyclic tests and on both push and pull sides for reverse cyclic tests. All load cells, strain gauges, and LVDTs have been connected to a data logger and all data readings were recorded each 0.1 mm change in displacement. Furthermore, pictures and photographs of the tested specimens have been taken continuously during the whole testing process. All cracks, which were developed throughout the test, have been marked and measured after each cycle.

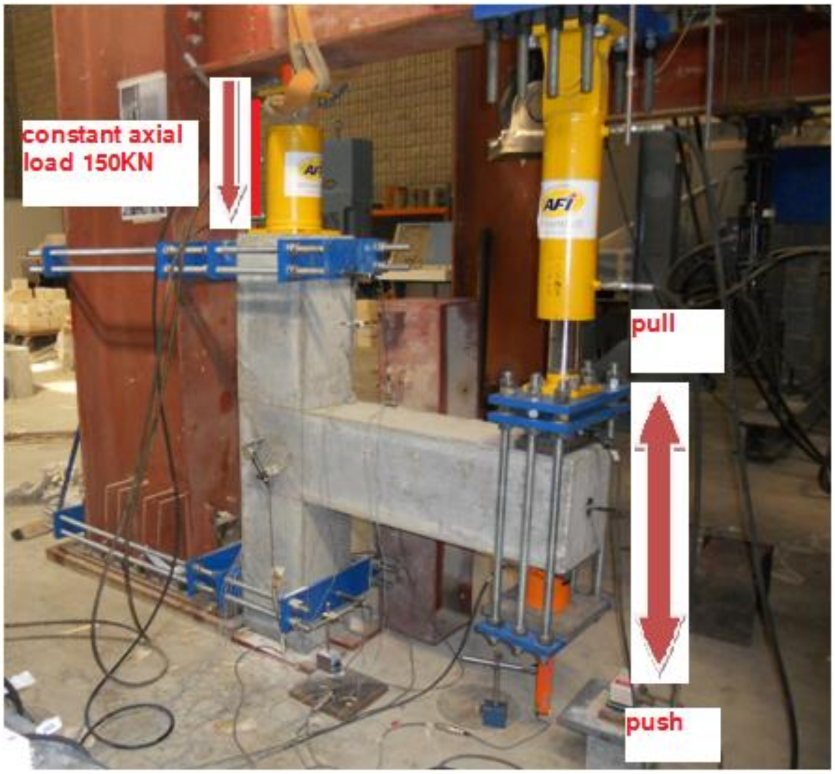

Figure 5 - 36: Testing procedure for the BCJ specimens

5.9 TESTING PROTOCOL

All BCJ specimens were tested at a quasi-static rate with the same ambient temperature. Theoretical loads at first crack as well as at yielding have been calculated before starting the tests. All BCJ specimens have been tested under deflection control approach and all the corresponding data, such as load, deflections, rotations, and cracks are recorded using a data logger at each 0.1 mm increment in the tip beam displacement.

Table 5 - 5 and Figure 5 - 37 illustrate the cyclic load pattern which has been used during the BCJ tests.

Table 5 - 5: Cyclic load pattern during the BCJ tests

No.	**Push**	**Pull**
	mm	mm
1	2	-2
2	4	-4
3	6	-6
4	8	-8
5	10	-10
6	12	-12
7	14	-14
8	16	-16
9	18	-18
10	20	-20
11	22	-22
12	24	-24
13	26	-26
14	28	-28
15	30	-30

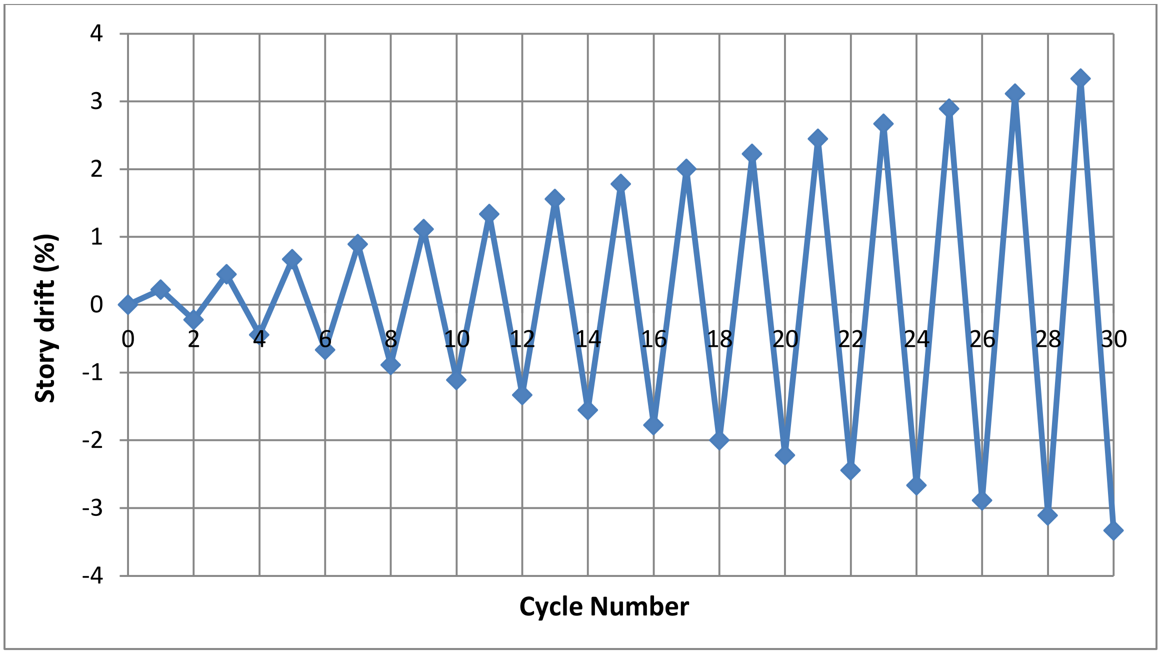

Figure 5 - 37: Cyclic load pattern during the BCJ tests

For cyclic and reverse cyclic tests of the specimens, a small increment of (2 mm) was applied to the beam tip to investigate the real response of the BCJ specimens. After each cycle (2 mm), the crack width was measured using the crack-measuring card and then after removing the load the residual crack was measured and recorded.

CHAPTER 6

EXPERIMENTAL TEST RESULTS OF BCJ SPECIMENS WITH SMAs

6.1 MONOTONIC TEST RESULTS FOR CONTROL BEAM COLUMN JOINT SPECIMEN (Con-BCJ-1)

For the control monotonic test, the load vs. story drift shows the yielding load (65 kN) and the maximum load which the control BCJ specimen can carry (75 kN). In addition, the maximum displacement it reached during the test is (38 mm) as shown in Figure 6 - 1.

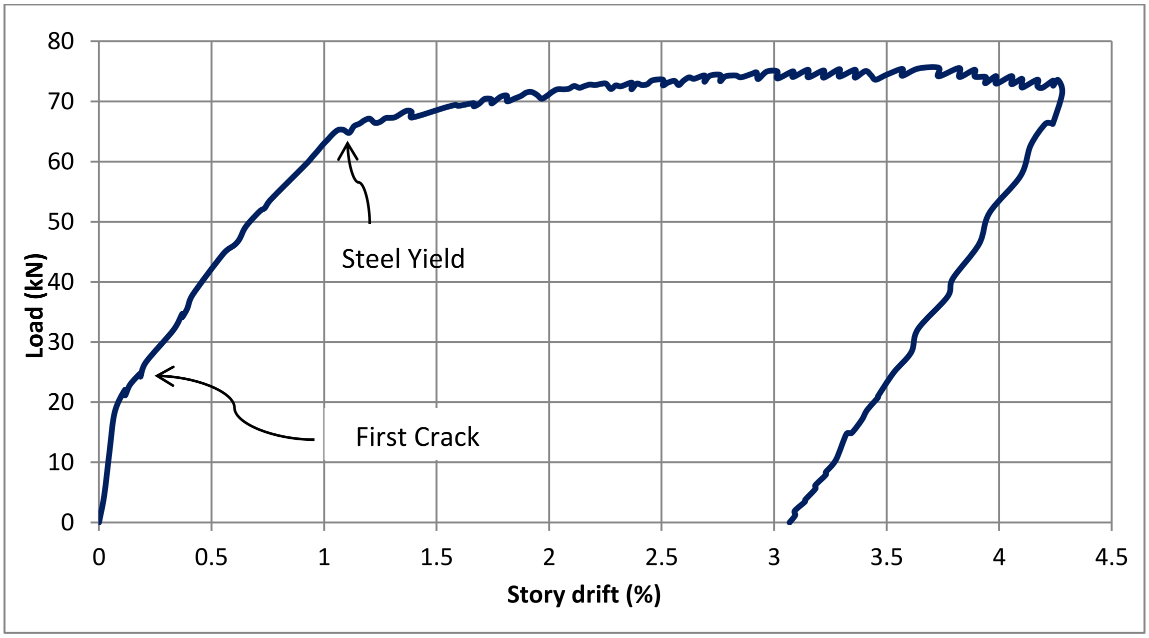

Figure 6 - 1: Load - Story drift curve for control monotonic load test Con-BCJ-1

During the experimental test, first flexural crack was found at the BCJ interface at the load of 25 kN and the displacement of 2.2 mm. Then, a second major flexural crack was formed at a small distance from the joint in the top surface of the beam at load of 30.8 kN and the displacement of 2.66 mm. After that, third and fourth cracks were formed on the beam top surface at different locations and loads. Figures 6 - 2 shows the formation of the cracks at the BCJ interface and beam.

Figure 6 - 2: The formation of cracks for Con-BCJ-1 specimen

At the end of the test, failure of Con-BCJ-1 specimen was a flexural failure at the BCJ interface. All cracks were formed in the beam and at the BCJ interface. After the yielding of the steel, the majority first and second cracks started to increase in width with increasing of displacement at the tip of the beam while the maximum load did not increase significantly. Figure 6 - 3 illustrates the specimen after finishing the test.

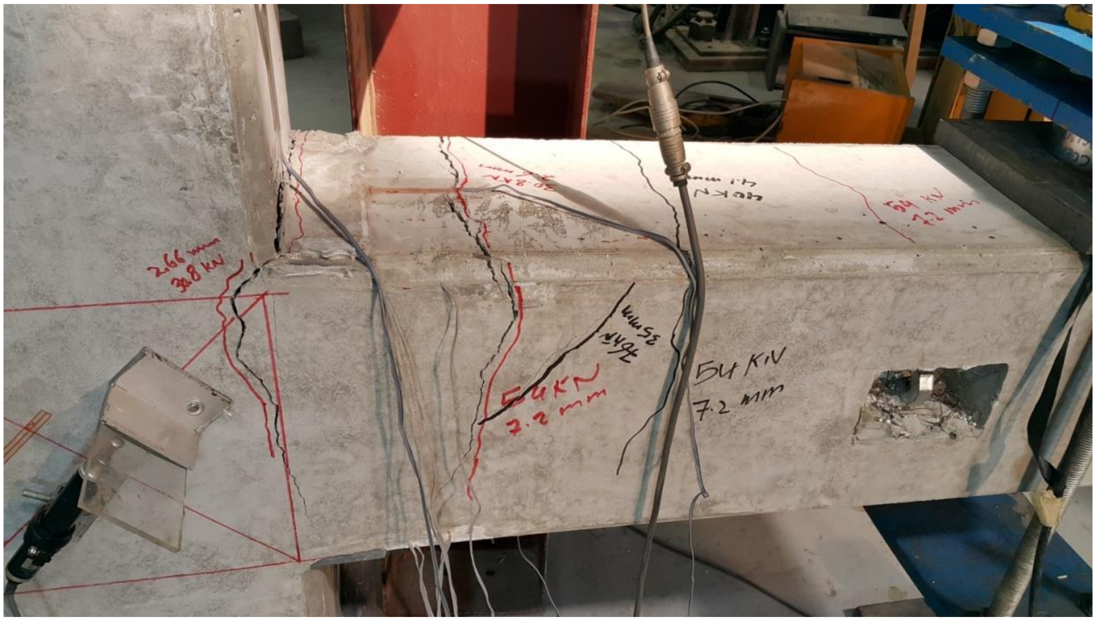

Figure 6 - 3: Failure of Con-BCJ-1 specimen

Strain gauges have been installed to record the strains in the steel reinforcement bars. Figure 6 - 4 illustrates graphs between strains and loads in the bottom and top steel reinforcement at the critical section of the beam that illustrates the static response according to the testing of the BCJ Con-BCJ-1 specimen.

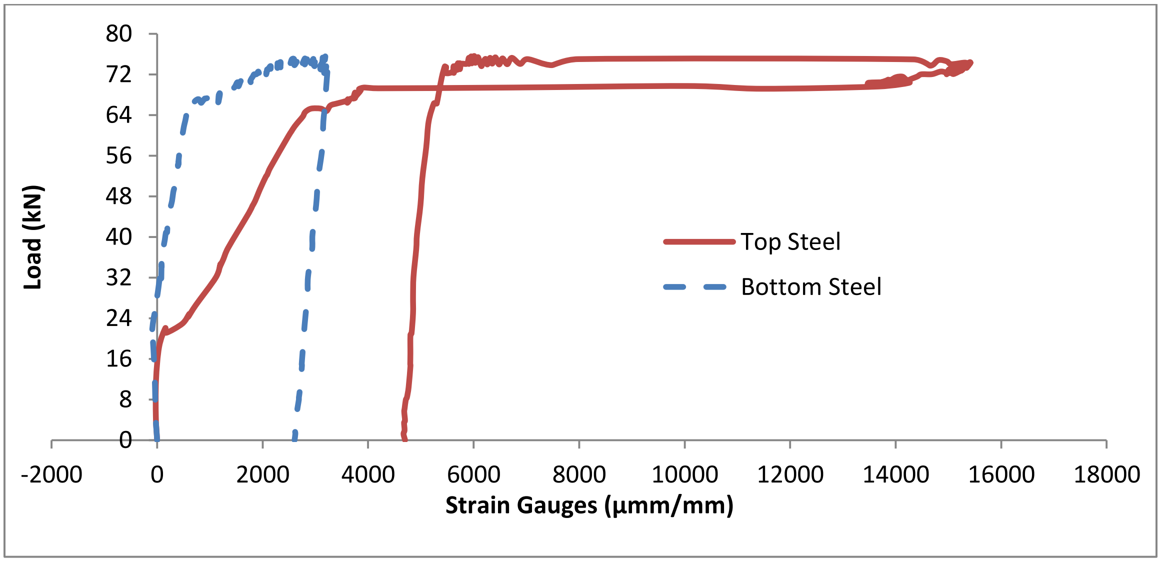

Figure 6 - 4: Steel strain gauges at top and bottom reinforcement of Con-BCJ-1

Strain gauges have been monitored and graphs were plotted between strains and loads for the control monotonic load testing of BCJ sample as illustrated in Figure 6 - 5.

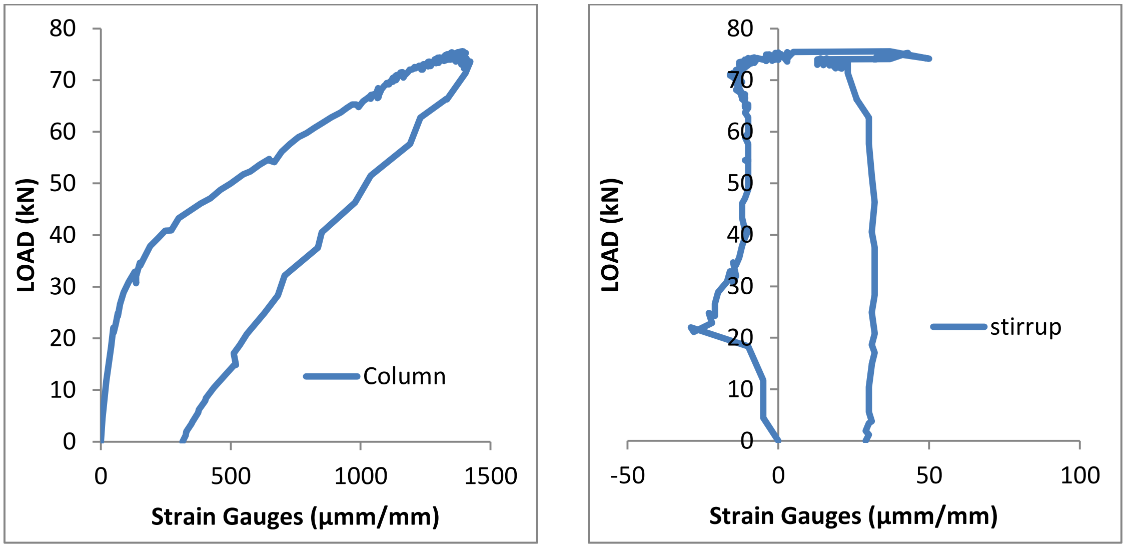

Figure 6 - 5: Steel strain gauges at column and stirrup of Con-BCJ-1 specimen

6.2 CYCLIC TEST RESULTS FOR CONTROL BEAM COLUMN JOINT SPECIMEN (Con-BCJ-2)

For the control cyclic test, the load vs. story drift shows the yielding load of (63 kN) and the maximum load which the beam column joint control specimen can carry (76 kN). In addition, the maximum displacement it reached during the test is (30 mm) as shown in Figure 6 - 6.

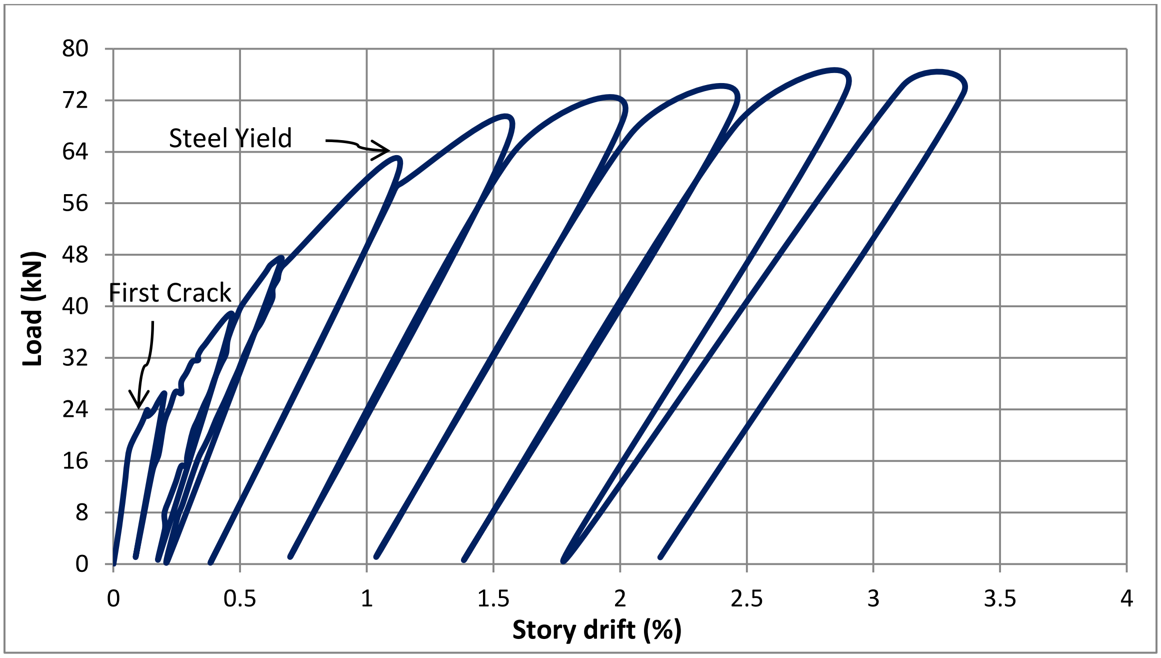

Figure 6 - 6: Load- Story drift curve for control cyclic load test Con-BCJ-2

During the experimental test, first flexural crack was found at the BCJ interface at the load of 26 kN and the displacement of 2.0 mm. Then, a second major flexural crack was formed at a small distance from the joint in the top surface of the beam at load of 38 kN and the displacement of 4.0 mm. At the same time, the third crack was formed at the beam top surface far away from second crack. Then, the forth-flexural crack was found at beam surface. Figure 6 - 7 illustrates the formation of cracks at the BCJ interface and beam.

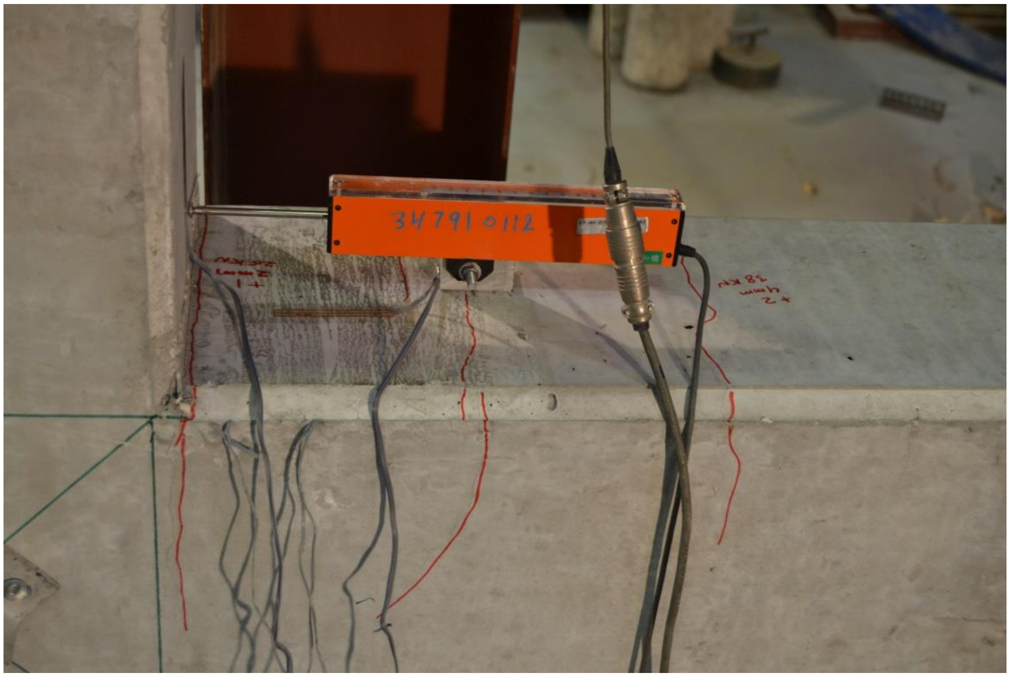

Figure 6 - 7: The formation of cracks for Con-BCJ-2 specimen

After each cycle, a crack-measuring card was used to measure the crack width after applying the load and after removing the load as illustrated in Figure 6 - 8.

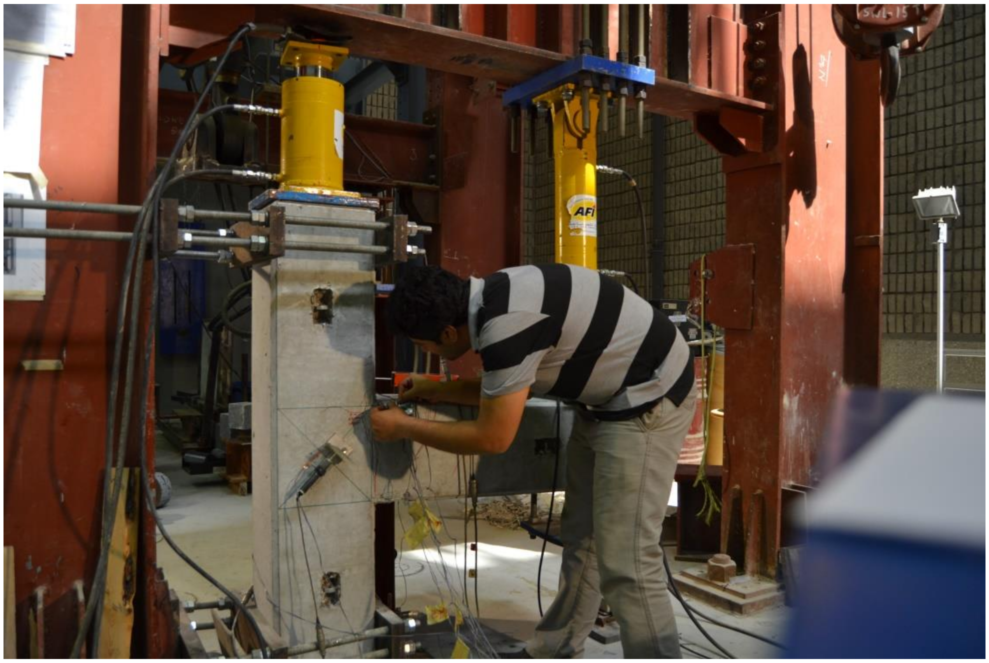

Figure 6 - 8: Measuring the crack width during the test

After yielding of steel, the first two major cracks became wider with increasing the beam tip displacement, while the third and fourth cracks remained the same without increasing in width significantly as illustrated in Figure 6 - 9.

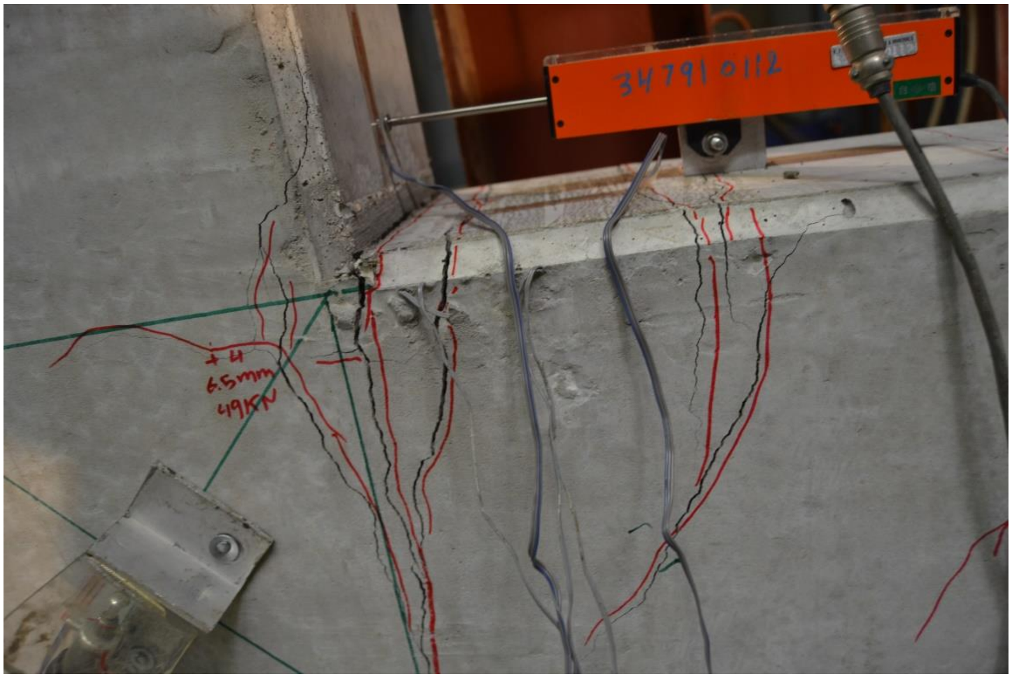

Figure 6 - 9: Increasing in the crack width during the test

The failure of the specimen was predominantly flexural failure at the BCJ interface. At failure, concrete started coming out from the bottom face of the joint. All cracks were found at the beam top surface and at the BCJ interface. After yielding of steel, the majority first and second cracks started to increase in width with the increase in displacement while the maximum load did not increase significantly. Figure 6 - 10 illustrates the specimen after finishing the test.

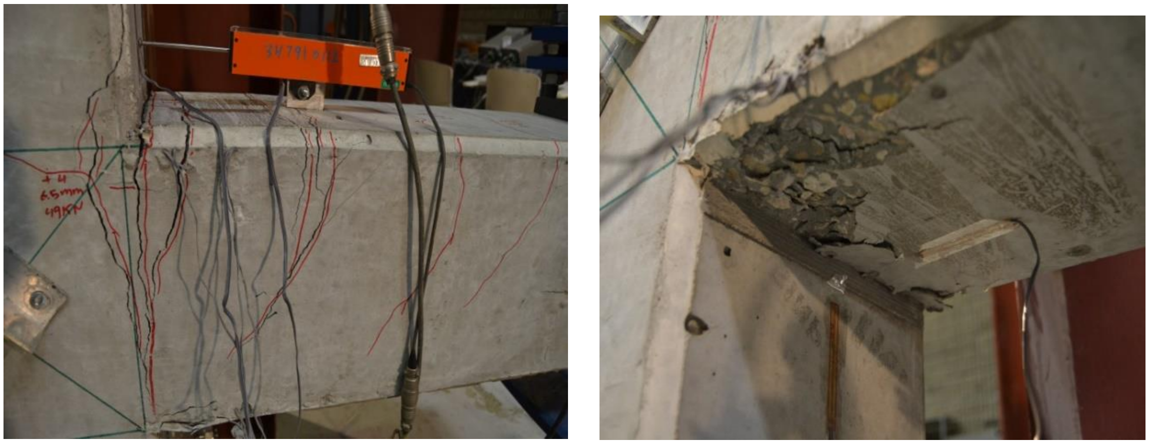

Figure 6 - 10: Failure of Con-BCJ-2 specimen

Strain gauges have been installed to record the strains in the steel reinforcement bars. Figure 6 - 11 illustrates graphs between strains and loads in the bottom and top steel reinforcement at the critical section of the beam, which illustrates the static response according to the testing of the BCJ Con-BCJ-2 specimen.

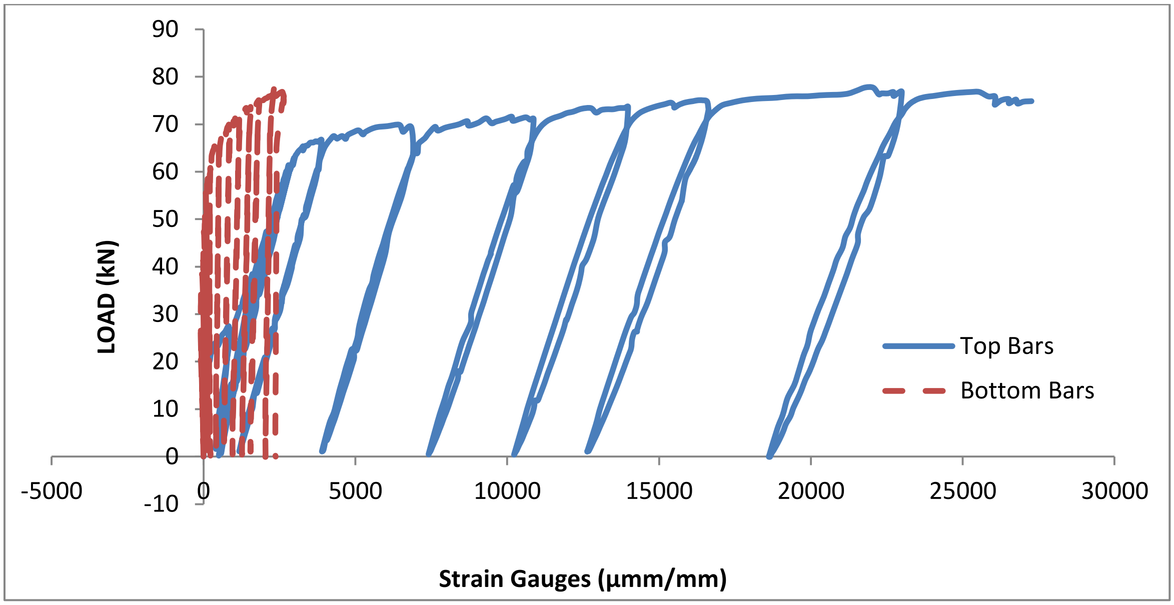

Figure 6 - 11: Steel strain gauges at top and bottom reinforcement of Con-BCJ-2

Strain gauges have been monitored and the graph was plotted between strains and loads for the control cyclic load testing of BCJ sample as illustrated in Figure 6 - 12.

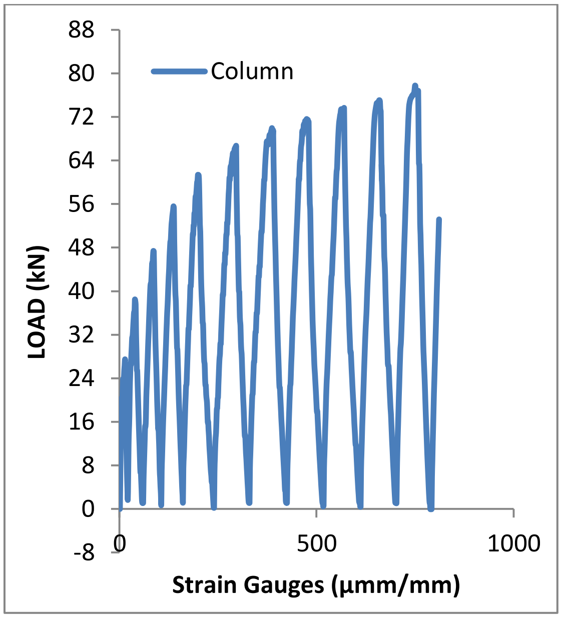

Figure 6 - 12: Steel strain gauges at column of Con-BCJ-2 specimen

Also, all crack measurements were taken during the test after applying the load and after removing the load. Figure 6 - 13 illustrates the crack recovery for the control cyclic test specimen.

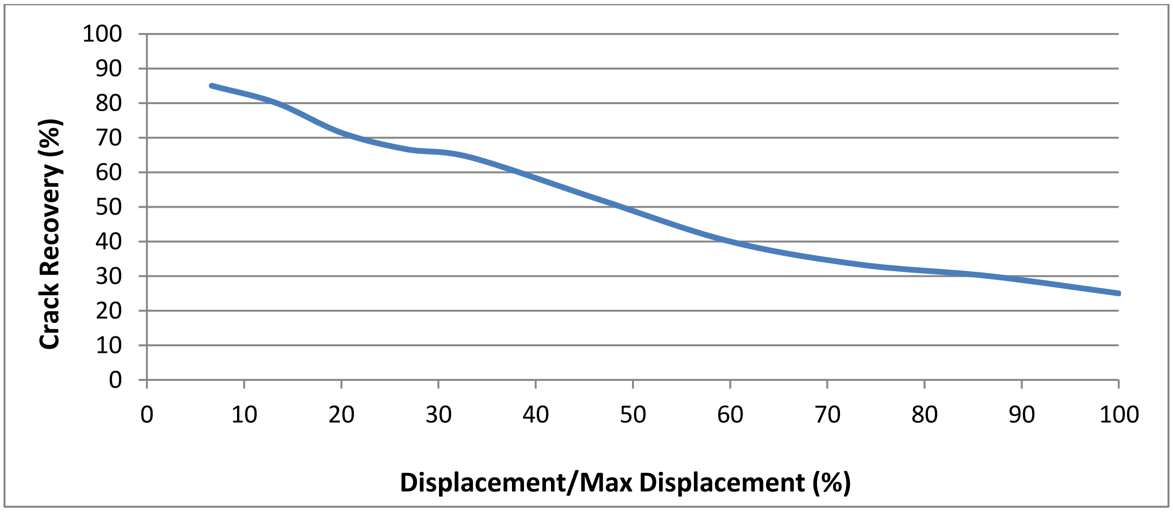

Figure 6 - 13: Crack recovery diagram for Con-BCJ-2 specimen

6.3 REVERSE CYCLIC TEST RESULTS FOR CONTROL BEAM COLUMN JOINT SPECIMEN (Con-BCJ-3)

For the control, reverse cyclic test, the load vs. story drift shows the yielding load (62 kN) and the maximum load which the BCJ control specimen can carry (71 kN). In addition, the maximum displacement it reaches during the test is (30 mm) as illustrated in Figure 6 - 14.

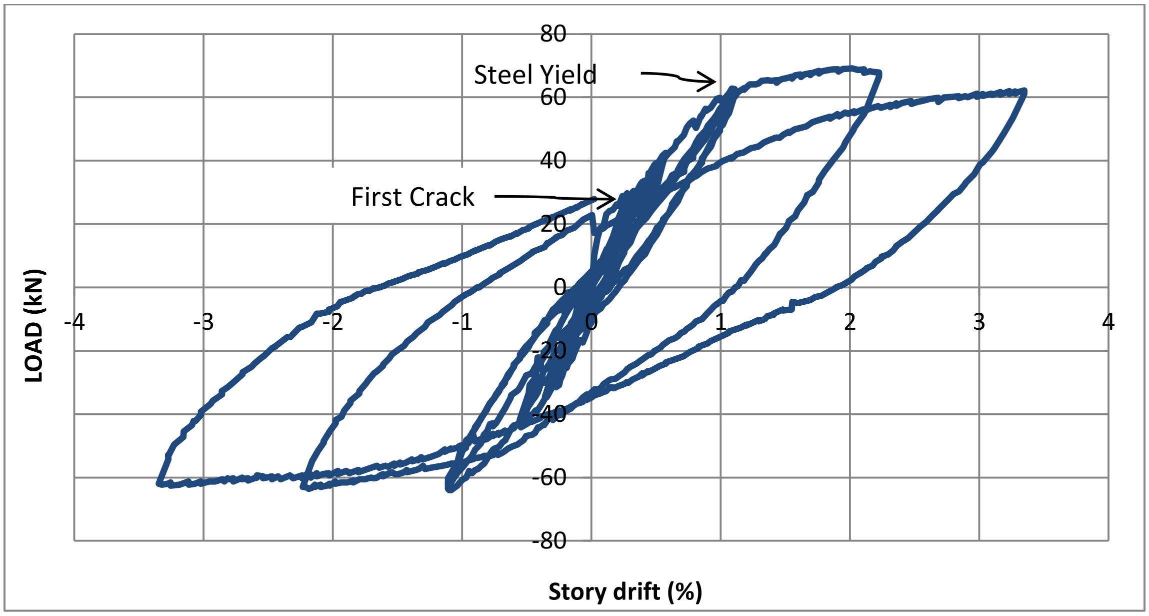

Figure 6 - 14: Load- Story drift curve for control reverse cyclic load test Con-BCJ-3

During the experimental test, first flexural crack was found at the BCJ interface at the load of 29 kN and the displacement of 2.5 mm. Then, a second major flexural crack was formed at a small distance from joint in beam surface at the load of 28 kN and the displacement of 2.9 mm. After that, third and fourth cracks were formed beam top surface at different positions and loads. Figure 6 - 15 illustrates the formation of the cracks at the BCJ interface and beam.

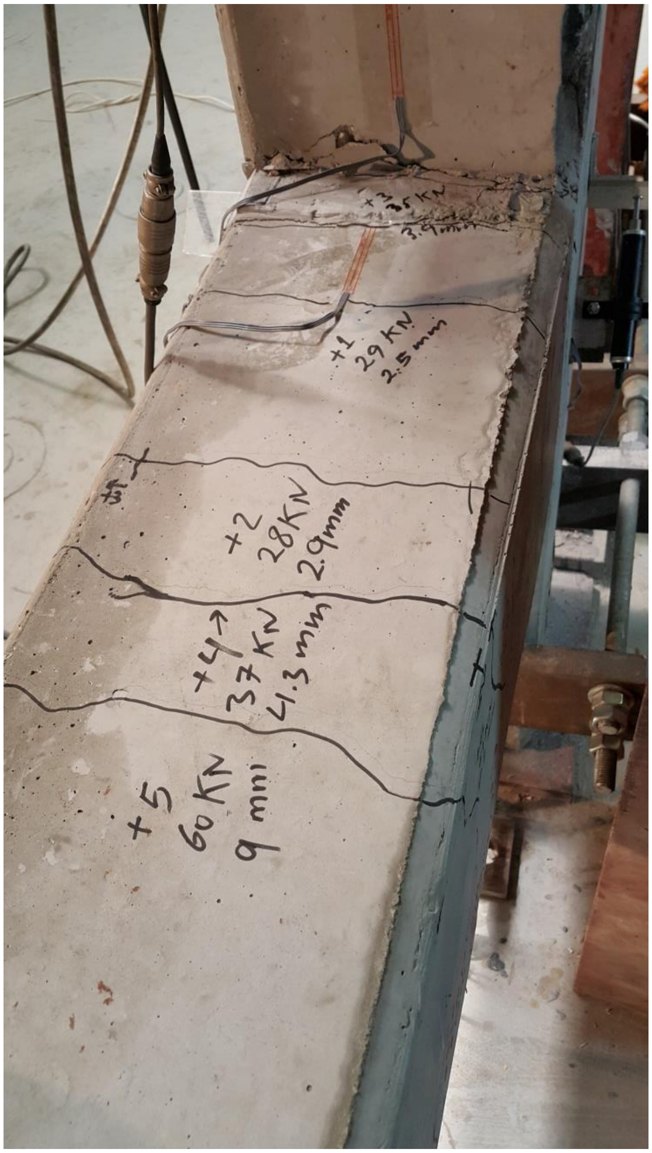

Figure 6 - 15: The formation of cracks for Con-BCJ-3

The failure at the end of the test was predominantly flexural failure at the BCJ interface. All cracks were formed at the beam and at the BCJ interface. After the yielding of the steel, the majority first and second cracks started to increase in width with the increase in displacement while the maximum load did not increase significantly. Figure 6 - 16 illustrates the specimen after finishing of the test.

Figure 6 - 16: Failure of Con-BCJ-3 specimen

Figure 6 - 17 shows the measuring of crack width during BCJ testing.

Figure 6 - 17: Measuring of crack width during BCJ testing for Con-BCJ-3 specimen

Strain gauges have been installed to record the strains in the steel reinforcement bars. Figure 6 - 18 illustrates graphs between strains and loads in the bottom and top steel reinforcement at the critical section of the beam, which illustrates the static response according to the testing of the BCJ Con-BCJ-3 specimen.

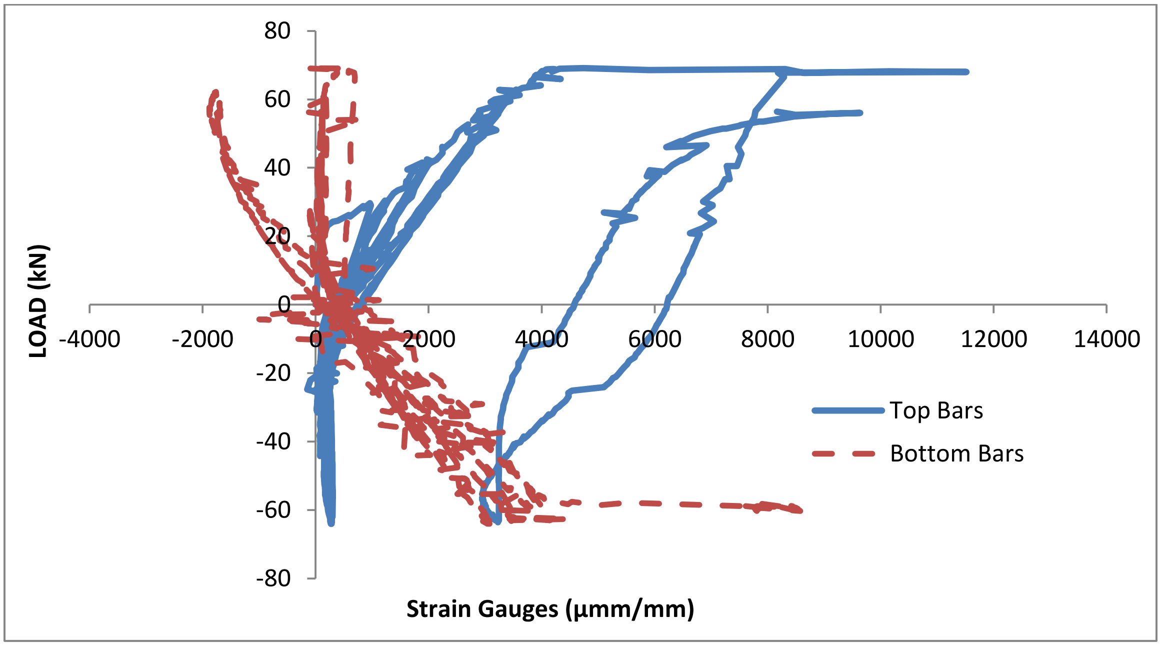

Figure 6 - 18: Steel strain gauges at top and bottom reinforcement of Con-BCJ-3

Strain gauges have been monitored and graph was plotted between strains and loads for the control, reverse cyclic load testing of BCJ sample as illustrated in Figure 6 - 19.

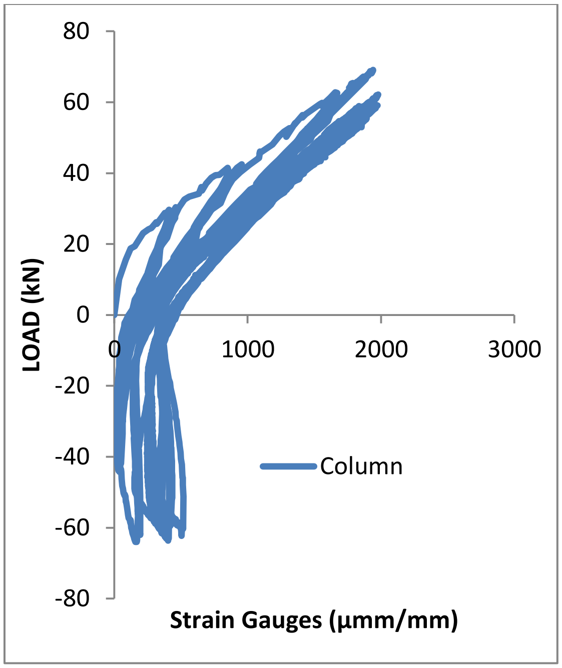

Figure 6 - 19: Steel strain gauges at column of Con-BCJ-3 specimen

In addition, all crack measurements were taken during the test after applying the load and after removing the load. Figure 6 - 20 shows the crack recovery for the control reverse cyclic test specimen.

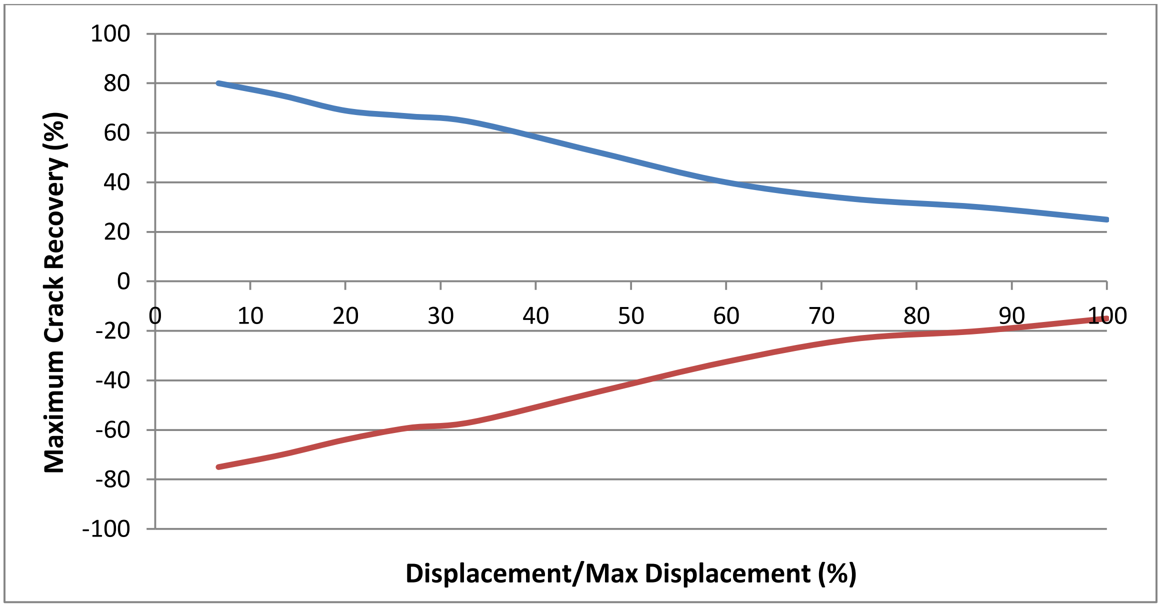

Figure 6 - 20: Crack recovery diagram for Con-BCJ-3 specimen

6.4 CYCLIC TEST RESULTS FOR SHAPE MEMORY ALLOY BEAM COLUMN JOINT SPECIMEN (NiTi-BCJ-1)

In this specimen, a number of three SMA bars have been used at the top of the beam in the critical section. These bars have been trained and ribbed before putting in the BCJ specimen and a cyclic test was performed for it. The load vs. story drift shows the maximum load which the BCJ SMA specimen (NiTi-BCJ-1) can carry (32 kN). In addition, the maximum displacement it reaches during the test is (30 mm) as shown in Figure 6 - 21.

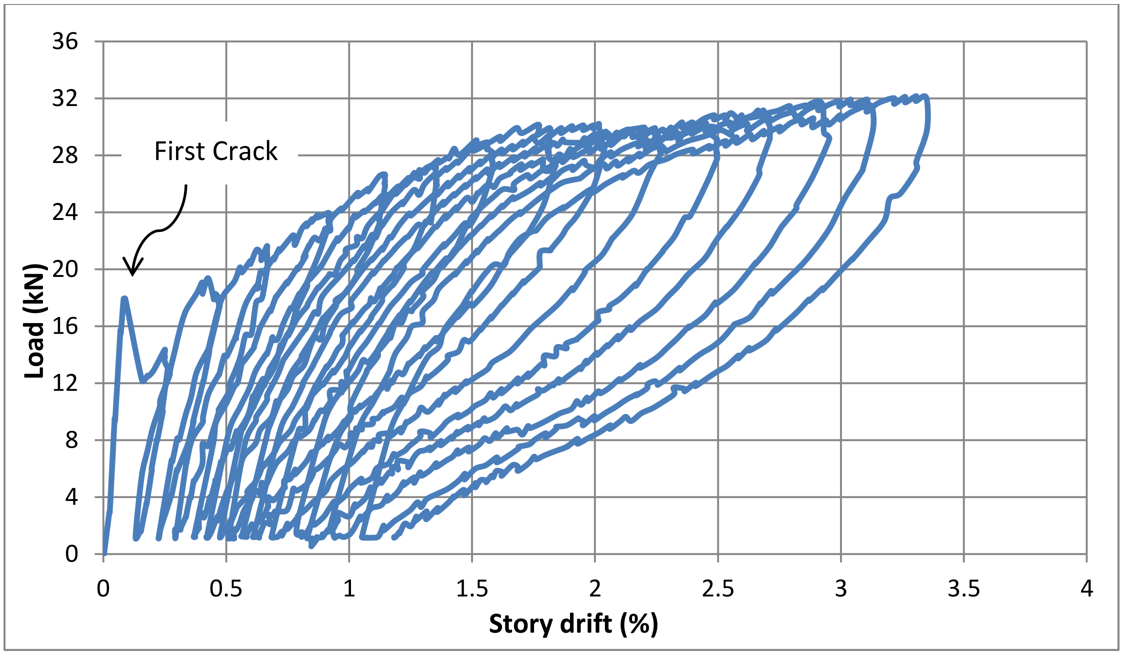

Figure 6 - 21: Load- Story drift curve for cyclic load test of NiTi-BCJ-1 specimen

During the test, only two major flexural cracks were found at the BCJ specimen. One of them at the BCJ interface and the second one at a small distance from the joint as illustrated in Figure 6 - 22. Both cracks started at loads of (18 kN) then load decreased suddenly from (18 kN) to (13.7 kN) at displacement of (2.2 mm).

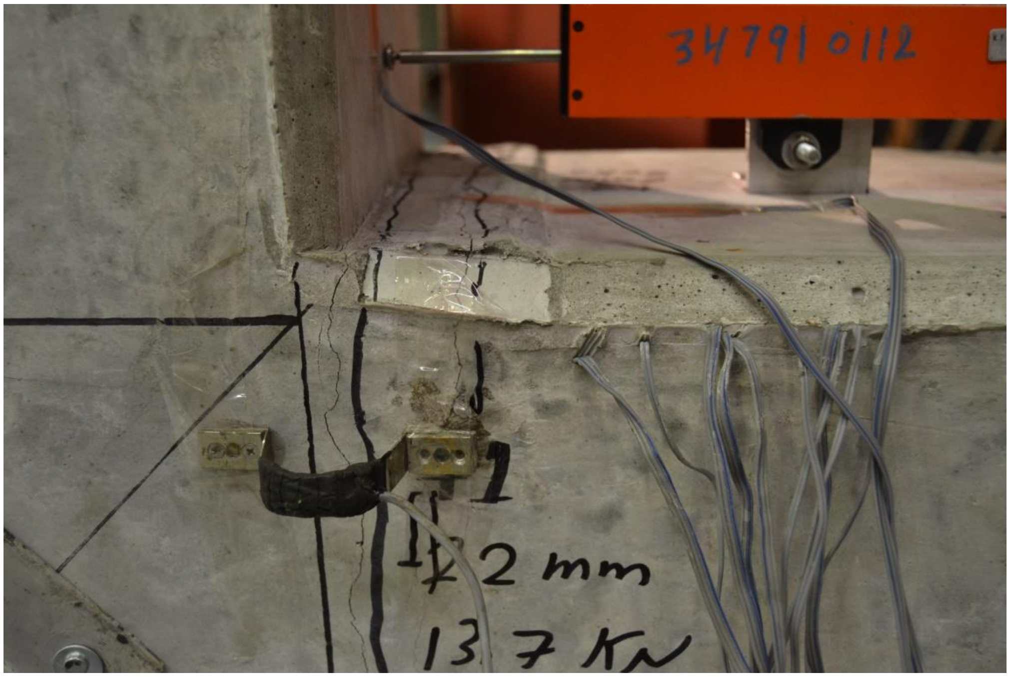

Figure 6 - 22: The formation of cracks for NiTi-BCJ-1 specimen

At each cycle, the cracks became wider with increasing of the beam tip displacement. However, with removing the load, cracks returned and closed every cycle during the whole test. Figure 6 - 23 shows the cracks at the last cycle after applying the load and after removing the load.

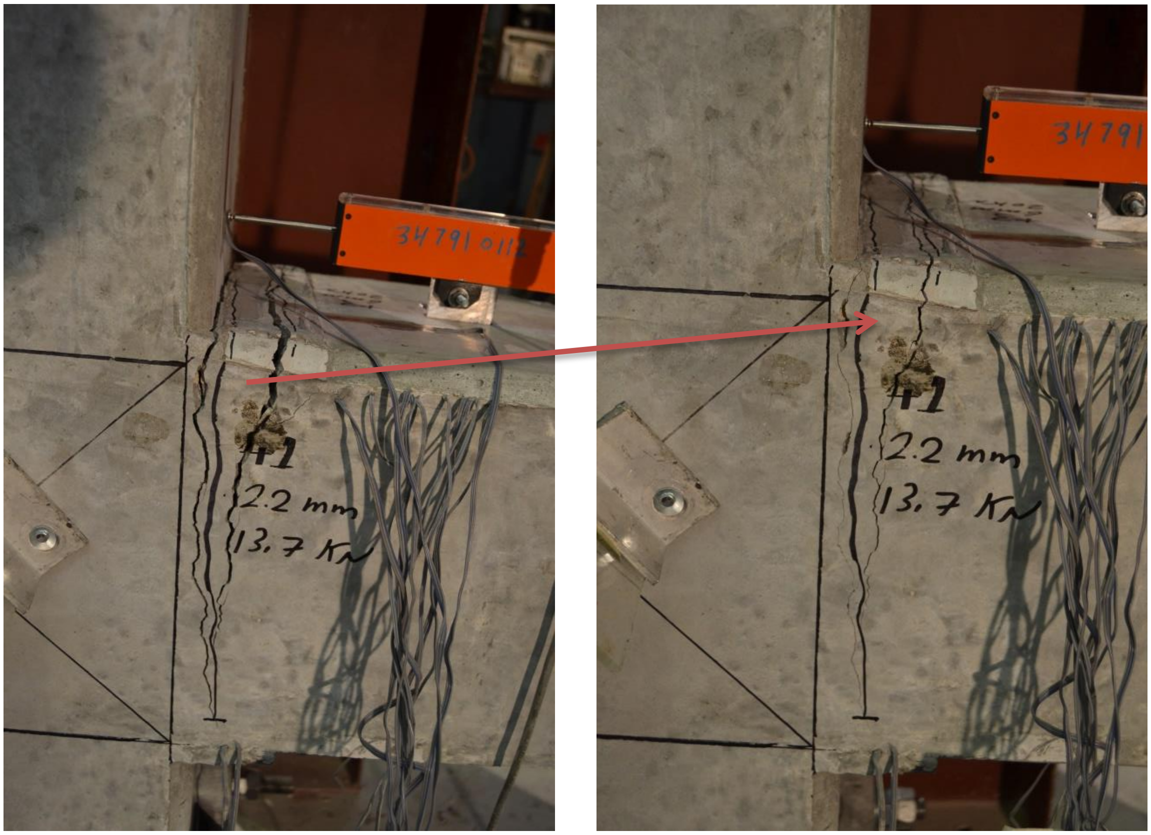

Figure 6 - 23: Opening and closing of the cracks for NiTi-BCJ-1

The failure of the specimen was predominantly flexural failure at the BCJ interface. At each cycle, the two major cracks became wider with increasing the beam tip displacement. Crack width for this test was bigger for the same displacement compared to control test samples. This is because of low modulus of elasticity for SMA reinforced bars comparing with steel reinforcement. Figure 6 - 24 shows the specimen after finishing the test.

Figure 6 - 24: Failure of NiTi-BCJ-1 specimen

Regarding the steel strain gauges, all strain gauges, which have been placed on SMA bars, are damaged. They just recorded very small strain, which is not expected. Therefore, all strain gauges in this specimen were ignored. All crack measurements were taken during the test after applying the load and after removing the load. Figure 6 - 25 illustrates the crack recovery for the cyclic test of (NiTi-BCJ-1) specimen.

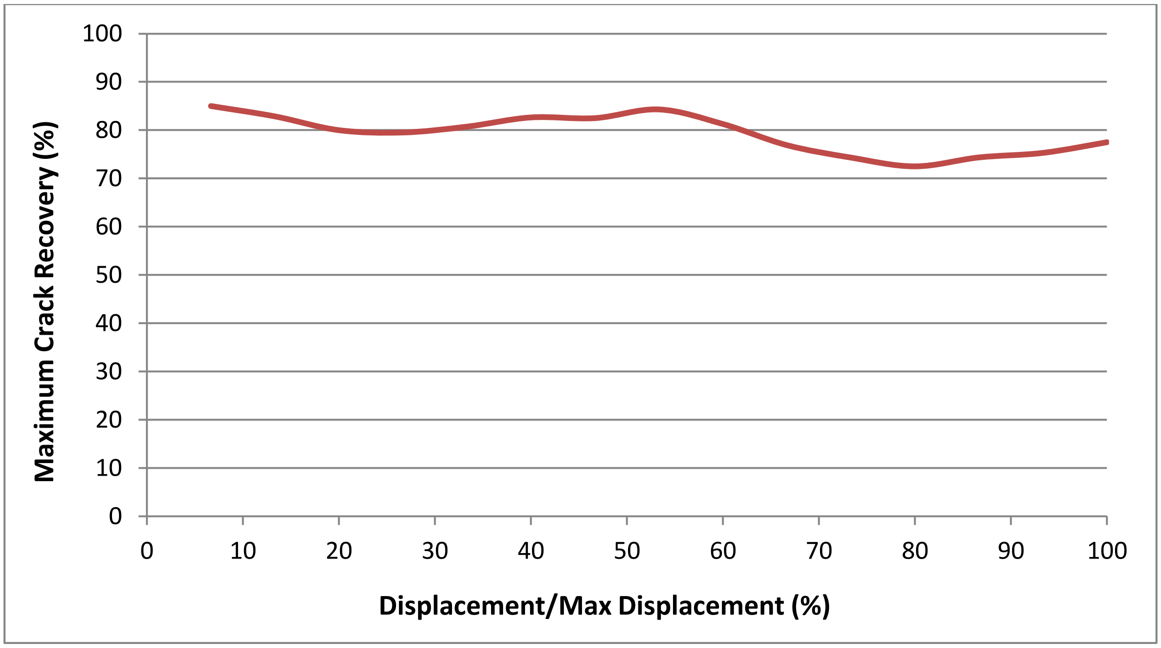

Figure 6 - 25: Crack recovery diagram for NiTi-BCJ-1 specimen

The previous graph shows a very good behavior of the BCJ in terms of closing the cracks after removing the applied loads. It shows a crack recovery of 80 % during the whole test, which mean that SMA bars remain in the martensite stage.

6.5 CYCLIC TEST RESULTS FOR SHAPE MEMORY ALLOY BEAM COLUMN JOINT SPECIMEN (NiTi-BCJ-2)

In this specimen, a number of three bars have been used at the top critical section of beam. Two of them are SMA bars and one steel bar. These SMA bars have been trained and ribbed before putting in the BCJ specimen and a cyclic test was performed for it. The load vs. story drift shows the maximum load which the beam column joint SMA specimen (NiTi-BCJ-2) can carry (48 kN). In addition, the maximum displacement it reaches during the test is (30 mm) as shown in Figure 6 - 26.

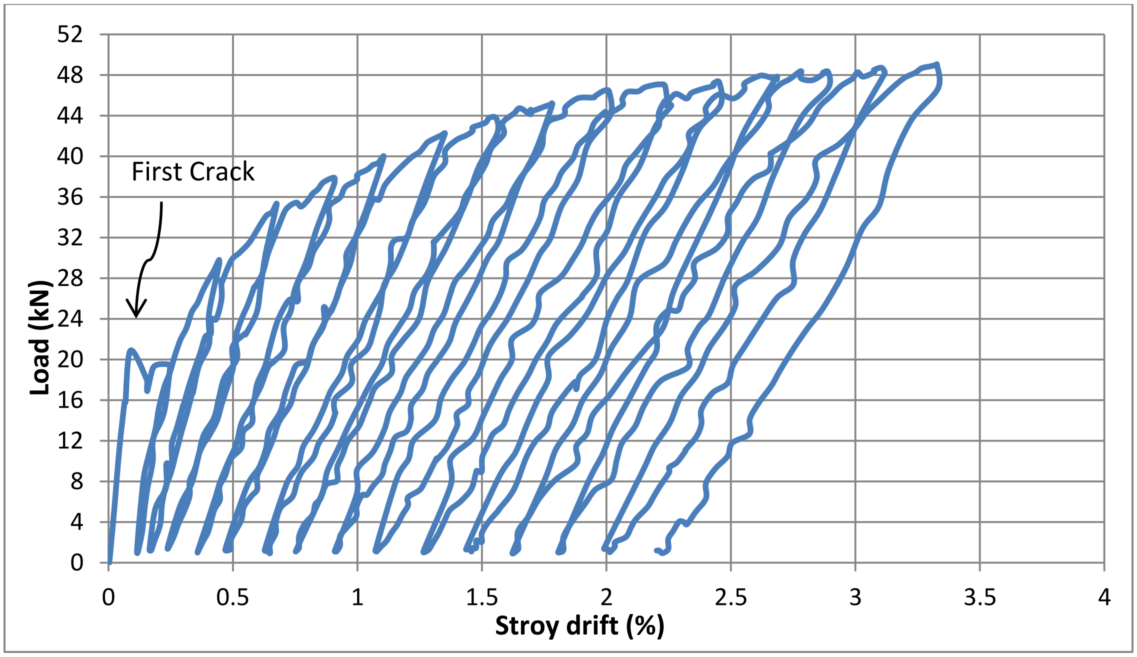

Figure 6 - 26: Load- Story drift curve for cyclic load test of NiTi-BCJ-2 specimen

During the experimental test, first flexural crack was found at the BCJ interface at the load of (20 kN) and the displacement of (1.5 mm). When the first crack occurred, load decreased from (20 kN) to (17 kN). Then, a second major flexural crack was formed at a small distance from joint in the beam at the load of (19 kN) and the displacement of (2 mm). After that, a third crack was formed at the beam top surface little away from the second crack at loads of (35 kN) and displacement of (6 mm). ‘Figure 6 - 27 illustrates the formation of the cracks at the BCJ interface and beam.

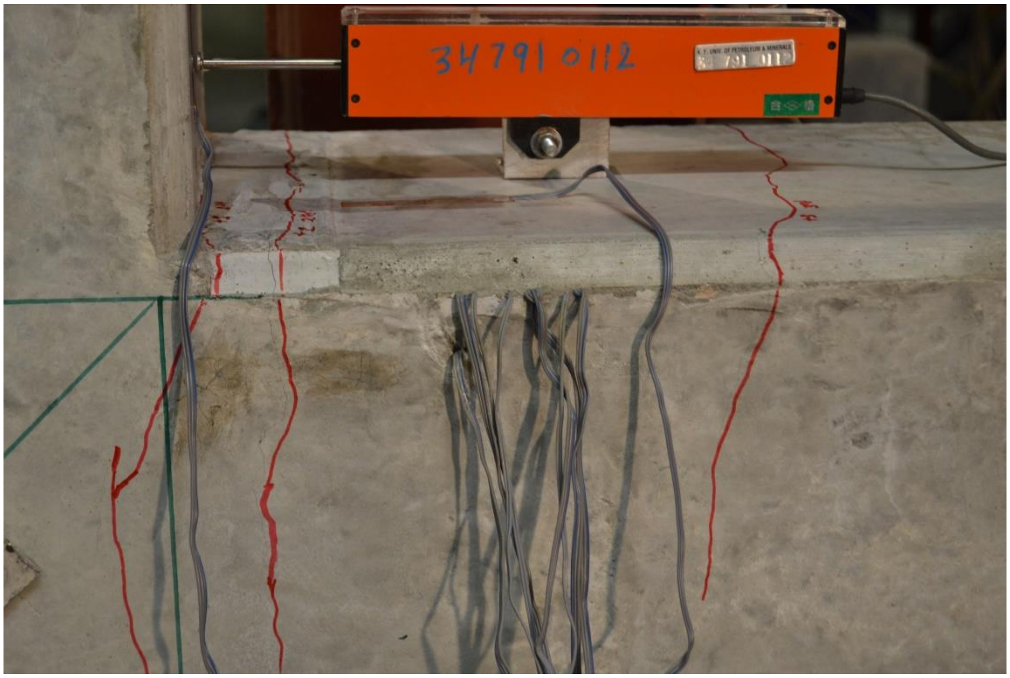

Figure 6 - 27: The formation of cracks for NiTi-BCJ-2 specimen

At each cycle, the two major cracks became wider with increasing of the tip beam displacement, while the third crack did not increase in width significantly. Figure 6 - 28 shows the cracks at the last cycle with applied load and after removing the load. It illustrated that SMA bars could not close the cracks because of the present of the steel bar. Even though, two SMA bars were used with just one steel bar yet after yielding of steel SMA bars did not recover the cracks after removing the load. However, this specimen shows larger load comparing to (NiTi-BCJ-1) since it contained one steel bar with SMA bars.

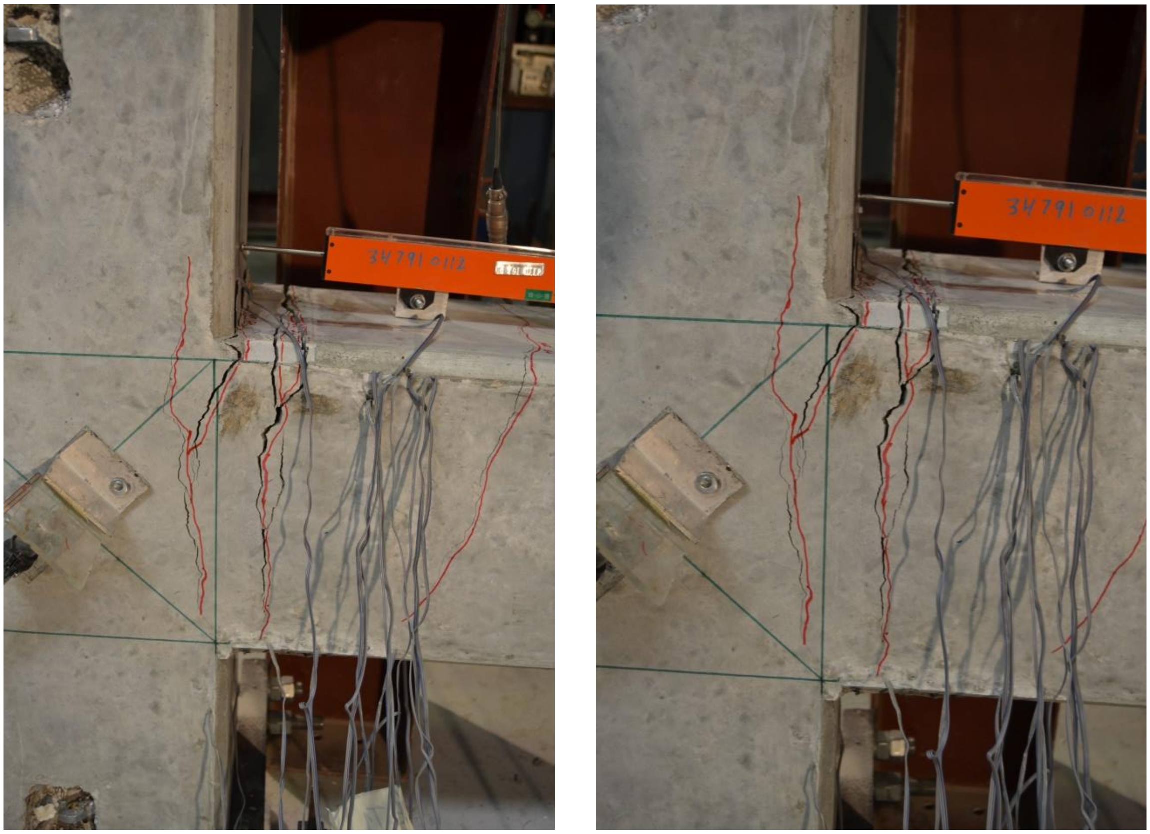

Figure 6 - 28: Opening of the cracks with applied load and after removing the load

The failure of the specimen was predominantly flexural failure at the BCJ interface. No diagonal cracks were formed in the joint. Figure 6 - 29 illustrates the specimen after finishing the test.

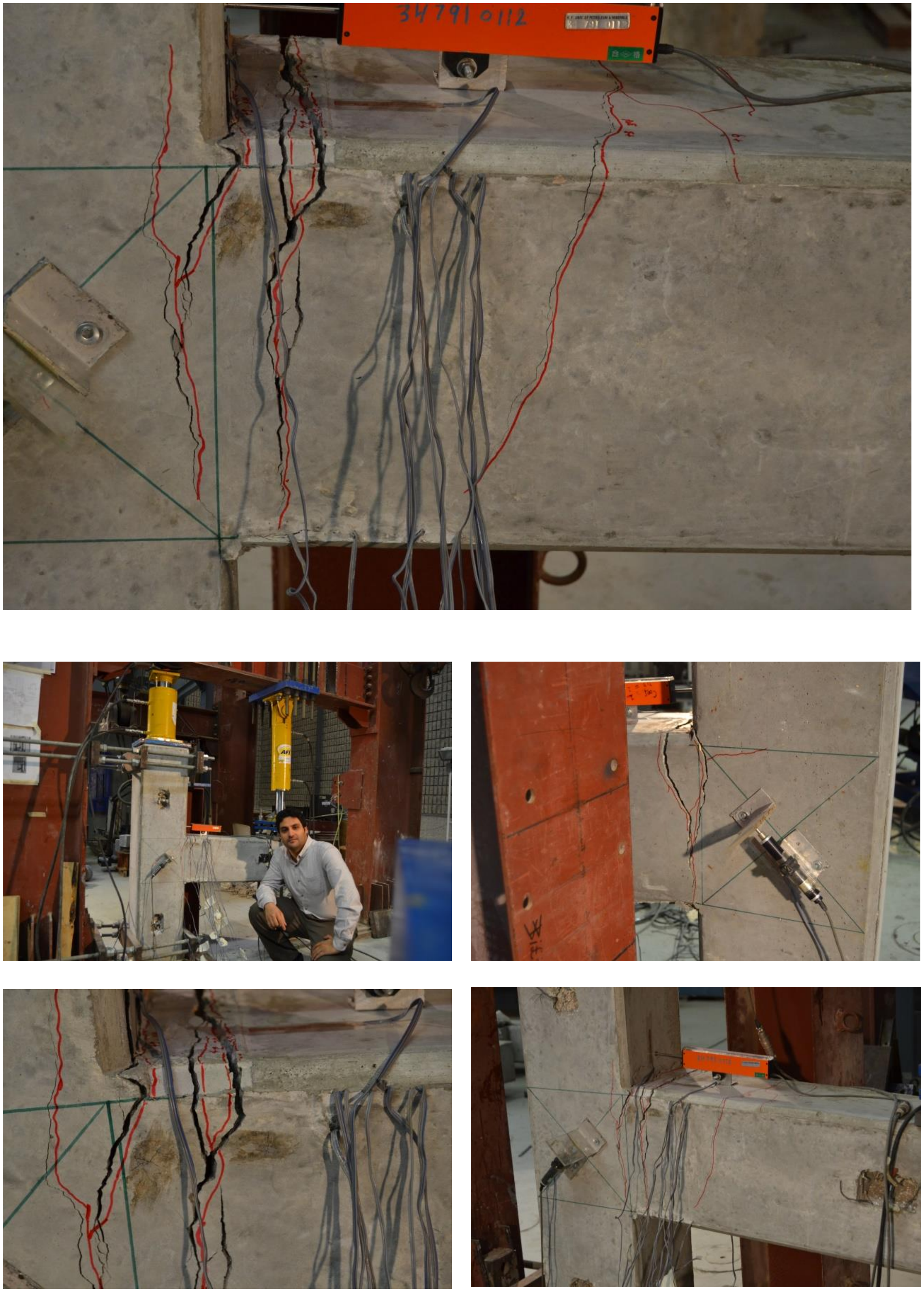

Figure 6 - 29: Failure of NiTi-BCJ-2 specimen

Regarding the steel strain gauges, all strain gauges, which have been placed on SMA bars, are damaged. They just recorded very small strain, which is not expected. Therefore, all strain gauges in this specimen were ignored. All crack measurements were taken during the test after applying the load and after removing the load. Figure 6 - 30 illustrates the crack recovery for the cyclic test of (NiTi-BCJ-2) specimen.

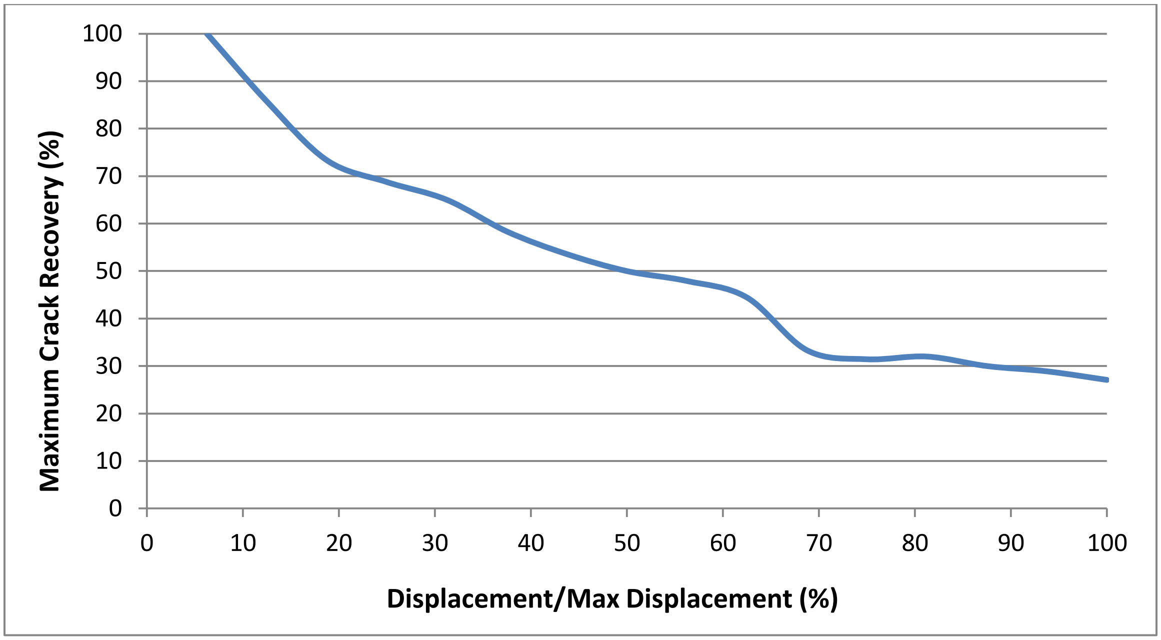

Figure 6 - 30: Crack recovery diagram for NiTi-BCJ-2 specimen

6.6 REVERSE CYCLIC RESULTS FOR SHAPE MEMORY ALLOY BEAM COLUMN JOINT (NiTi-BCJ-3)

In this BCJ specimen and due to shortage of availability of SMA bars, only a number of four SMA bars have been used at the beam critical section. Two bars have been placed at top and other two bars were placed at the bottom. These bars were plain bars and they have been trained before putting in the BCJ specimen. A reverse cyclic test was performed for it. The load vs. story drift shows the maximum load which the BCJ (NiTi-BCJ-3) specimen can carry (12 kN). In addition, the maximum displacement it reaches during the test is (20 mm) as shown in Figure 6 - 31.

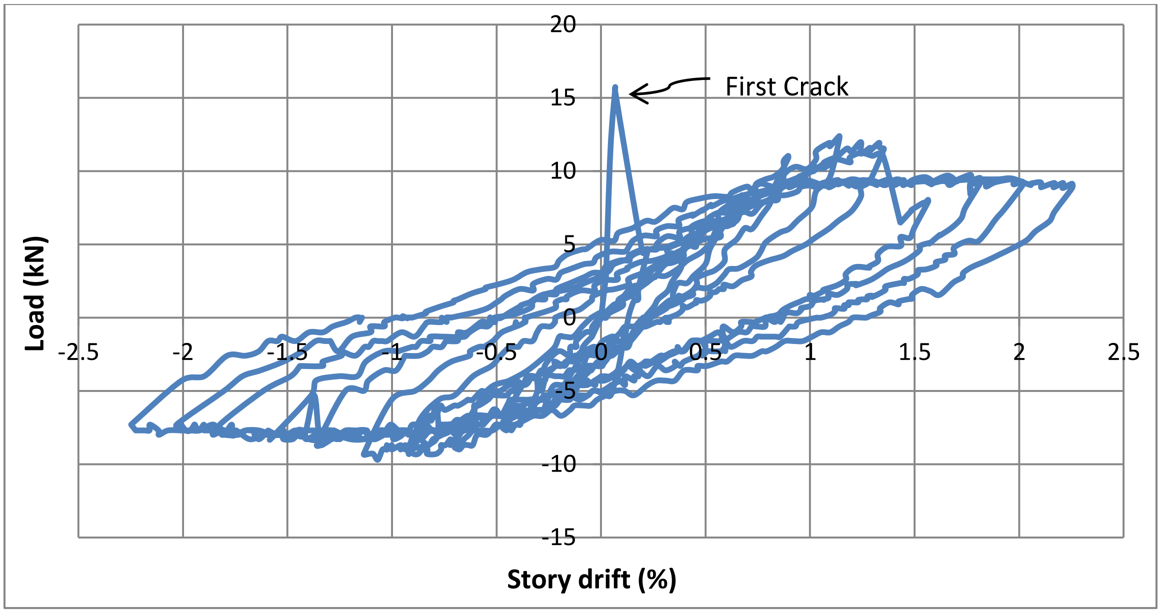

Figure 6 - 31: Load- Story drift curve for reverse cyclic load test for NiTi-BCJ-3

During the experimental test, only one main flexural crack was found at the BCJ specimen. It has taken place at the BCJ interface as shown in Figure 6 - 32. This crack was occurred at (16 kN) load, then it decreased suddenly to (4 kN) at a displacement of (1.8 mm).

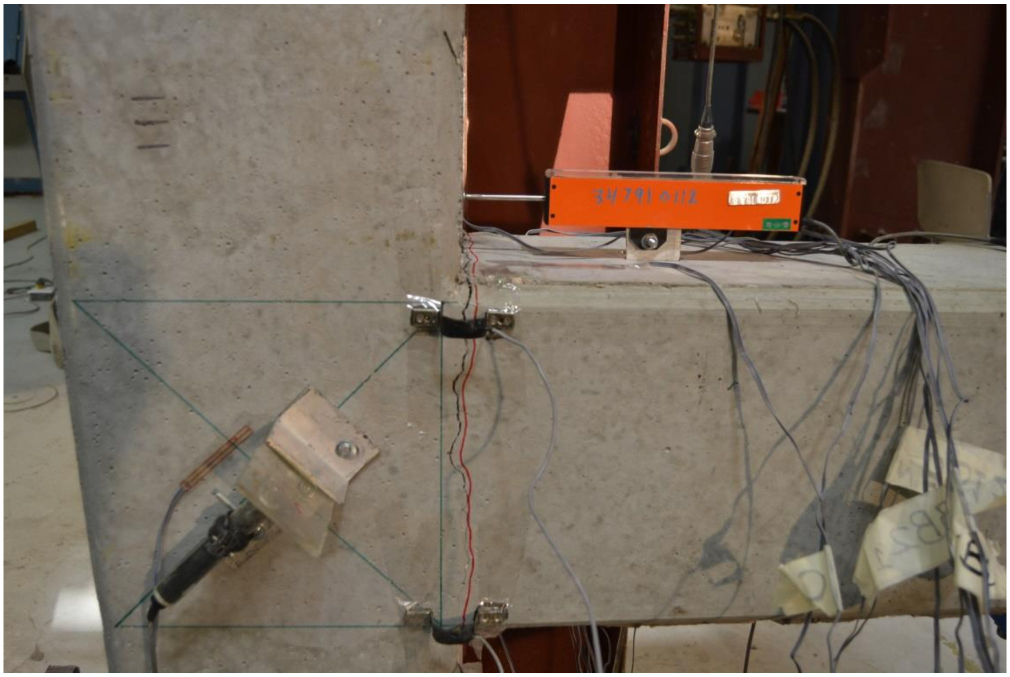

Figure 6 - 32: The formation of cracks for NiTi-BCJ-3 specimen

At each cycle, the crack became wider with increasing of the beam tip displacement. Due to losing the bond between plain SMA bars and concrete, the cracks could not been able to close after removing the loads. Figure 6 - 33 shows the crack at the last cycle with applied load and after removing the load.

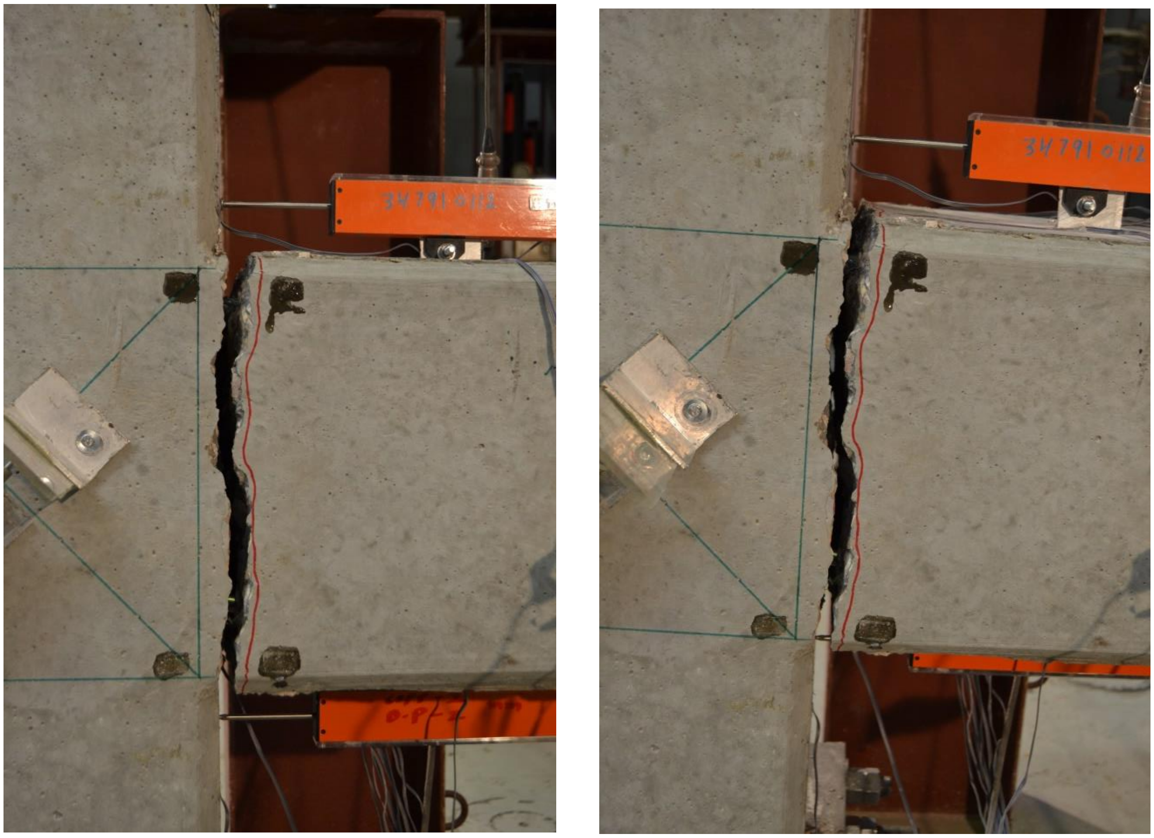

Figure 6 - 33: Opening of the cracks with applied load and after removing the load

The failure of the specimen was predominantly flexural failure at the BCJ interface. No diagonal or shear cracks were formed this Specimen. Figure 6 - 34 illustrates the specimen after finishing the test.

Figure 6 - 34: Failure of NiTi-BCJ-3 specimen

Regarding the steel strain gauges, all strain gauges, which have been placed on SMA bars, are damaged. They just recorded very small strain, which is not expected. Therefore, all strain gauges in this specimen were ignored. All crack measurements were taken during the test after applying the load and after removing the load. Figure 6 - 35 shows the crack recovery for the reverse cyclic test of (NiTi-BCJ-3) specimen.

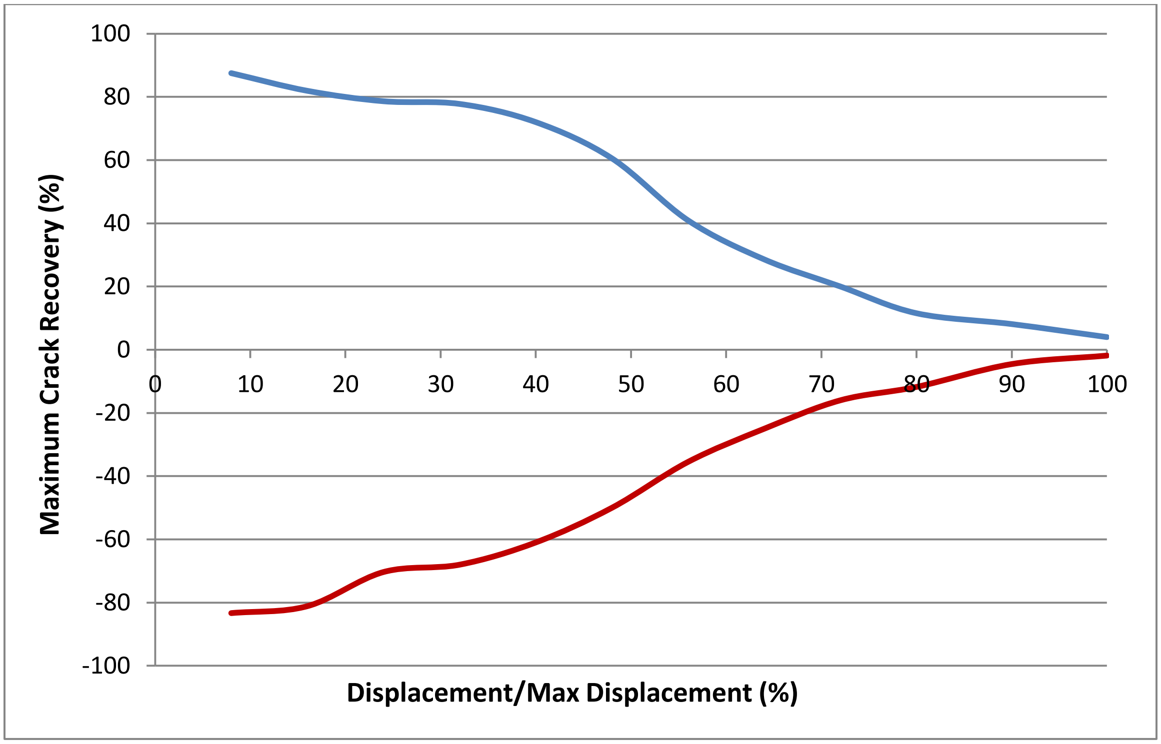

Figure 6 - 35: Crack recovery diagram for NiTi-BCJ-3 specimen

The previous graph shows that at the beginning of the test, the specimen could recover the cracks very good (80 % crack recovery) until almost 40 % of displacement. Then, the crack recovery decreased too much with increasing the beam tip displacement even more than control specimens, which indicated that a slippage between SMA bars and the couplers might be occurred.

6.7 REVERSE CYCLIC RESULTS FOR SHAPE MEMORY ALLOY BEAM COLUMN JOINT (NiTi-BCJ-4)

In this specimen, a number of two SMA bars have been used beside the steel reinforcement bars at the critical section of the beam. One plain bar was placed at the middle top reinforcement and the other one at the middle bottom reinforcement. These bars have been trained before putting in the BCJ specimen, and then a reverse cyclic test was performed for it. The load vs. story drift shows the maximum load which the BCJ (NiTi-BCJ-4) specimen can carry (45 kN). In addition, the maximum displacement it reaches during the test is (30 mm) as shown in Figure 6 - 36.

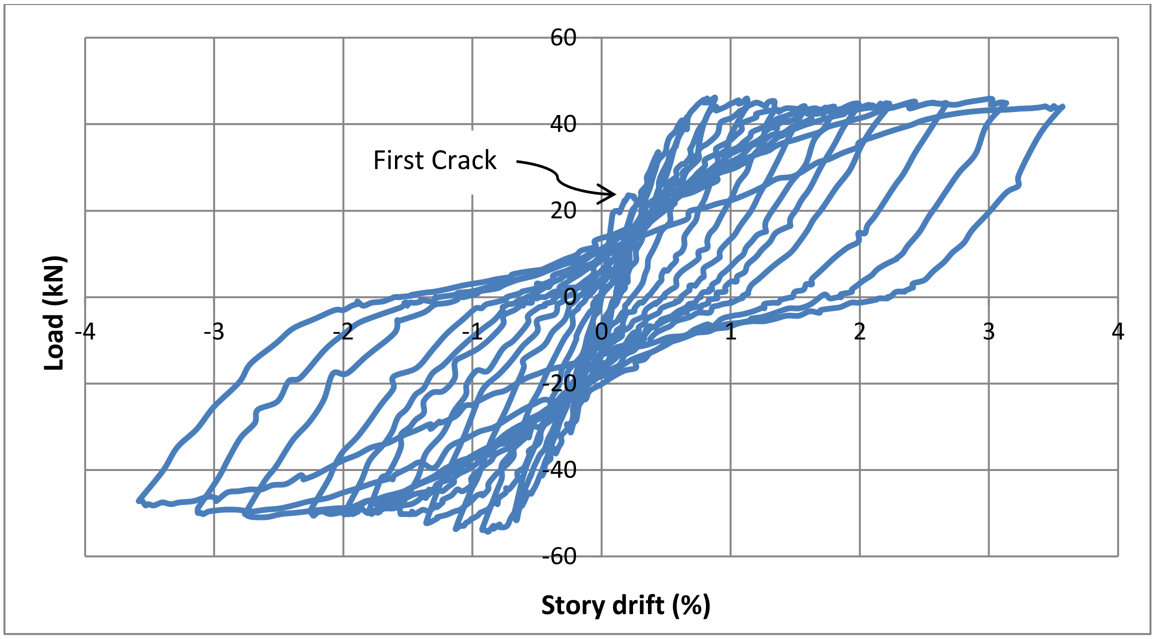

Figure 6 - 36: Load- Story drift curve for reverse cyclic load test of NiTi-BCJ-4

For the pushing downside, the first flexural crack was found at the BCJ interface at the load of 22 kN and the displacement of 1.7 mm. Then, a second major flexural crack was formed at a small distance from joint in the beam at the load of 22.6 kN and the displacement of 2 mm. After that, third and fourth cracks were found on the beam top face at different locations and loads. However, for the pulling up side, the first flexural crack was found at the BCJ interface at the load of (19 kN) and the displacement of (0.7 mm). Then, a second major flexural crack was formed at a small distance from joint in the beam at the load of 30 kN and the displacement of 2.8 mm. After that, third and fourth cracks were found at the bottom face of beam at different locations and loads. Figures 6 - 37 shows the formation of the cracks at the BCJ interface and beam.

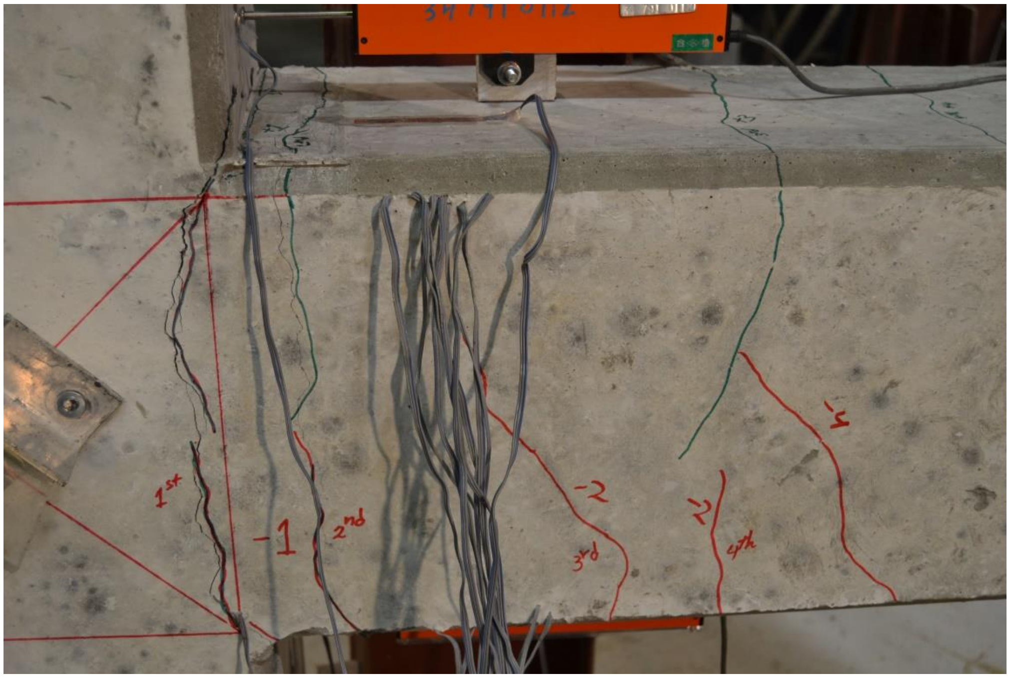

Figure 6 - 37: The formation of cracks for NiTi-BCJ-4 specimen

At each cycle, the two major cracks became wider with increasing of the beam tip displacement, while other cracks did not increase in width significantly. Figure 6 - 38 shows the cracks at the last cycle with applied load and after removing the load.

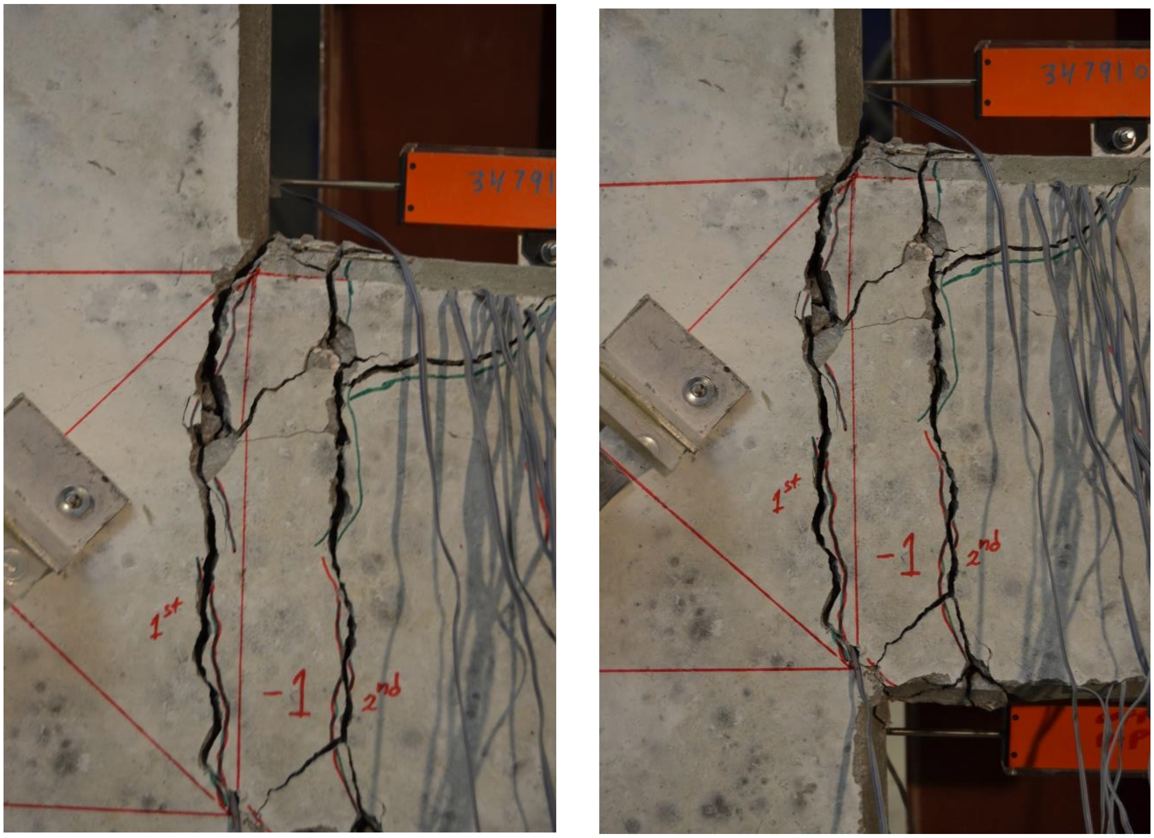

Figure 6 - 38: Opening of the cracks with applied load and after removing the load

The failure of the specimen was predominantly flexural failure at the BCJ interface. Figure 6 - 39 illustrates the specimen after finishing the test.

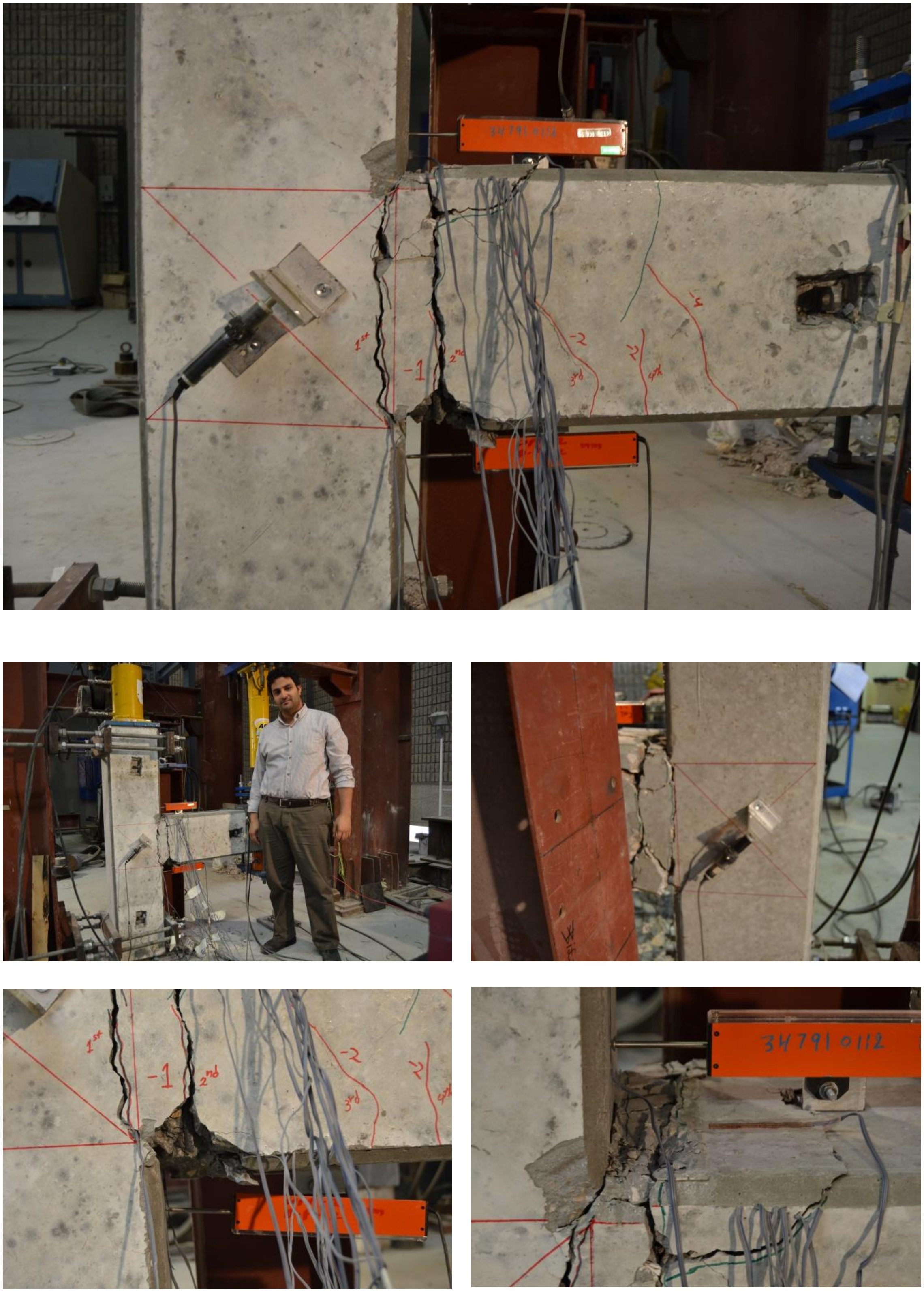

Figure 6 - 39: Failure of NiTi-BCJ-4 specimen

Regarding the steel strain gauges, all strain gauges, which have been placed on SMA bars, are damaged. They just recorded very small strain, which is not expected. Therefore, all strain gauges in this specimen were ignored. All crack measurements were taken during the test after applying the load and after removing the load. Figure 6 - 40 shows the crack recovery for the reverse cyclic test of (NiTi-BCJ-4) specimen.

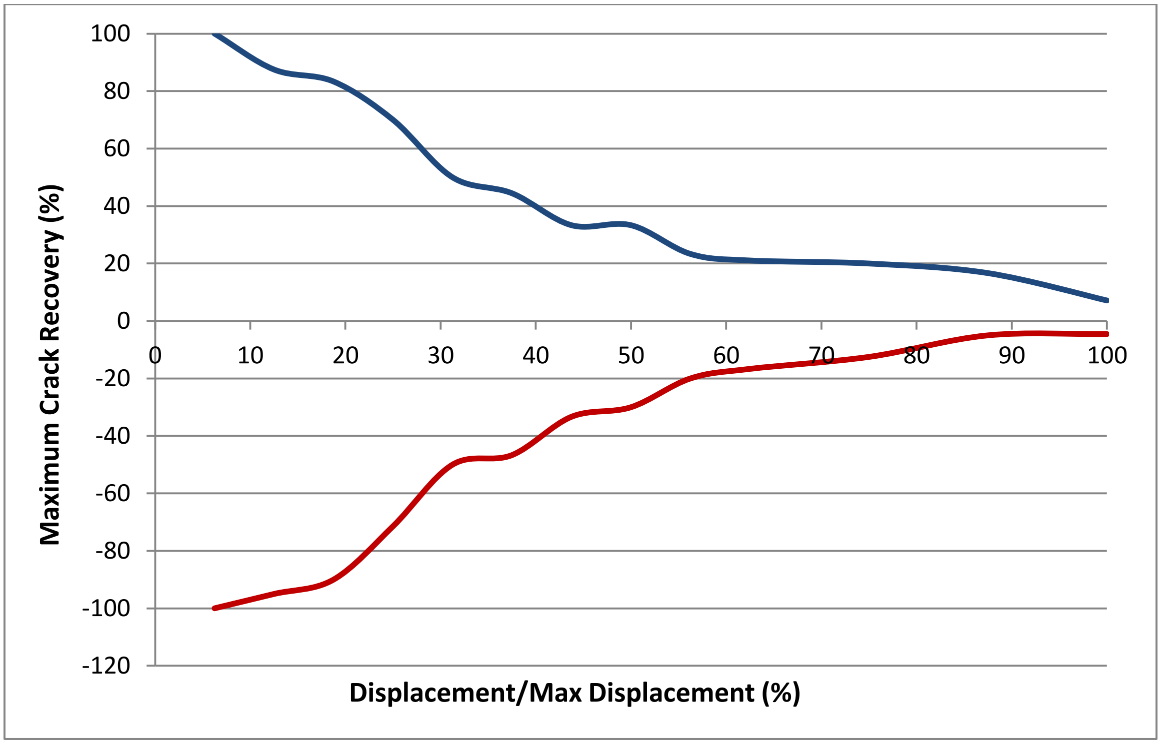

Figure 6 - 40: Crack recovery diagram for NiTi-BCJ-4 specimen

6.8 CYCLIC RESULTS FOR SHAPE MEMORY ALLOY BEAM COLUMN JOINT SPECIMEN (NiTi-BCJ-5)

In this specimen, a number of three SMA bars have been used at top critical section of beam. These bars have been used in the BCJ specimen as plain bars without training, and then a cyclic test was performed for it. The load vs. story drift shows the maximum load which the beam column joint SMA specimen (NiTi-BCJ-5) can carry (26 kN). In addition, the maximum displacement it reaches during the test during the test (35 mm) as shown in Figure 6 - 41. The purpose of making such specimen is for investigation the response of concrete element reinforced with SMA bars as delivered from the company without training or ribbing.

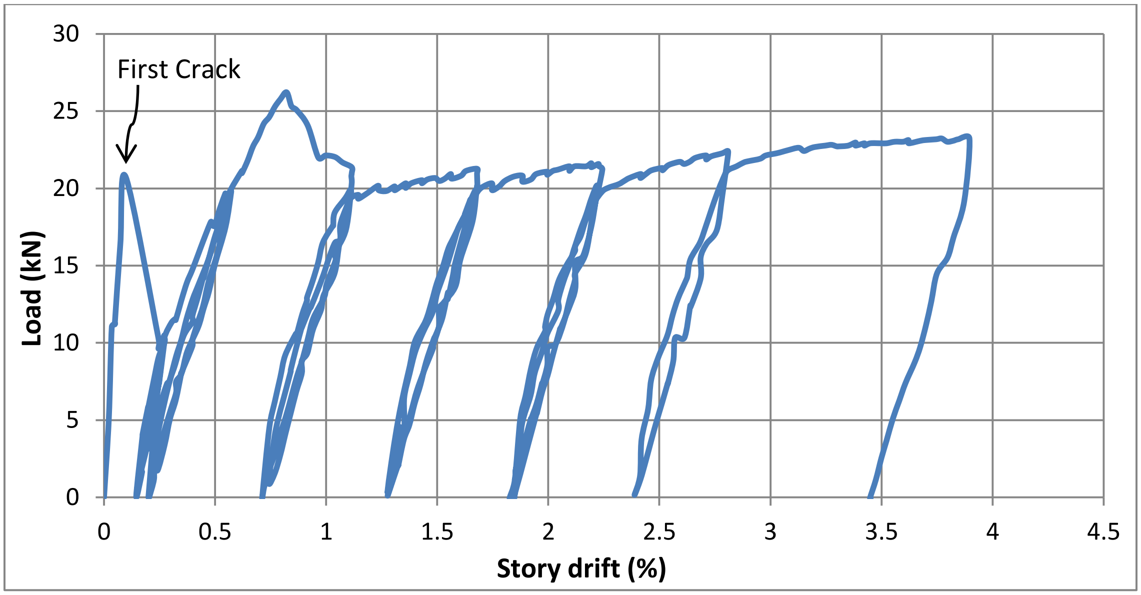

Figure 6 - 41: Load- Story drift curve for cyclic load test of NiTi-BCJ-5 specimen

During the test, only one major flexural crack was found at the BCJ specimen. This crack was formed a little away from the BCJ interface as shown in Figure 6 - 42. It was occurred at displacement of (2.2 mm) and loads of (22 kN) then load decreased suddenly from (22 kN) to (10 kN).

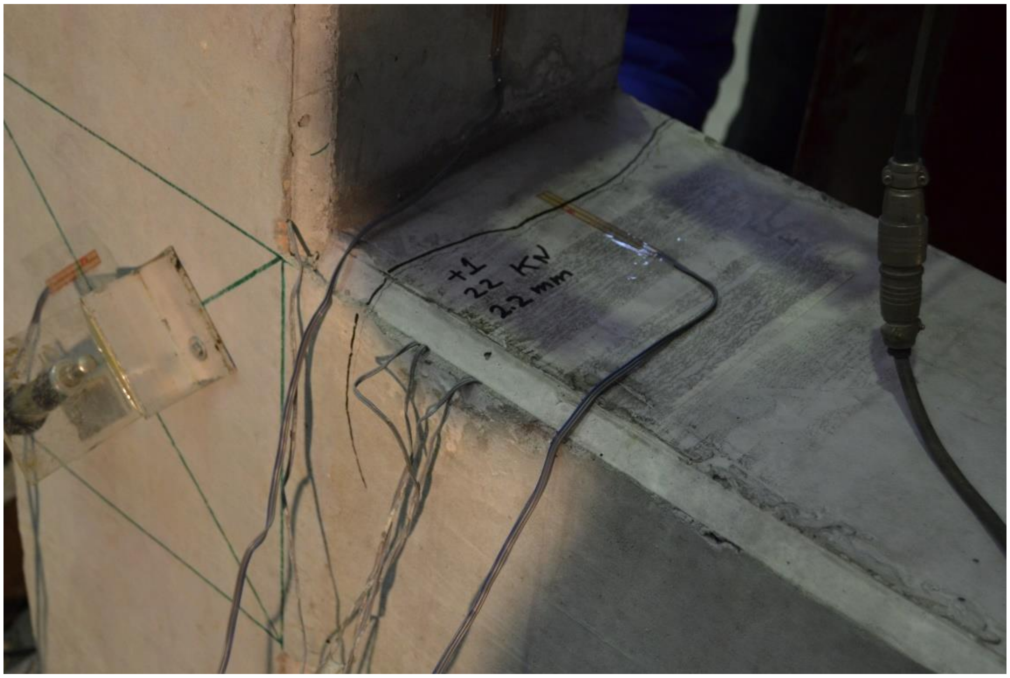

Figure 6 - 42: The formation of crack for NiTi-BCJ-5 specimen

At each cycle, the crack became wider with increasing of the tip beam displacement. This crack width did not return after removing the applied load even at the starting level of the experimental test.

The failure of the specimen was predominantly flexural failure at the BCJ interface. Figure 6 - 43 illustrates the specimen after finishing the test.

Figure 6 - 43: Failure of NiTi-BCJ-5 specimen

Regarding the steel strain gauges, all strain gauges, which have been placed on SMA bars, are damaged. They just recorded very small strain, which is not expected. Therefore, all strain gauges in this specimen were ignored. All crack measurements were taken during the test after applying the load and after removing the load. Figure 6 - 44 illustrates the crack recovery for the cyclic test of (NiTi-BCJ-5) specimen.

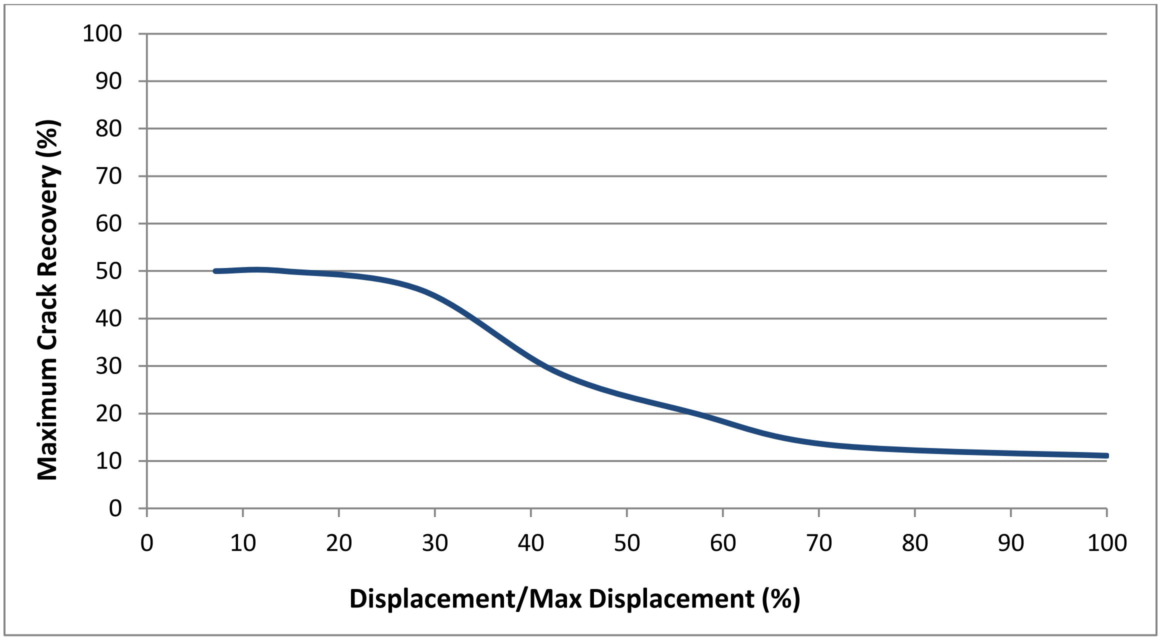

Figure 6 - 44: Crack recovery diagram for NiTi-BCJ-5 specimen

The previous graph shows a bad behavior of BCJ specimen in terms of crack closing even at a small deformation.

6.9 FLEXURAL AND SHEAR CAPACITY OF EXPERIMENTAL (BCJ) SPECIMENS

6.9.1 CHECK A FLEXURAL FAILURE OF CONTROL BCJ SPECIMENS

$$f_t = 0.625\sqrt{f_c'} \tag{6.1}$$

$$f_t = 0.625\sqrt{51} = 4.46\ MPa$$

$$f_t = -\frac{\sigma_a}{2} + \sqrt{\left(\frac{\sigma_a}{2}\right)^2 + v_{jh}^2} \tag{6.2}$$

where:

σ_a= column axial stress which equal to $\left(\frac{N}{A_g}\right) = \frac{150000}{300\times250} = 2MPa$

From previous equations

$$4.46 = -\frac{2}{2} + \sqrt{\left(\frac{2}{2}\right)^2 + v_{jh}^2}$$

$$v_{jh} = 5.367\ MPa$$

Predicted cracking shear in the BCJ is given by the following equation:

$$V_{cracking} = v_{jh} \times A_j = 5.367 \times 250 \times 275 = 369\ kN \tag{6.3}$$

At P = 62 kN, (at yielding of steel reinforcement)

$$\varepsilon_s = 0.0034 = \varepsilon_y$$

$$\varepsilon_s' = 0.000252 < \varepsilon_y$$

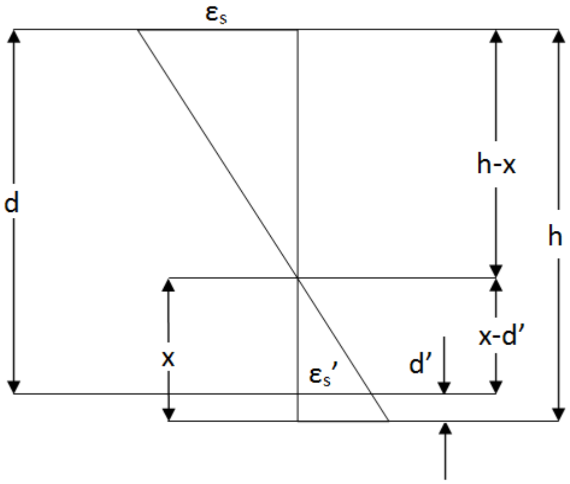

Figure 6 - 45: Strain diagram at the beam section

$$T = \varepsilon_s \times E_s \times A_s$$

$$T = 0.0034 \times 180 \times 336 = 205.63\ kN$$

$$C_s = \varepsilon_s' \times E_s \times A_s'$$

$$C_s = 0.000252 \times 180 \times 336 = 15.24\ kN$$

$$C_c = T - C_s$$

$$C_c = 205.63 - 15.24 = 190.4\ kN$$

$$V_j = T - V_c$$

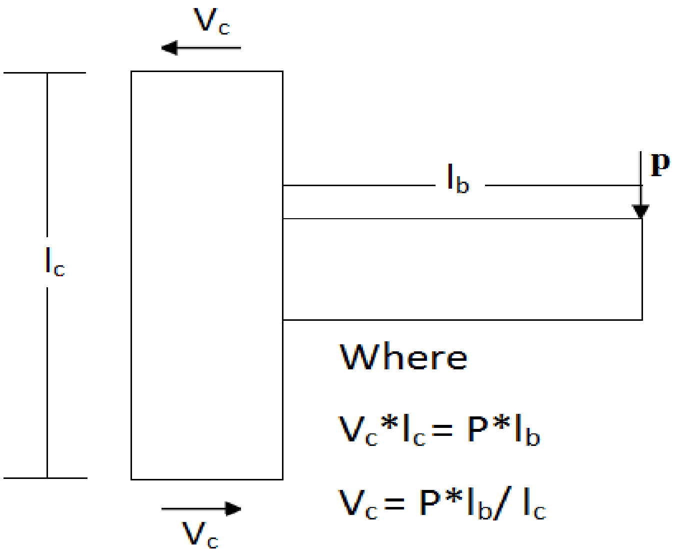

Figure 6 - 46: Shear in the Column

$$V_j = 190.4 - \frac{62 \times 900}{1400} = 150.54\ kN$$

$$V_j = 150.54\ KN \ll V_{cracking}(369\ kN)$$

It can be included that the failure of the Control BCJ specimen was flexural failure. Therefore, all the remaining BCJ will fail in flexural since they have less load capacity than control specimens do.

6.9.2 CALCULATE THE LOAD CAPACITY FOR CONTROL BCJ SPECIMENS (CON-BCJS)

$A_s = 3 \times 113 = 339\,mm^2 \quad , \quad b = 250\,mm \quad , \quad d = 275\,mm \quad ,$

$f_y = 610\,MPa \quad , \quad f_c^{/} = 51\,MPa$

$$\because T = C \quad \Rightarrow \quad 0.85 \times f_c^{/} \times a \times b = A_s \times f_y \quad \Rightarrow \quad a = \frac{339 \times 610}{0.85 \times 51 \times 250} = 19.08\,mm$$

$$\because z = d - \frac{a}{2} = 275 - \frac{19.08}{2} = 265.46\,mm$$

$$\Rightarrow \; Capacity\ moment\ (M) = \frac{339 \times 610 \times 265.46}{10^6} = 54.9\,kN.m$$

$$\because M = P \times L \qquad \Rightarrow \qquad Capacity\ load\ (P) = \frac{M}{L} = \frac{54.9}{0.9} = 61\,kN$$

6.9.3 CALCULATE THE LOAD CAPACITY FOR (NITI-BCJ-1) SPECIMEN

$A_s = 3 \times 113 = 339\,mm^2 \quad , \quad b = 250\,mm \quad , \quad d = 275\,mm \quad ,$

$f_y = 280\,MPa \quad , \quad f_c^{/} = 51\,MPa$

$$\because T = C \quad \Rightarrow \quad 0.85 \times f_c^{/} \times a \times b = A_s \times f_y \quad \Rightarrow \quad a = \frac{339 \times 280}{0.85 \times 51 \times 250} = 8.76\,mm$$

$$\because z = d - \frac{a}{2} = 275 - \frac{8.76}{2} = 270.62\,mm$$

$$\Rightarrow \; Capacity\ moment\ (M) = \frac{339 \times 280 \times 270.62}{10^6} = 25.68\,kN.m$$

$$\because M = P \times L \qquad \Rightarrow \qquad Capacity\ load\ (P) = \frac{M}{L} = \frac{25.68}{0.9} = 28.54\ kN$$

6.9.4 CALCULATE THE LOAD CAPACITY FOR (NITI-BCJ-2) SPECIMEN

$At\ yielding \quad T = 610 \times 113 + 280 \times 226 = 132210\ N$

$From\ Strain\ compatibility:$

$$\frac{\varepsilon_c + 0.014}{275} = \frac{0.014}{275 - x} \qquad Take\ x = 28\ mm$$

$\Rightarrow \varepsilon_c = 0.0016 \qquad \Rightarrow From\ Stress - Strain\ diagram \quad f_c = 39\ MPa$

$C = 39 \times 28 \times 250 \times 0.5 = 136500\ N \ \approx T$

$$\Rightarrow\ Capacity\ moment\ (M) = \frac{132210 \times (275 - \frac{28}{3})}{10^6} = 35.\ 1\ kN.m$$

$$\because M = P \times L \qquad \Rightarrow \qquad Capacity\ load\ (P) = \frac{M}{L} = \frac{35.1}{0.9} = 39\ kN$$

6.9.5 CALCULATE THE LOAD CAPACITY FOR (NITI-BCJ-3) SPECIMEN

$At\ yielding \quad T = 280 \times 226 = 63280\ N$

$From\ Strain\ compatibility:$

$$\frac{\varepsilon_c + 0.014}{275} = \frac{0.014}{275 - x} \qquad Take\ x = 18\ mm$$

$\Rightarrow \varepsilon_c = 0.001 \qquad \Rightarrow From\ Stress - Strain\ diagram \quad f_c = 28\ MPa$

$C = 28 \times 18 \times 250 \times 0.5 = 63000\ N \ \approx T$

$$\Rightarrow\ Capacity\ moment\ (M) = \frac{63000 \times (275 - \frac{18}{3})}{10^6} = 17\ kN.m$$

$$\because M = P \times L \qquad \Rightarrow \qquad Capacity\ load\ (P) = \frac{M}{L} = \frac{17}{0.9} = 18.9\ kN$$

6.9.6 CALCULATE THE LOAD CAPACITY FOR (NITI-BCJ-4) SPECIMEN

$At\ yielding \quad T = 610 \times 226 + 280 \times 113 = 169500\ N$

$From\ Strain\ compatibility$:

$$\frac{\varepsilon_c + 0.014}{275} = \frac{0.014}{275 - x} \qquad Take\ x = 32.5\ mm$$

$\Rightarrow \varepsilon_c = 0.0018 \qquad \Rightarrow From\ Stress\ - Strain\ diagram \quad f_c = 41.5\ MPa$

$C = 41.5 \times 32.5 \times 250 \times 0.5 = 168594\ N\ \approx T$

$$\Rightarrow\ Capacity\ moment\ (M) = \frac{169500 \times (275 - \frac{32.5}{3})}{10^6} = 44.77\ kN.m$$

$$\because M = P \times L \qquad \Rightarrow \qquad Capacity\ load\ (P) = \frac{M}{L} = \frac{44.77}{0.9} = 49.8\ kN$$

6.10 CRACK CALCULATIONS OF EXPERIMENTAL BCJ SPECIMENS

Crack width for all experimental BCJ specimens has been measured during the tests. Table 6 – 1 illustrate the calculations of crack width as well as crack spacing for Oh and Kang approach.

Table 6 - 1: Crack spacing and crack width for Oh and Kang approach

Parameters	Control Specimen	NiTi-BCJ-1 Specimen	NiTi-BCJ-2 Specimen	NiTi-BCJ-3 Specimen	NiTi-BCJ-4 Specimen
C	25	25	25	25	25
d_b	12	12	12	12	12
n	3	3	3	2	3
h_1	138.65	215	203	215	182.7
h_2	177.65	254	242	254	221.7
A_{s1}	113	113	113	113	113
A_{ceff}	19500	19500	19500	19500	19500
ε_s	0.0034	0.014	0.0105	0.014	0.007
S_m	77.16	76.83	76.85	88	76.9
w_{max}	0.236	1.86	1.33	2.13	0.8

Table 6 – 2 illustrate the calculations of crack width as well as crack spacing for CEB – FIP Code approach.

Table 6 - 2: Crack spacing and crack width for CEB – FIP Code approach

Parameters	Control Specimen	NiTi-BCJ-1 Specimen	NiTi-BCJ-2 Specimen	NiTi-BCJ-3 Specimen	NiTi-BCJ-4 Specimen
C	25	25	25	25	25
d_b	12	12	12	12	12
S	74	74	74	160	74
K_1	0.4	0.4	0.4	0.8	0.534
ε_1	0.0034	0.014	0.0105	0.014	0.007
ε_2	0.0034	0.014	0.0105	0.014	0.007
K_2	0.25	0.25	0.25	0.25	0.25
A_s	339	339	339	226	339
A_{ceff}	19500	19500	19500	19500	19500
ρ_{eff}	0.0174	0.0174	0.0174	0.0116	0.0174
S_m	133.76	133.76	133.76	288.9	156.87
W_m	0.456	1.87	1.4	4.04	1.1
w_{max}	0.77	3.2	2.4	6.87	1.86

Table 6 – 3 illustrate the calculations of crack width as well as crack spacing for Chowdhury and Loo approach.

Table 6 – 4 illustrate the calculations of crack width as well as crack spacing for The Euro Code approach.

Table 6 – 5 illustrates a comparison between imperial equations for maximum crack width calculations and experimental results.

Table 6 - 3: Crack spacing and crack width for Chowdhury and Loo approach

Parameters	Control Specimen	NiTi-BCJ-1 Specimen	NiTi-BCJ-2 Specimen	NiTi-BCJ-3 Specimen	NiTi-BCJ-4 Specimen
C	25	25	25	25	25
d_b	12	12	12	12	12
S_{avg}	74	74	74	160	74
ρ	0.00493	0.00493	0.00493	0.00329	0.00493
f_s	610	280	390	280	500
E_s	180000	20000	73333	20000	126667
S_m	214	214	214	283.74	214
W_m	0.725	3	1.14	3.97	0.845
w_{max}	1.09	4.5	1.71	6	1.27

Table 6 - 4: Crack spacing and crack width for The Euro Code approach

Parameters	Control Specimen	NiTi-BCJ-1 Specimen	NiTi-BCJ-2 Specimen	NiTi-BCJ-3 Specimen	NiTi-BCJ-4 Specimen
ρ	0.00493	0.00493	0.00493	0.00329	0.00493
d_b	12	12	12	12	12
K_1	0.8	0.8	0.8	1.6	1.07
K_2	0.5	0.5	0.5	0.5	0.5
ε_s	0.0034	0.014	0.0105	0.014	0.007
S_m	293.4	293.4	293.4	779.5	375.6
W_m	1	4.1	3.1	10.9	2.6
w_{max}	1.7	7	5.2	18.6	4.5

Table 6 - 5: Maximum crack width for experimental and empirical equations

Calculation approach	Control Specimen	NiTi-BCJ-1 Specimen	NiTi-BCJ-2 Specimen	NiTi-BCJ-3 Specimen	NiTi-BCJ-4 Specimen
Experimental Results at yielding of SMA	0.7	0.8	1	2.5	0.7
Experimental Results at maximum	2	5.5	4.5	17	5
Oh and Kang	0.236	1.86	1.33	2.13	0.8
CEB – FIP Code	0.77	3.2	2.4	6.87	1.86
Chowdhury and Loo	1.09	4.5	1.71	6	1.27
The Euro Code	1.7	7	5.2	18.6	4.5

The previous table illustrates that Euro Code is the best approach for calculating the maximum crack width, which give a good agreement with experimental test results. However, Oh and Kang approach shows a good matching with experimental crack width at yielding point of SMA bars for SMA – BCJ specimens while CEB – FIP code illustrates good agreement with control experimental crack width at yielding point of steel bars.

CHAPTER 7

FINITE ELEMENT MODELING OF BCJ SPECIMENS WITH SMAs

7.1 NUMERICAL SIMULATION CONDUCTED FOR BCJs IN ANSYS SOFTWARE ENVIRONMENT

Finite element simulation and their verification with experimental results are becoming very important to idealize exact and real response of actual specimens. In addition, it becomes easy to predict the behavior of the same element with different steel and SMA configuration without performing experimental tests by using finite element simulation. Finite Element Analysis (FEA) of BCJ has been carried out using the commercial F.E software ANSYS 12.1, which is well known for modeling concrete structures due to its advanced numerical tools and the wide range of concrete material models. All the properties of concrete, steel, and SMA materials are installed to the ANSYS program in order for getting the real behavior and simulation of the BCJ structures.

In this thesis, three-dimensional models have been used for studying the response of BCJ reinforced with and without SMA bars under cyclic as well as reverse cyclic loads that are:

1. 3D model of control (Con-BCJ-1) under monotonic loads
2. 3D model of control (Con-BCJ-2) under cyclic loads

3. 3D model of control (Con-BCJ-3) under reverse cyclic loads
4. 3D model of SMA (NiTi-BCJ-1) under cyclic loads
5. 3D model of SMA (NiTi-BCJ-2) under cyclic loads
6. 3D model of SMA (NiTi-BCJ-3) under reverse cyclic loads – Perfect Bonding
7. 3D model of SMA (NiTi-BCJ-3) under reverse cyclic loads – Anchored in couplers
8. 3D model of SMA (NiTi-BCJ-4) under reverse cyclic loads – Perfect Bonding
9. 3D model of SMA (NiTi-BCJ-4) under reverse cyclic loads – Anchored in couplers

For the simulation of BCJ in ANSYS for this research, half of the BCJ was modeled and symmetry properties have been conducted to minimize the time for analyzing and decrease the size of result files as illustrated in Figure 7 - 1. Furthermore, numerical results illustrate good matching with experimental results until the softening stage of BCJ since ANSYS program cannot capture the behavior of softening part for concrete elements. Consequently, finite element analysis was performed for all BCJ models till the start of softening then it stopped running.

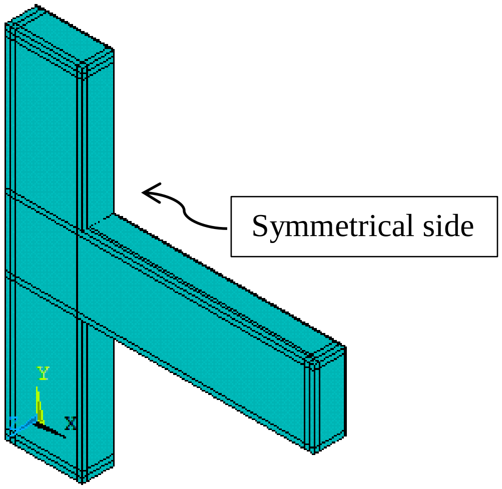

Figure 7 - 1: BCJ modeling in ANSYS

7.2 ELEMENT TYPES AND MATERIAL PROPERTIES OF THE BCJ MODEL

Willam and Warnke model has been used to model the concrete material and Elastic-perfectly plastic model for the steel. The SMA was modeled using Auricchio and Sacco model implemented in ANSYS. Line elements have been used for modeling longitudinal column stirrups and steel bars while solid elements have been used for modeling top and bottom reinforcement of the beam in the BCJ including the parts of SMA as illustrated in Figure 7 - 2

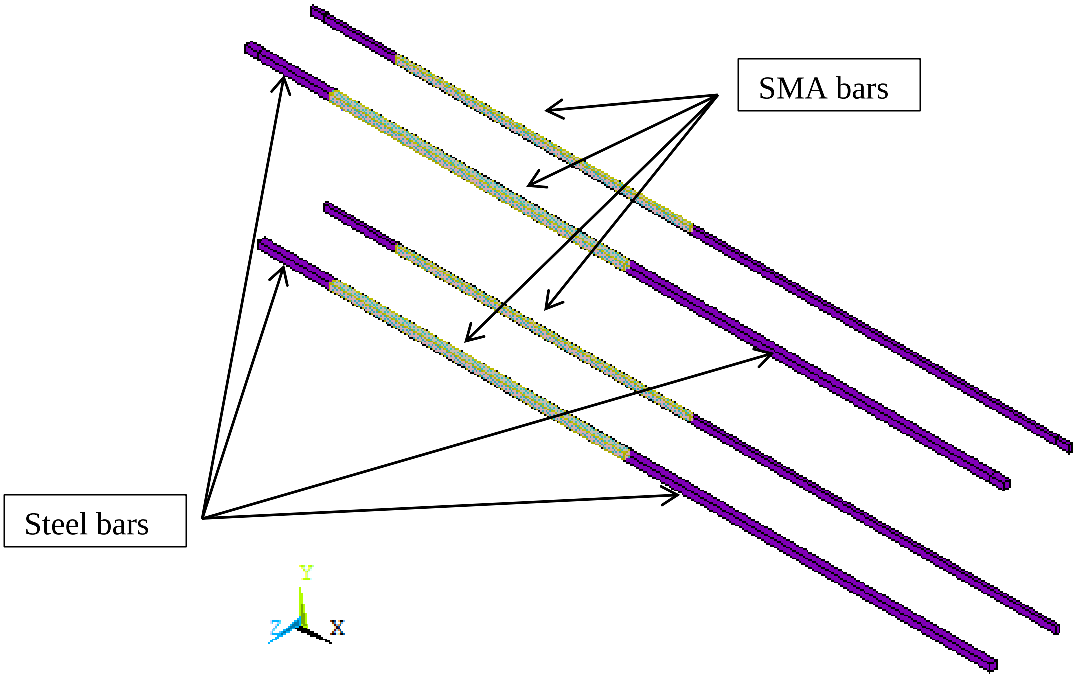

Figure 7 - 2: Top and bottom reinforcement in the beam

7.2.1 ELEMENT TYPE USED FOR MODELING

Table 7 - 1 shows type of the elements which has been used for each part of the BCJ model in ANSYS

Table 7 - 1: Type of elements used in modeling of BCJ

Part	**Element Type**
Concrete	Solid 65
Top and Bottom reinforcement in Beam	Solid 185
All column stirrups and steel reinforcement	Link 180

7.2.2 MATERIAL MODELS

Tables 7 - 2, 7 - 3, & 7 - 4 show the material properties of concrete, steel, and shape memory alloy respectively which have been conducted for modeling of BCJ in ANSYS.

Table 7 - 2: Material properties of concrete

Modules of elasticity	32500 MPa		**Poisson Ratio**	0.2
Strain	**Stress (MPa)**			
0.0004	13		Opened Shear Transfer Coefficient	0.3
0.0006	18		Close Shear Transfer Coefficient	0.9
0.0009	25		Uniaxial Cracking Stress	4.5
0.0012	32		Uniaxial Crushing Stress	51
0.0015	38			
0.002	44			
0.0025	48			
0.003	51			

Table 7 - 3: Material properties of steel

Modules of elasticity	180 GPa		**Poisson Ratio**	0.3
Yield Stress for main steel bars	610		**Tang Modulus**	0
Yield Stress for Stirrups	576		**Tang Modulus**	0

Table 7 - 4: Material properties of Shape Memory Alloy (SMA)

Modules of elasticity	20 GPa
Poisson Ratio	0.2
SIG-SAS	280 MPa
SIG-FAS	330 MPa
SIG-SSA	90 MPa
SIG-FSA	40 MPa
EPSILON	0.0335
ALPHA	1

7.3 MESHING AND BOUNDARY CONDITION

Dynamic analysis in ANSYS has been used in this simulation. Hexahedral swiping mesh has been used for the whole model each 10 by 10 mm square elements. Figure 7 - 3 shows the 3-D finite element model for BCJ after meshing. Bottom end of the column was coupled and constrained in x, y, and z directions and Top end of the column was coupled and constrained in the x and z direction only. The beam tip was coupled in y direction to apply the displacement. (150 kN) axial loads were applied at the top surface of the column.

Figure 7 - 4 shows the applied axial loads as well as boundary condition for the model. Figure 7 - 5 shows the steel reinforcement model embedded in the BCJ.

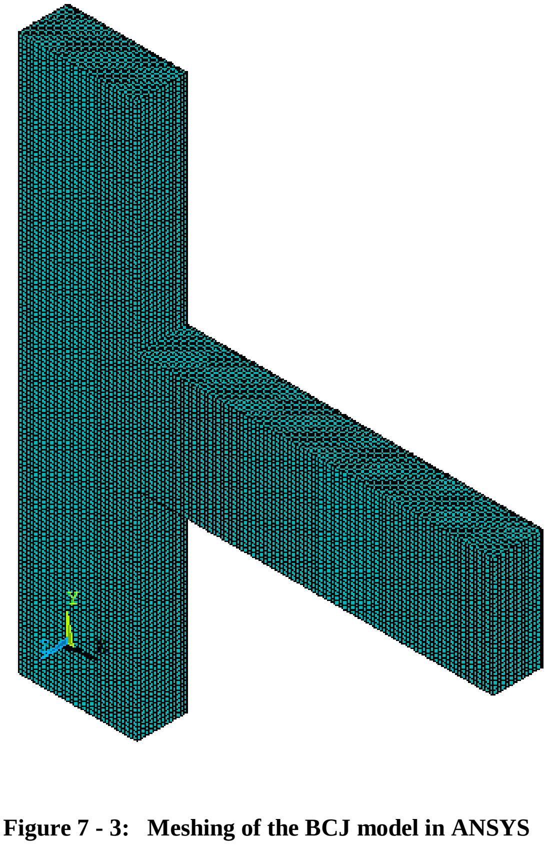

Figure 7 - 3: Meshing of the BCJ model in ANSYS

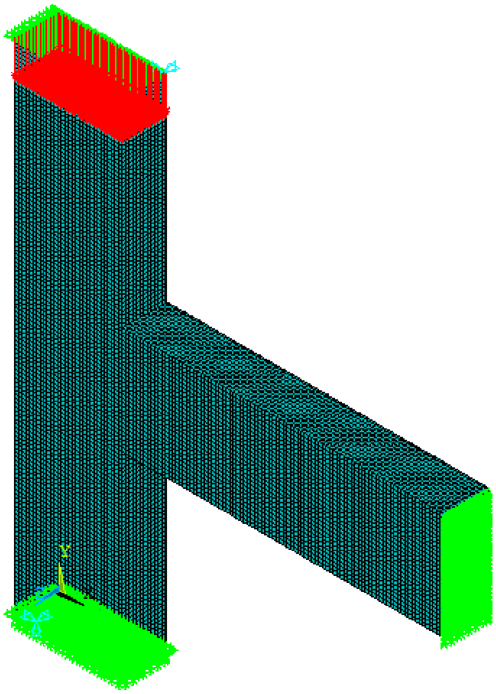

Figure 7 - 4: Boundary conditions and axial load applied for the BCJ model

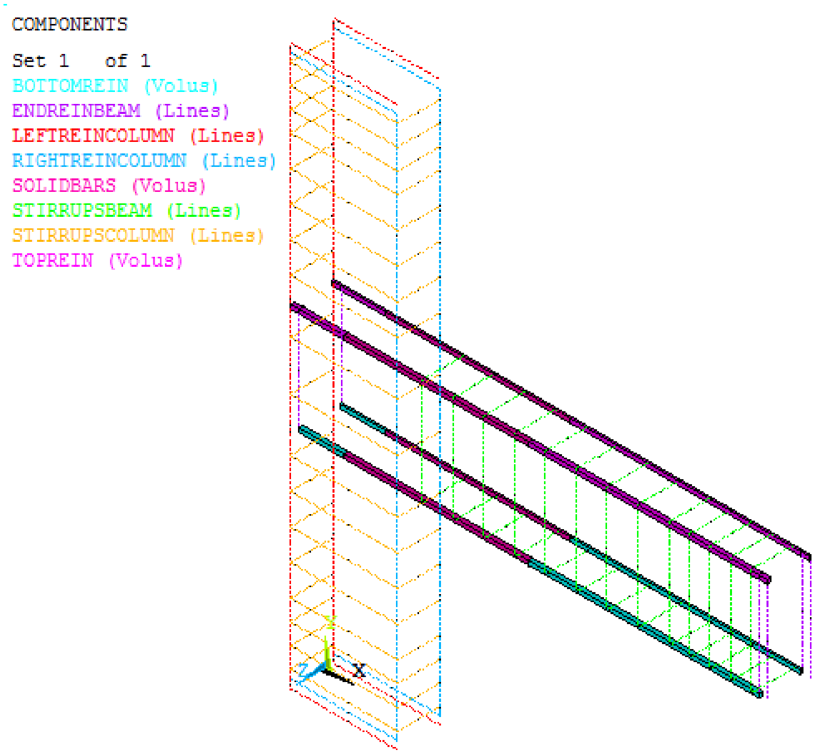

Figure 7 - 5: Reinforcement bars for the BCJ model

7.4 NUMERICAL SIMULATION OF MONOTONIC TEST FOR CONTROL BCJ (Con-BCJ-1) SPECIMEN

The finite element simulation and experimental results of load – story drift response for control BCJ (Con-BCJ-1) specimen under monotonic load is illustrated in Figure 7 - 6.

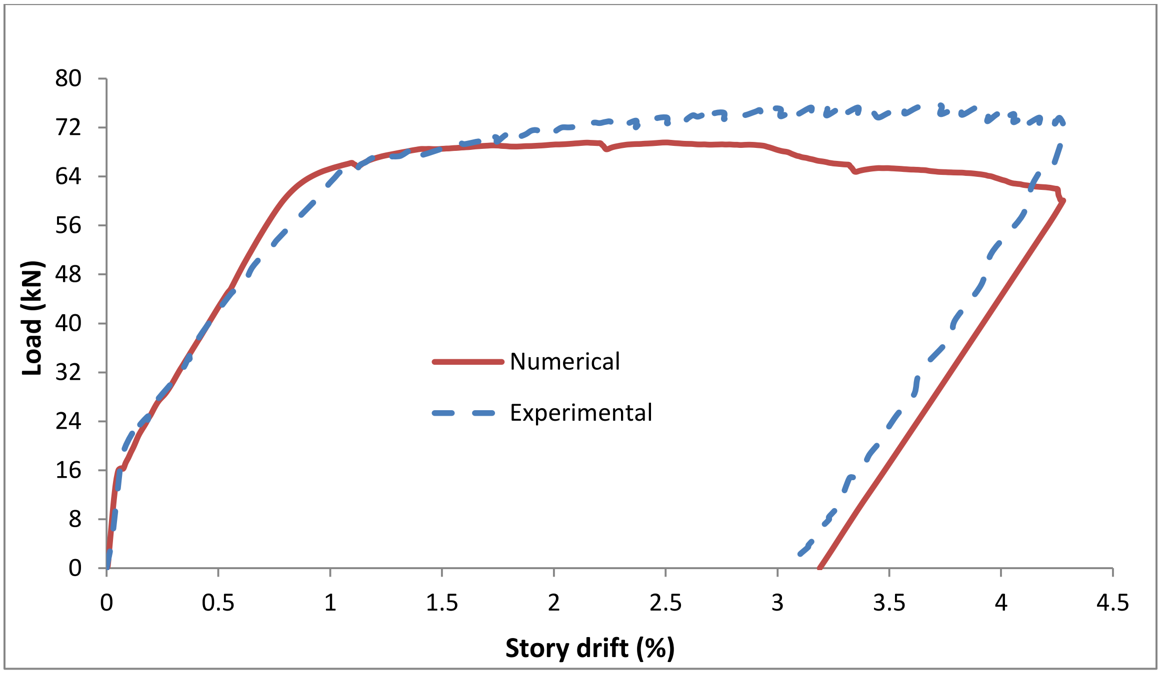

Figure 7 - 6: Load – Story drift curve of (Con-BCJ-1) specimen

As illustrated in the previous figure, the finite element simulation response is matching closely with experimental results. There is a small difference in the ultimate load between numerical and experimental response due to hardening of the steel reinforcement, which is not considered in finite element simulation.

7.5 NUMERICAL SIMULATION OF CYCLIC TEST FOR CONTROL BCJ (Con-BCJ-2) SPECIMEN

The finite element simulation and experimental results of load – story drift response for control BCJ (Con-BCJ-2) specimen under cyclic load is illustrated in Figure 7 - 7.

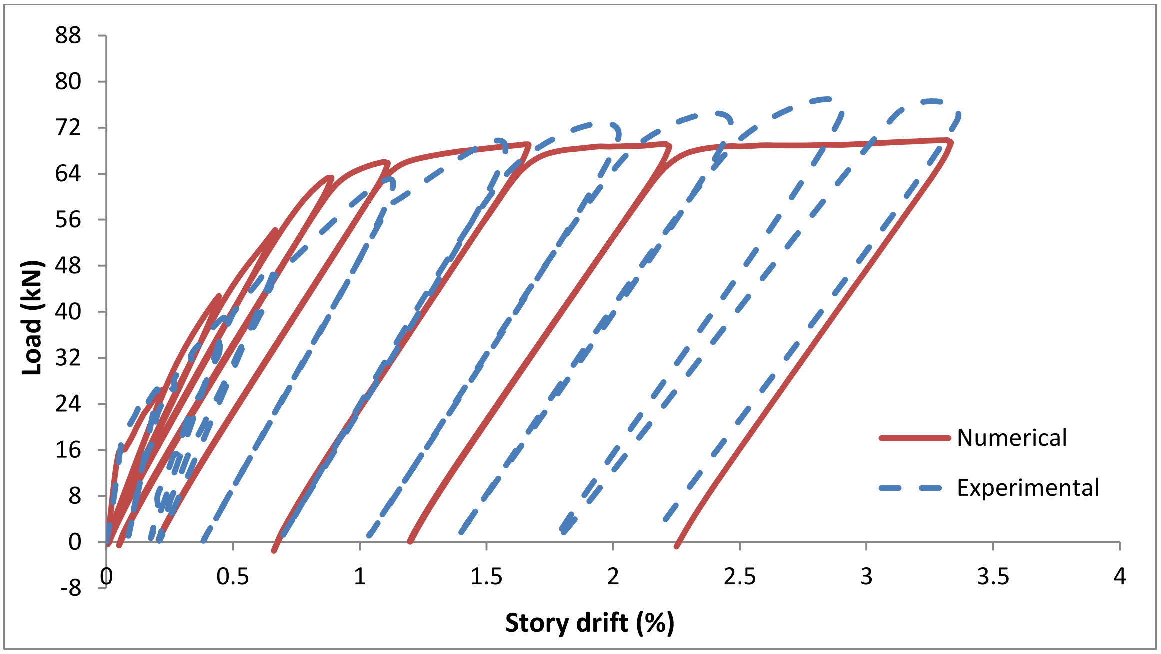

Figure 7 - 7: Load – Story drift curve for (Con-BCJ-2) specimen

As illustrated in the previous figure, the finite element simulation response is matching closely with experimental results. There is a small difference at the peak load between numerical and experimental response due to hardening of the steel reinforcement, which is not considered in finite element simulation.

Flexural cracks were occurred at the interface of BCJ and beam face. Figure 7 - 8 illustrates the development of the cracks in the finite element simulation. Figure 7 - 9 shows crack locations between numerical and experimental investigation.

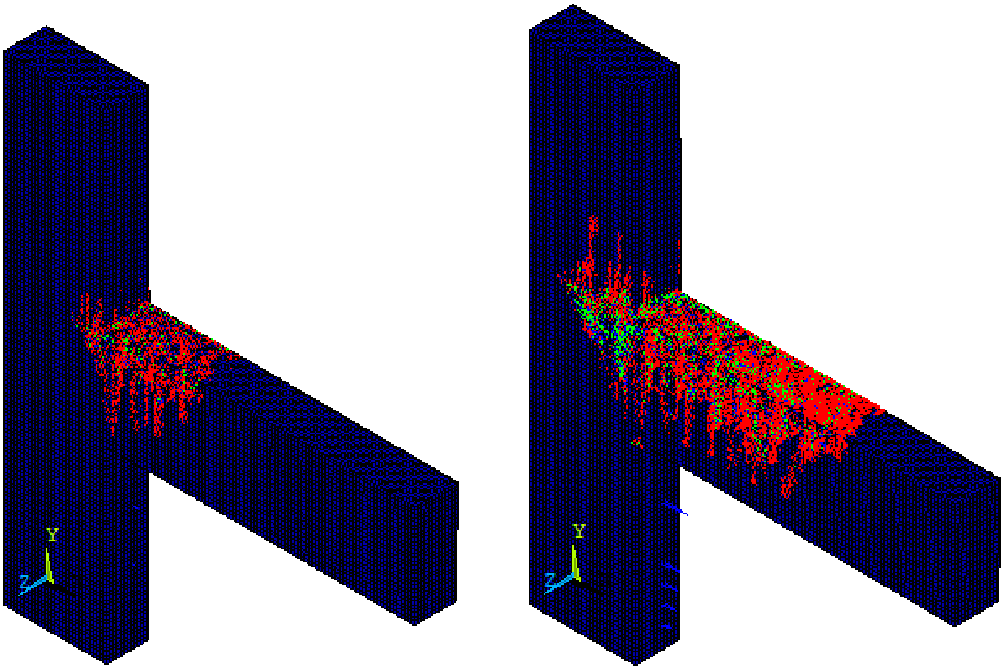

Figure 7 - 8: Development of flexural crack for (Con-BCJ-2)

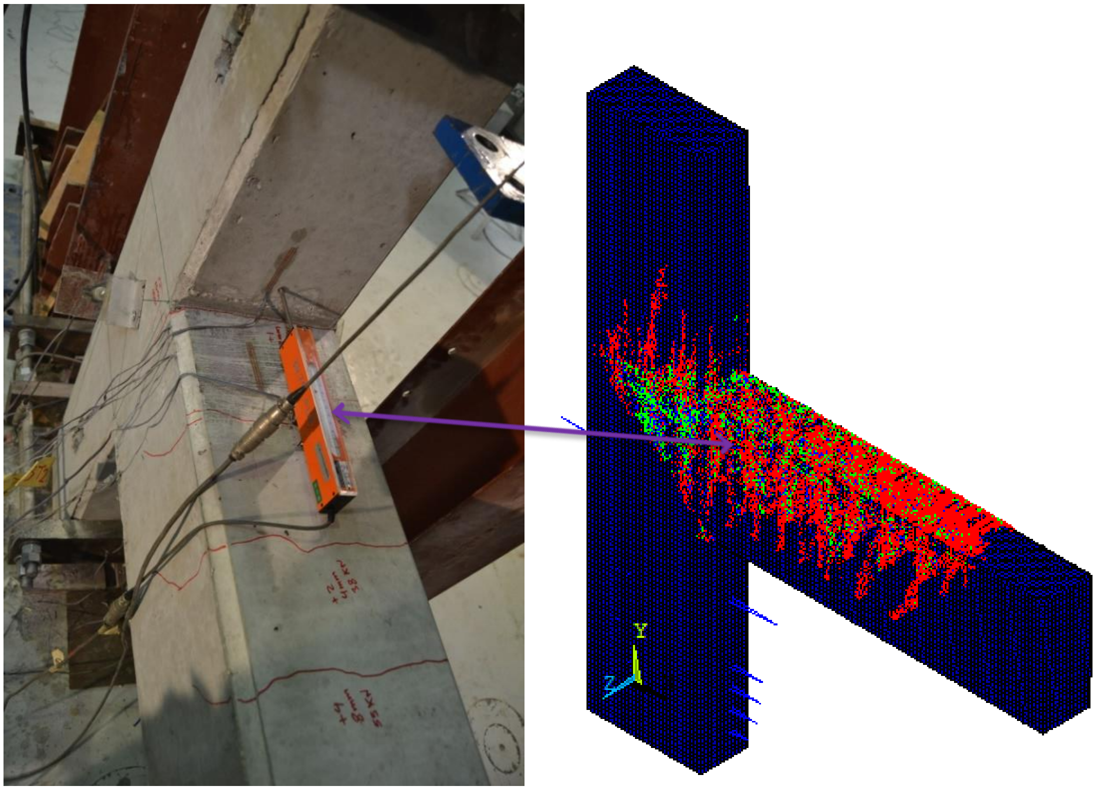

Figure 7 - 9: Location of flexural crack between experimental and numerical results

The simulation shows a development of more than one crack in the beam column interface. Stresses and strains for top and bottom steel bars at a displacement of 10 mm down are shown in Figures 7 - 10 & 7 - 11, respectively.

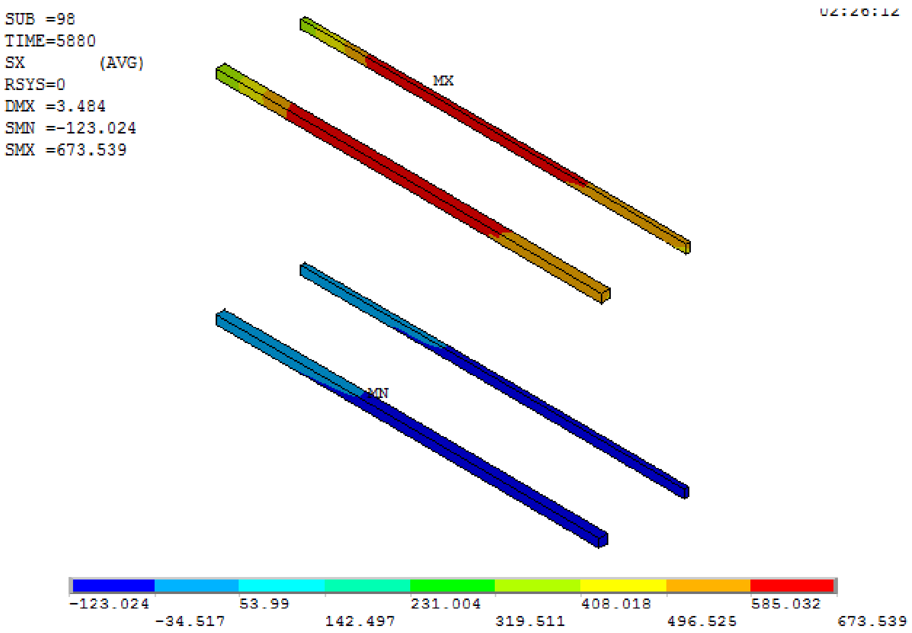

Figure 7 - 10: Stress in steel bars at a displacement of 10 mm for (Con-BCJ-2)

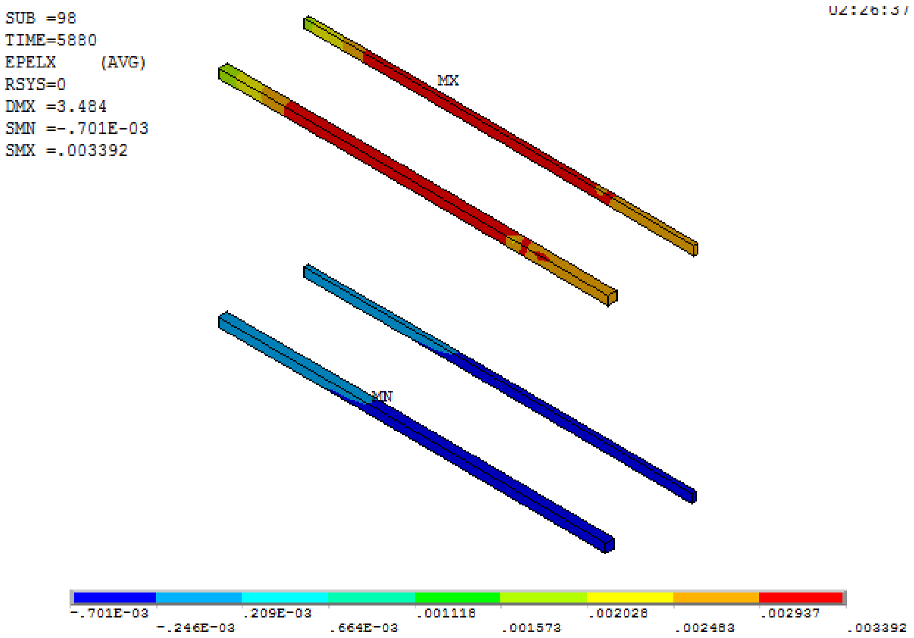

Figure 7 - 11: Strain in steel bars at a displacement of 10 mm for (Con-BCJ-2)

Stresses and strains for top and bottom steel bars at zero loads are illustrated in Figures 7 – 12 & 7 - 13 respectively.

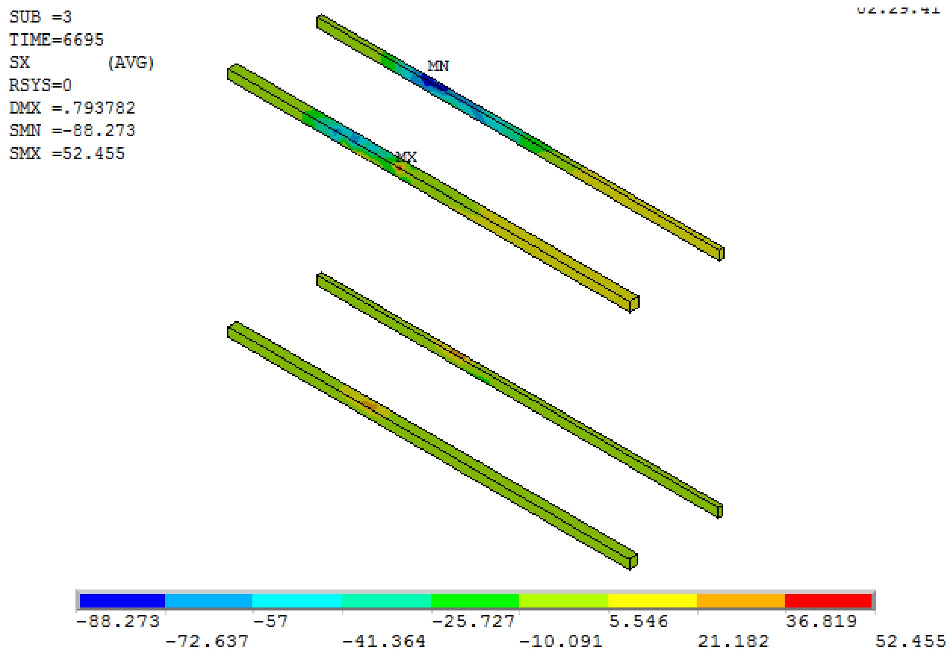

Figure 7 - 12: Stresses in the steel reinforcement bars at zero loads for (Con-BCJ-2)

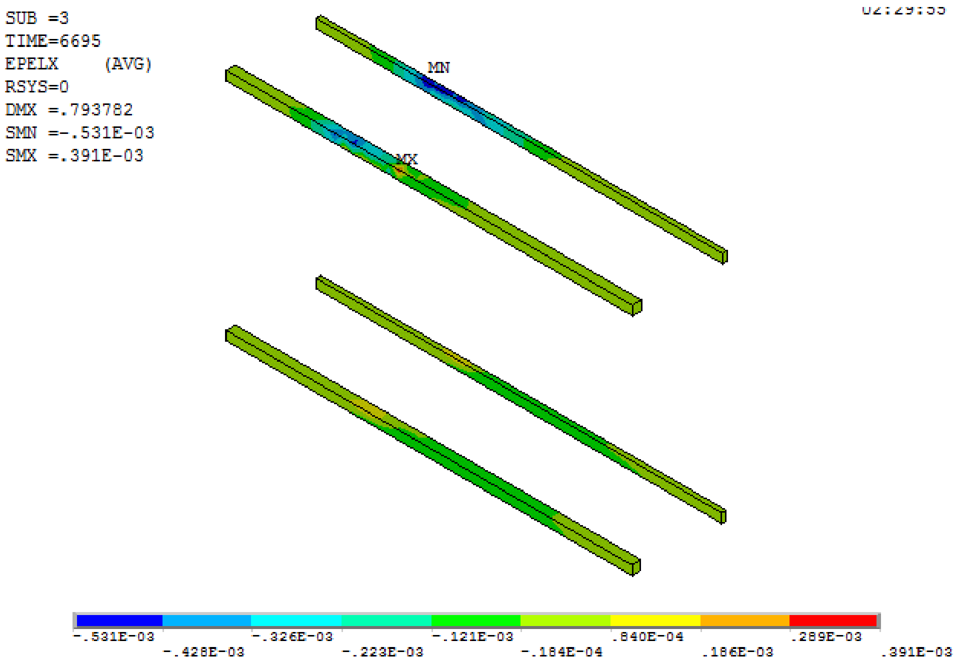

Figure 7 - 13: Strain in the steel reinforcement bars at zero loads for (Con-BCJ-2)

7.6 NUMERICAL SIMULATION OF REVERSE CYCLIC TEST FOR CONTROL BCJ (Con-BCJ-3) SPECIMEN

The finite element simulation and experimental results of load – story drift response for control BCJ (Con-BCJ-3) specimen under reverse cyclic load is illustrated in Figure 7 - 14.

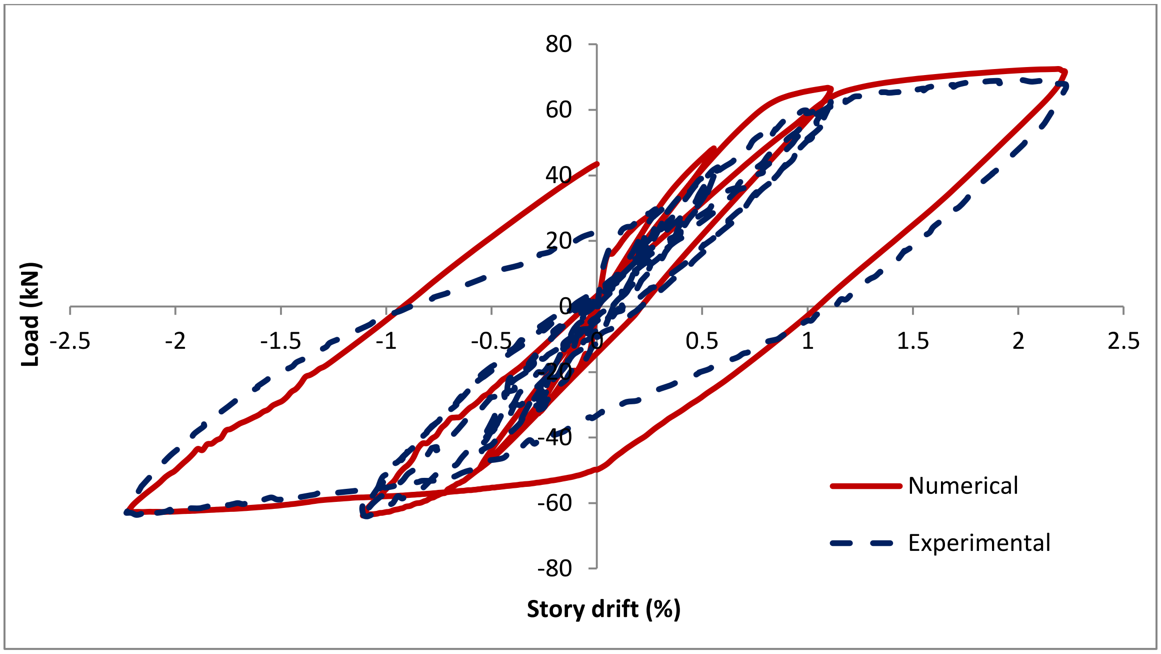

Figure 7 - 14: Load – Story drift curve for (Con-BCJ-3) specimen

As illustrated in the previous figure, the finite element simulation results are matching very closely with the experimental results.

Flexural cracks were occurred at the interface of BCJ and beam face. Figure 7 - 15 illustrates the development of the cracks in finite element simulation. Figure 7 - 16 shows crack locations between numerical and experimental investigation.

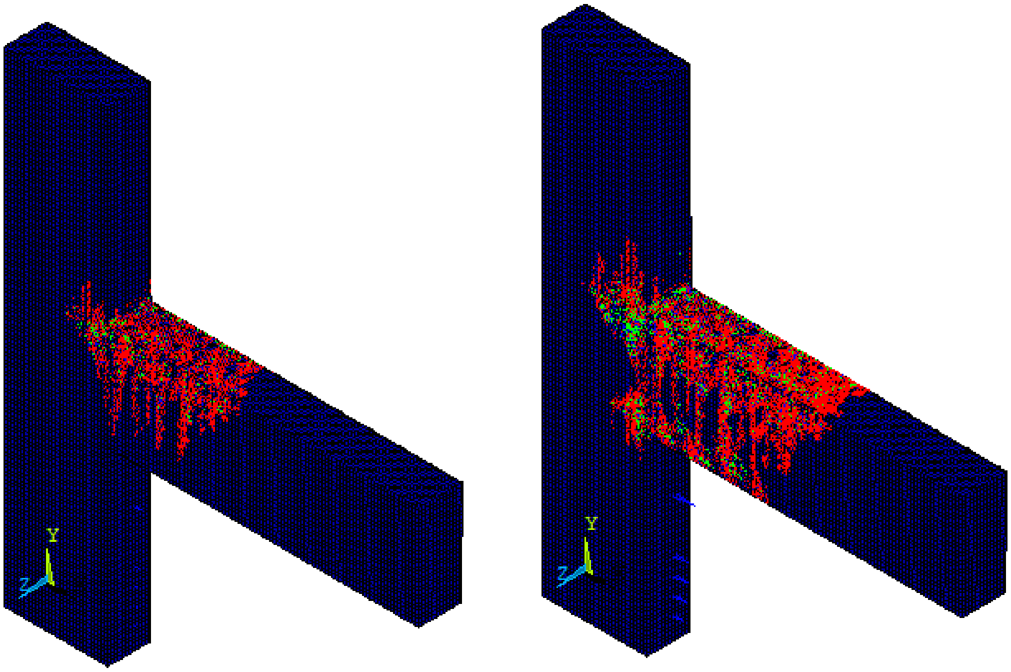

Figure 7 - 15: Development of flexural crack for (Con-BCJ-3)

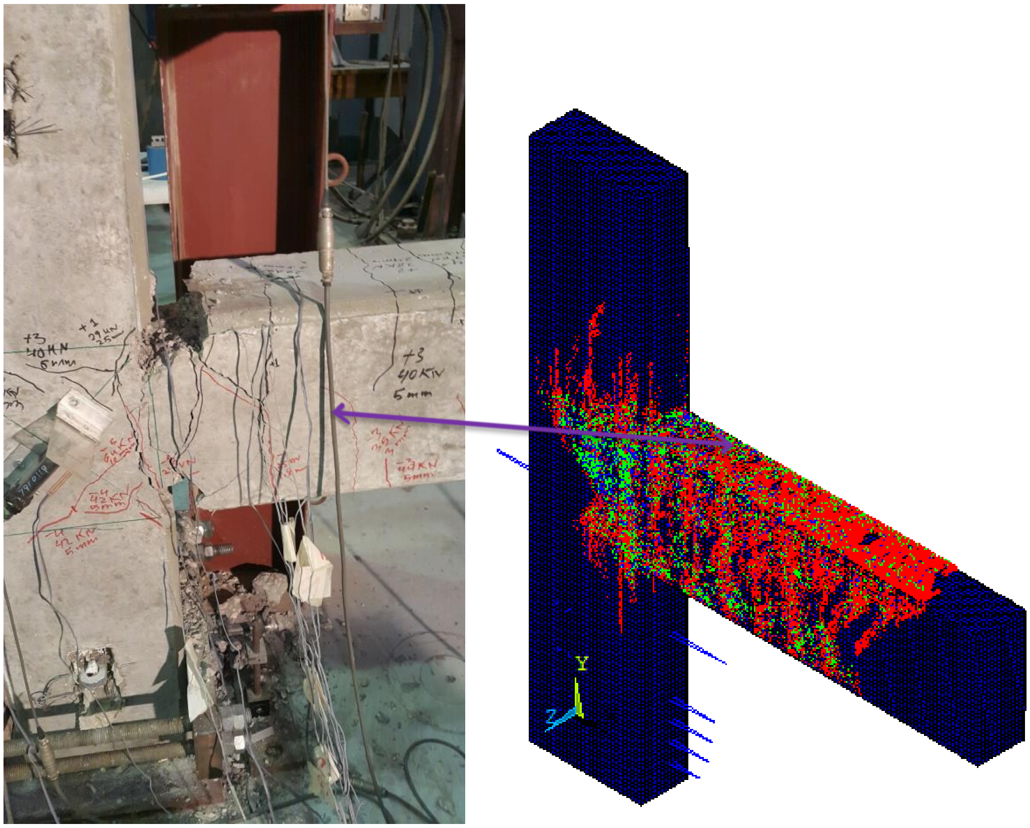

Figure 7 - 16: Location of flexural crack between experimental and numerical results

The simulation shows a development of more than one crack in the beam column interface. Stress and strain for top and bottom steel bars at a displacement of 10 mm down are shown in Figures 7 - 17 & 7 - 18 respectively.

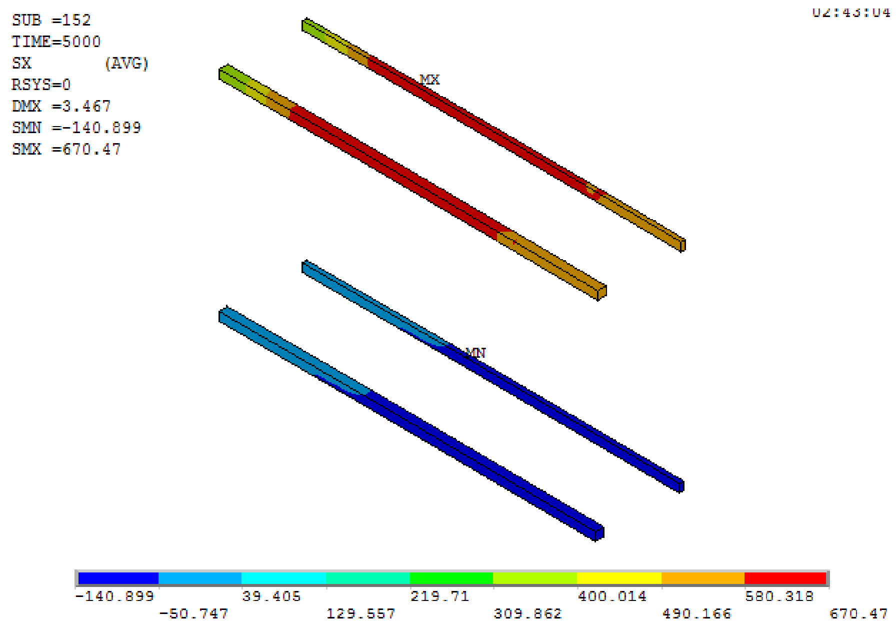

Figure 7 - 17: Stress in steel bars at a displacement of 10 mm for (Con-BCJ-3)

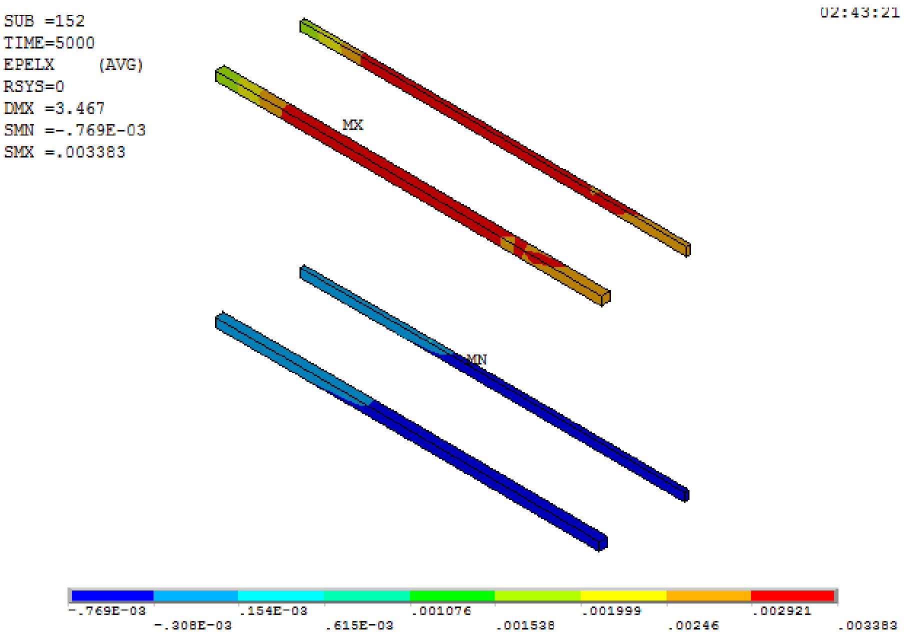

Figure 7 - 18: Strain in steel bars at a displacement of 10 mm for (Con-BCJ-3)

Stress and strain for top and bottom steel bars at zero loads are shown in Figures 7 – 19 & 7 - 20 respectively.

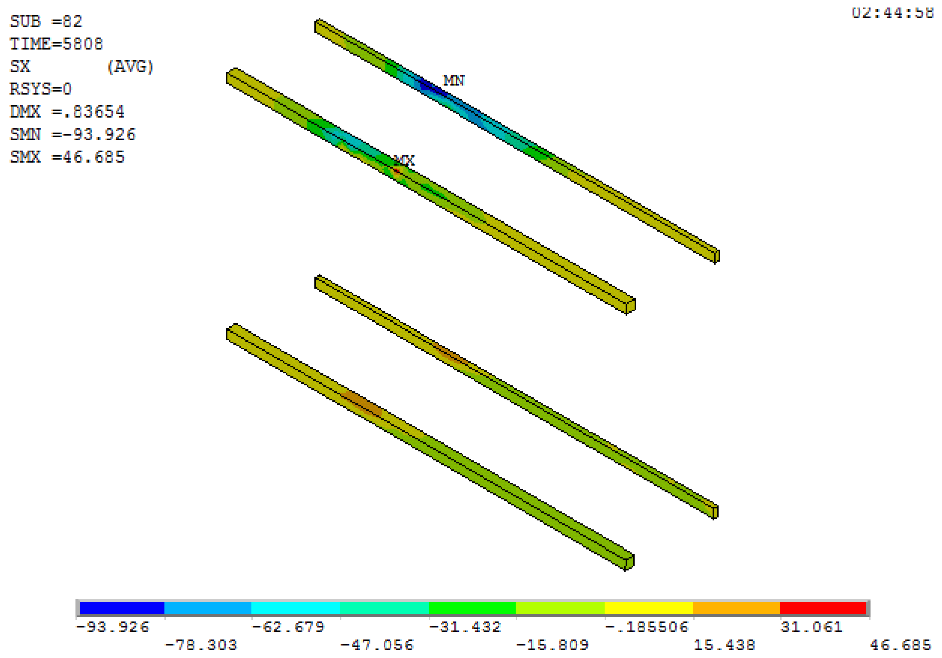

Figure 7 - 19: Stresses in the steel reinforcement bars at zero loads for (Con-BCJ-3)

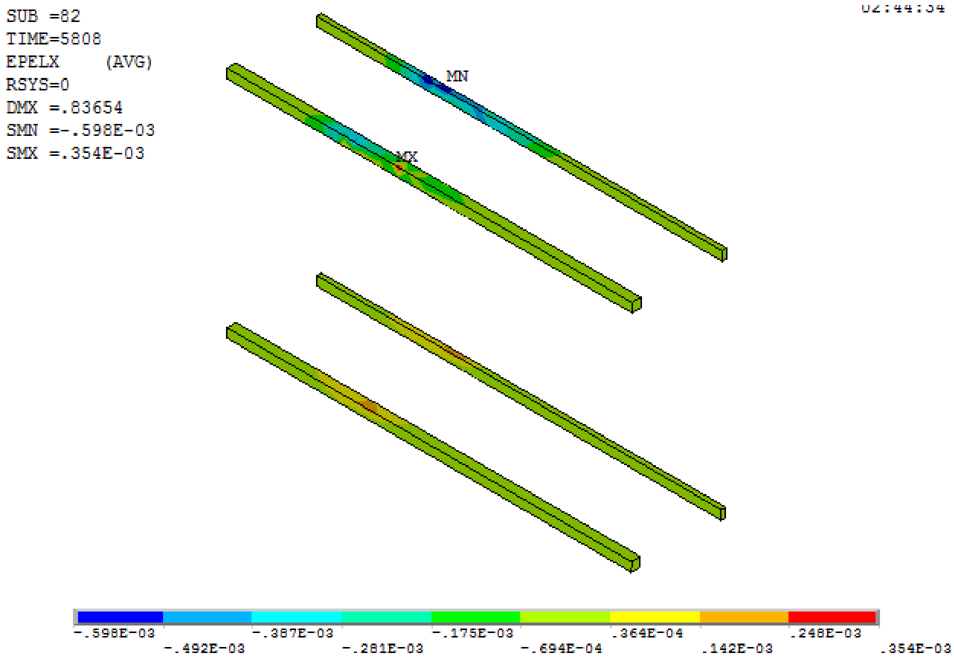

Figure 7 - 20: Strain in the steel reinforcement bars at zero loads for (Con-BCJ-3)

7.7 NUMERICAL SIMULATION OF CYCLIC TEST FOR SMA - BCJ (NiTi-BCJ-1) SPECIMEN

The finite element simulation and experimental results of the load – story drift response for SMA - BCJ (NiTi-BCJ-1) specimen under cyclic load is illustrated in Figure 7 - 21.

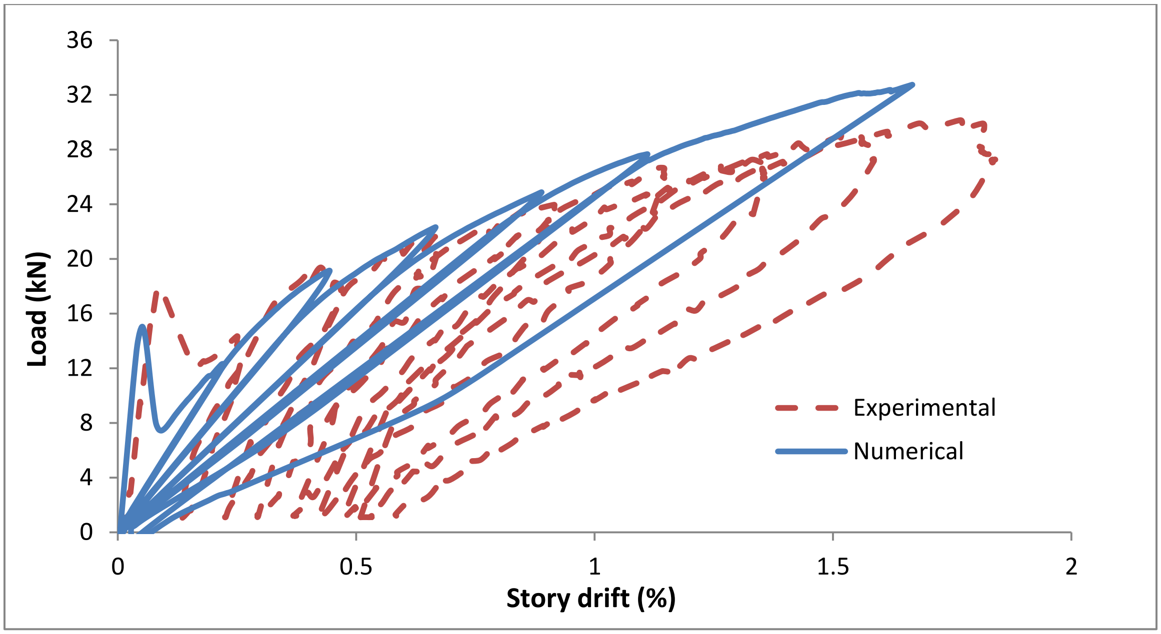

Figure 7 - 21: Load – Story drift curve for (NiTi-BCJ-1) specimen

As illustrated in the previous figure, the finite element simulation results are matching very closely with the experimental results. In finite element simulation, the ultimate load was 32 kN similar to experimental results unless in FEA it reached the ultimate load at a distance of 15 mm while in the experiment it was 30 mm. However, experimentally at 15 mm deflection, the beam tip load was 30 kN.

Flexural cracks were occurred at the interface of BCJ then cracks started to become wider. Figure 7 - 22 illustrates the development of the cracks in finite element simulation.

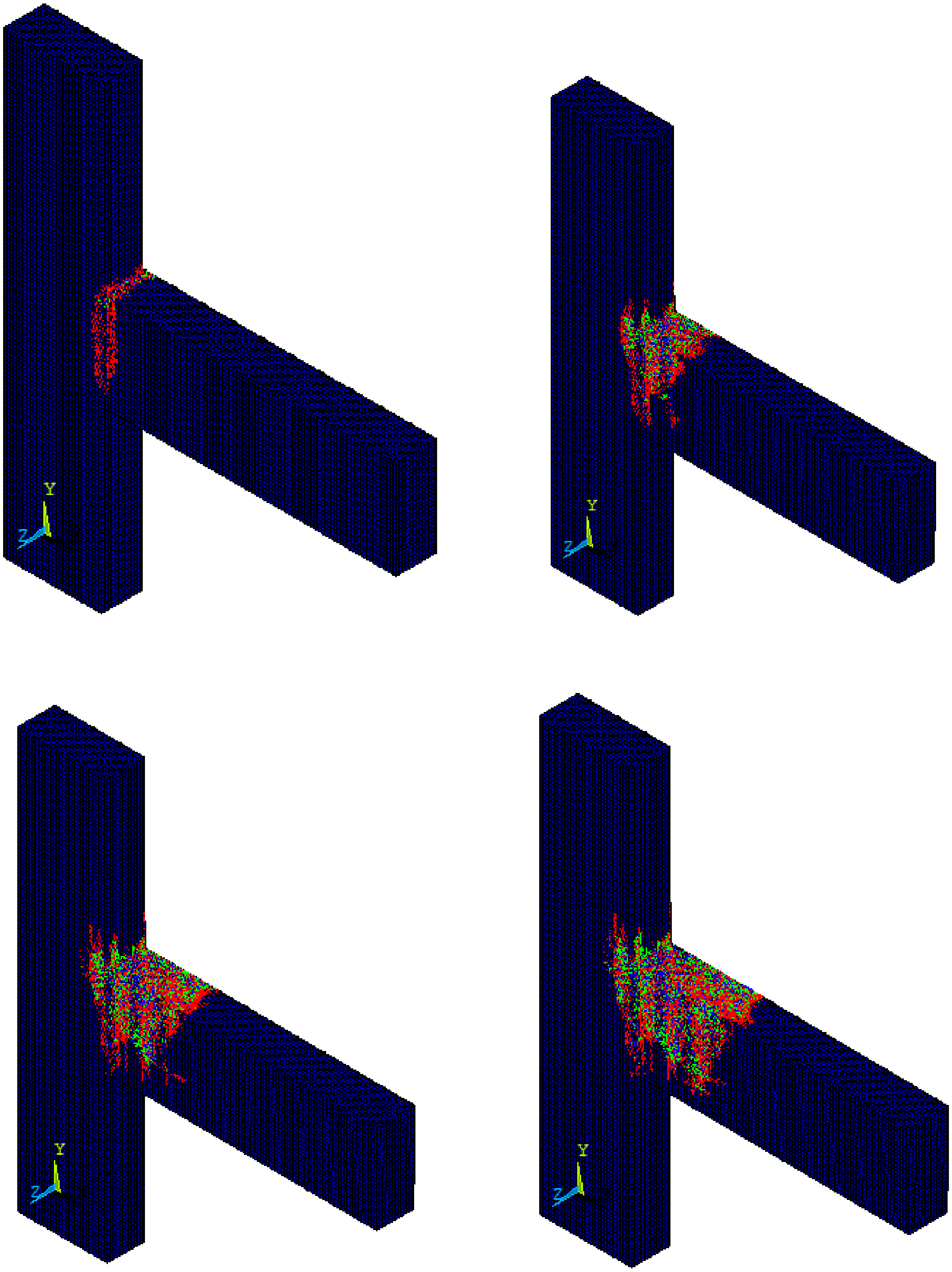

Figure 7 - 22: Development of flexural cracks for (NiTi-BCJ-1)

Figure 7 - 23 shows cracks locations between numerical and experimental investigation.

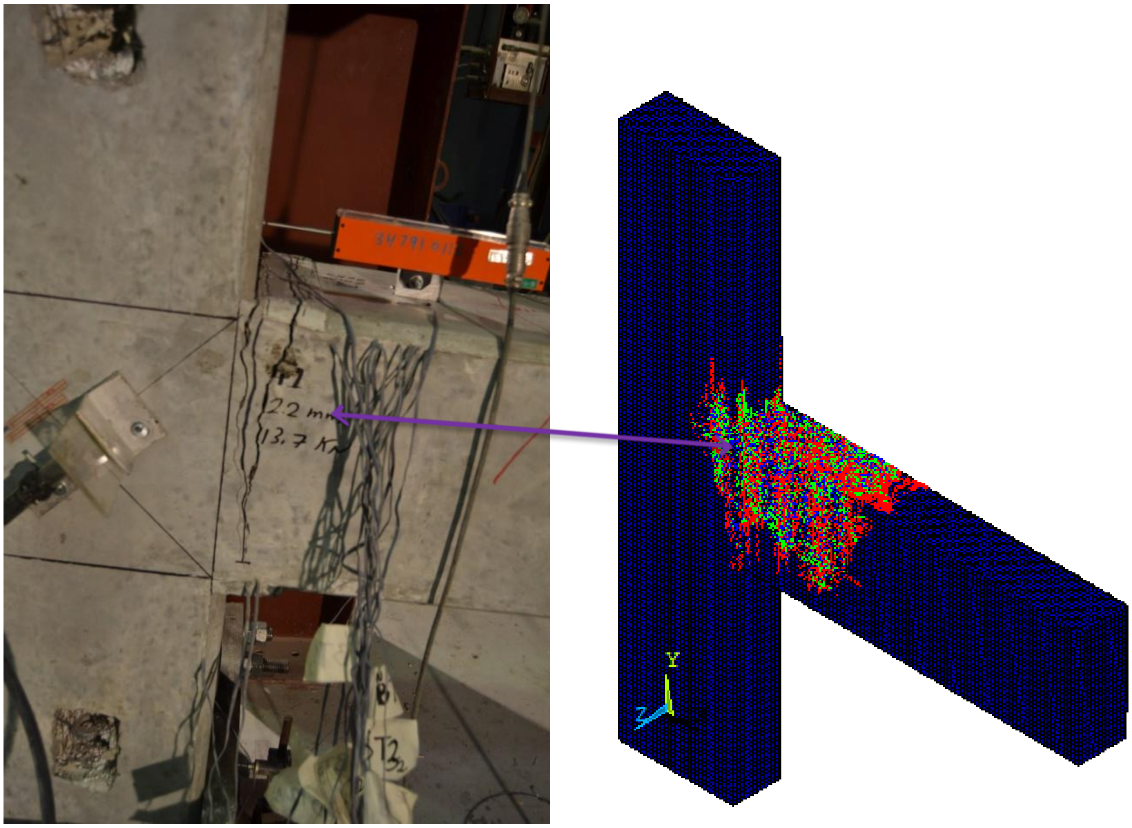

Figure 7 - 23: Locations of cracks between experimental and numerical results

The finite element simulation shows a development of more than one crack in the beam column interface.

Stresses and strains for top and bottom SMA bars at a deflection of 10 mm down are shown in Figures 7 – 24 & 7 - 25 respectively.

Stresses and strains for top and bottom SMA bars at zero loads are shown in Figures 7 – 26 & 7 - 27, respectively.

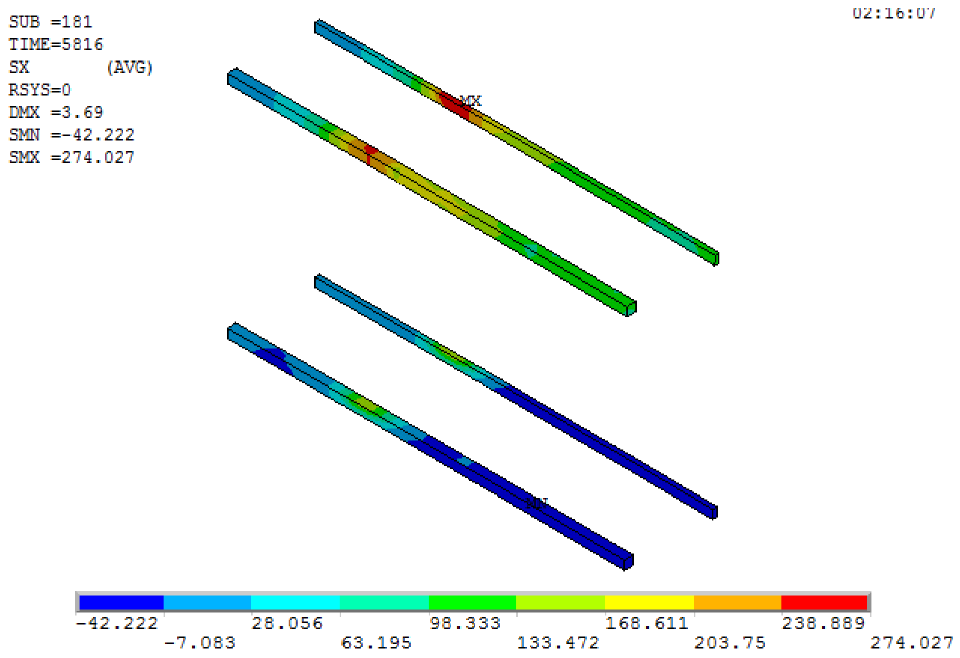

Figure 7 - 24: Stress in the SMA bars at a deflection of 10 mm for (NiTi-BCJ-1)

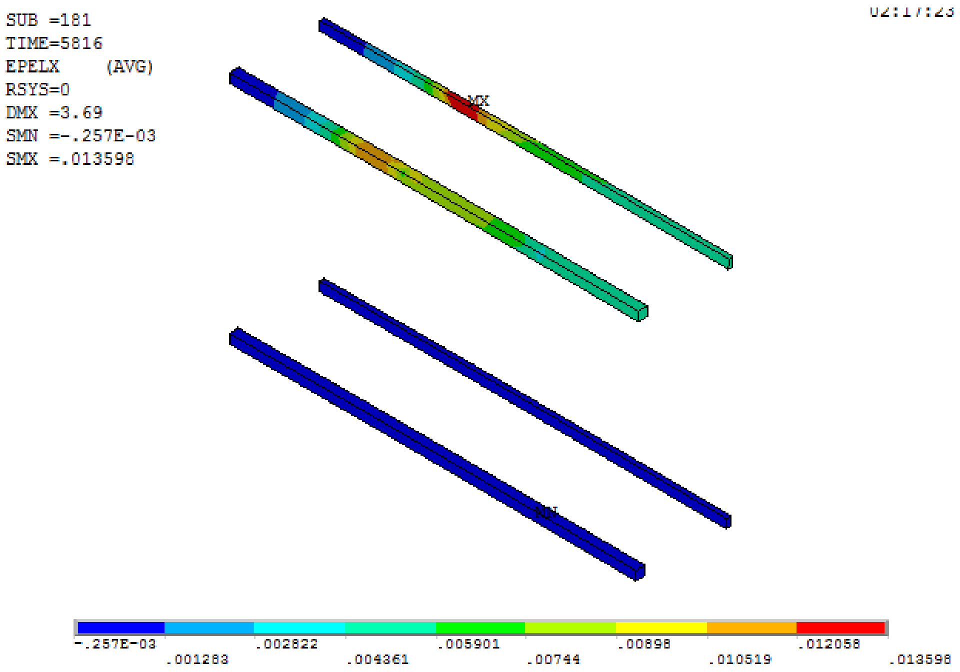

Figure 7 - 25: Strain in the SMA bars at a deflection of 10 mm for (NiTi-BCJ-1)

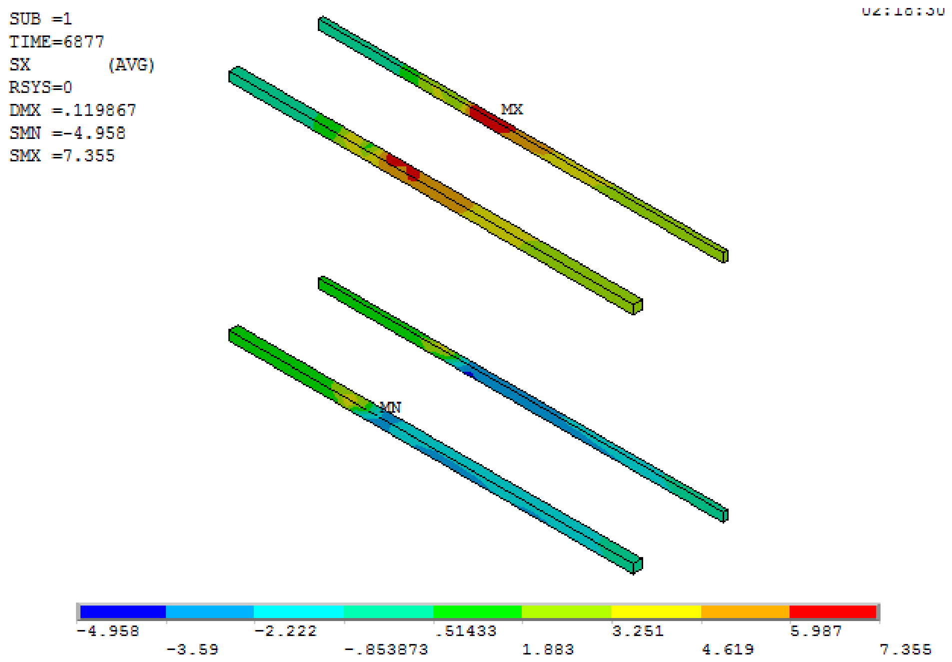

Figure 7 - 26: Stress in the SMA bars at zero loads for (NiTi-BCJ-1)

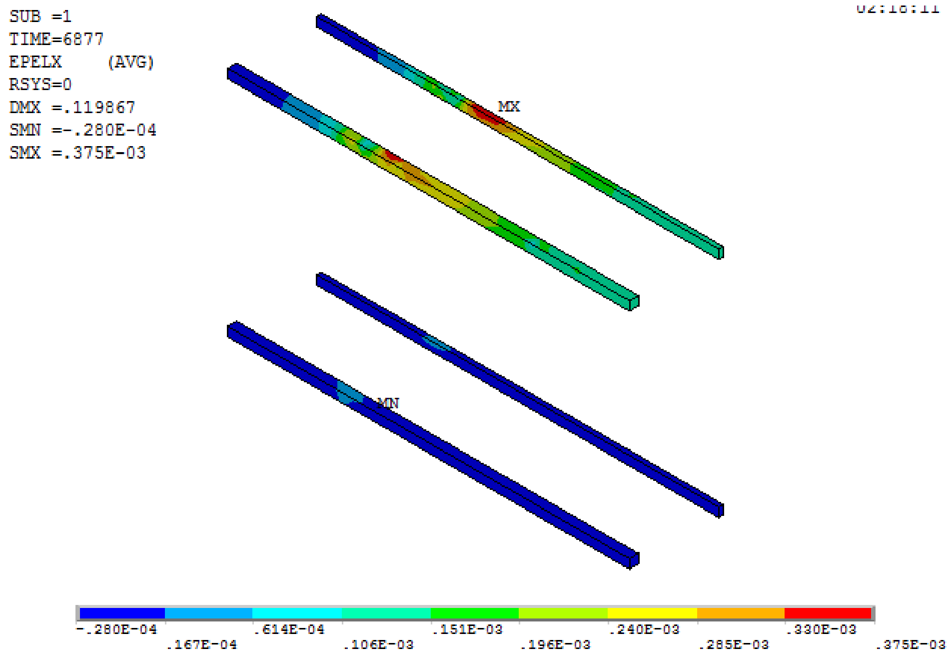

Figure 7 - 27: Strain in the SMA bars at zero loads for (NiTi-BCJ-1)

From previous figures, the maximum Stress in the SMA bars at a displacement of 10 mm is (274 MPa) and strain is (0.0136 mm/mm) which is approximately yielding point. However, at zero loads, stress value at SMA bar became (7 MPa) and strain is (0.00275 mm/mm) which is almost zero. Consequently, it shows that stresses and strains in the SMA bar returned back to almost zero without any permanent values.

Due to the material constitutive modeling of SMA in ANSYS and because of losing of bond and slippage from the couplers in the experimental tests, results of the load displacement curve for (NiTi-BCJ-1) returned back to zero for all cycles according with removing loads which are not matching exactly with the experimental response.

7.8 NUMERICAL SIMULATION OF CYCLIC TEST FOR SMA - BCJ (NiTi-BCJ-2) SPECIMEN

The finite element simulation and experimental results of the load – story drift response for SMA - BCJ (NiTi-BCJ-2) specimen under cyclic load is shown in Figure 7 - 28.

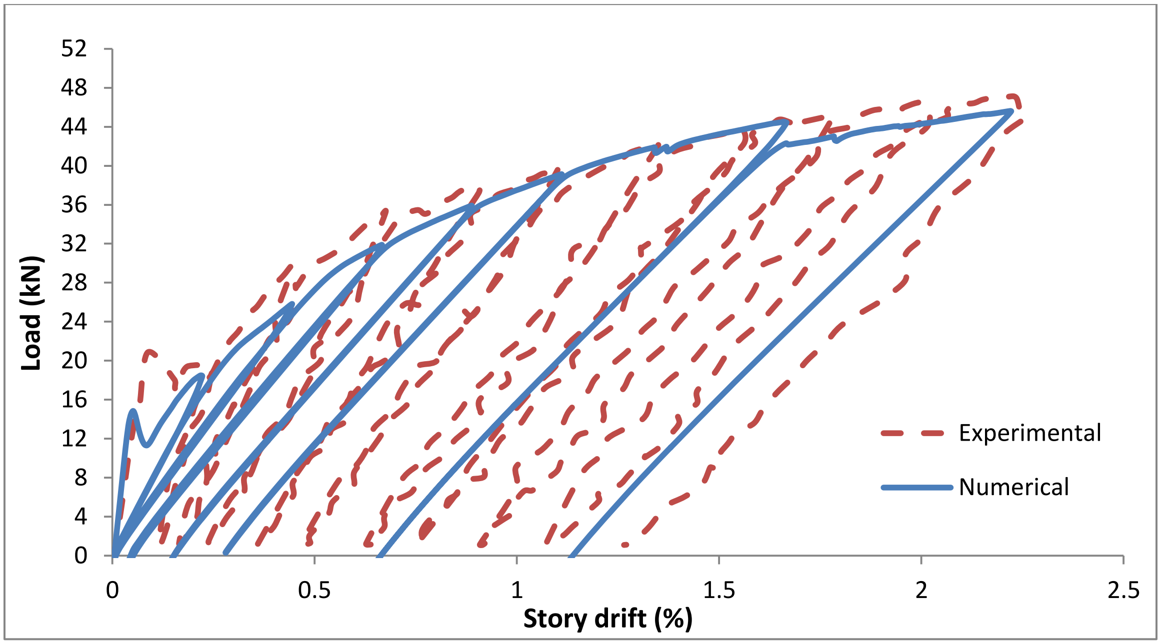

Figure 7 - 28: Load – Story drift curve for (NiTi-BCJ-2) specimen

As illustrated in the previous figure, the finite element simulation results are matching very closely with the experimental results. Although, there were two SMA bars at the top section of the beam combined with 1 steel bar, SMA bars cannot return the displacement to zero at zero loads which is matching exactly with experimental investigation.

Flexural cracks were occurred at the interface of BCJ then started to become wider. Figure 7 - 29 illustrates the development of the cracks in finite element simulation.

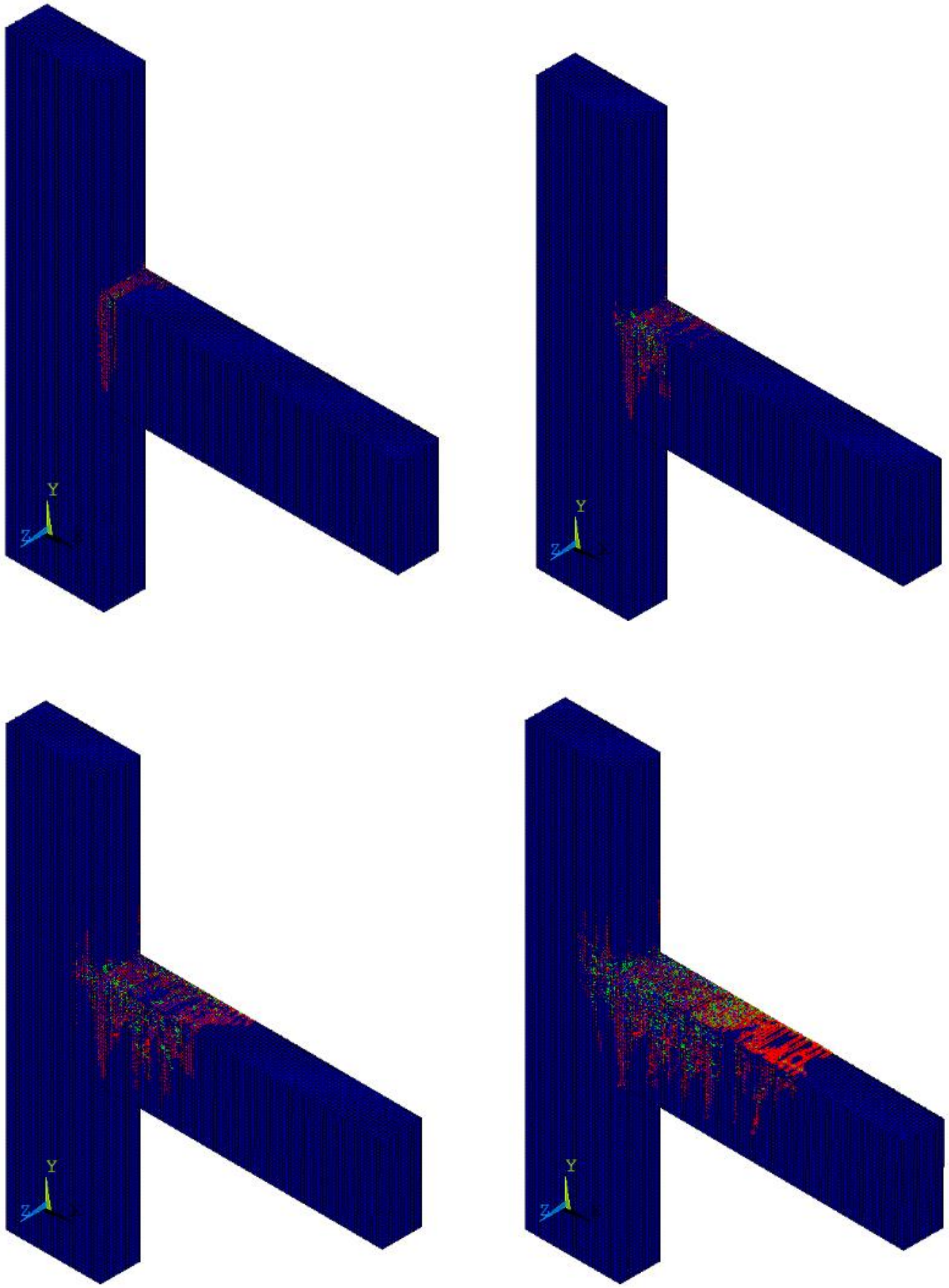

Figure 7 - 29: Development of flexural cracks for (NiTi-BCJ-2)

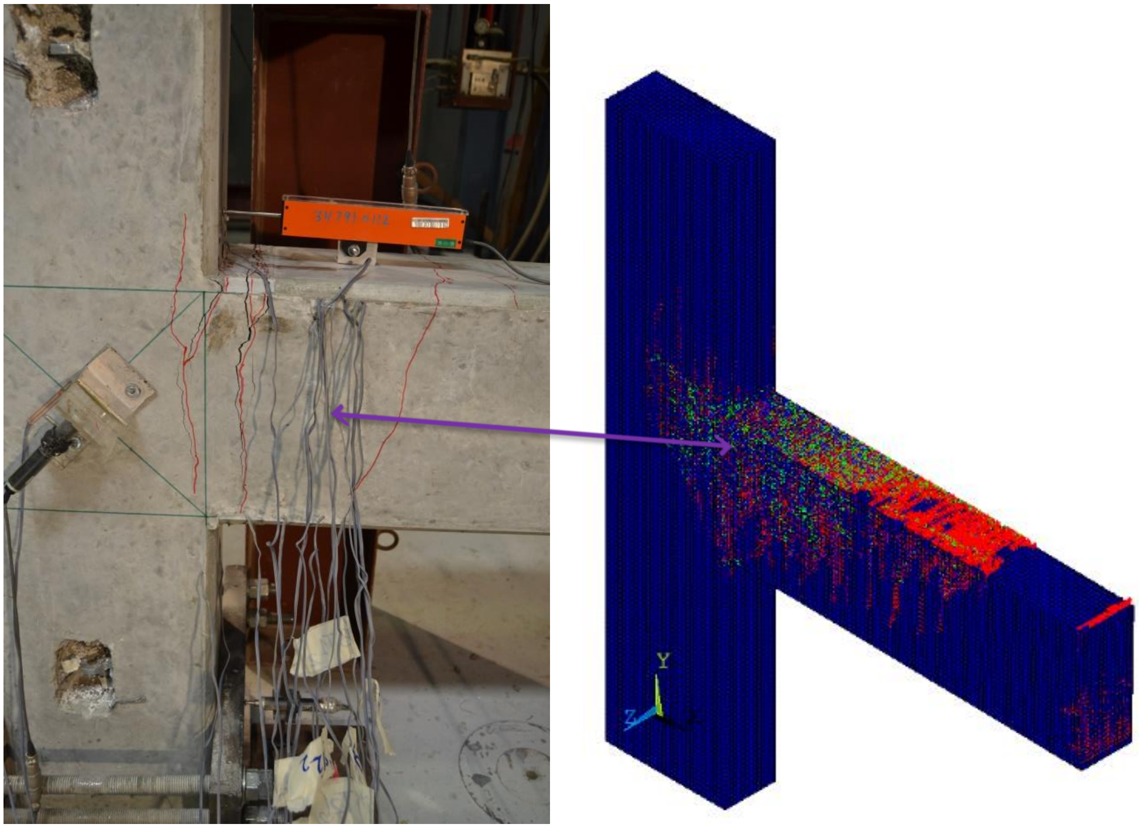

Figure 7 - 30: Location of flexural crack between numerical and experimental results

This simulation shows a development of more than one crack in the BCJ interface as illustrated in Figure 7 - 30.

Stresses and strains for top and bottom SMA bars at a deflection of 10 mm down are shown in Figures 7 – 31 & 7 - 32 respectively.

Stresses and strains for top and bottom SMA bars at zero loads are shown in Figures 7 – 33 & 7 - 34 respectively.

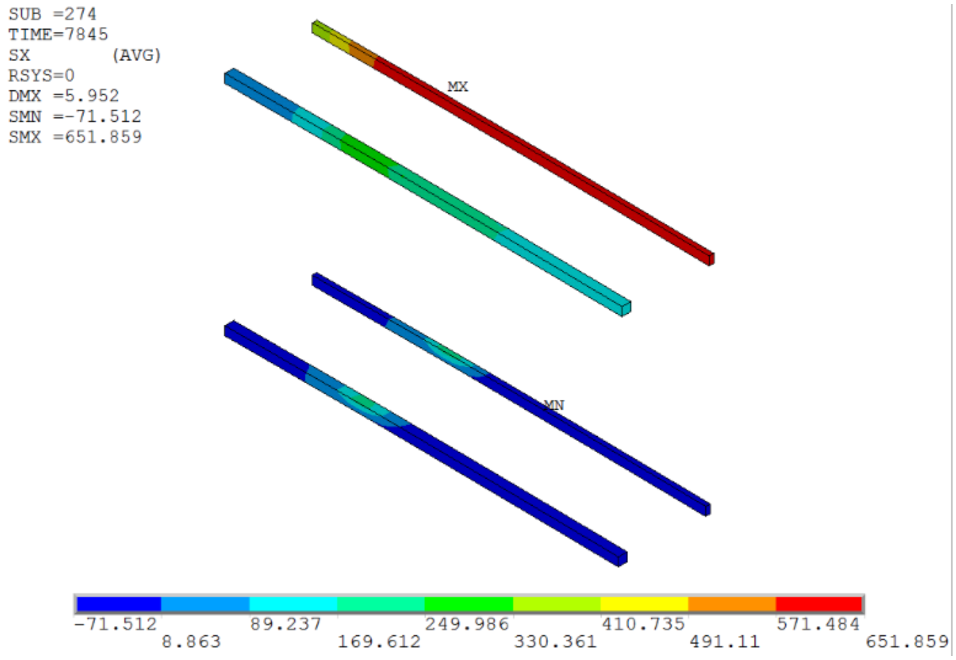

Figure 7 - 31: Stress in the SMA bars at a deflection of 10 mm for (NiTi-BCJ-2)

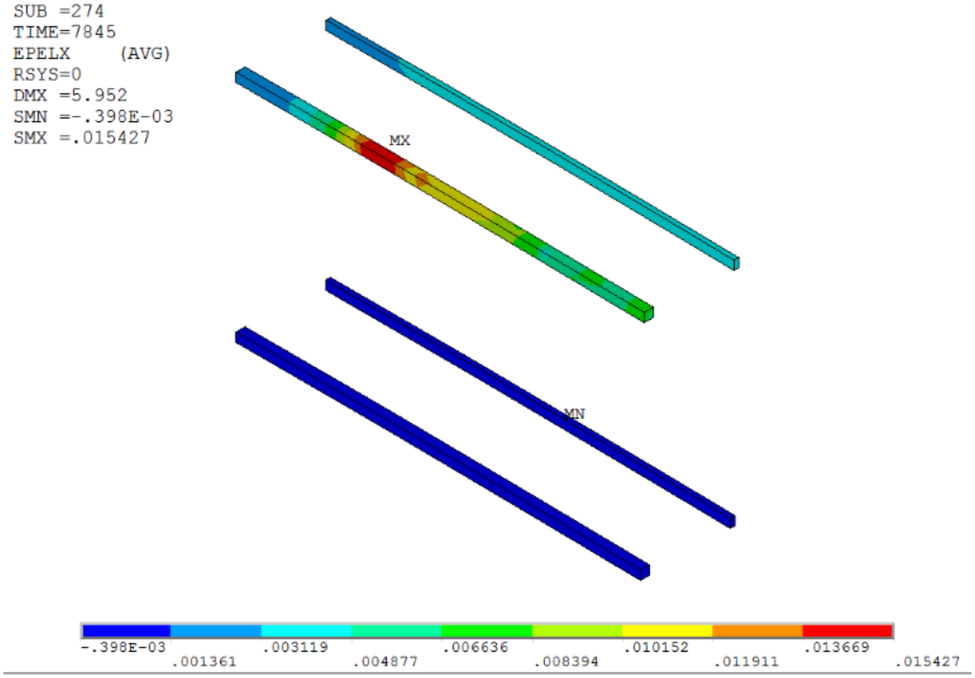

Figure 7 - 32: Strain in the SMA bars at a deflection of 10 mm for (NiTi-BCJ-2)

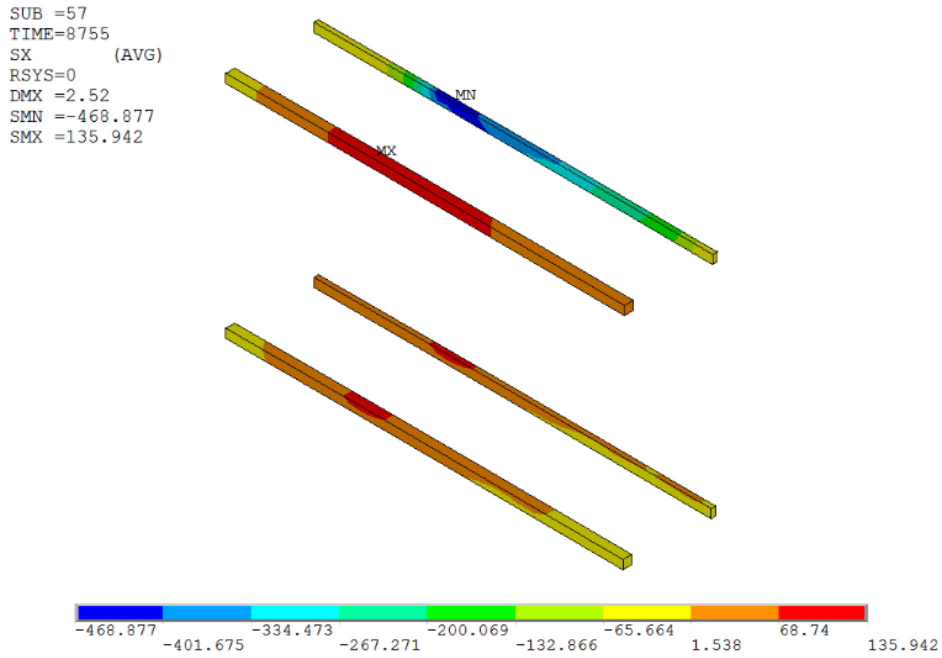

Figure 7 - 33: Stress in the SMA bars at zero loads for (NiTi-BCJ-2)

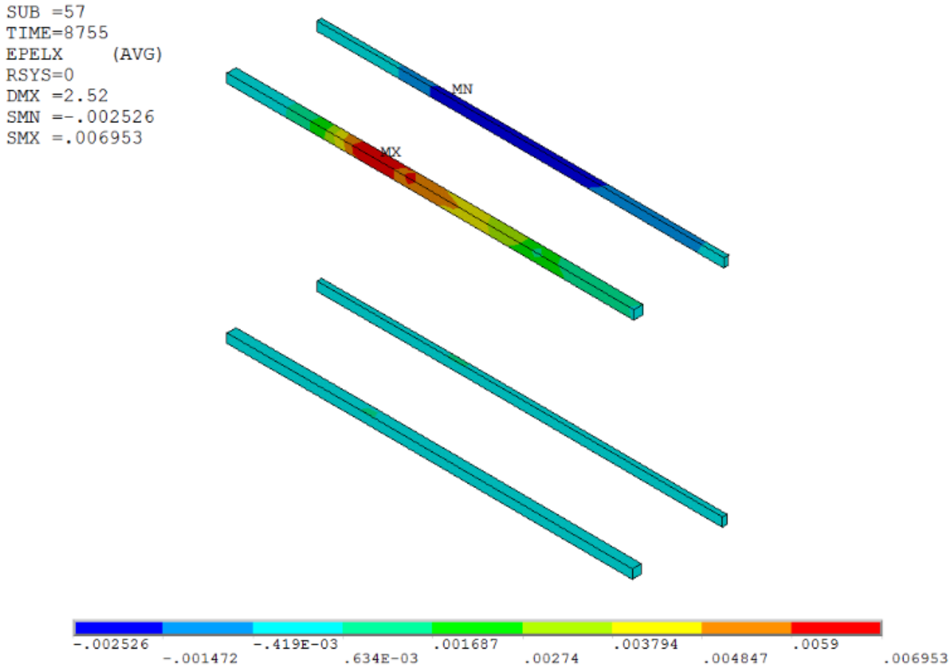

Figure 7 - 34: Strain in the SMA bars at zero loads for (NiTi-BCJ-2)

From previous figures, it can be observed that the stress at the steel bar at a displacement of 10 mm down is (651 MPa) and strain is (0.004 mm/mm) which means that steel bar has yielded. Similarly, SMA bar is shown a stress of (330 MPa) and the strain of (0.015 mm/mm) which means also that SMA bar has yielded as well. However, at zero load, the stress at the steel bar is (-468 MPa) which means that the steel bar at a high compression stress while the stress at the SMA bar at zero load is (135 MPa).

In conclusion, SMA bars tried to return the steel bar to its original shape which indicated by the high value of compression stress in the steel bar but it could not.

7.9 NUMERICAL SIMULATION OF REVERSE CYCLIC TEST FOR SMA - BCJ (NiTi-BCJ-3) SPECIMEN

In this case, since the SMA bars in this specimen are plain bars’ two models have been analyzed one with perfect bonding between SMA bars and the surrounding concrete and one with No bonding between SMA bars and the surrounding concrete.

7.9.1 PERFECT BONDING BETWEEN SHAPE MEMORY ALLOY BARS AND CONCRETE

The finite element simulation and experimental results of load – story drift behavior for SMA - BCJ (NiTi-BCJ-3) – perfect bonding - specimen under reverse cyclic load is illustrated in Figure 7 - 35.

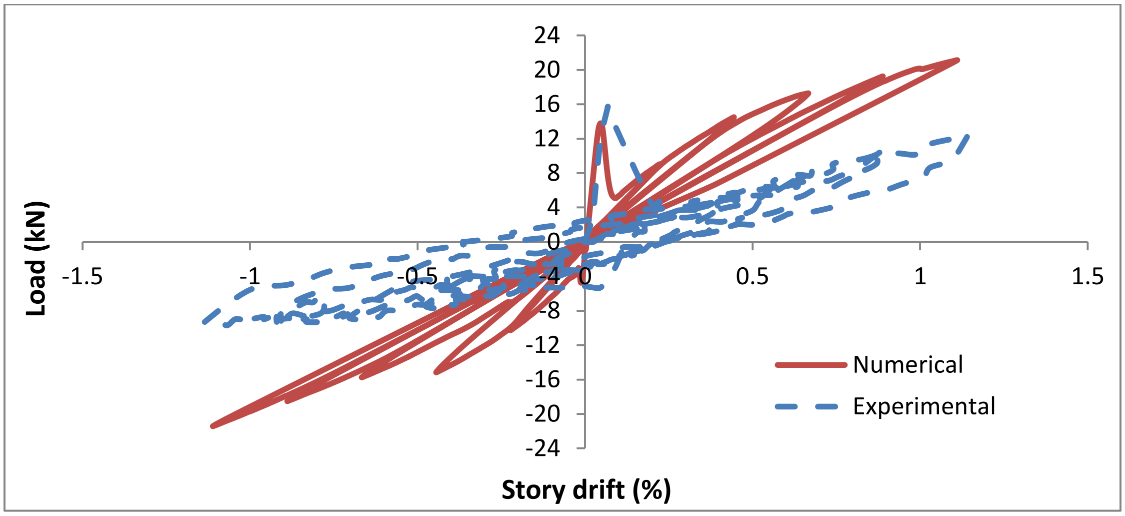

Figure 7 - 35: Load – Story drift curve for (NiTi-BCJ-3) – Perfect Bonding

Due to perfect bonding simulation, the load displacement response shows a higher load capacity compared to the experimental test results. Flexural crack was occurring on the interface of BCJ then it started becoming wider. Figure 7 - 36 shows the development of the flexural crack in finite element simulation.

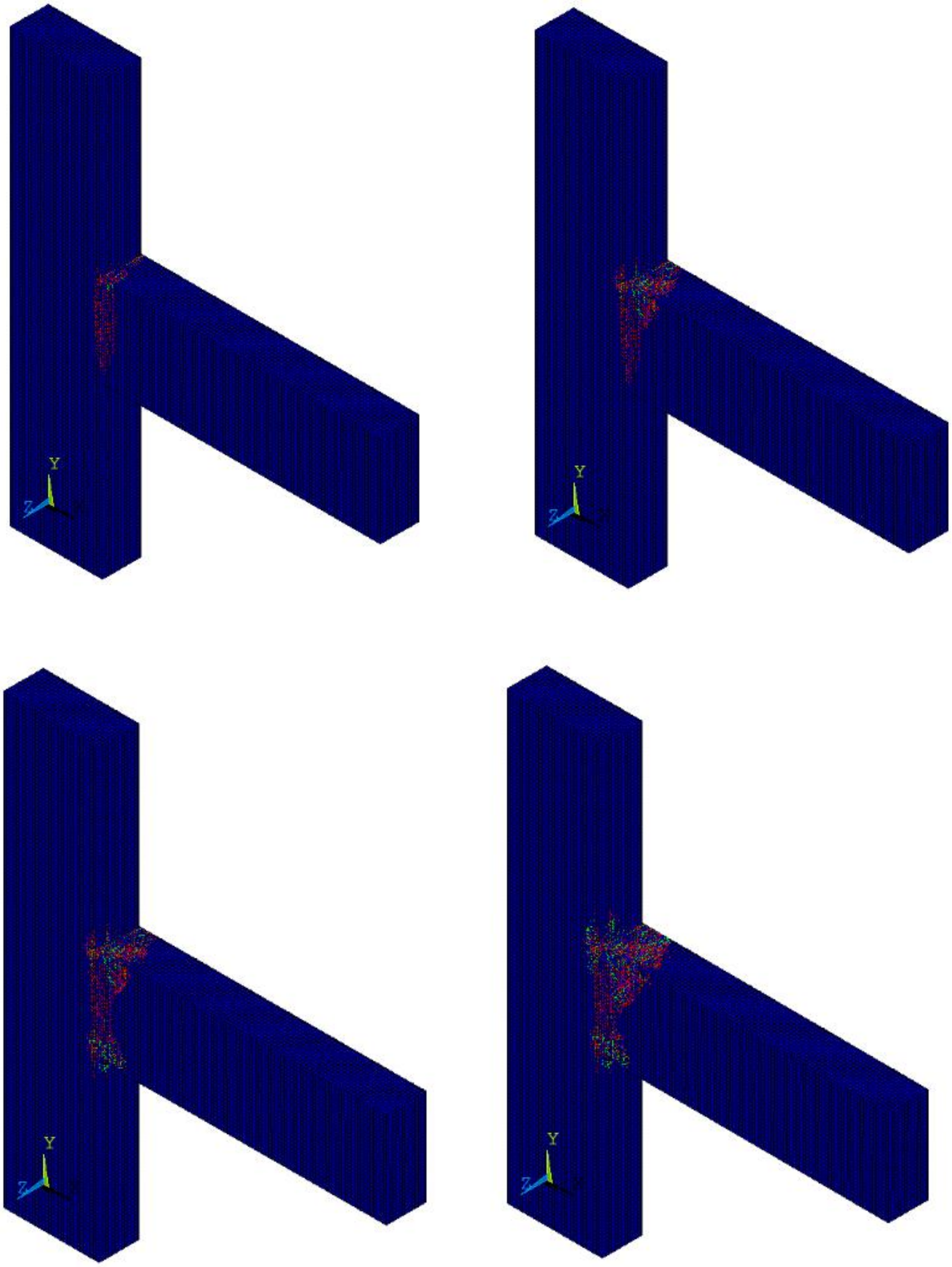

Figure 7 - 36: Development of flexural crack for (NiTi-BCJ-3) – Perfect Bonding

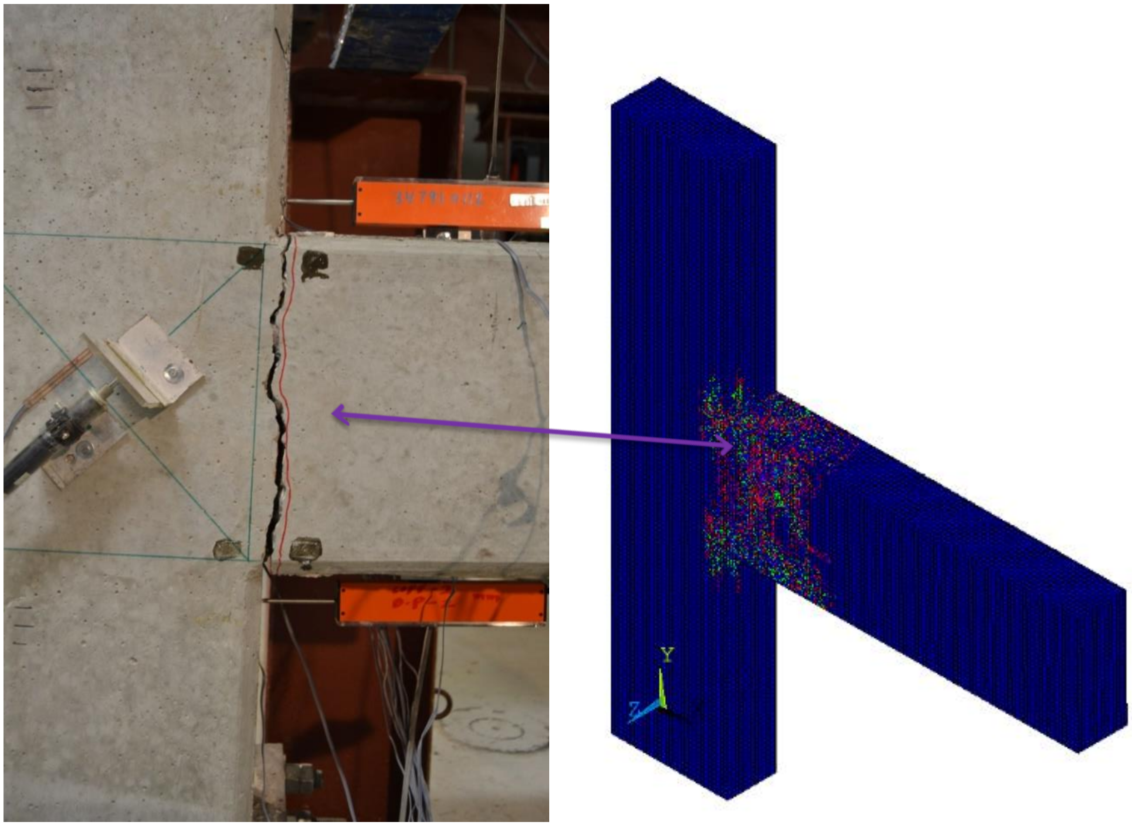

Figure 7 - 37: Location of flexural crack between numerical and experimental results

The simulation shows developments of one main crack at the BCJ interface as illustrated in Figure 7 - 37.

Stresses and strains for top and bottom SMA bars at a deflection of 10 mm down are shown in Figures 7 – 38 & 7 - 39 respectively.

Stresses and strains for top and bottom SMA bars at zero loads are shown in Figures 7 – 40 & 7 - 41 respectively.

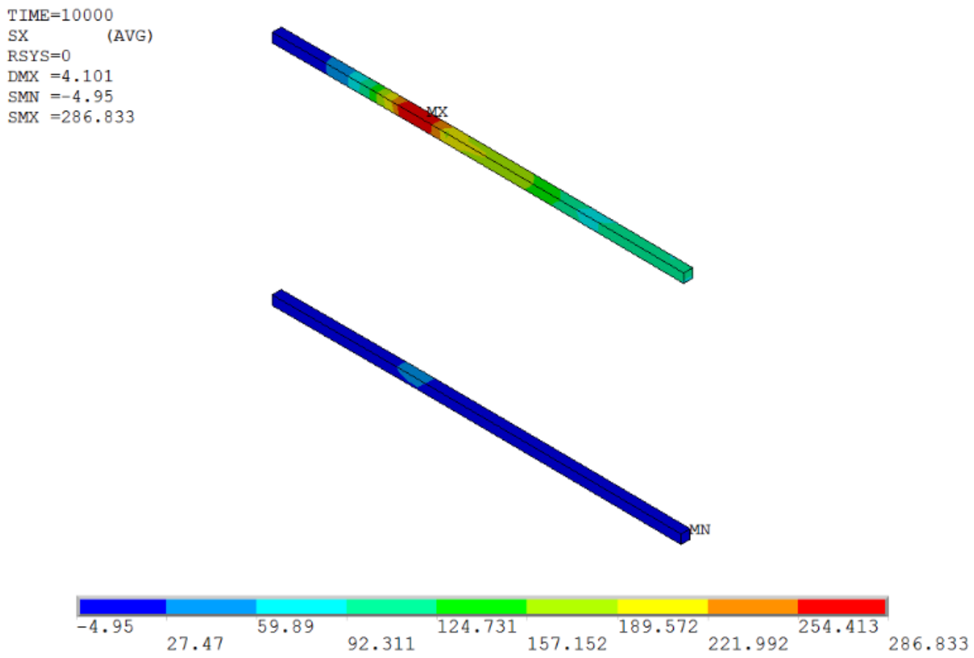

Figure 7 - 38: Stress in bars at 10 mm down for (NiTi-BCJ-3)–Perfect Bonding

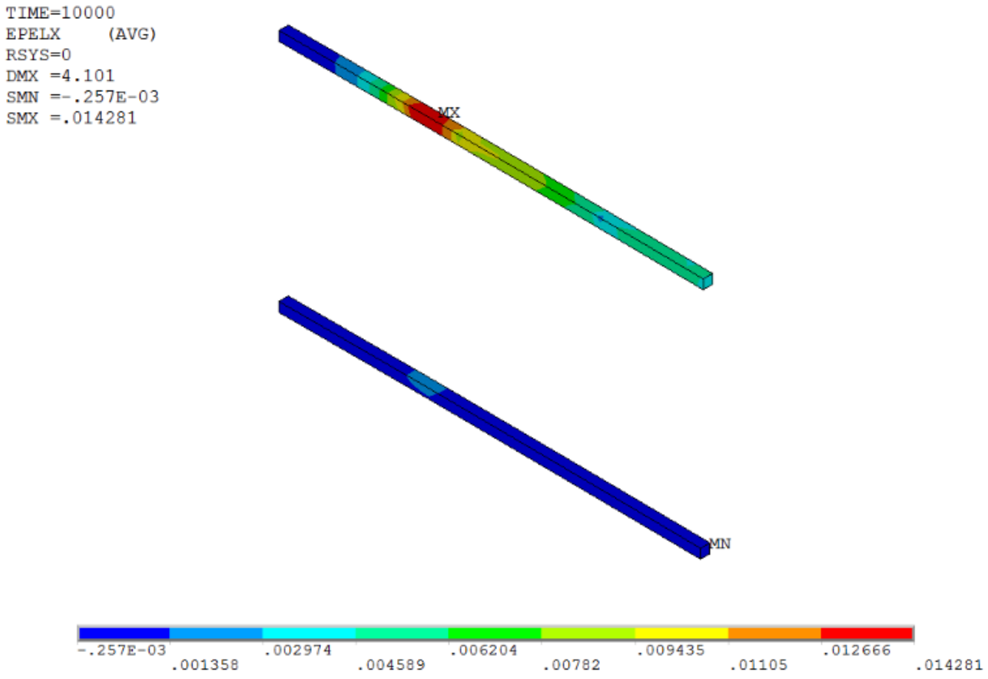

Figure 7 - 39: Strain in bars at 10 mm down for (NiTi-BCJ-3)–Perfect Bonding

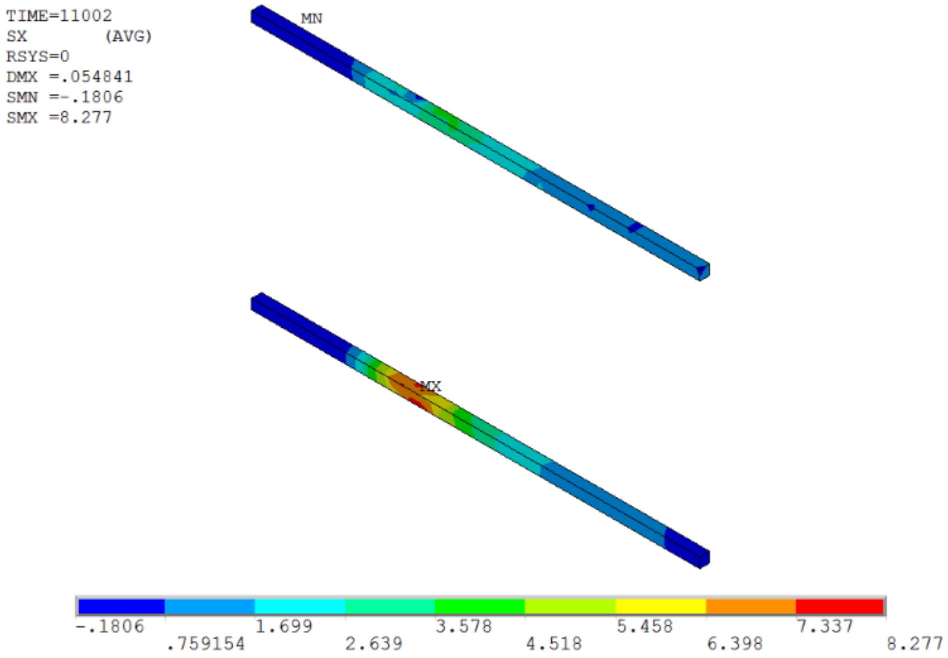

Figure 7 - 40: Stress in bars at zero loads for (NiTi-BCJ-3) – Perfect Bonding

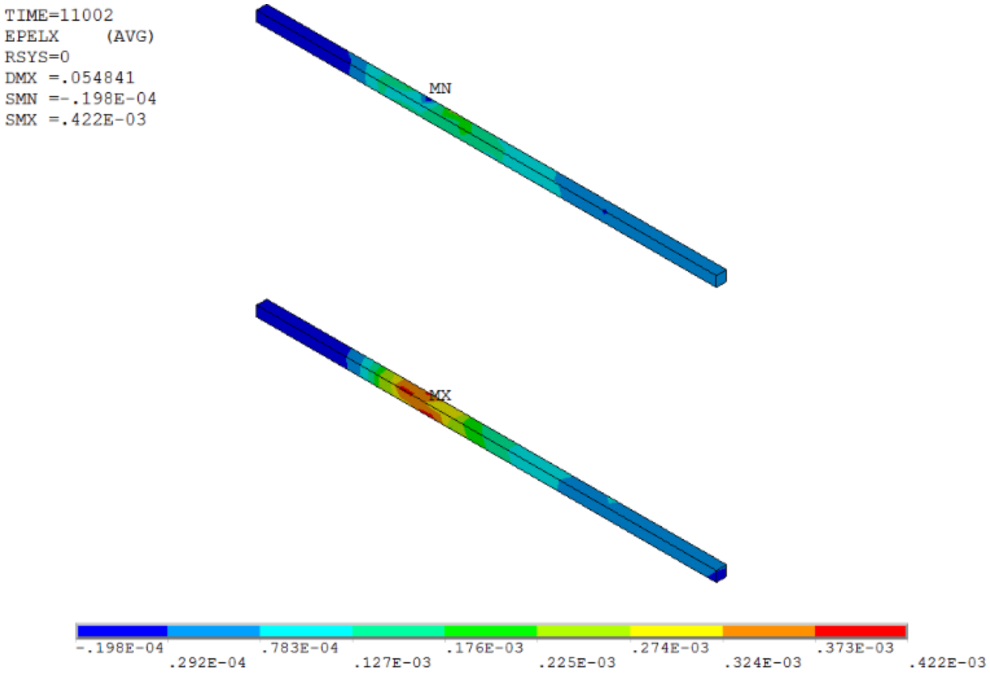

Figure 7 - 41: Strain in bars at zero loads for (NiTi-BCJ-3) – Perfect Bonding

7.9.2 NO BONDING BETWEEN SHAPE MEMORY ALLOY BARS AND CONCRETE

The finite element simulation and experimental results of load – story drift response for SMA - BCJ (NiTi-BCJ-3) – Anchored in the couplers - specimen under reverse cyclic load is shown in Figure 7 - 42.

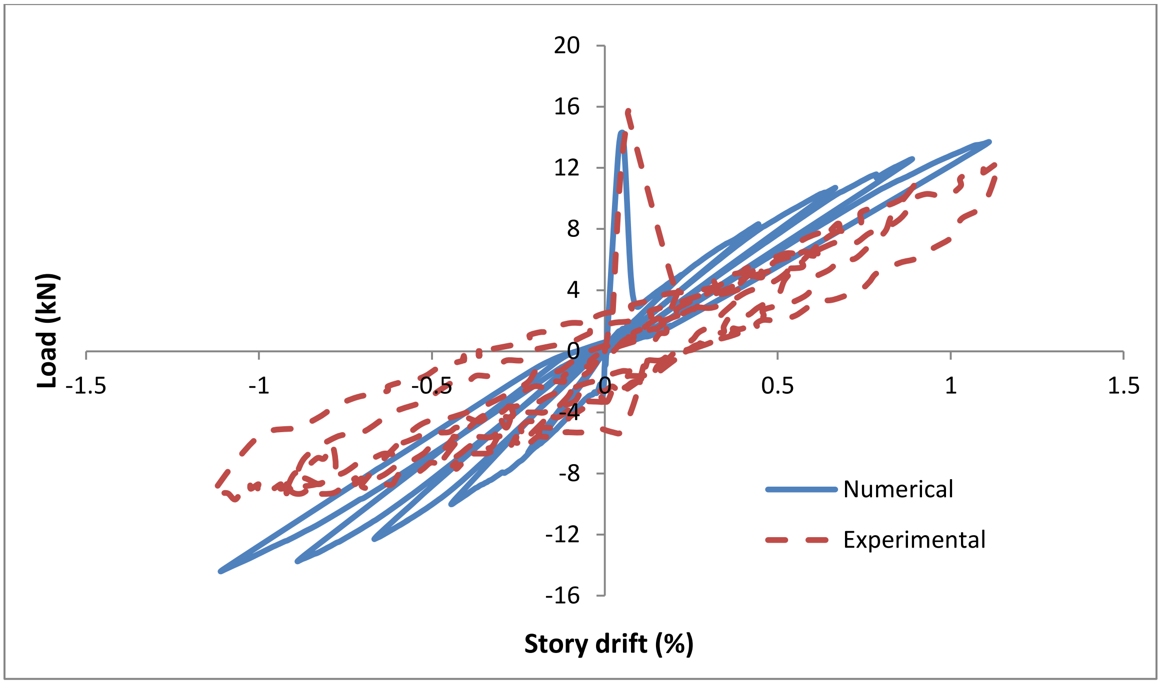

Figure 7 - 42: Load – Story drift curve for (NiTi-BCJ-3) – Anchored in the couplers

Due to releasing the bond, the load displacement response shows good matching between experimental and numerical results. Flexural crack was occurred at the interface of BCJ then it started to become wider. Figure 7 - 43 shows the development of the crack in finite element simulation.

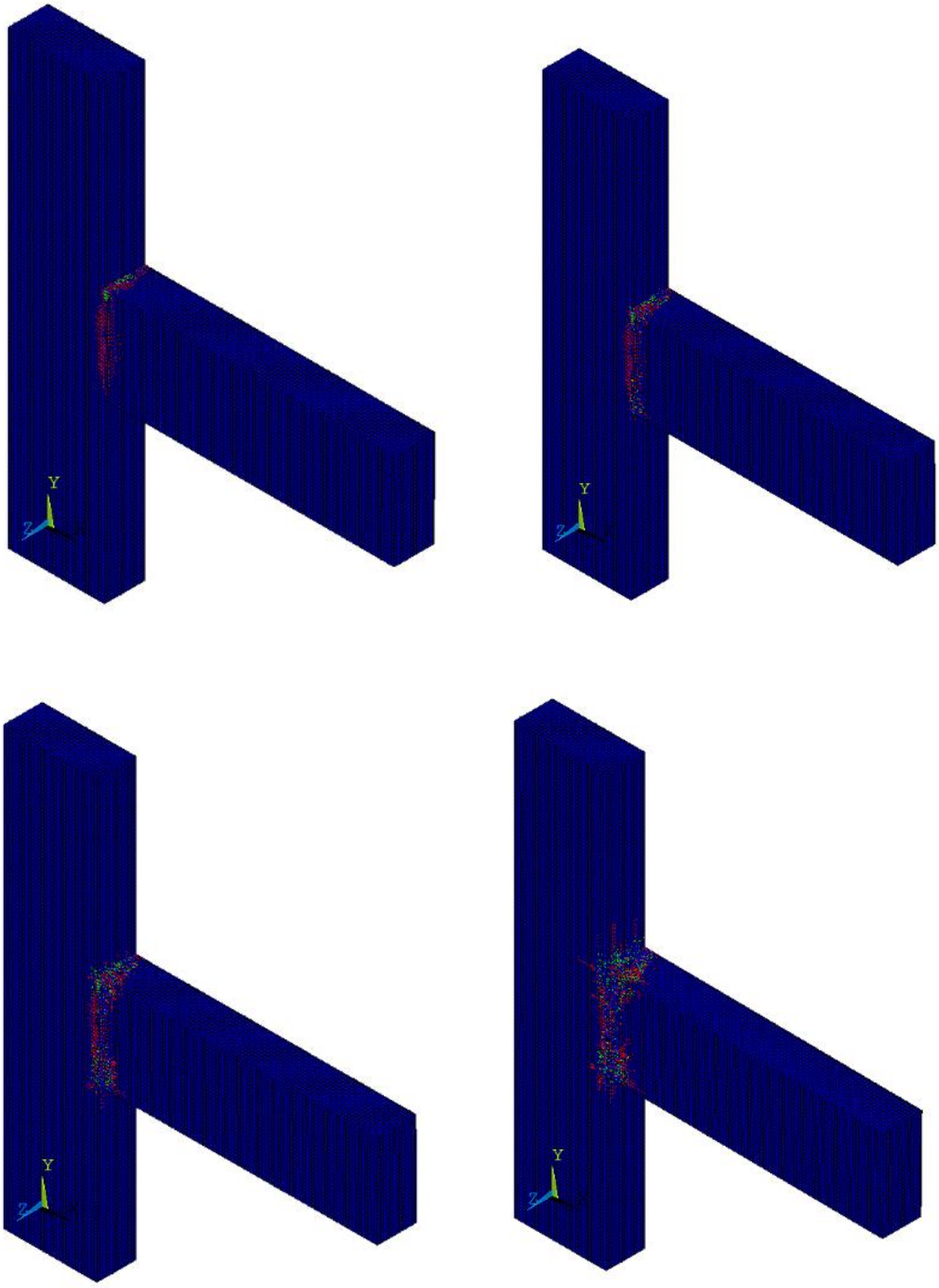

Figure 7 - 43: Development of crack for (NiTi-BCJ-3)–Anchored in the couplers

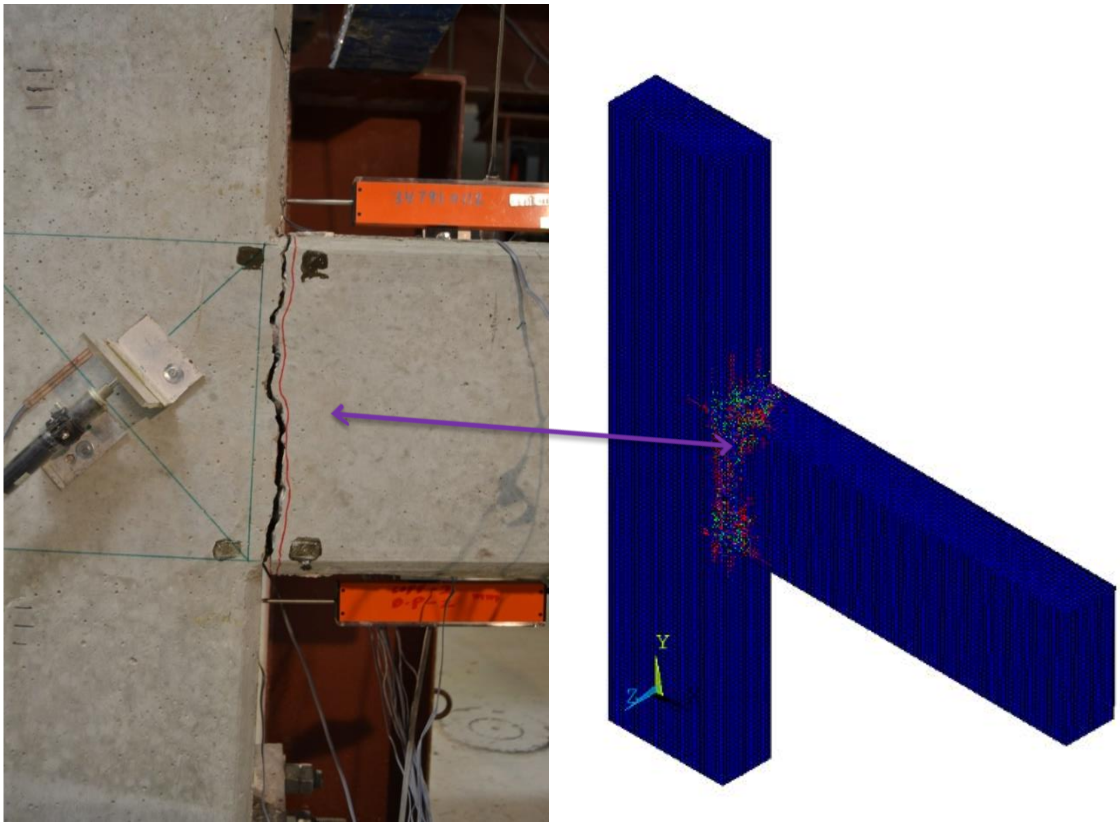

Figure 7 - 44: Location of flexural crack between numerical and experimental results

The simulation shows a development of one major crack at BCJ interface similar to experimental results as illustrated in Figure 7 - 44.

Stresses and strains for top and bottom SMA bars at a deflection of 10 mm down are shown in Figures 7 – 45 & 7 - 46 respectively.

Stresses and strains for top and bottom SMA bars at zero loads are shown in Figures 7 – 47 & 7 - 48 respectively.

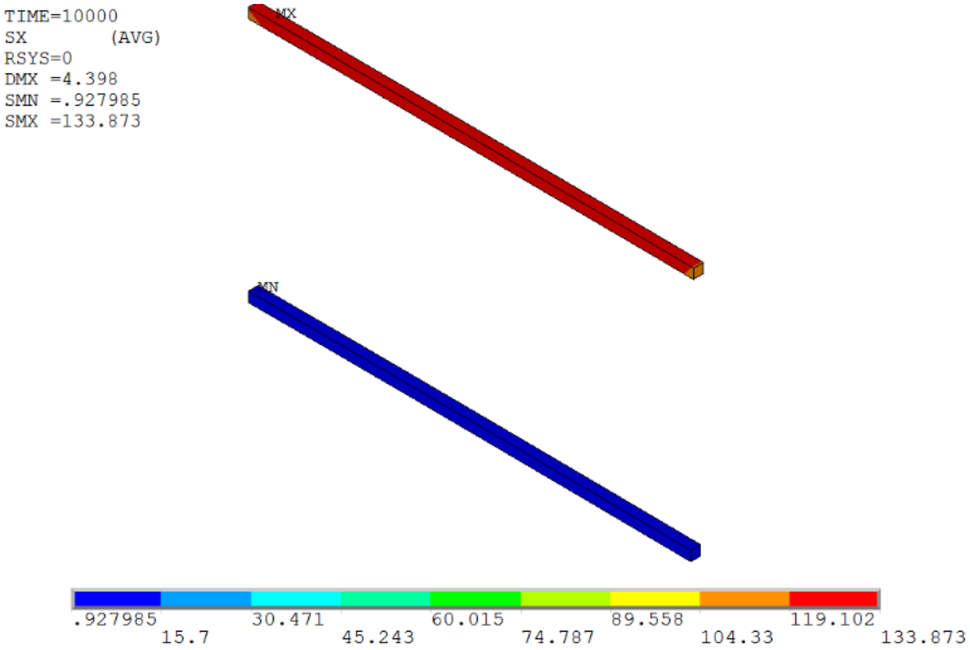

Figure 7 - 45: Stress in bars at 10 mm for (NiTi-BCJ-3)–Anchored in couplers

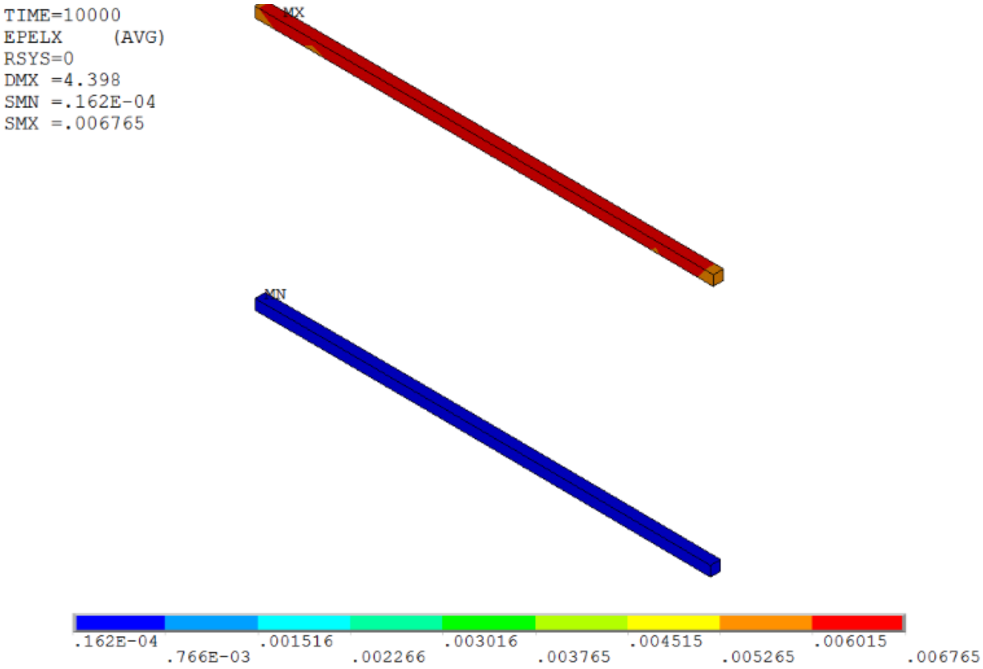

Figure 7 - 46: Strain in bars at 10 mm for (NiTi-BCJ-3 –Anchored in couplers

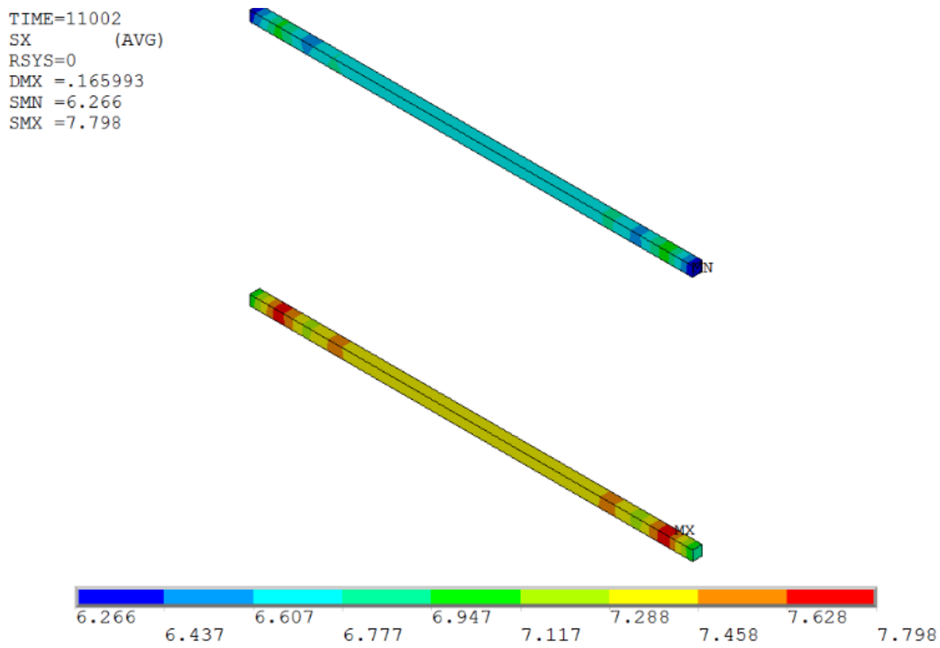

Figure 7 - 47: Stress in bars at zero loads for (NiTi-BCJ-3)–Anchored in couplers

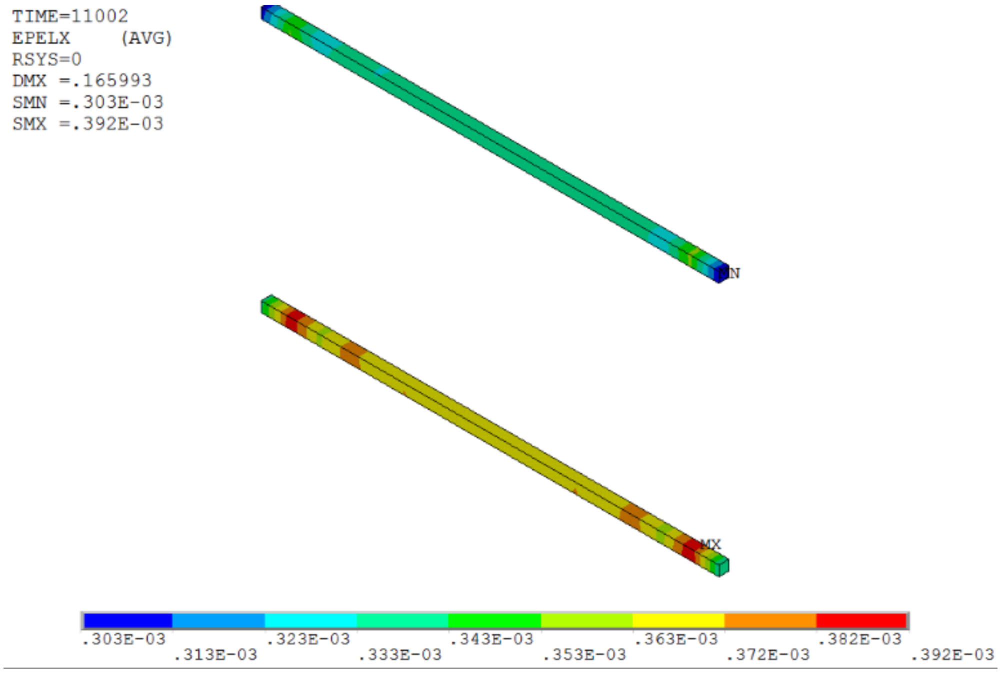

Figure 7 - 48: Strain in bars at zero loads for (NiTi-BCJ-3)–Anchored in couplers

From previous figures and for the perfect bonding case, Stress at SMA bars at a displacement of 10 mm is (286 MPa) which means that SMA bar has yielded. While for Anchored in the couplers case, the stress at the same displacement is too much less (133 MPa) which shows the effect of the bond between concrete and SMA bars. However, at zero loads and for both cases, stresses returned back almost to zero.

7.10 NUMERICAL SIMULATION OF REVERSE CYCLIC TEST FOR SMA - BCJ (NiTi-BCJ-4) SPECIMEN

In this case, since the SMA bars in this specimen are plain bars' two models have been analyzed one with perfect bonding between SMA bars and the surrounding concrete and one with No bonding between SMA bars and the surrounding concrete.

7.10.1 PERFECT BONDING BETWEEN SHAPE MEMORY ALLOY BARS AND CONCRETE

The finite element simulation and experimental results of load – story drift behavior for SMA - BCJ (NiTi-BCJ-4) – Perfect Bonding - specimen under reverse cyclic load is illustrated in Figure 7 - 49.

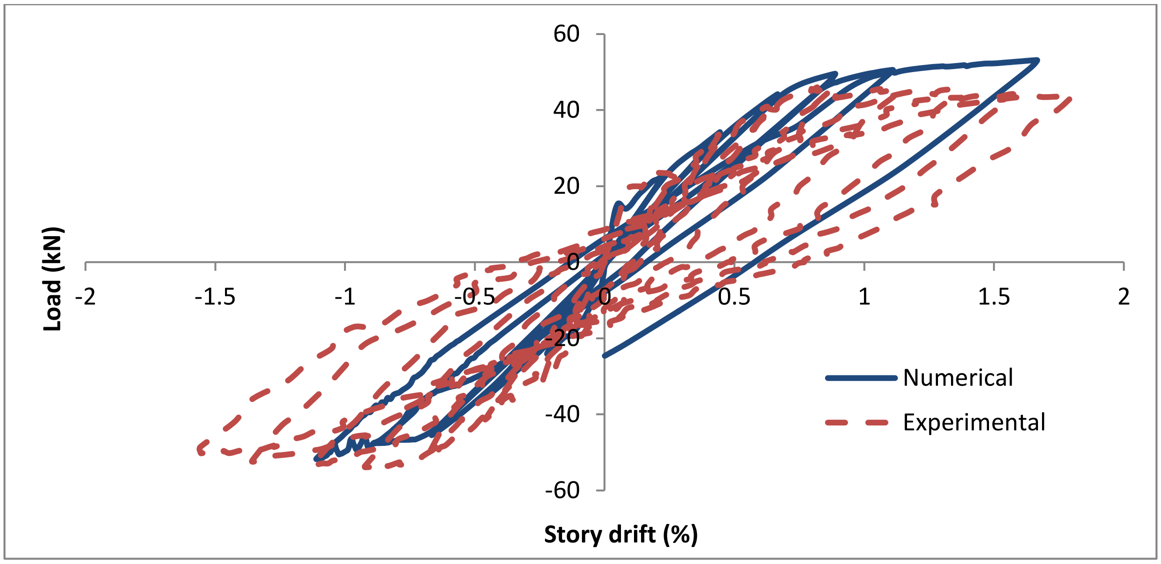

Figure 7 - 49: Load – Story drift curve for (NiTi-BCJ-4) – Perfect Bonding

Due to perfect bonding simulation, the load displacement response shows a little bit higher load capacity compared to the experimental test results. Flexural cracks were occurred at BCJ interface and beam surface. Figure 7 - 50 illustrates the development of the cracks in finite element simulation.

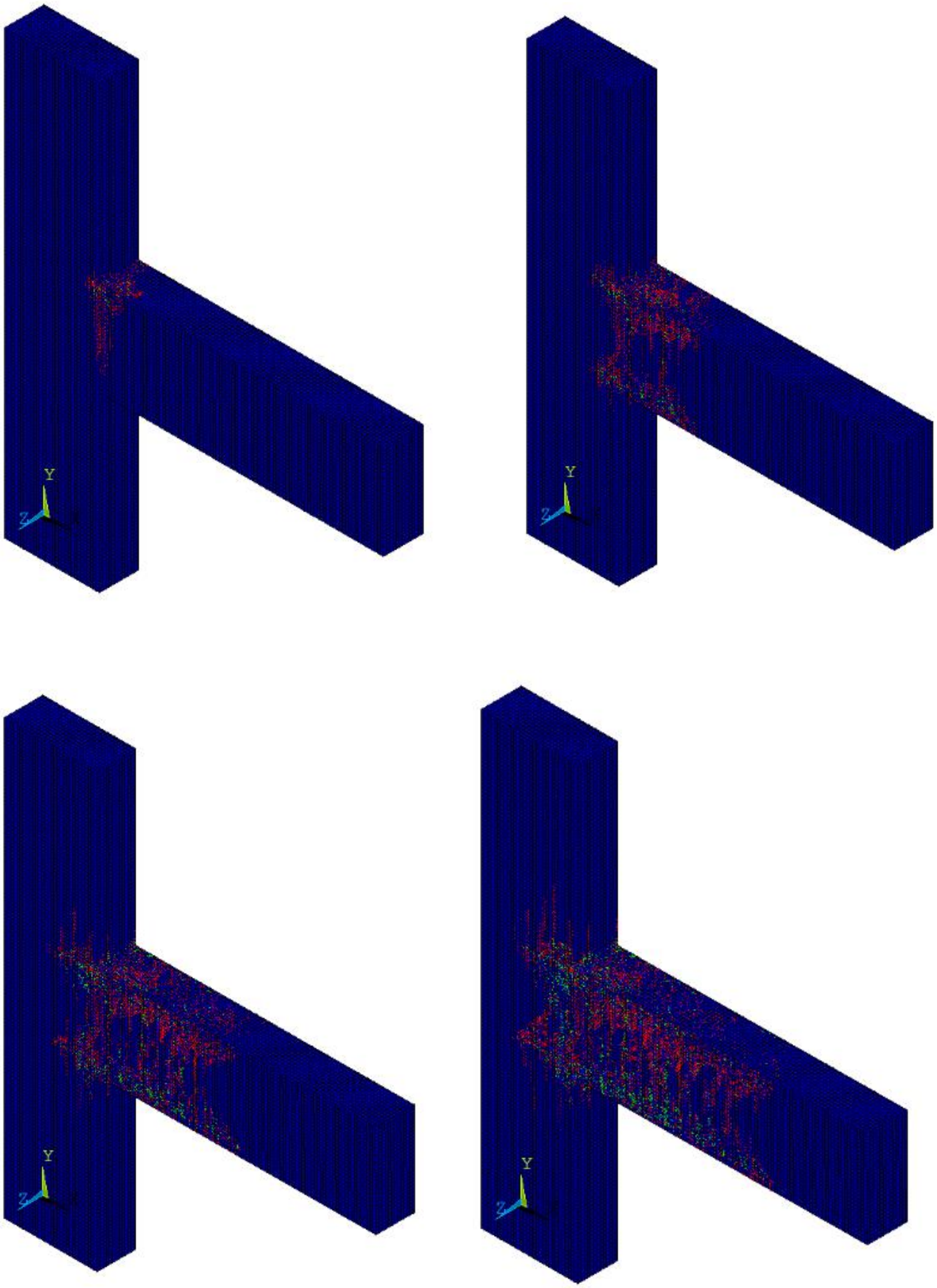

Figure 7 - 50: Development of flexural crack for (NiTi-BCJ-4) – Perfect Bonding

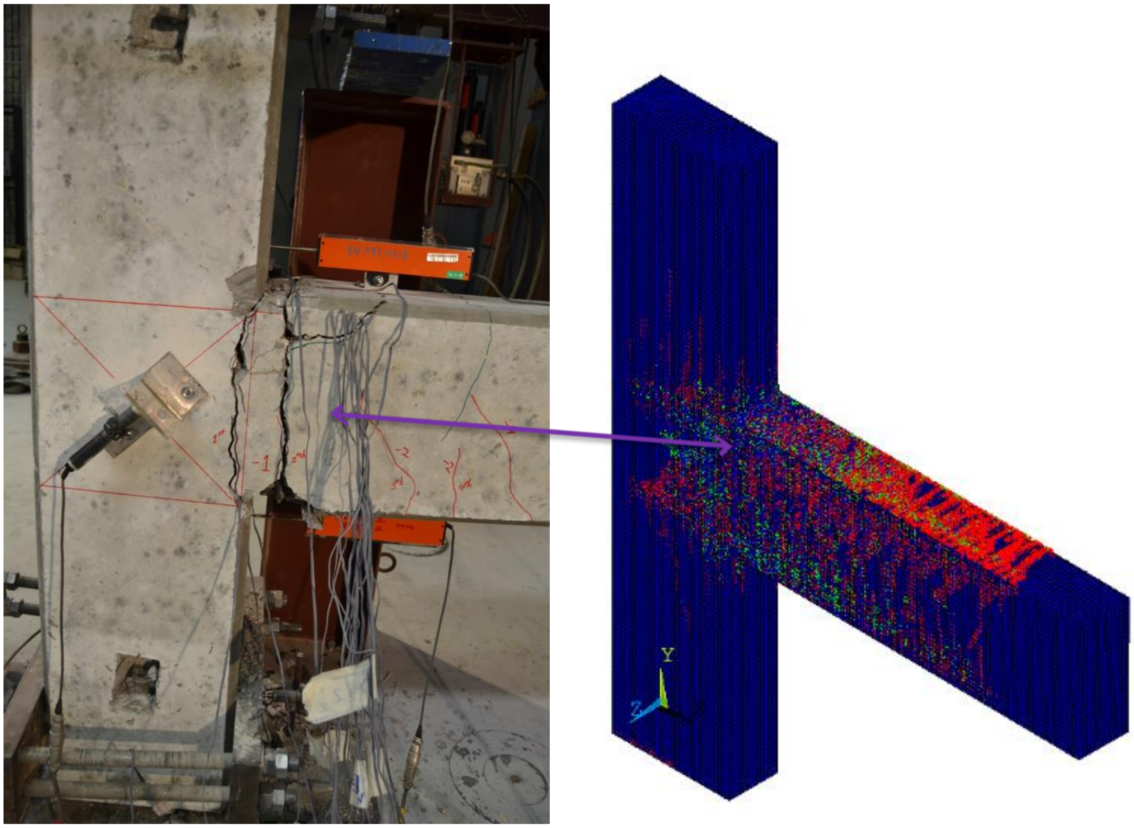

Figure 7 - 51: Location of flexural crack between numerical and experimental results

The simulation shows a development of more than one crack in the beam column interface similar to the experiment results as shown in Figure 7 - 51.

Stresses and strains for top and bottom SMA bars at a deflection of 10 mm down are shown in Figures 7 – 52 & 7 - 53 respectively.

Stresses and strains for top and bottom SMA bars at zero loads are shown in Figures 7 – 54 & 7 - 55 respectively.

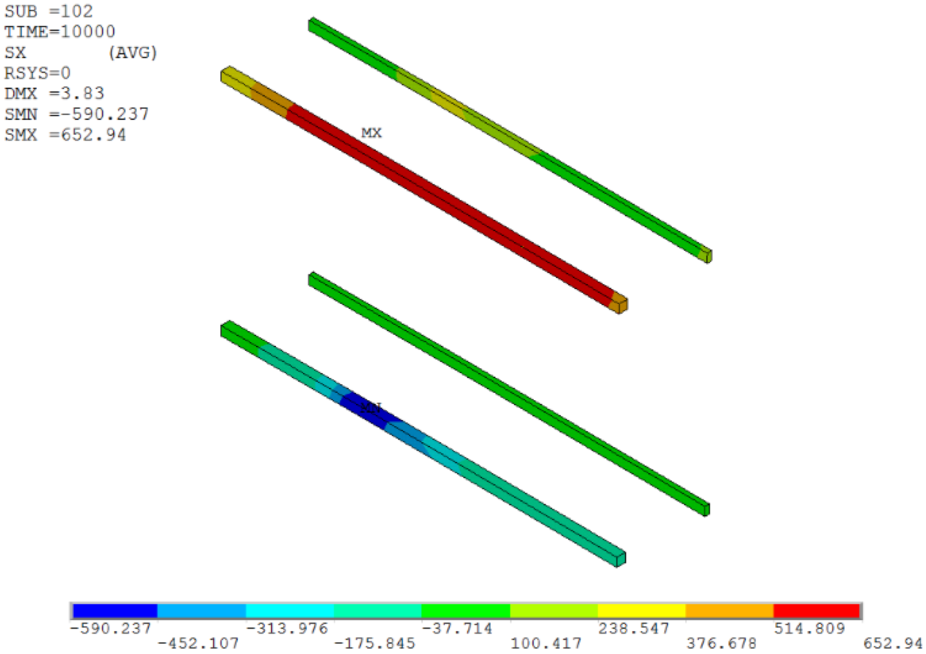

Figure 7 - 52: Stress in bars at 10 mm down for (NiTi-BCJ-4)–Perfect Bonding

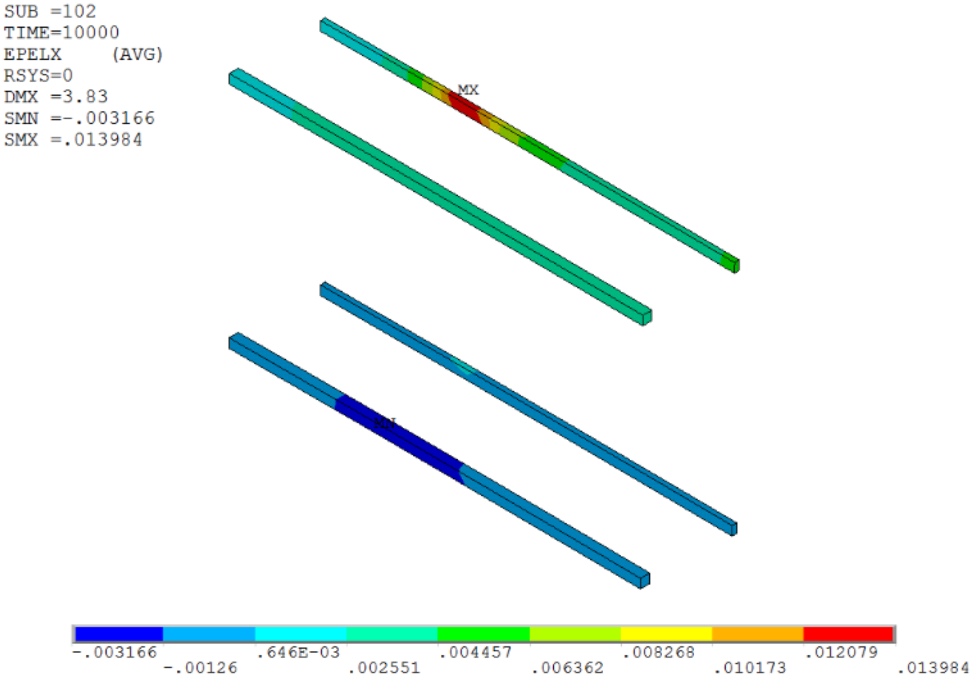

Figure 7 - 53: Strain in bars at 10 mm down for (NiTi-BCJ-4 –Perfect Bonding

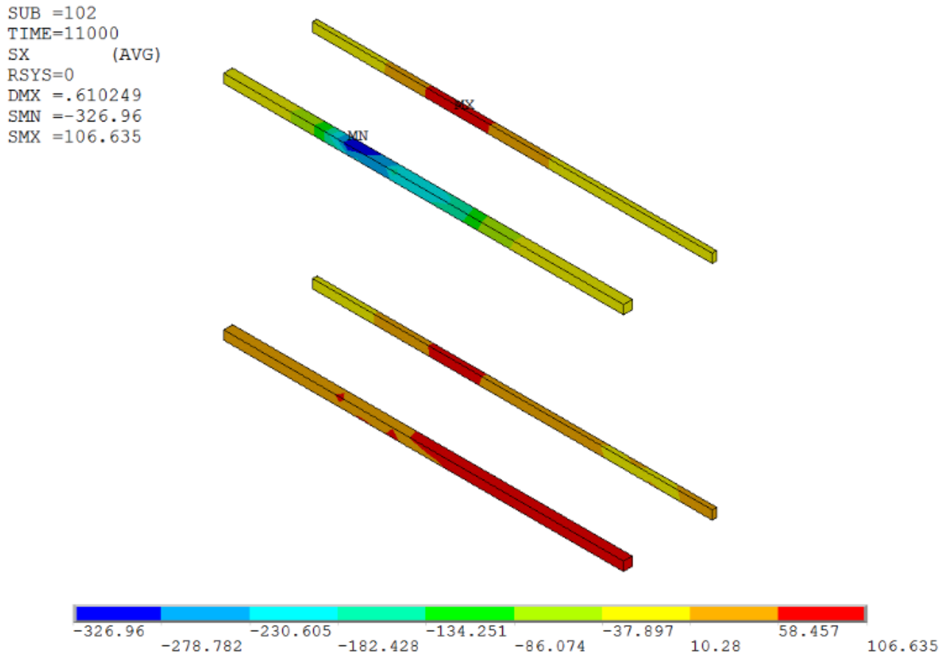

Figure 7 - 54: Stress in bars at zero loads for (NiTi-BCJ-4) – Perfect Bonding

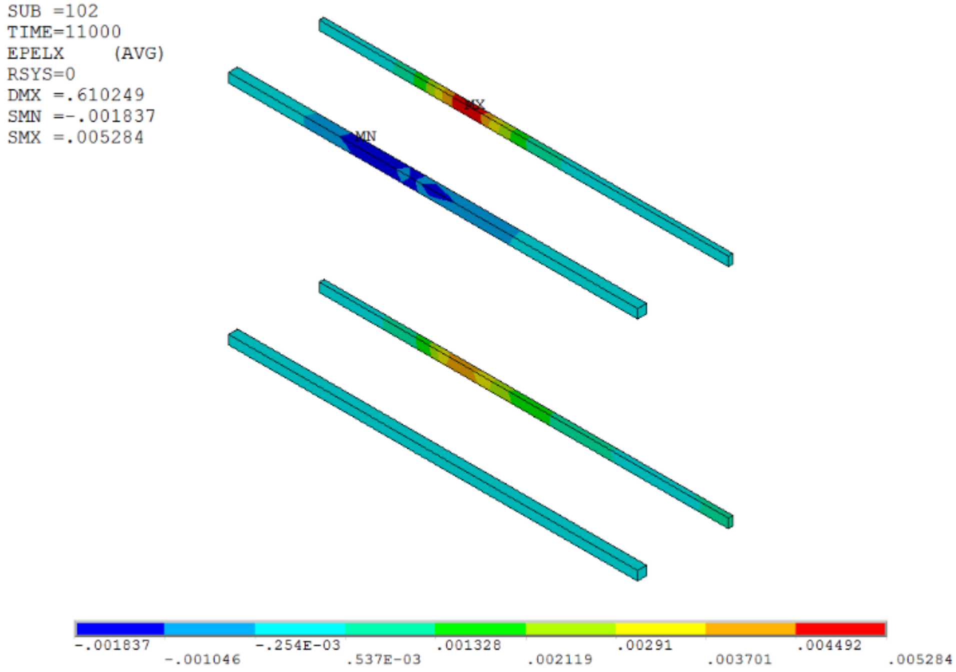

Figure 7 - 55: Strain in bars at zero loads for (NiTi-BCJ-4) – Perfect Bonding

7.10.2 NO BONDING BETWEEN SHAPE MEMORY ALLOY BARS AND CONCRETE

The finite element simulation and experimental results of the load – story drift response for SMA - BCJ (NiTi-BCJ-3) – Anchored in the couplers - specimen under reverse cyclic load is illustrated in Figure 7 - 56.

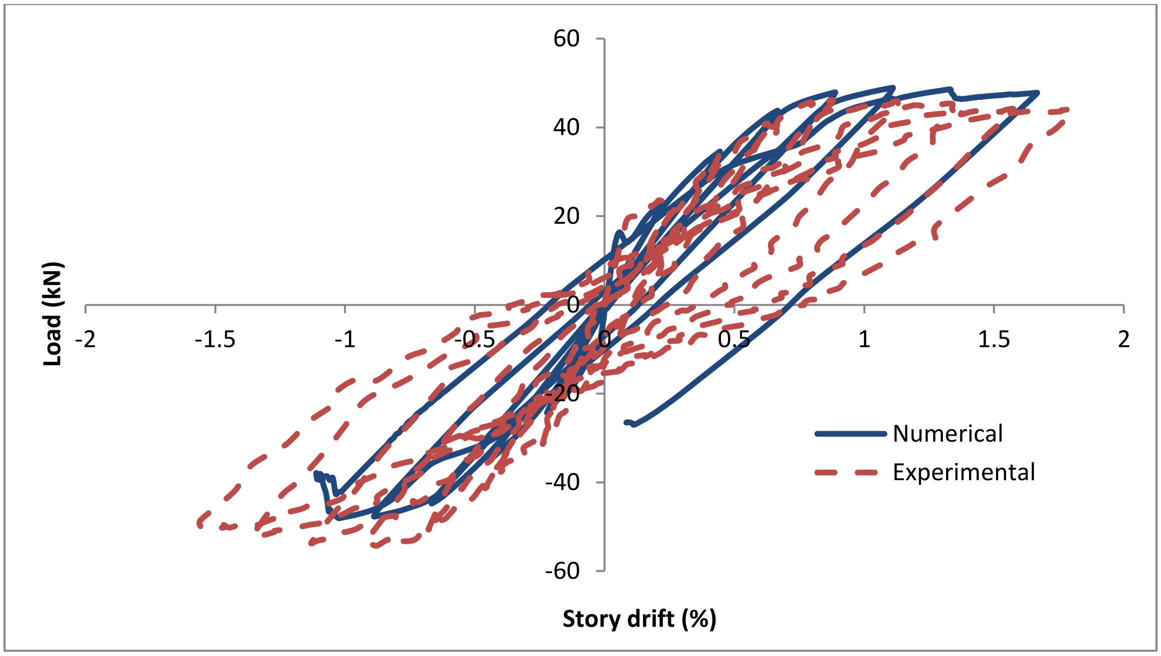

Figure 7 - 56: Load – Story drift curve for (NiTi-BCJ-4) – Anchored in the couplers

Due to releasing the bond, the load displacement response shows good matching between experimental and numerical results. Flexural cracks were occurred at the interface of BCJ and beam faces. Figure 7 - 57 illustrates the development of the cracks in finite element simulation.

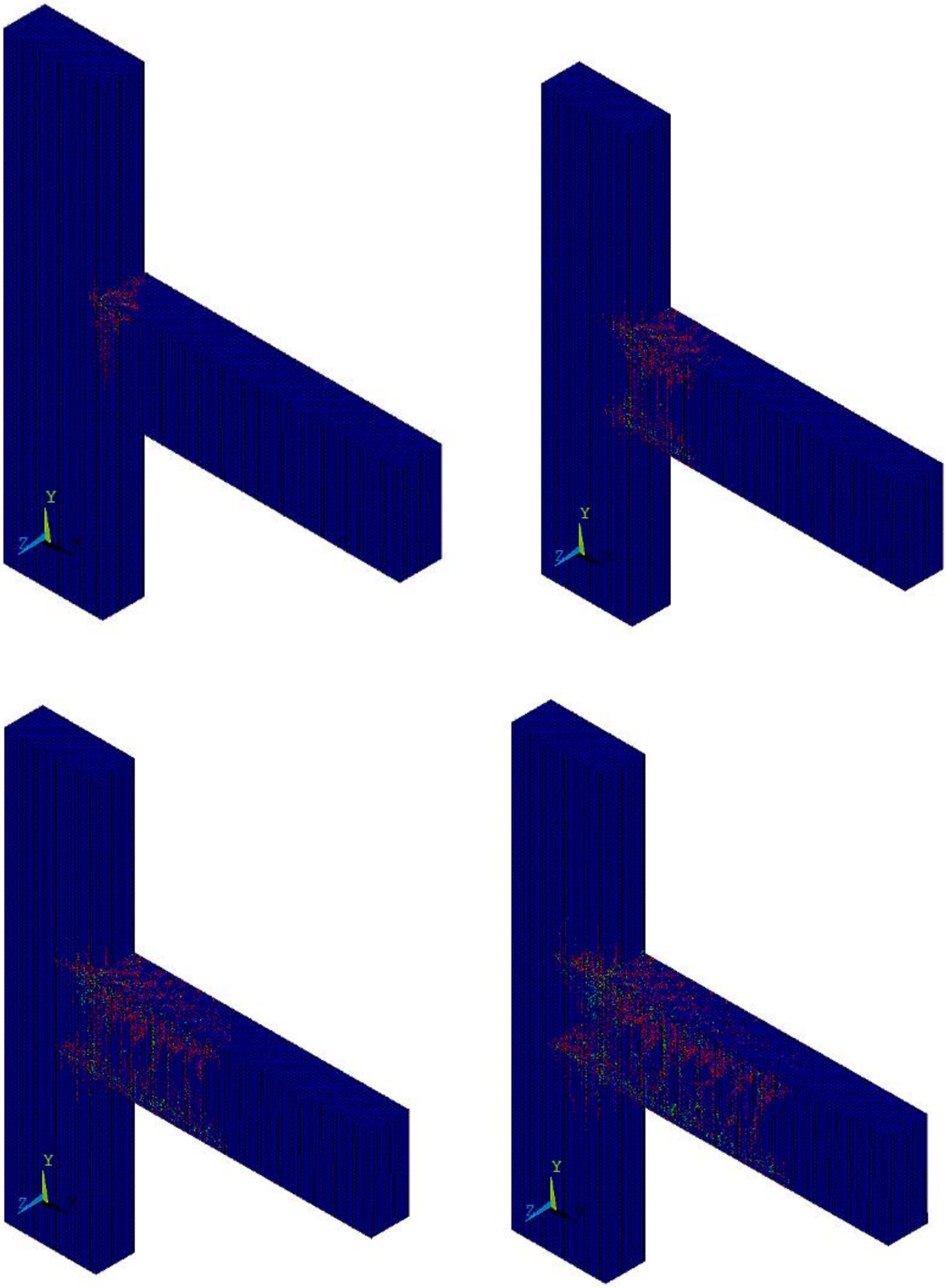

Figure 7 - 57: Development of cracks for (NiTi-BCJ-4) – Anchored in the couplers

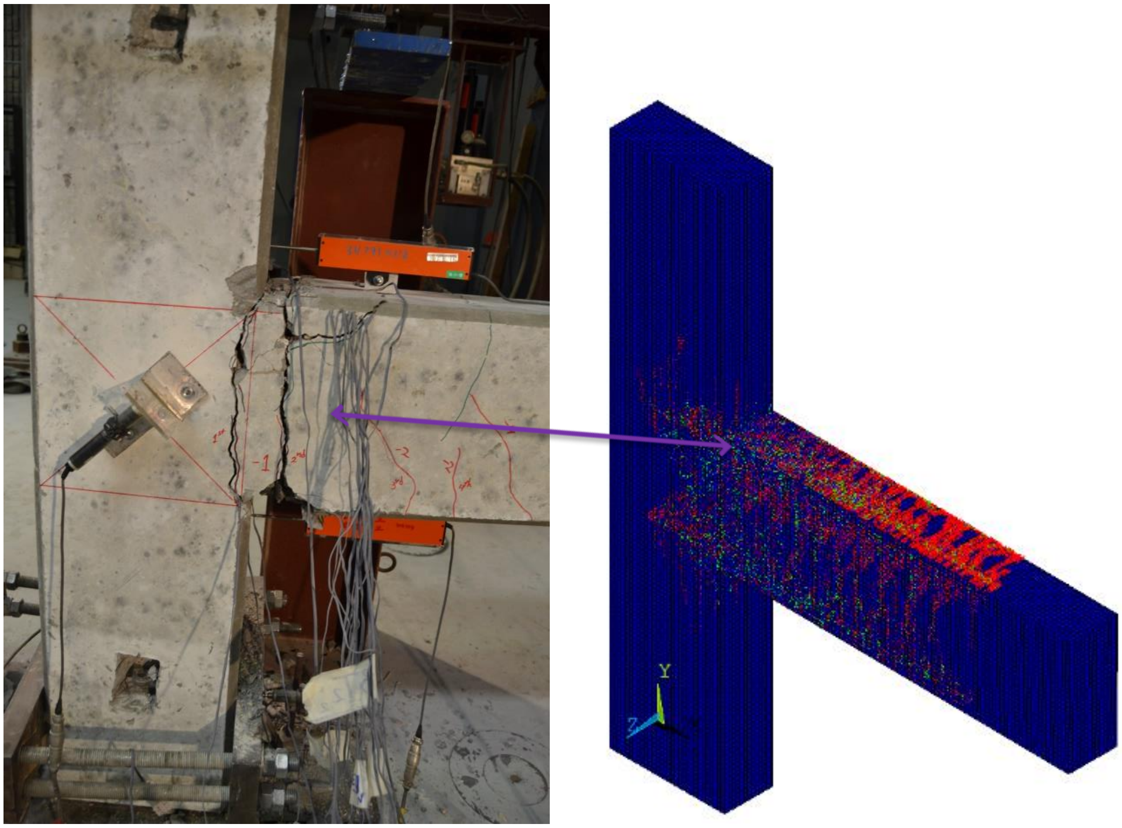

Figure 7 - 58: Location of flexural crack between numerical and experimental results

The simulation shows a development of one major crack at BCJ interface similar to experimental results as illustrated in Figure 7 - 58.

Stresses and strains for top and bottom SMA bars at a deflection of 10 mm down are shown in Figures 7 – 59 & 7 - 60 respectively.

Stresses and strains for top and bottom SMA bars at zero loads are shown in Figures 7 – 61 & 7 - 62 respectively.

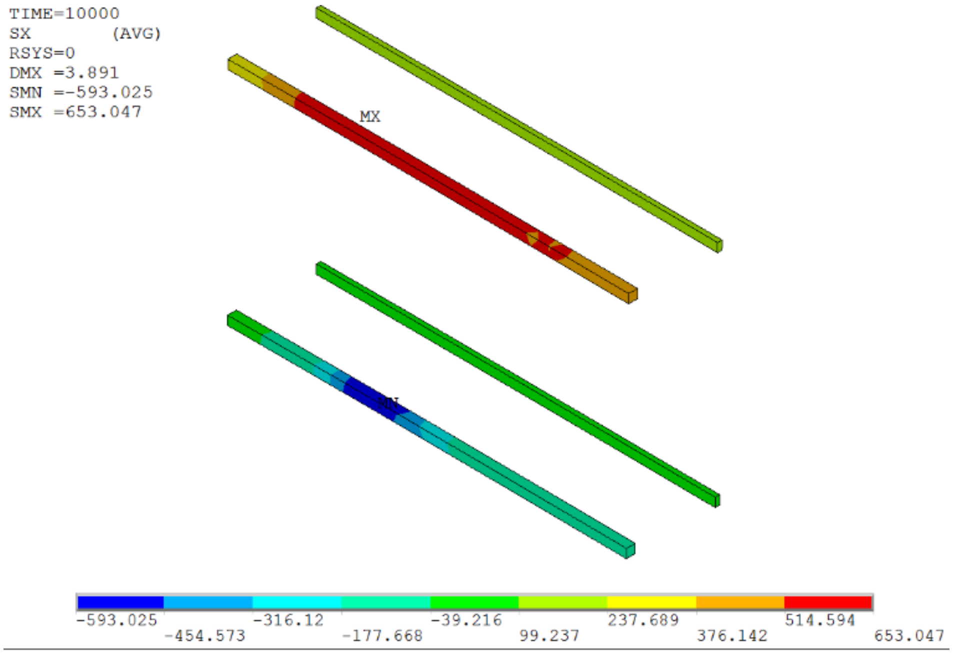

Figure 7 - 59: Stress in bars at 10 mm for (NiTi-BCJ-4)–Anchored in couplers

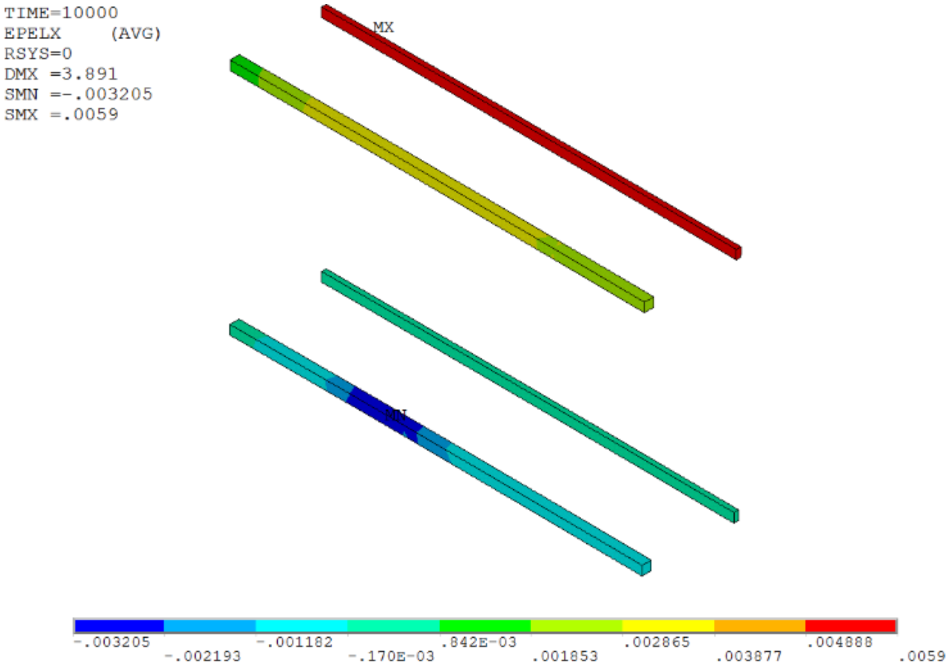

Figure 7 - 60: Strain in bars at 10 mm for (NiTi-BCJ-4)–Anchored in couplers

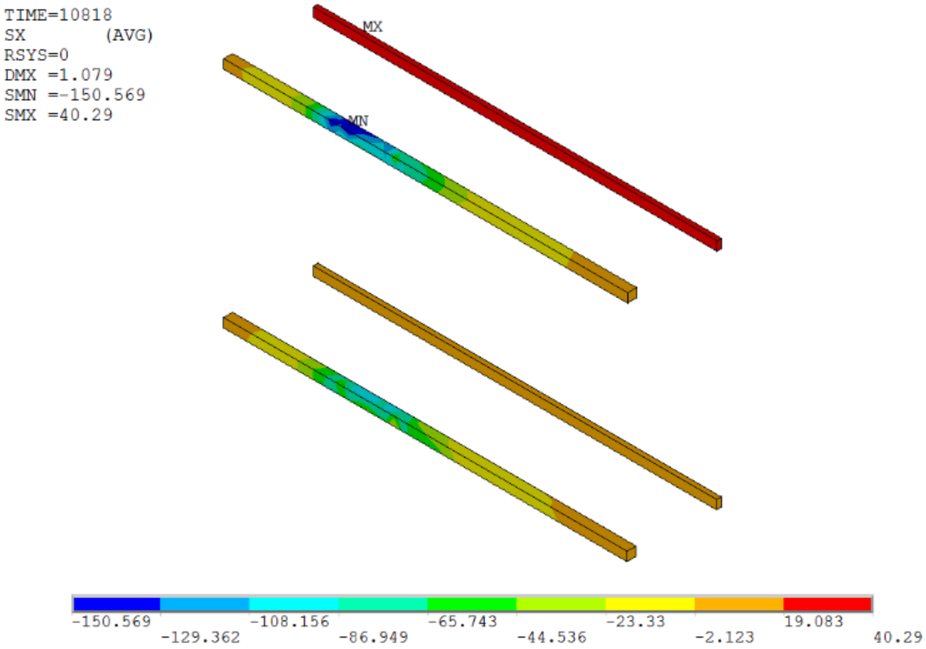

Figure 7 - 61: Stress in bars at zero loads for (NiTi-BCJ-4)–Anchored in couplers

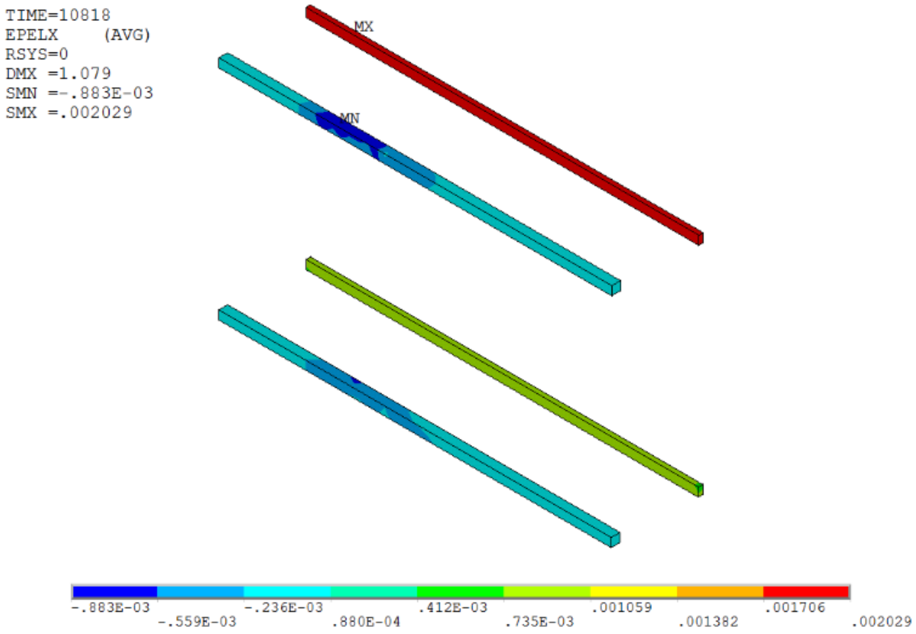

Figure 7 - 62: Strain in bars at zero loads for (NiTi-BCJ-4)–Anchored in couplers

From previous figures and for perfect bonding case, it can be observed that the stress at the steel bar at a displacement of 10 mm down is (653 MPa) and strain is (0.004 mm/mm) which means that steel bar has yielded. Similarly, SMA bar is shown a stress of (300 MPa) and strain of (0.014 mm/mm) which means also that SMA bar has yielded as well. However, at zero loads, the stress at the steel bar is (-327 MPa) which means that the steel bar at a high compression stress while the stress at the SMA bar at zero load is (106 MPa).

On the other hand and for Anchored in the couplers case, it can be observed that the stress in the steel bar at a displacement of 10 mm down is (653 MPa) and strain is (0.004 mm/mm) which means that steel bar has yielded the same like perfect bonding case. Nevertheless, SMA bar is shown a stress of (150 MPa) and strain of (0.006 mm/mm) at the same displacement which means that SMA bar has not yielded yet. However, at zero loads, the stress at the steel bar is (-150 MPa) which means that the steel bar is at a high compression stress while the stress at the SMA bar at zero load is (40 MPa) only.

In conclusion and for both perfect bonding and Anchored in the couplers cases, SMA bar tried to return back the steel bars to their original shapes which indicated by the high value of compression stress in the steel bars but it could not due to high modulus of elasticity of steel.

CHAPTER 8

CONCLUSIONS AND RECOMMENDATIONS

8.1 CONCLUSIONS

Based on experimental investigation, which has been carried out for Control and SMA - BCJ specimens at KFUPM and Numerical simulation of BCJ using the ANSYS program, following conclusions may be drawn:

1. BCJ specimen with ribbed and trained SMA bars shows excellent results in terms of crack recovery, residual displacement, and load capacity.
2. BCJ specimen with plain and trained SMA bars shows some crack recovery and residual displacement initially, but after the loss of bond between SMA bars and surrounding concrete, the plain SMA bars show no crack recovery.
3. BCJ hybrid steel and SMA reinforced specimens with trained and both ribbed and plain SMA bars could not give a good crack recovery because after yielding of steel bars, the SMA bars were not able to return it back to the original shape due to high modulus of elasticity of steel bars.
4. The finite element simulation of SMA reinforced BCJ using SMA constitutive model implemented in ANSYS shows a good matching in terms of ultimate load, cracks development, pre and post yielding stiffness, and the hysteretic response observed in the experiment.

5. Finite Element Simulation of BCJ in ANSYS was a big challenge due to a huge number of elements and very small time increments for analyzing – more than one TB for each model.
6. SMA bars should be trained and it is observed that it should be ribbed before using in the structural elements to achieve the full potential of SMA.
7. Given the high initial cost of the material, the use of SMA bars in RC structures should be limited to critical regions of plastic hinge only, with the minimum required amount for closing cracks and avoiding failure of the elements due to slenderness or buckling collapse.
8. The SMA bars can be used to mitigate the earthquake risk due to their high-energy dissipation capability and thereby reduce cost repair after a major earthquake.
9. Mechanical couplers required for coupling the SMA and steel bars should be injected with very high strength epoxy and located at an adequate distance from the critical sections.
10. The usage of SMA bars with low modulus of elasticity (used in this research) is not recommended in RC structures. Good quality SMA bars with high modulus of elasticity at least not less than one-third of that for steel should be used.

8.2 RECOMMENDATIONS FOR FUTURE WORK

1. Experimental investigation of hybrid systems with a combination of SMA and FRP bars having the similar modulus of elasticity should be investigated.
2. This research can be extended to include high quality of superelastic SMA bars with a higher modulus of elasticity.
3. Special strain gauges need to be used for measurements of strains for SMA bars, as the conventional strain gauges were unable to capture the large strains in SMA's.
4. Investigate the behavior of internal and corner BCJs reinforced with embedded SMA bars.
5. Investigate the behavior of using SMA material in different reinforced concrete structures such as slabs, walls, and columns.

REFERENCES

1. Abdulridha, A., Palermo, D., Foo, S., & Vecchio, F. J. (2013). Behavior and modeling of superelastic shape memory alloy reinforced concrete beams.Engineering Structures, 49, 893-904.
2. Alam, M.S., Youssef, M.A. and Nehdi, M. (2007), Seismic behaviour of concrete beam-column joints reinforced with superelastic shape memory alloys, 9th Canadian Conf. on Earthquake Engineering, June, ON, Canada 2007, Paper no. 1125, 10 p.
3. ANSYS, Inc. Version 12.1.2012.
4. Brinson, L.e. 1993. One-dimensional constitutive behavior of shape memory alloys: Thermomechanical derivation with non-constant material functions and redefined martensite internal variable. Journal ofIntelligent Material Systems and Structures, 4: 229-242.
5. Bruno, S., and Valente, C. 2002. Comparative response analysis of conventional and innovative seismic protection strategies. Earthquake Engineering and Structural Dynamics, 31: 1067-1092.
6. Deng Z. C. and Li Q. B. (2002). Actuating effects of embedded Shape Memory Alloy on Concrete Beam, China civil engineering journal, 35(2), 41-47.
7. DesRoches, R., and Smith, B. 2004. Shape memory alloys in seismic resistant design and retrofit: a critical review of their potential and limitations. Journal of Earthquake Engineering, 8: 415-429.
8. Dolce, M. and Cardone, D. 2001a. Mechanical behaviour of shape memory alloys for seismic applications 1. Martensite and austenite Ni-Ti bars subjected to torsion. International Journal of Mechanical Sciences, 43: 2631-2656.
9. Dolce, M., Cardone, D., Marnetto, R., Mucciarelli, M., Nigro, D., Ponzo, F.C., and Santarsiero, G. 2004. Experimental Static and Dynamic Response of a Real RC Frame Upgraded with SMA Re-Centering and Dissipating Braces. Proceedings of the 13th World Conference on Earthquake Engineering, Canada, Paper no. 2878.

10. Goo, B.C., and Lexcellent, C. 1997. Micromechanics-based modeling of two-way memory effect of a single crystalline shape-memory alloy, Acta Materialia, 45: 727-737.
11. Hanson, N. W., and Connor, H. W. 1967. Seismic resistance of reinforced concrete beam-column joints. Journal of the Structural Division, American Society of Civil Engineers Proceedings, 5537, 93(ST5): 533-560.
12. Hardwicke, C.U. 2003. Recent developments in applying smart structural materials. JOM, ABIIINFORM Trade & Industry, 55: 15-16.
13. Hodgson, D.E. 2000. Fabrication, heat treatment and joining of nitinol components. Proceedings of the Third International Conference on Shape Memory and Superelastic Technologies, Pacific Grove, CA, pp. 11 - 24.
14. Hong-Nan Li, Di Cui1, Gangbing Song, and Y. L. Mo.(2006) , Experimental Investigation on Self-rehabilitation of Intelligent Concrete Beams Reinforced with Superelastic Shape Memory Alloys. Earth & Space 2006: ASCE Conf. Proc. doi:10.1061/40830(188)139.
15. Huang, M., and Brinson, L.C. 1998. Multivariant model for single crystal shape memory alloy behaviour. Journal of the Mechanics and Physics of Solids, 46: 1379-1409.
16. Indirli, M., Castellano, M.G., Clemente, P., and Martelli, A. 2001. Demo-application of shape memory alloy devices: The rehabilitation of the S. Giorgio Church Bell-Tower. Proceedings of SPIE, Vol. 4330, pp. 262-272.
17. Janke, L., Czaderski, C., Motavalli, M., and Ruth, J. 2005. Applications of shape memory alloys in civil engineering structures - overview, limits and new ideas. Materials and StructureslMateriaux et Constructions, 38: 578-592.
18. Leon, R.T., DesRoches, R., Ocel, J. and Hess, G. (2001). Innovative Beam Column Using Shape Memory Alloys, Proceeding of SPIE. 4330, 227-237.
19. Ma, N., and Song, G. 2005. Study of damping capacities ofnitinol shape memory alloys in martensite, austenite, and martensite-austenite co-existence phases. Proceedings of SPIE--the international society for optical engineering, Vol. 5760, pp. 142 -151.

20. Ma, N., Song, G., and Tarefder, R.A. 2004. Vibration control of a frame structure using shape memory alloy braces. Proceedings of the 3rd International Conference on Earthquake Engineering, Nanjing University of Technology, China, Chapter 4, Paper No. 12.
21. Maji A. K. and Negret I. (1998). Smart Prestressing with Shape Memory Alloy, Journal of Engineering Mechanics, 124(10), 1121-1128.
22. McCormick, J., and DesRoches, R. 2003. Seismic Response Using Smart Bracing Elements. Proceedings of the Extreme Loading Conference, Toronto, Canada. McNaney, J.M., Imbeni, V., Jung, Y., Papadopoulos, P., and Ritchie, R.O. 2003. An experimental study of the superelastic effect in a shape-memory nitinol alloy under biaxial loading. Mechanics of Materials, 35: 969 986.
23. Megget, L. M., and Park, R. 1971. Reinforced concrete exterior beam-column joints under seismic loading. New Zealand Engineering (Wellington), 26(11): 341-353.
24. Meinheit, D. F., and Jirsa, J. O. 1981. Shear strength of RC beam-column connections. Journal of Structural Division, ASCE, 107(ST. 11): 2227-2244.
25. Orgeas, L., Liu, Y., and Favier, D. 1997. Experimental study of mechanical hysteresis of NiTi during ferroelastic and superelastic deformation. Journal De Physique. IV : JP, 7 :C5-4 77 -C5-482.
26. Otsuka, K and Wayman, C.M. 1999. Shape memory materials, 1st Paperback Edition, Cambridge University Press, Cambridge. Park, G., Muntges, D.E., and Inman, D.J. 2003. Self-repairing joints employing shapememory alloy actuators. JOM: The Member Journal of the Minerals, Metals & Materials Society, 55: 33-37
27. Saiidi, M.S. and Wang, H.:2006, Exploratory Study of Seismic Response of Concrete Columns with Shape Memory Alloys Reinforcement. ACI Structural Journal, 103(3),436-443.
28. Saiidi, M.S., Zadeh, M.S., Ayoub, C. andItani, A.:2007, Pilot study of behavior of Concrete Beams Reinforced with Shape Memory Alloys. J Mater Civil Eng, 19(6), 454-61.

29. Shannag, M. J., and Alhassan, M. A 2005. Seismic upgrade of interior beam-column subassemblages with high-performance fiber-reinforced concrete jackets. ACI Structural Journal, 102(1): l31-l38.

30. Shin, M. and Andrawes, B. (2010b) Experimental Study of Concrete Columns confined with Shape Memory Alloys. 9th U.S. National and 10thCanadian Conference on Earthquake Engineering, Toronto, Canada, July*25-29.*

31. Song G., Mo Y. L., Otero K. and Gu H. (2004). Develop intelligent Reinforced Concrete Structures Using Shape Memory Alloys and Piezoceramics, The third international conference on Earthquake Engineering, Nanjing, China.

32. Song, G., Ma, N., and Li, H.-N. 2006. Application of shape memory alloys in civil structures. Engineering Structures, 28: 1266-1274.

33. Song, G., Mo, Y.L., Otero, K. and Gu, H. 2005. Develop intelligent reinforced concrete structures using shape memory alloys and piezoceramics. Proceedings of the 3rd International Conference on Earthquake Engineering, China, Chapter 5, Paper No. 11..

34. Soroushian, P., Ostowari, K., Nossoni, A., and Chowdhury, H. 2001. Repair and strengthening of concrete structures through application of corrective posttensioning forces with shape memory alloys. Transportation Research Record, 1770: 20-26.

35. Ullakko, K. 1996. Magnetically controlled shape memory alloys: a new class of actuator materials. Journal of Materials Engineering and Performance, ASM International, 5: 405-409.

36. Uzumeri, S. M., and Seckin, M. 1974. Behaviour of reinforced concrete beam-column joints subjected to slow load reversals. Report 74-05, Department of Civil Engineering, University of Toronto, Toronto, Ontario, Canada, 85 p.

37. Wilson, J.C and Wesolowsky, MJ. 2005. Shape memory alloys for seismic response modification: A state-of-the-art review. Earthquake Spectra, 21: 569-601.

VITAE

Name :MOHAMMED ABDULKAREM AL-HURI

Nationality :YEMENI

Date of Birth :12/7/1986

Email :mdhoury@gmail.com

Address :KFUPM

Academic Background :CIVIL ENGINEERING (STRUCTURES)